Investigation of the impact of extraterrestrial energetic particles on stratospheric nitrogen compounds and ozone on the basis of three dimensional model studies

Nadine Wieters

Universität Bremen 2013

Investigation of the impact of extraterrestrial energetic particles on stratospheric nitrogen compounds and ozone on the basis of three dimensional model studies

Dem Fachbereich für Physik und Elektrotechnik
der Universität Bremen

zur Erlangung des akademischen Grades Dr. rer. nat.
vorgelegte Dissertationsschrift

von
Dipl. Phys. Nadine Wieters

1. Gutachter: Prof. Dr. J. Notholt
2. Gutachter: Prof. Dr. C. von Savigny

Eingereicht am: 12.2.2013
Kolloquium: 17.6.2013

1. Gutachter: Prof. Dr. J. Notholt
Institut für Umweltphysik
Universität Bremen
Otto-Hahn-Allee 1
28359 Bremen

2. Gutachter: Prof. Dr. Ch. von Savigny
Institut für Physik
Ernst-Moritz-Arndt-Universität Greifswald
Felix-Hausdorff-Str. 6
17489 Greifswald

Eingereicht am: 12.2.2013
Tag des Promotionskolloquiums: 17.6.2013

für meine Familie

Abstract

As a result of solar events like Coronal Mass Ejections (CMEs) and solar flares, highly energetic charged particles including protons and electrons can precipitate in the direction of the Earth. Having sufficient energies, these particles can penetrate down to the middle atmosphere and lead to a change in the chemical composition of the atmosphere. In particular during strong events, these charged particles induce an ionisation in the atmosphere that can reach down to the lower stratosphere. This ionisation is followed by a fast positive ion chemistry that causes a strong increase in reactive HO_x (H, OH, HO_2) an NO_x (N, NO, NO_2). HO_x and NO_x constituents eventually destroy O_3 in catalytical reaction cycles. Furthermore, NO_x is long-lived during polar winter and can be transported into the middle and lower stratosphere, where it can contribute to the O_3 depletion.

The increase in NO_x in the upper and middle atmosphere due to solar events and the consequential depletion of O_3 has been observed as during the Solar Proton Event (SPE) in October/November 2003 by satellite instruments. In atmospheric models, the generation of HO_x and NO_x can be well described by parametrisations to include in neutral models. Whereas other changes, for instance in chlorine compounds, can not be described sufficiently by this parametrisation.

The purpose of this PhD thesis is, to investigate the impact of strong solar particle events on the abundance in NO_x and O_3 in the stratosphere and mesosphere on the basis of three-dimensional model studies.For this purpose a three-dimensional Chemistry and Transport Model (CTM) has been extended to the upper atmosphere (lower thermosphere). To include the processes in the mesosphere and lower themosphere a new meteorological data set has been implemented to the model. To describe the ionising effect of energetic particle on the atmosphere, three-dimensional ionisations rates from Atmospheric Ionization Module Osnabrück (AIMOS) were implemented into the model.

The previous version of the CTM uses a so-called family approach to solve the chemical equations. This family approach is a appropiate assumption in the stratosphere, but cannot be applied in the mesosphere and thermosphere. To consider chemical processes in the upper atmosphere a non family version of the chemical code have been implemented into the CTM.

To investigate the impact of precipitating particles on chlorine compounds, additional parametrisations have been implemented in a case model study from the University of Bremen Ion Chemistry (UBIC) model.

With this extended version of the three-dimensional CTM of the stratosphere, mesosphere, and lower thermosphere, different model simulations for the period between 2002-2009 have been performed. This period covered the maximum phase of the 23. solar cycle with several medium and strong SPEs as well as the rather quiet declining phase of cycle 23 and the beginning of cycle 24.

Contents

List of Figures

List of Tables

Part I

Introduction & Fundamentals

1 Introduction and motivation

During Energetic Particle Precipitation (EPP) events, highly energetic charged particles from different populations (protons and electrons) and origins (solar and geomagnetic) enter the polar atmosphere. The impact of this particle precipitation on the chemical composition of the middle and upper atmosphere (stratosphere, mesosphere, and lower thermosphere) has been investigated in the framework of this PhD thesis on the basis of model simulation studies. Model studies, thereby, offer the possibility to consider different aspects apart from each other. For instance, the comparison of model simulations for different scenarios, for instance, with and without the consideration of particle events, or considering different particle populations separately. Besides the possibilities that model studies provide to grant the study of EPP events with respect to different aspects, the study of the impact of EPP events on the chemical composition and in particular on 'ozone distributions in the stratosphere at high latitudes in periods following certain solar proton events may be very important in validating photochemical models of the stratosphere' (Crutzen *et al.*, 1975).

EPP events can be divided into two types regarding the particle population (proton or electrons); Solar Proton Events (SPEs) and Energetic Electron Precipitation (EEP) events. Such events can be single events, since they originate from different source processes, or accompany each other, for instance during the large SPE 2003.

The direct initial chemical effect of the proton and electron precipitation events is the ionisation of the main compounds in the atmosphere, namely N_2 and O_2. The altitude range of the main ion production, thereby, depends on the energies of the precipitating particles. During very strong SPEs, the particles can have energies in the range of a few keV up to some hundred MeV and precipitate down to altitudes below 30 km. An example of such a strong event is the SPE during October/November 2003, also referred to as the Halloween Storm 2003 or SPE 2003.

The investigations of precipitating particles and their impact on the abundance on atmospheric constituents have been carried out since the 1970s by several authors, e.g. Weeks *et al.* (1972), Crutzen *et al.* (1975), Swider & Keneshea (1973). The production of ions and following reactions will lead to the production of hydrogen and nitrogen species (H, OH, HO_2 (HO_x) and N, NO, NO_2 (NO_x)). These species can destroy O_3 through catalytic reactions (Lary, 1997). Hydrogen species are short-lived and destroy O_3 mainly above 45 km, whereas nitrogen species have a longer life-time, especially under dark conditions during polar winter. Because of the relatively long life-time of NO_x during polar winter, these compounds can be transported within the polar vortex down to the stratosphere and can destroy O_3 there for a relatively long time period. The expected effects of the different particle populations are for strong SPEs primarily in the stratosphere and mesosphere and for EEP events mainly in the mesosphere and thermosphere. However, the impact of SPEs and EEP events can also become important for the stratosphere when dynamical processes yield their impact to lower altitudes. For instance, during polar winter conditions when enhanced NO_x values are transported into the stratosphere within the polar vortex. But also through downward processes after Sudden Stratospheric Warmings (SSWs) when enhanced NO values produced in the thermosphere propagate down to the stratosphere. This is known as the indirect effect of EEP events (Randall *et al.*, 2005) and can cause significant NO enhancements even during periods with low solar and geomagnetic activity.

Many model studies have been carried out with respect to an enhanced proton flux, e.g. studies about the Halloween SPE 2003 by different authors (e.g. Jackman *et al.*, 2005a). These model results show that during very strong events, such as the SPE 2003, the O_3 depletion in the lower mesosphere and upper stratosphere due to the increase in HO_x can be of more than 70%. The impact of NO_x on the O_3 abundance is most important below 45 km, and the effect of the downward transport of NO_x during polar winter can cause O_3 depletion's of around 20% in the stratosphere, for several weeks past the event. The decrease in O_3 abundance can even persist for up to several months after large SPEs (Jackman *et al.*, 2005a). Therefore, EPP events during polar winter are of particular importance to be investigated, since the decrease in O_3 abundance in lower altitudes arises from a combination of solar activity and atmospheric dynamics. On the other way around, EPP events can have a significant impact on atmospheric dynamics (Krivolutsky *et al.*, 2006; Jackman *et al.*, 2007; Becker & von Savigny, 2010) and cause temperature changes even at the Earth's surface (Seppälä *et al.*, 2009).

The production of HO_x and NO_x constituents due to the ionisation during particle events can be parametrised to be implemented in neutral atmospheric chemistry models. Such a parametrisation, based on studies by, e.g. Solomon *et al.* (1981), Porter *et al.* (1976), shows good results in simulating the effect on these constituents during EPP events in the stratosphere and mesosphere and especially during SPEs, (e.g. Jackman *et al.* (2005a)). This parametrisation reproduces the formation of HO_x and NO_x due to reactions involving positive ions which are produced during the events. In addition, observations (von Clarmann *et al.*, 2005) as well as model studies (Winkler *et al.*, 2009, 2011) indicate that also reactions with negative ions and recombination reactions can lead to an increase in reactive chlorine compounds. This effect is rather short-lived and more confined to the stratosphere.

The above mentioned impacts in the stratosphere and lower mesosphere are mainly caused during large SPEs, since the highly energetic proton fluxes have a direct impact in that altitude region. Besides SPEs, electron precipitation during EEP events has also an impact on the upper atmosphere and contributes to the formation of HO_x and NO_x. Results of model simulations including both particle populations (protons and electrons) suggest that EEP events also have a direct effect of the electrons in the lower mesosphere and upper stratosphere (Wissing *et al.*, 2010). Observations, on the other hand, give no evidence of such a direct impact of electrons in these altitude regions that are not related to transport processes from above (Funke *et al.*, 2011). In the model simulations this direct impact is probably due to an overestimation in the implemented ionisation rates in the altitude range between 50-70 km (J. M. Wissing, personal communication). However, a case model study indicates that this overestimation leads only to a very small enhancement in the production of, e.g. NO_2. Precipitating electrons do have a large impact above 70 km, in the mesosphere and thermosphere during EEP events as well as during relatively undisturbed conditions, due to a more or less constant background flux of auroral electrons into the thermosphere and upper mesosphere that produces nitrogen compounds like NO. During and after certain dynamical conditions, such as SSWs, this NO due to auroral electron precipitation can be transported into the stratosphere and can contribute to O_3 depletion there. To take this impact into account in model simulations, the region of the upper mesosphere and lower thermosphere has to be considered in the model.

A consequential effect of the precipitating particles on O_3 abundance as well as on hydrogen compounds is an influence in changing the radiative and chemical atmospheric heating rates. A decrease in radiative heating due to O_3 losses in the mesosphere can lead to a change in the atmospheric residual circulation (Becker & von Savigny, 2010).

The overall structure of this thesis is composed of three thematic parts. This current first part (Part I Introduction & Fundamentals) includes three chapters starting with this Introduction and motivation followed by reviews of the physical and chemical properties of the Earth's atmosphere (Chapter 2) and of the interaction between the Earth's atmosphere and processes originating at the Sun (Chapter 3). In Chapter 4 some basics about atmospheric modelling are given. The second part (Part II Model description and further development) presents the methods of the model and its main components in Chapter 6. The further developments of the model are discussed in Chapter 7. The input data used to run the model are briefly described in Chapter 8. The carried out model simulations and case studies are described in Chapter 9. Part III Results & Discussion presents the results and findings of this study. Is is subdivided into the following themed sections. It begins with a introductory survey and summary of Part III in Chapter 11. Chapter 12 presents the results of model simulations about the impact of energetic particles on the chemical composition for the Halloween event during October/November 2003. The change in abundance of several constituents is presented. A brief comparison to observations is also presented in this chapter. Chapter 13 compares several different particle events during the simulated period 2002-2009. The focus will be on species like HO_x, NO_x, and O_3. Chapter 14 focuses on the different impacts due to different particle populations. It will show results on the different direct and indirect effects of proton as well as electron precipitation events in the stratosphere and mesosphere. It is also focused on the behaviour of the different model versions and their different impacts on the chemical compositions during particle events. In Chapter 15 the impact of parametrised production rates on the activation of reactive chlorine compounds will be investigated. Chapter 16 will present results of the impact on the change in atmospheric chemical composition on the heating in the atmosphere and discusses and gives an outlook on further investigations on possible impacts on dynamical processes during particle events. Finally Chapter 17 gives a summary and concludes the findings of this study.

2 Physical and chemical properties of the Earth's atmosphere

In this Chapter, the main structure of the atmosphere and some physical and chemical basic properties are discussed.

2.1 The main structure and composition of the atmosphere

2.1.1 The vertical structure

The vertical structure of the atmosphere can be divided into layers by different properties: mixing, temperature, and ionisation. Below 100 km the mixing of the atmosphere is mainly due to turbulent mixing and collision processes of air molecules. The molar mass is independent of the altitude. This region is called the **homosphere**. Above the homosphere diffusion dominates. This region is called the **heterosphere**, and the molar mass is dependant on altitude.

The homosphere can be divided into layers depending on the vertical temperature profile.

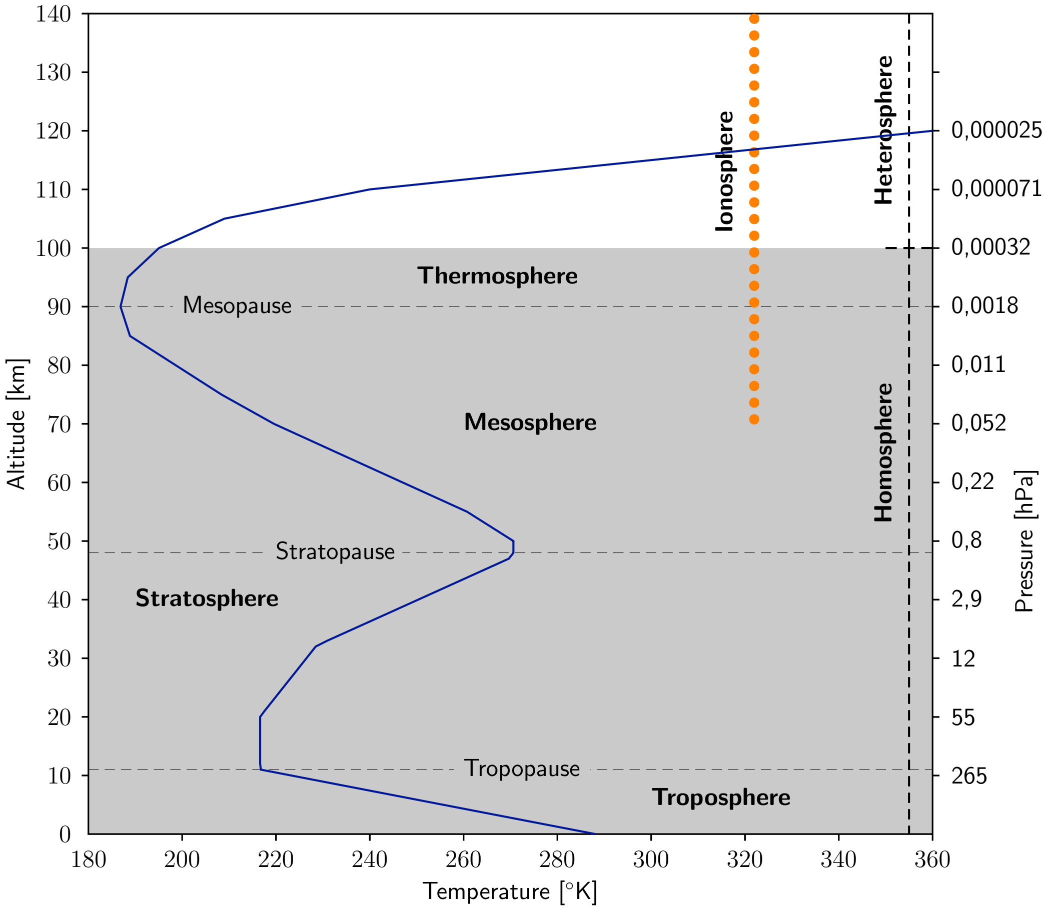

Figure 2.1 *Display of the Earth's atmospheric layers and the vertical temperature profile. Adapted from Brasseur & Solomon (2005). Temperature data for the U.S. Standard Atmosphere are taken from Jacobson (2005) (grey shaded region).*

A sketch of the atmosphere and its layers is shown in Figure 2.1. Due to the temperature gradient, the atmosphere is divided into four layers: troposphere, stratosphere, mesosphere, and thermosphere. The lowermost layer is called the troposphere. Within this layer, the temperature decreases by approx. 0.65 K/100 m until it reaches the tropopause in approx. 11 km (17 km at the equator and 7 km near the poles during polar winter). Then the temperature increases in the stratosphere. This is mainly due to the absorption of UV radiation by ozone. Ozone also has its maximum in terms of volume mixing ratio in the stratosphere at approx. 25-32 km altitude. This ozone maximum forms a thin layer which is called the ozone-layer. It shields the lower atmosphere and the Earth's surface below from UV radiation. Within the mesosphere, the temperature decreases again, mainly because the ozone density also decreases. In the mesosphere the temperature increases to very high values due to the absorption of short wave radiation by oxygen and nitrogen.

2.1.2 The basic composition

The basic composition of the Earth's atmosphere is summarised in Table 2.1. It contains mainly molecular nitrogen (N_2) and molecular oxygen (O_2). Molecules with only a very small abundance in the atmosphere are called trace gases. Although the amount in the atmosphere can by very small, these trace gases have a large influence on atmospheric chemical as well as dynamical processes. For instance, mainly O_3 determines the whole temperature structure in the stratosphere.

Table 2.1 *Main chemical composition of the Earth's atmosphere. Values taken from Salby (2012).*

Constituent	Mixing ratio
Molecular nitrogen (N_2)	0.7808
Molecular oxygen (O_2)	0.2095
Water vapour (H_2O)	$\leq$0-0.030
Argon (A)	0.0093
Carbon dioxide (CO_2)	380 ppmv
Ozone (O_3)	10 ppmv
Methane (CH_4)	1.8 ppmv
Nitrous oxide (N_2O)	320 ppbv
Carbon monoxide (CO)	70 ppbv
Nitric oxide NO	0.1 ppbv
Trichlorofluoromethane (CFC-11, $CFCl_3$)	0.2 ppbv
Dichlorodifluoromethane (CFC-12, CF_2Cl_2)	0.5 ppbv

2.2 Basic principles of atmospheric physics and chemistry

In this Section the basic principles in atmospheric physics and chemistry that are important for this study are described.

2.2.1 Volume mixing ratio - parts by volume

The amount of, for instance, an atmospheric trace gas can be described by the *volume mixing ratio (vmr)*. This is the fraction of the total number of molecules of a trace gas in a unit volume of air referred to a certain number of air molecules. For example, 10 ppmv of ozone means that there are 10 molecules of ozone per every 10^6 molecules of air in a unit volume of air. Since the volume mixing ratio is a ratio, it is a dimensionless quantity. One advantage of the volume mixing ratio is that it remains constant when the air density changes. Therefore, the volume mixing ratio in an air parcel will not change only due to the transport of that parcel. The mixing ratios used in this study are abbreviated in Table 2.2.

Table 2.2 *Abbreviations of volume mixing ratios.*

ppmv	parts per million by volume	10^{-6}
ppbv	parts per billion by volume	10^{-9}
pptv	parts per trillion by volume	10^{-12}

2.2.2 Total ozone column

The total abundance of ozone in an air column that reaches from the Earth's surface to the top of the atmosphere can be referred to as the total ozone column. It is defined as the total number of ozone molecules in an overhead column with a cross-sectional area of 1 cm^2. The amount of ozone molecules in this column can be specified in terms of *Dobson Units (DUs)*. One DU is the amount of $2.7 \cdot 10^{16}$ molecules per cm^2. If 1 DU would be brought to ground level pressure, it would expand a column of an area of 1 cm^2 and a height of 0.01 mm.

2.2.3 Potential temperature

The potential temperature θ_p represents the temperature that an air parcel would have if it is compressed adiabatically to ground level pressure (p_0=1000 hPa). It is defined as

$$\theta_p = T\left(\frac{1000\ \text{hPa}}{p_d}\right)^{R/c_p} \tag{2.1}$$

where R is the gas constant and c_p the specific heat of dry air.

In atmospheric modelling, the potential temperature can be used as the vertical coordinate. In a θ_p coordinate system, the vertical advection in the stratosphere can be derived from diabatic heating rates, since adiabatic processes are conserved along isentropes (level of constant potential temperature).

2.3 Ozone chemistry of the stratosphere and mesosphere

The main focus in this study is the impact of Energetic Particle Precipitation (EPP) on ozone. This Section will therefore mainly focus on ozone related chemistry, in particular in polar regions of the stratosphere and mesosphere, since the major effect of EPP events are in the polar middle and upper atmosphere.

Ozone chemistry includes all three main principle chemical reaction types; photochemical reactions or photodissociation

$$\mathrm{AB} + h\nu \rightarrow \mathrm{A} + \mathrm{B},$$

gas phase reactions

$$\mathrm{A} + \mathrm{B} \rightarrow \mathrm{C} + \mathrm{D},$$

$$\mathrm{A} + \mathrm{B} + M \rightarrow \mathrm{AB} + M.$$

As described above, ozone is the main driver of the temperature profile in the stratosphere. It absorbs UV radiation, which in turn protects plants and life forms at the Earth's surface from this possible harmful radiation.

In the stratosphere, the reactions of ozone production and destruction were first stated by Chapman (1930), and are therefore, named the *Chapman cycle.* This cycle includes the following reactions:

$$\mathrm{O_2} + h\nu \longrightarrow \mathrm{O} + \mathrm{O} \tag{R 2.2}$$

$$\mathrm{O} + \mathrm{O_2} + M \longrightarrow \mathrm{O_3} + M \tag{R 2.3}$$

$$\mathrm{O_3} + h\nu \longrightarrow \mathrm{O} + \mathrm{O_2} \tag{R 2.4}$$

$$\mathrm{O} + \mathrm{O_3} \longrightarrow 2\mathrm{O_2} \tag{R 2.5}$$

$$\mathrm{O} + \mathrm{O} + M \longrightarrow \mathrm{O_2} + M \tag{R 2.6}$$

Ozone is produced through photolysis of molecular oxygen (R 2.2) forming atomic oxygen that reacts in a following three-body reaction with molecular oxygen to form ozone (R 2.3). It is destroyed also through photolysis forming atomic and molecular oxygen (R 2.4), atomic oxygen then reacts with O_3 forming again molecular oxygen (R 2.5).

The formation of O_3 increases until it reaches its maximum in terms of vmr at around 30 km altitude. This maximum is called the *ozone layer.* The ozone layer with respect to number density lies in an altitude that is lower than for vmr at around 25 km. Since atmospheric density and pressure decrease exponentially and the production rate of reaction (R 2.3) is pressure dependent, the amount of molecular oxygen is decreasing as well as the formation of O_3 through O_2 photolysis. But the ozone profile can not be explained only by reactions (R 2.3) and (R 2.4) alone. It was found by, e.g. Bates & Nicolet (1950), Crutzen (1971), that odd hydrogen and odd nitrogen compounds are also involved in the catalytic destruction of ozone, as discussed below.

A second ozone maximum in the mesosphere has already been observed by, e.g. Evans & Llewellyn (1972). Smith & Marsh (2005) discussed processes that lead to this second ozone maximum at the mesopause region. They found, that the second ozone maximum at the mesopause at around 85-90 km is due to a maximum in atomic oxygen, and that it is very dependent on temperature. They computed night-time O_3 values of up to 15 ppm at 0.001 hPa (see Smith & Marsh (2005), Figure 4).

Marsh *et al.* (2001) report a tertiary ozone maximum at around 72 km altitude. It occurs in the middle mesosphere in winter high-latitudes, just equatorward of the polar night terminator and when catalytic ozone losses due to odd hydrogen compounds (see below) are reduced. This ozone maximum is then produced through photolysis of molecular oxygen and following reaction with atomic oxygen (reactions R 2.2 and R 2.3). Sofieva *et al.* (2009) presented observations of such a tertiary ozone maximum during different northern polar winters of 2-4 ppmv.

The catalytic destruction cycles of stratospheric ozone were thoroughly investigated by Lary (1997), and can be summarised as follows in respect to the most important cycles involved during EPP events. Since the main atmospheric change due to EPP events is the production of nitrogen and hydrogen compounds, it is focused here on those catalytic cycles, that include these compounds, namely H, OH, HO_2, N, NO, and NO_2. Another part of this study investigates the impact of negative ion chemistry on the production of chlorine species during SPEs. Therefore the catalytic cycles involving chlorine compounds, like HCl, ClO, Cl, and $ClONO_2$ is also discussed here. The reaction cycles are taken from Lary (1997).

Catalytic cycles involving HO_x (H, OH, HO_2) are

OH/HO_2, HO_x cycle 1

$$\mathrm{OH + O_3 \longrightarrow HO_2 + O_2} \tag{R 2.7}$$
$$\mathrm{HO_2 + O_3 \longrightarrow OH + 2\,O_2} \tag{R 2.8}$$

H/OH/HO_2, HO_x cycle 4

$$\mathrm{H + O_2 \xrightarrow{\mathit{M}} HO_2} \tag{R 2.9}$$
$$\mathrm{HO_2 + O(^3P) \longrightarrow OH + O_2} \tag{R 2.10}$$
$$\mathrm{OH + O(^3P) \longrightarrow H + O_2} \tag{R 2.11}$$

OH/HO_2, HO_x cycle 5

$$\mathrm{OH + O_3 \longrightarrow HO_2 + O_2} \tag{R 2.12}$$
$$\mathrm{HO_2 + O(^3P) \longrightarrow OH + O_2} \tag{R 2.13}$$

One HO_x cycle also includes HO_2 and also ClO, and therefore, is a link between hydrogen and chlorine chemistry:

HO_2/ClO, HO_x cycle 2

$$\mathrm{ClO + HO_2 \longrightarrow HOCl + O_2} \tag{R 2.14}$$
$$\mathrm{HOCl + h\nu \longrightarrow Cl + OH} \tag{R 2.15}$$
$$\mathrm{Cl + O_3 \longrightarrow ClO + O_2} \tag{R 2.16}$$
$$\mathrm{OH + O_3 \longrightarrow HO_2 + 2\,O_2} \tag{R 2.17}$$

Other catalytic cycles involving chlorine compounds are

Cl/ClO, ClO_x cycle 1

$$\mathrm{ClO + O(^3P) \longrightarrow Cl + O_2} \tag{R 2.18}$$
$$\mathrm{Cl + O_3 \longrightarrow ClO + O_2} \tag{R 2.19}$$
$$\tag{R 2.20}$$

ClO/ClO, ClO_x cycle 2

$$ClO + ClO \xrightarrow{M} Cl_2O_2 \tag{R 2.21}$$
$$Cl_2O_2 + h\nu \longrightarrow Cl + ClOO \tag{R 2.22}$$
$$ClOO \xrightarrow{M} Cl + O_2 \tag{R 2.23}$$
$$2\,x(Cl + O_3 \longrightarrow ClO + O_2 \tag{R 2.24}$$

Cycles that combine the chlorine and the nitrogen chemistry are

Cl/NO_2, ClO_x cycle 3

$$ClO + NO \longrightarrow Cl + NO_2 \tag{R 2.25}$$
$$NO_2 + O(^3P) \longrightarrow NO + O_2 \tag{R 2.26}$$
$$Cl + O_3 \longrightarrow ClO + O_2 \tag{R 2.27}$$

ClO/NO_2, ClO_x cycle 4

$$ClO + NO_2 \xrightarrow{M} ClONO_2 \tag{R 2.28}$$
$$ClONO_2 + h\nu \longrightarrow Cl + NO_3 \tag{R 2.29}$$

The other very important cycle during SPE events is the NO_x cycle:

NO/NO_2, NO_x cycle 1

$$NO + O_3 \longrightarrow NO_2 + O_2 \tag{R 2.30}$$
$$NO_2 + O(^3P) \longrightarrow NO + O_2 \tag{R 2.31}$$

Lary (1997) also discussed the effectiveness of each catalytic cycle. Their result can be summarised as follows: O_3 is catalytically destroyed by odd hydrogen species mainly above 45 km, and due to catalytic reactions involving odd nitrogen species below 45 km.

The effect on ozone through the catalytic destruction cycle due to odd nitrogen shows a diurnal dependence. Figure 2.2 shows the diurnal variation of different nitrogen species. For instance, NO_2 shows a clear diurnal cycle, since it is destroyed by photolysis during day-time. During night-time conditions, the life-times of NO_x compounds are significantly enhanced, so that the catalytic destruction cycle of ozone during polar night in high latitudes plays an important role in ozone chemistry during EPP events. The long life-times of NO_x compounds during polar night in high latitudes make dynamical processes become also a significant impact on ozone loss also in the middle and lower stratosphere, since NO_x is transported to lower altitudes within the polar vortex (see Section 2.5). During very strong SPEs, this may lead to ozone depletion even in altitudes around 40 km, as will be discussed in detail in the results part of this study.

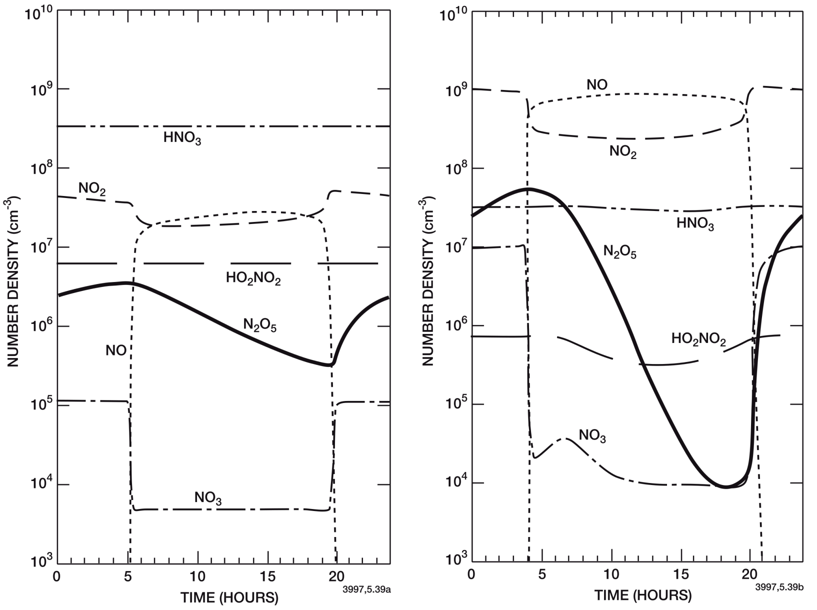

Figure 2.2 *Diurnal variation for different nitrogen species for May at 65°N at 20 km (left panel) and 40 km (right panel). Figure taken from Brasseur & Solomon (2005, Chap. 5, Pg. 346, Fig. 5.39); with kind permission from Springer Science and Business Media.*

2.4 Heating mechanisms in the stratosphere and mesosphere

There are different heating mechanisms in the atmosphere. Joule heating, radiative heating and cooling, chemical heating, convection, latent heat release, and transport of sensible heat. The two latter mechanisms are more relevant for the troposphere and heat exchange with the Earth surface. Relevant for the stratosphere, mesosphere, and lower thermosphere are the first three mechanisms, (i) Joule heating due to particle precipitation, (ii) heating and cooling through absorption of short-wave and long-wave radiation and emission of long-wave radiation, and (iii) heating due to exothermic chemical reactions.

2.4.1 Radiative heating and cooling

Heating in the atmosphere can occur through absorption of short-wave UV radiation and absorption of long-wave infrared radiation. Cooling is driven by the emission of long-wave infrared radiation. The main heating mechanism in the stratosphere and lower mesosphere is the absorption of UV radiation by O_3 (Kiehl & Solomon, 1986). Different UV wavelength regions are absorbed by O_3 at different altitudes:

- $>$ 40 km: absorption by O_3 at 240-300 nm (Hartley band)
- $<$ 32 km: absorption by O_3 at 397-730 nm (Chappuis band)
- 25-32 km: absorption by O_3 at 305-397 nm (Huggins band) and 240-300 nm (Hartley band)

The primary absorption mechanism of O_3 in the stratosphere (30-60 km) is photo dissociation of O_3 through reaction (R 2.4). O_3 can also absorb infrared radiation in the 9.6 μm

Table 2.3 *Exothermic reactions involving odd hydrogen and oxygen, its reaction rate constants and exothermicity ΔE. The values are taken from Mlynczak & Solomon (1991).*

Reaction	Rate constant (k_r)	Heat of reaction (-ΔE kcal/mole)	
$O + OH \longrightarrow H + O_2$	$2.2 \cdot 10^{-11} \exp(120/T)$ cm^{3}s^{-1}	-16.77	R 2.32
$H + O_2 \xrightarrow{M} HO_2$	$5.7 \cdot 10^{-32} \exp(300/T)^{1.6}$ cm^{3}s^{-1}	-49.10	R 2.33
$H + O_3 \longrightarrow OH + O_2$	$1.4 \cdot 10^{-10} \exp(-470/T)$ cm^{3}s^{-1}	-76.90	R 2.34
$O + HO_2 \longrightarrow OH + O_2$	$3.0 \cdot 10^{-11} \exp(200/T)$ cm^{3}s^{-1}	-53.27	R 2.35
$O + O \xrightarrow{M} O_2$	$4.7 \cdot 10^{-33}(300/T)^2$ cm^{6}s^{-1}	-119.40	R 2.36
$O + O_2 \xrightarrow{M} O_3$	$6.0 \cdot 10^{-34}(300/T)^{2.3}$ cm^{6}s^{-1}	-25.47	R 2.37

band. This infrared radiation is emitted from molecules below and then reabsorbed by O_3. A second heating mechanism by absorption is the photo dissociation of O_2 through reaction (R 2.2) in the mesosphere and lower thermosphere (50-110 km).

Cooling in the atmosphere is driven mainly due to the emission of long-wave infrared radiation. The most important emitter is CO_2 in the 15 μm band. The amount of heating and cooling in the atmosphere can by described through *heating rates* in the units [K/day]. The radiation scheme that is used to calculate such heating rates in the model calculations is described in Section 6.4.

2.4.2 Chemical heating due to exothermic reactions

Mlynczak & Solomon (1991) calculated and compared radiative and chemical heating rates in the middle atmosphere, between 50-105 km, by different processes and for different exothermic reactions involving odd hydrogen and oxygen species. These six exothermic reactions are:

$$O + OH \longrightarrow H + O_2 \tag{R 2.32}$$

$$H + O_2 + M \longrightarrow HO_2 + M \tag{R 2.33}$$

$$H + O_3 \longrightarrow OH + O_2 \tag{R 2.34}$$

$$O + HO_2 \longrightarrow OH + O_2 \tag{R 2.35}$$

$$O + O + M \longrightarrow O_2 + M \tag{R 2.36}$$

$$O + O_2 + M \longrightarrow O_3 + M \tag{R 2.37}$$

Following Mlynczak & Solomon (1991), the calculation of the heating rate ($\frac{\partial T}{\partial t}$) of a bimolecular reaction, of which the total exothermicity is converted into heat, is given by:

$$\frac{\partial T}{\partial t} = \frac{2}{7} \frac{k_r [R_1][R_2] \Delta E}{k_B M}, \tag{2.38}$$

where k_r is the reaction rate, $[R_1]$ and $[R_2]$ are the concentrations of the reactants, and ΔE is the exothermicity of the particular reaction, k_B is the Boltzmann's constant, and M is the total number density. For a termolecular reaction, the heating rate is calculated by

$$\frac{\partial T}{\partial t} = \frac{2}{7} \frac{k_r [R_1][R_2] \Delta E}{k_B}. \tag{2.39}$$

The exothermicities or heat of reaction (ΔE) for the considered reactions involving odd hydrogen and oxygen species are listed in Table 2.3.

2.4.3 Non-LTE

A molecule is in Local Thermodynamical Equilibrium (LTE) ‘if the population among its energy levels is determined predominantly by collisions.’ (López-Puertas & Taylor, 2001). Non-LTE conditions occur when the rate of collisions between the molecules becomes low due to low atmospheric density (Smith, 2012), and the population of energy levels is ‘dominated by radiative processes (absorption and emission of photons)’ (López-Puertas & Taylor, 2001). For CO_2, for instance, non-LTE conditions lead to reduced infrared CO_2 cooling rates over the LTE situation (Smith, 2012). The non-LTE effect becomes important in altitudes above ~80 km (Feofilov & Kutepov, 2012).

2.5 An overview on atmospheric dynamics

Following Smith (2012), the mean circulation in the atmosphere can be summarised as follows:

- The zonal mean net mass flux/circulation in the atmosphere is described by the Transformed Eulerian Mean (TEM) or residual circulation.
- It is driven by dissipating waves (Rossby waves, gravity waves, Kelvin waves).
- This mean circulation is referred to in the stratosphere as the *Brewer-Dobson circulation*.
- In the lower stratosphere, the mean circulation goes from the tropics to the poles; air that rises in the tropics, enters the stratosphere, and moves toward both, summer and winter pole (see Figure 2.3).
- In the upper stratosphere, the mean circulation transports air from the summer pole toward the winter pole.
- Descending air above the winter pole is referred to as the *polar vortex.*
- The circulation in the mesosphere is driven by dissipation and/or breaking of gravity waves.

The mean circulation leads to the following zonally averaged temperature distribution:

- very low temperatures in the tropical tropopause
- very low temperatures in the summer mesopause

Figures 2.4(a) and 2.4(b) show zonal mean temperatures from two dynamical models, the LIMA model (Berger, 2008) and the KMCM (Becker, 2009), respectively, for January and July. Both models show the temperature patterns described above: low temperatures in the tropopause at around 15 km in the tropics, very low temperatures in the summer mesopause around 85-90 km and a maximum in the summer stratopause at around 50 km.

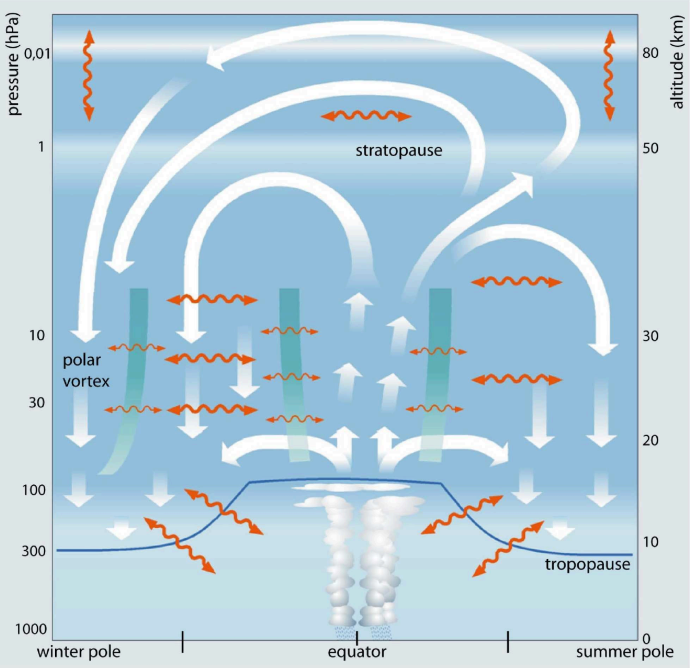

Figure 2.3 *Illustration of the mean atmospheric circulation. Adapted from Bönisch* et al. *(2011).*

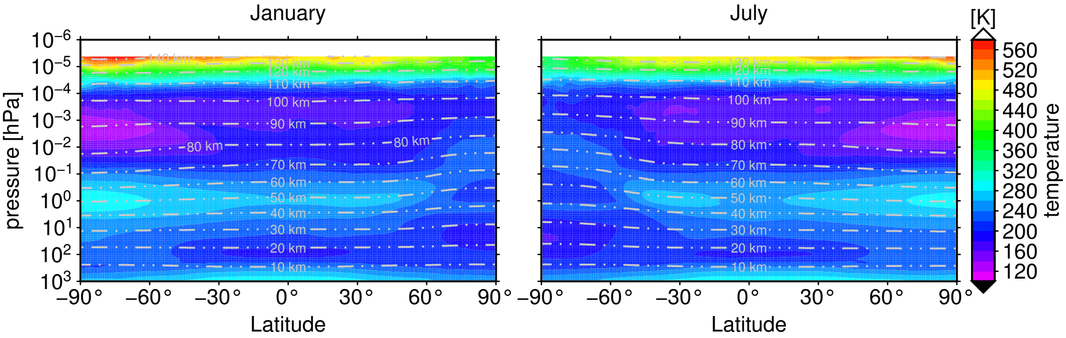

(a) LIMA zonal mean temperatures for 1 January 2009 (left) and 1 July 2009 (right).

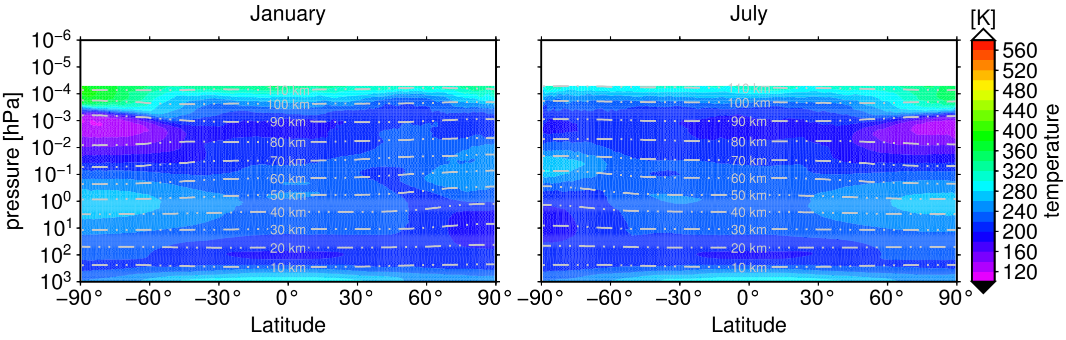

(b) KMCM zonal mean temperatures for January (left) and July (right).

Figure 2.4 *Zonal mean temperatures as calculated with the LIMA model (upper panel) and the KMCM model (lower panel).*

3 The Sun and its interaction with the Earth's atmosphere

The Sun has an important influence on the Earth's environment and on life. It is the main natural energy source at the Earth's surface. Besides the supply of energy, the Sun can influence the Earth through different processes that originate at the Sun and influence and cause disturbances in geomagnetic processes. Such processes can have impacts on the Earth in different forms and magnitudes. To describe these solar and geomagnetic processes, the structure of the Sun, its magnetic field, as well as the Earth's magnetic field and the interaction between solar and geomagnetic field will be described briefly in the following.

3.1 The structure of the Sun and its magnetic field

A sketch of the Sun's main structure is presented in Figure 3.1(a). The Sun roughly consists (inside out) of an inner core, the radiation zone, the convection zone, and the photosphere. The photosphere is the visible surface of the Sun. It is followed by the Sun's atmosphere that is structured in four layers: the chromosphere, the transition zone (not shown), the corona, and the heliosphere. In the inner core, the energy is produced through fusion of atomic hydrogen into helium. In the following radiation zone, energy travels outward from the core by thermal radiation. In the convection zone, heat will be transported to the Sun's

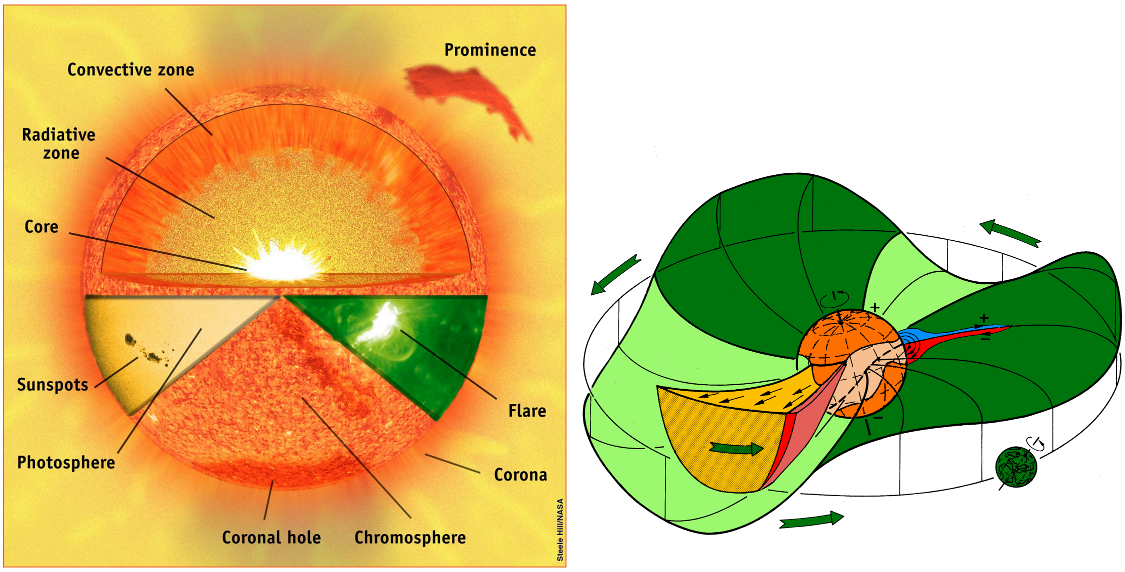

(a) Structure of the Sun.

(b) The 'Ballerina' model.

Figure 3.1 *(a) The parts of the Sun. This gives a basic overview of the Sun's parts. The three major interior zones are the core (the innermost part of the Sun where energy is generated by nuclear reactions), the radiative zone (where energy travels outward by radiation through about 70% of the Sun), and the convection zone (in which convection currents circulate the Sun's energy to the surface). The flare, sunspots and photosphere, chromosphere, and the prominence are all clipped from actual SOHO images of the Sun. SOHO (ESA & NASA) (b) The shape of the Sun's magnetosphere can be described as the ballerina model (Alfvén, 1977). It is formed due to the rotation of the Sun. Figure adapted from Schwenn (2006).*

surface through convection. These convection areas can be seen in the chromosphere as a granulation, because the convection zone reaches into the chromosphere. The visible surface of the Sun is the photosphere. Above that, visible light can escape into space. Above the photosphere and the convection zone is the chromosphere. It is outshined by the photosphere below. In order to see, for instance, the solar granulation of the convection zone, filters have to be used. Above the chromosphere is the corona. It is also outshined by the photosphere, but can be seen in the visible during solar eclipse as a bright circle around the Sun disc when it is covered by the moon. Since the photosphere is so bright, most solar phenomena can only be seen when appropriate filters are applied. A phenomenon that can been seen in the visible are sunspots as dark spots in the photosphere. Solar eruptions, like flares and CMEs can only be observed by using filters. The different solar phenomena regarding Energetic Particle Precipitation (EPP) events are described in more detail in Section 3.4.1.

The magnetic field of the Sun is caused by its rotation. The rotation results in magnetic field lines that are shaped like spirals, called the *Parker spiral*. The heliosphere, the magnetosphere of the Sun, can be described and modelled in the so-called *ballerina model* (Alfvén, 1977) shown in Figure 3.1(b). Additionally, the Sun shows a differential rotation; areas at the equator are rotating faster than at the poles.

3.2 The Earth's magnetic field

A schematic representation of the Earth's magnetic field is presented in Figure 3.2. It is illustrated as a vertical cut along the Sun-Earth axis with the Sun on the left side (not shown). The magnetic field of the Earth is mainly shaped by the *solar wind* (see Section 3.4.1). It also shields and protects the Earth from solar wind particles entering into the Earth's atmosphere, at least in regions with closed magnetic field lines. A rather simplified

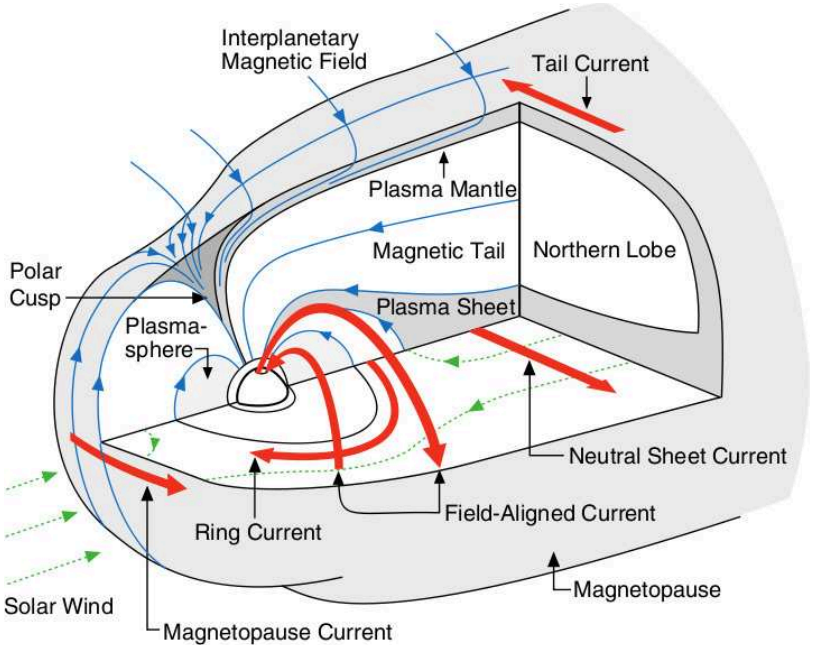

Figure 3.2 *Schematic diagram of the Earth's magnetosphere. Adapted from Russell (2000).*

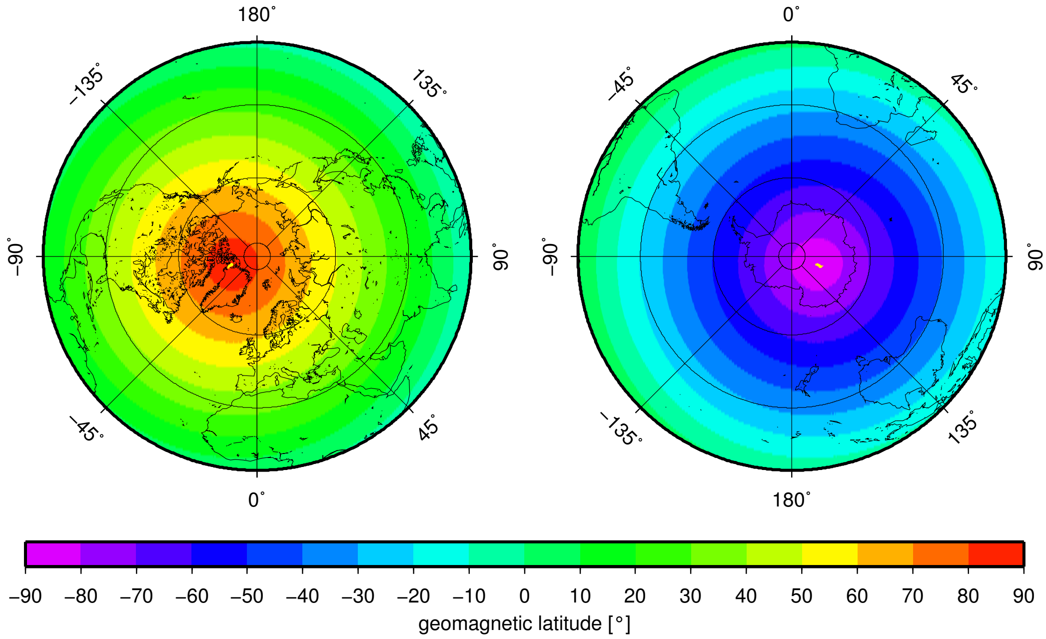

Figure 3.3 *Distribution of geomagnetic latitudes for 2012 for the Northern (left panel) and the Southern (right panel) Hemisphere. The yellow dots represent the geomagnetic North and South Pole since 1900. Data are taken from the International Geomagnetic Reference Field (IGRF-11) as provided by the World Data Center for Geomagnetism [`http://wdc.kugi.kyoto-u.ac.jp`].*

explanation for the magnetic field of the Earth is that electric currents in the liquid outer core cause a magnetic field similar to one of a magnetic dipole. The dipole axis does not match exactly the axis of rotation of the Earth. The magnetic poles, therefore, do not match the geographical poles.

The geographic positions of the geomagnetic poles are not constant. Also the area of the polar cusps, the area at the poles with open field lines in which particles can penetrate into the Earth's atmosphere, depends on the strength of the solar wind and can reach very low latitudes during high solar winds and solar activity. The geographic position of the geomagnetic North and South Poles and geomagnetic latitudes are displayed in Figure 3.3.

3.3 Solar variability and space weather

Space weather and its influence on the Earth is highly driven by the activity of the Sun. The solar activity is changing periodically in a 11-year cycle. One visible indicator of this 11-year cycle is the abundance of sunspots in the chromosphere of the Sun's surface. The occurrence of sunspots was investigated already by Galileo in the 17th century. The sunspot occurrence maxima and minima follow a 11-year period, which means, that 11 years after a sunspot maximum the Sun again reaches a maximum in sunspot numbers and therefore in solar activity. The number of sunspots observed for the period of 1818-2010 is presented in Figure 3.4. The counting number since approx. 1755 of the individual solar cycle is indicated at the bottom axis of the graph. The solar activity can be seen in other indices and measurements. For example, the proton flux measured by the different GOES instruments is presented in Figure 3.12.

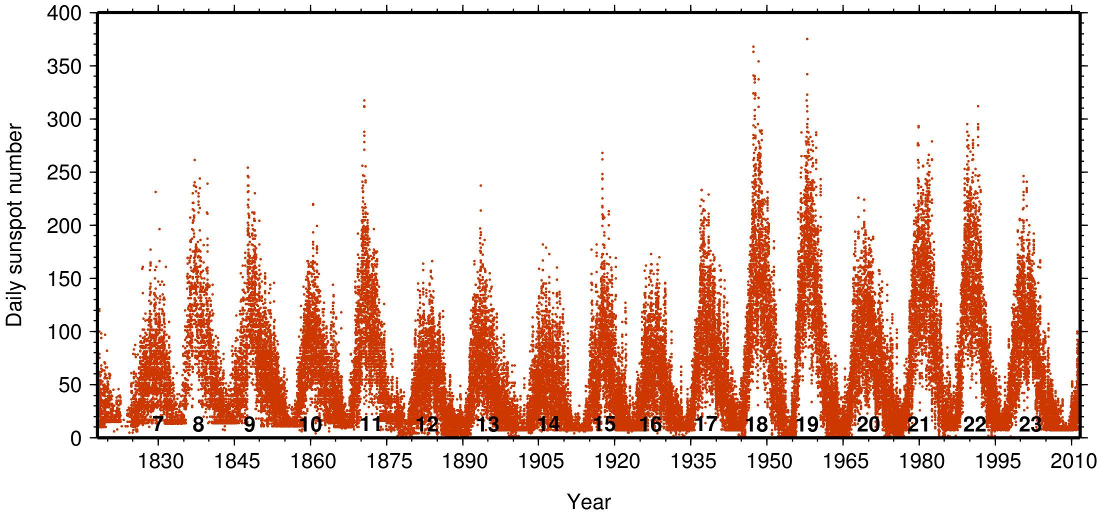

Figure 3.4 *Daily sunspot number for the period 8 January 1818 to 30 September 2011. Data are from the Space Physics Interactive Data Resource (SPIDR) provided by the National Geophysical Data Center (NGDC). The black numbers indicate the counting number of the particular solar cycle, the period of one sunspot minima to the next minima.*

3.4 Energetic particle precipitation events

Energetic Particle Precipitation (EPP) events are high fluxes of energetic particles like protons and electrons that enter the Earth's atmosphere. All processes that can cause these precipitating particles are related to the Sun and its activity. Hence, EPP events are connected to the 11-year solar cycle (Figure 3.4). The precipitating particles can be differentiated by their different origins and acceleration mechanisms. The origin of the particles can be either at the Sun and/or its environment and interplanetary medium (solar particles) or from within the Earth's magnetosphere (geomagnetic particles). Following Schrijver & Siscoe (2010), precipitating particles that are of *solar* origin can be referred to as Solar Energetic Particles (SEPs). They can be further classified into different types originating from different processes:

- particles during solar events, these particles can be divided into two different subclasses:
  - particles that are accelerated by solar flares
  - particles that are accelerated by a fast-moving shock wave driven by a Coronal Mass Ejection (CME)
- particles that are accelerated in the Corotating Interaction Regions (CIRs) in the outer heliospheric solar wind

Precipitating particles that have their origin in the Earth's magnetosphere are referred to as geomagnetic particles. These particles then associated to geomagnetic storms and substorms:

- particles that are associated with an interplanetary shock, caused by an interplanetary CME, as it crosses the Earth

- particles that are accelerated due to disturbances in the magnetotail (see Figure 3.2)

Under consideration of the particle type, EPP events can be divided into Solar Proton Events (SPEs) and Energetic Electron Precipitation (EEP) events. SPEs are mainly associated to solar events, whereas EEP events are mainly caused by geomagnetic storms. Both events can occur together or in individual events. Besides these more or less frequent events that occur occasionally, a somehow constant flow of solar particles reaches the Earth with the solar wind that is as well modulated by solar activity.

The phenomena that can cause EPP events are introduced in the next section.

3.4.1 Solar phenomena causing and affecting energetic particle events at the Earth

The solar wind The solar wind is a more or less constant flow of plasma from the Sun into the interplanetary space. The main influence on the Earth is that it shapes its magnetic field and therefore the magnetosphere of the Earth. Since the plasma consists of charged particles, the solar wind will trace its magnetic field into the interplanetary space. It consists mainly of ions, electrons, and protons. It can be distinguished between three types of solar wind. The fast solar wind originates from the coronal holes at the poles of the Sun (see also Figure 3.1(a)) and is dominating the solar wind during ‘quiet’ Sun conditions. The slow solar wind originates more from areas near the Sun’s equator between ±30°. A third type of solar wind is more pronounced during periods with high solar activity, and therefore refers to more active solar conditions. This type also originates near the Sun’s equator. The solar wind is important in the context of energetic particle events, since it is the source of charged particles that are for example trapped in the Earth’s magnetosphere in the radiation belts. Charged particles can enter the Earth’s magnetic field under certain conditions that are described as *magnetic reconnection* processes (see below) between the Interplanetary Magnetic Field (IMF) and the geomagnetic field.

Corotating Interaction Regions (CIRs) CIRs are structures in the solar wind that arise from the interaction between high-speed and low-speed solar wind. At CIRs, magnetic reconnection can occur (see below).

Magnetic reconnection *Magnetic reconnection* can occur when the involving magnetic fields have opposed directions. Magnetic reconnection can occur in different regions at the Sun, in the interplanetary medium, the solar wind (see above), between the Earth’s magnetic field and the IMF, and in the magnetotail. The magnetic reconnection leads to the transfer of charged particles between magnetic fields, and the conversion of magnetic energy into kinetic energy, thermal energy, and particle acceleration.

During solar flares and CMEs (see below) magnetic reconnection processes lead to particle ejection during flares and particle acceleration in CMEs.

Magnetic reconnection between the day-side IMF and the magnetic field of the Earth leads to the injection of charged particles out of the solar wind into the Earth’s day-side magnetosphere. During ‘quiet’ conditions, these particles are then trapped in the Earth’s radiation belts. But the reconnection of the IMF and the Earth’s magnetosphere can also lead to severe geomagnetic storms when the IMF get a southward component (B_z), and particles can be accelerated during reconnection processes in the magnetotail towards the Earth out of the plasma sheath (see below).

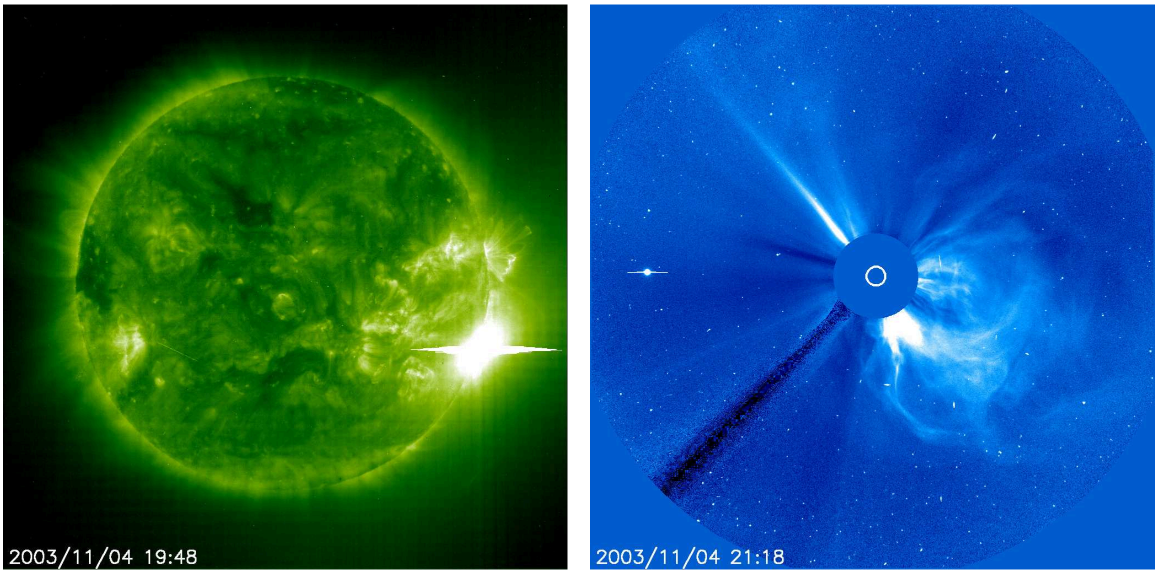

Figure 3.5 *Solar flare (left figure) and Coronal Mess Ejection (CME) (right figure) during the Halloween storm an 4 November 2003. The picture was taken by the EIT 195 Extreme ultraviolet Imager (left) and LASCO C3 coronagraph (right). [Courtesy of SOHO/EIT consortium. SOHO is a project of international cooperation between ESA and NASA.]*

Several processes can lead to a B_z component in the IMF. Tsurutani *et al.* (1988) have reviewed origins of B_z components in the IMF as follows:

- CME-driven shock waves
- compression and deflection of the solar wind in the CIRs (see above) of the Sun's magnetosphere

Solar flares Solar flares are, besides sunspots, one of the solar phenomena, that have been observed long before the first launch of observing satellites. The first solar flare observations were carried out by R. C. Carrington (1826-1875). One of the largest EPP events, including several large solar flares and CMEs have been observed by Carrington during the Carrington Event in 1859.

A solar flare is defined as a sudden atmospheric brightening, traditionally in the chromospheric Hα[i] emission. More general, flares are flashes of electromagnetic radiation over a wide spectral range (radio waves, infrared, visible, UV, X-rays, and γ-rays). The different kinds of radiation come from different parts of the flare site and are released at different times of the flare process (Schwenn, 2006). The strength of solar flares are classified by the intensity of their X-ray emission. A significant fraction of the flare energy goes into this geomagnetic radiation, the rest goes into heating and acceleration of particles (Schwenn, 2006).

There are two main phases during solar flares: *impulsive* and *gradual* (Schrijver & Siscoe, 2010). During the impulsive phase large amounts of energy are released and high emissions

---

[i] Hα is the visible red spectral line of hydrogen in the Balmer series at 656.28 nm.

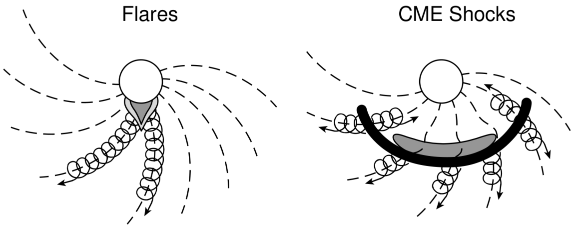

Figure 3.6 *Different origins and acceleration mechanisms of Solar Energetic Particle (SEP) events. In point-like flares (left) solar particles can escape in a narrow band. During Coronal Mass Ejections (CMEs) (right), particles are trapped and a shock can form and accelerate particles from the ambient plasma. Adapted from Reames (1999).*

of X-rays are observed. Highly energetic flares involve the occurrence of CMEs during this phase. The gradual phase emits strong thermal radiation.

Satellite images of a solar flare and a subsequent CME on 4 November 2003 are shown in Figure 3.5.

Coronal Mass Ejections Coronal Mass Ejections (CMEs) are large ejections of gas and plasma from the Sun's corona into interplanetary space; explosive ejections of quasi-spherical magnetic clouds that expand rapidly and shoot outward (Schrijver & Siscoe, 2010).

A more special CME is a *halo* CME, because it is going directly in the direction towards the Earth. They are occurring close to the disk centre and often appear to surround the occulting disk of the coronograph. An image taken by the SOHO LASCO C3 coronograph is shown in the right panel of Figure 3.5.

Fast CMEs can drive large-scale density waves out into space and can form shock waves (Schwenn, 2006) and cause large SEP events at the Earth.

3.4.2 Solar energetic particle events

Huge solar eruptions like flares and CMEs cause the ejection and acceleration of charged particles into the interplanetary space. These particle accelerations will be referred to as Solar Energetic Particle (SEP) events; they originate from the Sun, its atmosphere (corona), and the solar wind. In comparison, geomagnetic storm particles are accelerated during geomagnetic storms and substorms (see below) out of the Earth's magnetosphere. Solar particles that are accelerated and result in SEP events can reach energies between a few keV and some GeV. Very fast particles can reach the Earth in only a few minutes. Since the occurrence of SEP events can be directly related to flares and CMEs, these events are much more frequent during solar maximum than during solar minimum.

Following Reames (1999, 2002), Kallenrode (2003), Cliver (2008) (and references therein), SEP events can be classified into two different types depending on the particle origin and acceleration mechanism: *impulsive* and *gradual* SEP events. Kallenrode (2003) designates two distinct particle populations with different acceleration mechanisms: Flare Accelerated Particles (FAPs) and Particle Accelerated at CME Shocks (PACSs). The different acceleration mechanisms are shown in an illustration by Reames (1999) in Figure 3.6. The flare (left) releases an impulsive event and emits hot flare plasma material. Gradual events result from CME driven shocks (right) that accelerate particles from the ambient coronal plasma and the

Table 3.1 *Basic properties of impulsive and gradual Solar Energetic Particle (SEP) events. Adapted from Kallenrode (2003).*

	Impulsive	Gradual
Event rate	Some ten/a	~10/a
Event duration	Hours - days	Days
Main particle flux	Electrons	Protons
Accompanying CMEs	Sometimes	Yes

solar wind (Reames *et al.*, 1996; Reames, 2002). According to the current knowledge, large SEP events are being driven by CME shock waves rather than by solar flares (see Reames *et al.* (1996), and references therein). Flares and CMEs do not necessarily accompany each other. Gradual events can occur due to an erupting filament as part of the CME with no accompanying flare, whereas impulsive events are mainly associated with impulsive flares without any CME signatures (Schwenn, 2006). Not every CME results in a SEP event; only a few percent are fast enough to form a shock wave that is able to sufficiently accelerate particles to form severe SEP events at Earth. The dominant solar particle populations that are accelerated during the different event types are electrons due to impulsive events and protons due to gradual events (Reames, 1999). Impulsive events are more frequent than gradual events. Some properties of the two event classes are summarised in Table 3.1.

Reames (2002), Gopalswamy *et al.* (2002), Kallenrode (2003) suggest SEP events that show both, impulsive and gradual behaviour. Gopalswamy *et al.* (2002) investigated the impact of CME interaction on SPE events, and suggest, that the mixed impulsive-gradual signatures in SEP events can be associated to a primary CME shock re-accelerating ions from previous SEP events, see also Reames (2002).

3.4.3 Interplanetary shocks, geomagnetic storms and substorms

As described above, fast CMEs and disturbances in the CIR can cause interplanetary shock waves. These shock waves can cause disturbances in the IMF and the interplanetary medium and subsequent disturbances, such as the compression in the Earth's magnetic field. This leads to acceleration processes within the magnetosphere and precipitating particles into the atmosphere.

Disturbances of the interplanetary medium that cause a southward pointing component of the IMF (Tsurutani *et al.*, 1988), lead to strong magnetic reconnection of the IMF and the magnetosphere at the day-side of the Earth's magnetosphere, as described above. This can lead to magnetic reconnection processes in the magnetotail, accelerating electrons out of the plasma sheath outward and inward from the reconnection site and cause geomagnetic or auroral substorms (Akasofu, 1964). Since the plasma sheath is connected to the magnetic field lines that form the polar cusps, electrons can precipitate into the Earth's atmosphere within the aural oval. The form and radius of the polar cusps is dependent on the strength of the solar wind and the strength of the geomagnetic storm. Along the cusps edge, electrons can enter the atmosphere down to approx. 90 km altitude. The electron precipitation will mainly excite highly abundant atmospheric species like N_2 and O_2 into excited states. During spontaneous relaxation, these molecules will loose energy by the emission of geomagnetic

Figure 3.7 *Aurora Borealis at NyÅlesund, Spitsbergen on 24 October 2012. Photo courtesy of Matthias Buschmann.*

radiation; oxygen emits in green light and nitrogen blue or red. These events are known as 'Auroras'. A photograph of such an *Aurora Borealis* taken at NyÅlesund, Spitsbergen by Matthias Buschmann is shown in Figure 3.7.

3.5 Impact of energetic particles on the Earth's atmosphere

Energetic particles that enter the Earth's atmosphere are called *precipitating particles.* Since these particles have different sources, acceleration mechanisms, and energy spectra they have different entry paths into the Earth's atmosphere. The impact of different precipitating particle populations differ in the spatial location of the main impact and in the penetration depth into the atmosphere.

3.5.1 Particle motion in the magnetic field

The three principle motions of a particle in a magnetic field are shown in Figure 3.8. The motion is described by the Lorentz force:

$$m\frac{d\vec{v}}{dt} = q\vec{E} + \frac{q}{c}\vec{v} \times \vec{B} \tag{3.1}$$

This leads to gyro-rotation (left panel), bouncing motion (middle panel), and a drift motion (right panel).

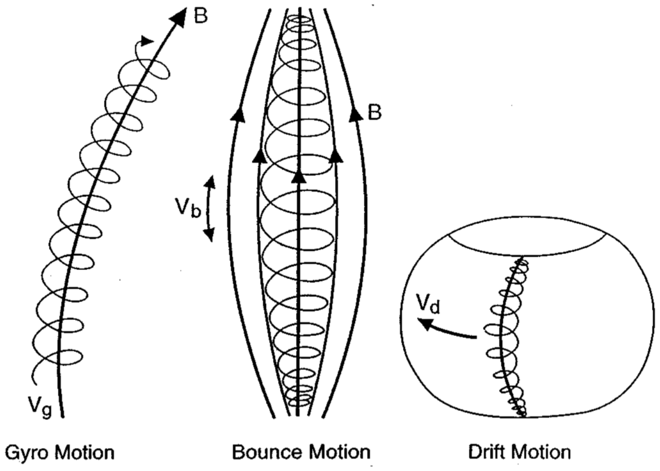

Figure 3.8 *Particle motion in a magnetic field. Adapted from Russell (2000).*

3.5.2 Particle entry into the Earth's atmosphere

The precipitation of energetic particles from SEP events and particles from geomagnetic storms enter the Earth's atmosphere along its magnetic field lines.

During high fluxes of protons the Earth's magnetic field normally acts as a protection shield that only allows these solar protons to enter the Earth's atmosphere over the polar caps.

Energetic particles during solar events can penetrate into the Earth's atmosphere in polar regions within the polar cap from ~60° geomagnetic latitude poleward where the Earth's magnetic field lines are open. But during very large shocks, for instance, the magnetic field can be disturbed such that accompanying protons can enter the inner magnetosphere and become trapped in the field and/or enter the Earth's atmosphere within the polar cusps.

Auroral electrons from the radiation belt are accelerated through disturbances in the magnetotail. They are injected into the Earth's atmosphere along geomagnetic field lines that are connected to the magnetotail. Auroral particles will therefore enter the atmosphere mainly in the auroral oval around 67° geomagnetic latitude (Feldstein & Starkov, 1967). The radius of the auroral oval is influenced by geomagnetic storms (Milan *et al.*, 2009). Since the position of the geomagnetic pole is not constant, the shape of the polar cap and the auroral oval is also not constant and is varying over time with solar and geomagnetic activity.

Trapped electrons in the radiation belt are accelerated through geomagnetic storms from Interplanetary Coronal Mass Ejections (ICMEs) and geomagnetic substorms. Both events induce an electric field. During strong geomagnetic storms the electric field is caused by a compression of the magnetosphere as the shock passes the Earth. During substorms, a disturbance in the magnetotail produces this electric field.

3.5.3 Penetration depths of energetic particles

The vertical ionisation rate profiles for different particles and radiation, and thus, their different penetration depths into the atmosphere are depicted in Figure 3.9. In the studies presented here, it will be focused mainly on solar protons, solar electrons, and auroral electrons that are accelerated out of the radiation belt into the magnetosphere during shocks.

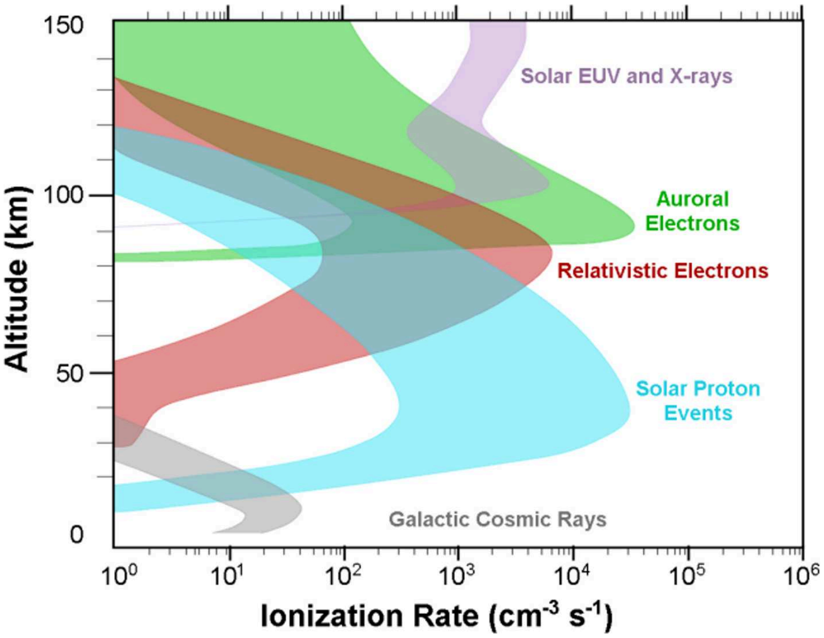

Figure 3.9 *Penetration depths into the atmosphere for different particles and radiation. Adapted from Jackman (HEPPA 2 workshop 2009, Boulder, Colorado, USA)*

The altitude of maximum ionisation, and therefore the penetration depths of the particles depend on the energies of the particles. As shown in Figure 3.9, highly energetic solar protons, that can occur during strong SPEs, can precipitate into the lower stratosphere and even below. All particle types show a maximum in ionisation rates at a certain altitude. This altitude is here called the main penetration depths of the different particle types. Protons show this maximum around 35 km, in the middle to lower stratosphere. Solar electrons can also precipitate into the stratosphere, but more to higher altitudes between 30-50 km. But their maximum ionisation effect is in the upper mesosphere. Auroral electrons precipitate only into the upper mesosphere to altitudes above 80 km with a maximum of ionisation in 90 km altitude.

3.5.4 Energy deposition and interactions of the precipitating particles with the atmosphere

The particles can penetrate into the atmosphere to altitudes depending on the their energies, as mentioned above, until their energy is lost. This energy is partly going into heat (Joule heating) and partly into ionisation and other interactions in the atmosphere (Schrijver & Siscoe, 2010). *Joule heating* is the frictional heating during collisions between plasma and neutral particles (Schrijver & Siscoe, 2010).

Interactions of the precipitating particles with the neutral constituents of the atmosphere are mainly

ionisation

$$X_2 + e^- \longrightarrow X_2^+ + 2\,e^- \tag{R 3.2}$$

dissociation

$$X_2 + e^- \longrightarrow X + X + e^- \tag{R 3.3}$$

dissociative ionisation

$$X_2 + e^- \longrightarrow X + X^+ + 2\,e^- \tag{R 3.4}$$

processes.

3.5.5 The direct impact of the precipitating particles and the following ion chemistry

The impact of the precipitating particles on atmospheric species is initiated by secondary electrons (e^-) induced by the precipitating particle event. As described by, e.g. Crutzen *et al.* (1975), Rusch *et al.* (1981), the most abundant species like O_2 and N_2 are ionised and dissociated by these secondary electrons:

$$N_2 + e^- \longrightarrow N_2^+ + 2\,e^- \tag{R 3.5}$$
$$N_2 + e^- \longrightarrow N + N^+ + 2\,e^- \tag{R 3.6}$$
$$N_2 + e^- \longrightarrow N + N + e^- \tag{R 3.7}$$
$$O_2 + e^- \longrightarrow O_2^+ + 2\,e^- \tag{R 3.8}$$
$$O_2 + e^- \longrightarrow O + O^+ + 2\,e^- \tag{R 3.9}$$

Rusch *et al.* (1981) described the formation of odd nitrogen during a SPE.

The production of nitrogen, nitrogen ions, and oxygen ions through reactions R 3.5-R 3.9 is followed by the reactions

$$N_2^+ + O \longrightarrow NO^+ + N \tag{R 3.10}$$
$$N_2^+ + e^- \longrightarrow N + N \tag{R 3.11}$$
$$O^+ + N_2 \longrightarrow NO^+ + N \tag{R 3.12}$$
$$N^+ + O_2 \longrightarrow O^+ + NO \longrightarrow NO^+ + O \longrightarrow O_2^+ + N \tag{R 3.13}$$
$$NO^+ + e^- \longrightarrow N + O \tag{R 3.14}$$

The resulting nitrogen atoms are either in the ground state ($N(^4S)$) or in the excited state ($N(^2D)$) and can react with O_2 to form NO

$$N(^4S) + O_2 \longrightarrow NO + O \tag{R 3.15}$$
$$N(^2D) + O_2 \longrightarrow NO + O \tag{R 3.16}$$

$N(^4S)$ can also react with NO:

$$N(^4S) + NO \longrightarrow N_2 + O \tag{R 3.17}$$

and lead to a destruction of odd nitrogen species.

The formation of nitrogen species results in the catalytic destruction of ozone, as described in Section 2.3. Reactions R 2.30 and R 2.31 destroy ozone and catalytically produce nitrogen species. These reactions compete with reactions that can destroy nitrogen species:

$$N + NO \longrightarrow N_2 + O \tag{R 3.18}$$
$$N + NO_2 \longrightarrow N_2O + O \tag{R 3.19}$$

The production of hydrogen compounds during SPEs was suggested by Swider & Keneshea (1973). The ionisation of oxygen molecules leads via the formation of oxonium (H_3O^+) to the production of OH and H. Solomon *et al.* (1981) have described the ion chemistry of the formation of odd hydrogen in more detail as follows: via the ionisation of oxygen molecules (see reaction R 3.8) and the following reactions

$$O_2^+ + O_2 + M \longrightarrow O_4^+ + M \qquad \text{(R 3.20)}$$
$$O_4^+ + H_2O \longrightarrow O_2^+{\cdot}H_2O + O_2 \qquad \text{(R 3.21)}$$

oxonium will be produced that will form odd hydrogen compounds through three different processes:

$$O_2^+{\cdot}H_2O + H_2O \longrightarrow H_3O^+{\cdot}OH + O_2 \qquad \text{(R 3.22)}$$
$$H_3O^+{\cdot}OH + e^- \longrightarrow H + OH + H_2O \qquad \text{(R 3.23)}$$

$$O_2^+{\cdot}H_2O + H_2O \longrightarrow H_3O^+{\cdot}OH + O_2 \qquad \text{(R 3.24)}$$
$$H_3O^+{\cdot}OH + H_2O \longrightarrow H_3O^+{\cdot}H_2O + OH \qquad \text{(R 3.25)}$$
$$H_3O^+{\cdot}H_2O + nH_2O \longrightarrow H_3O^+(H_2O)_{n+1} \qquad \text{(R 3.26)}$$
$$H_3O^+(H_2O)_{n+1} + e^- \longrightarrow H + (n+2)H_2O \qquad \text{(R 3.27)}$$

$$O_2^+{\cdot}H_2O + H_2O \longrightarrow H^+{\cdot}H_2O + OH + O_2 \qquad \text{(R 3.28)}$$
$$H^+{\cdot}H_2O + n(H_2O) \longrightarrow H_3O^+(H_2O)n \qquad \text{(R 3.29)}$$
$$H_3O^+(H_2O)n + e^- \longrightarrow H(n)H_2O \qquad \text{(R 3.30)}$$

Swider & Keneshea (1973), as well as Solomon *et al.* (1981) determined how much odd hydrogen is produced per ionisation. It arises that about two odd hydrogen compounds are produced per ionisation.

The ozone depletion due to odd hydrogen is the main depletion process of ozone during an SPE in altitudes between 50-70 km, since reactions with NO and NO_2 are not efficient enough to reduce O and O_3 concentrations between 50-70 km. Below 45 km ozone depletion by odd nitrogen compounds becomes very important (Crutzen *et al.*, 1975; Lary, 1997). Both, odd hydrogen and odd nitrogen compounds, destroy ozone in catalytic reaction cycles, as already described in Section 2.3.

Besides the depletion of O_3, the increase in HO_x and NO_x has an impact on chlorine compounds through neutral reactions. The increase of OH, for instance, will lead to the formation of reactive chlorine through the reaction

$$HCl + OH \rightarrow Cl + H_2O. \qquad \text{(R 3.31)}$$

Reactive atomic chlorine forms ClO through

$$Cl + O_3 \rightarrow ClO + O_2 \qquad \text{(R 3.32)}$$

that reacts with enhanced HO_2 values to form HOCl via

$$ClO + HO_2 \rightarrow HOCl + O_2. \qquad \text{(R 3.33)}$$

Chlorine nitrate is formed through the reaction with enhanced NO_2 by

$$ClO + NO_2 + M \rightarrow ClONO_2 + M. \tag{R 3.34}$$

Apart from the impact of positive ion chemistry, observations (von Clarmann *et al.*, 2005) as well as model studies (Winkler *et al.*, 2009, 2011) have suggested that SPEs have a direct impact on chlorine compounds through negative ion chemistry. Von Clarmann *et al.* (2005) showed that enhanced ClO and HOCl values were observed during the October/November 2003 SPE by the Michelson Interferometer for Passive Atmospheric Sounding (MIPAS) instrument, concluding this enhancement as an indication of an enhanced abundance of HO_x constituents during the event. But they also suggested the direct decomposition of HCl by ion cluster chemistry to be an additional source of ClO. Through simulations for the July 2000 SPE with the University of Bremen Ion Chemistry (UBIC) model, Winkler *et al.* (2009, 2011) showed that the reproduction of the HCl decrease concurs better with observations if negative ion reactions are taken into account in the simulations. The direct impact of this negative ion chemistry on chlorine species are the reactions of uncharged compounds with ions and recombination reactions. Several anions X^-, like O_2^-, O^-, CO_3^-, OH^-, NO_2^-, or NO_3^-, react with HCl forming Cl^-

$$HCl + X^- \rightarrow Cl^- + \text{products}. \tag{R 3.35}$$

$ClONO_2$ is decomposed by the reaction with CO_3^- via

$$ClONO_2 + CO_3^- \rightarrow ClO + NO_3^- + CO_2 \tag{R 3.36}$$

(see Winkler *et al.* (2009, 2011) and references therein).

3.5.6 The influence of energetic particles events on atmospheric dynamics

The impact of EPP events can also have an influence of atmospheric dynamics. As show in different studies by, e.g. Krivolutsky *et al.* (2006), Jackman *et al.* (2007), Seppälä *et al.* (2009), Nesse Tyssøy *et al.* (2010), Becker & von Savigny (2010), EPP events can disturb atmospheric temperatures, winds, atmospheric circulation, as well as surface temperatures. The cause of these influences is the disturbed abundance of ozone and a resultant change in radiative heating of the atmosphere. The impact of particle precipitation on atmospheric heating rates is discussed in more detail in Section 16.

3.6 The impact of energetic particle precipitation events on human life and technology

Following Schwenn (2006) and Pulkkinen (2007), solar events can cause severe effects on human life and technology:

- Radiation released by flares can heat up the terrestrial atmosphere such that satellites are slowed down and drop into lower orbits.
- Radiation can harm astronauts travelling through interplanetary space, outside the Earth's protective magnetosphere.
- Induced currents effect electric power transmission networks, pipelines, navigation and communication systems.

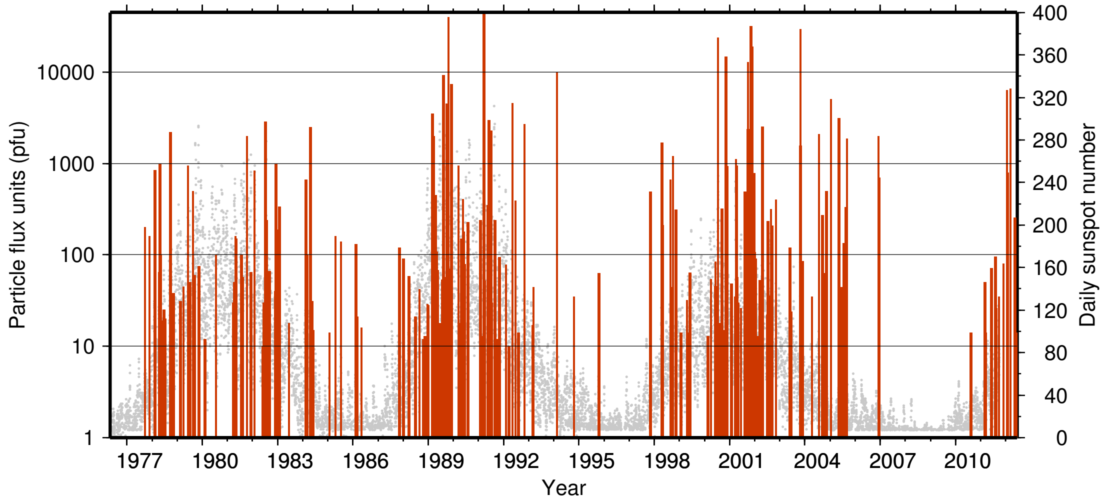

(a) Solar proton events and daily sunspot number for 1976-2012

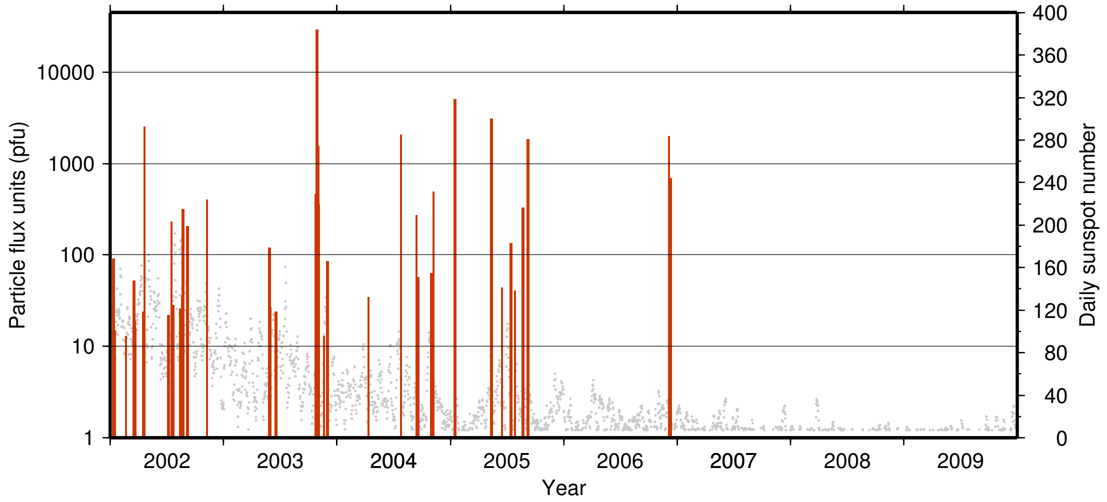

(b) Solar proton events and daily sunspot number for the investigated period 2002-2009

Figure 3.10 *Solar proton event occurrences (a) from April 1967 until June 2012 and (b) for 2002 until 2009 (orange bars) and daily sunspot numbers (grey dots). The SPEs are characterised as 5-minute averages of proton fluxes for energies higher than 10 MeV in proton flux units* $[1\,\mathrm{pfu} = 1\,\mathrm{p}/(\mathrm{cm}^2\,\mathrm{s\,sr})]$. *Data adapted from* `http://www.swpc.noaa.gov/ftpdir/indices/SPE.txt`, *prepared by the U.S. Dept. of Commerce, NOAA, Space Weather Prediction Center. The daily sunspot number data are from the Space Physics Interactive Data Resource (SPIDR) provided by the National Geophysical Data Center (NGDC)*

3.7 Energetic particle precipitation events during 2002-2009

3.7.1 Energetic particles events during the investigated period 2002-2009

In this study, the effect of EPP events for the period of 2002-2009 will be investigated. It covers the declining phase of the solar cycle 23 (Figure 3.4). In this period, several very large SPEs occurred as well as periods with very low solar and geomagnetic activity (Figure 3.10).

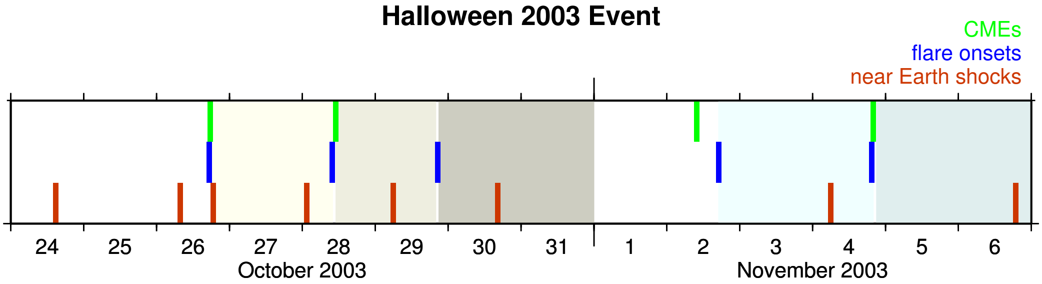

Figure 3.11 *Time evolution of solar and geomagnetic events for October/November 2003. The blue bars mark the time of a flare, and the orange bars indicate the onset of a shock. Shaded areas are periods of high particle fluxes. Data obtained from Gopalswamy* et al. *(2005), Mewaldt* et al. *(2005), and* `http://www.swpc.noaa.gov/ftpdir/indices/SPE.txt`*.*

The different impacts of different strong SPEs events and periods with low solar activity are discussed in the Results part in Section 13. The major impact of EPP events will be discussed in the following for the SPE during October/November 2003. This events will be described in more detail in the following section.

3.7.2 Solar and geomagnetic Events during October/November 2003

The solar eruptions during October/November 2003 were the most extreme events in the solar cycle 23. About 80 CMEs, eleven X-class flares, the largest SEP events, and several interplanetary shocks (Gopalswamy *et al.*, 2005) were observed during October/November 2003. In the following, this period will be referred to as the '*Halloween 2003 SPE*' or SPE 2003. In the following, the Halloween 2003 Event will be described in more detail to distinguish the different solar and geomagnetic events. Since only particle precipitation events are considered in the studies presented here, only events that cause particle fluxes in the Earth's atmosphere are of interest. These particle fluxes can be either caused by flares that cause ICMEs, shocks near the Sun that accelerate interplanetary plasma near/out of the corona, or shocks near the Earth's magnetosphere, that can accelerate geomagnetic particles precipitating into the Earth's atmosphere, so-called geomagnetic storms. During the Halloween 2003 Event several of these different events occurred. Some of the largest SPEs and geomagnetic storms happened in the past solar cycle 23.

One part of this study is addressed to the question, whether precipitating electrons from both sources have an influence on stratospheric nitrogen and ozone. To study this question, the SPE 2003 was chosen, because several solar events happened during the event, causing solar as well as geomagnetic particle fluxes into the atmosphere. To distinguish between solar and geomagnetic particles in their impact on the upper atmosphere, we have to separate the SPE 2003 event into days of different activity source. In Figure 3.11 the different solar events are marked depending on their occurrence. CMEs are marked as green bars, solar flares are marked as blue bars, shocks are marked as red bars, and shaded areas indicate periods with high particle fluxes.

During the solar storm of October-November 2003, proton and electron fluxes comparable to the largest observed during the previous solar maximum occurred (Mewaldt *et al.*, 2005). Several large halo CMEs on 26+28 October and 2+4 November 2003 caused highly energetic particle fluxes with maximum proton fluxes on 26+29 October and 3+5 November. During

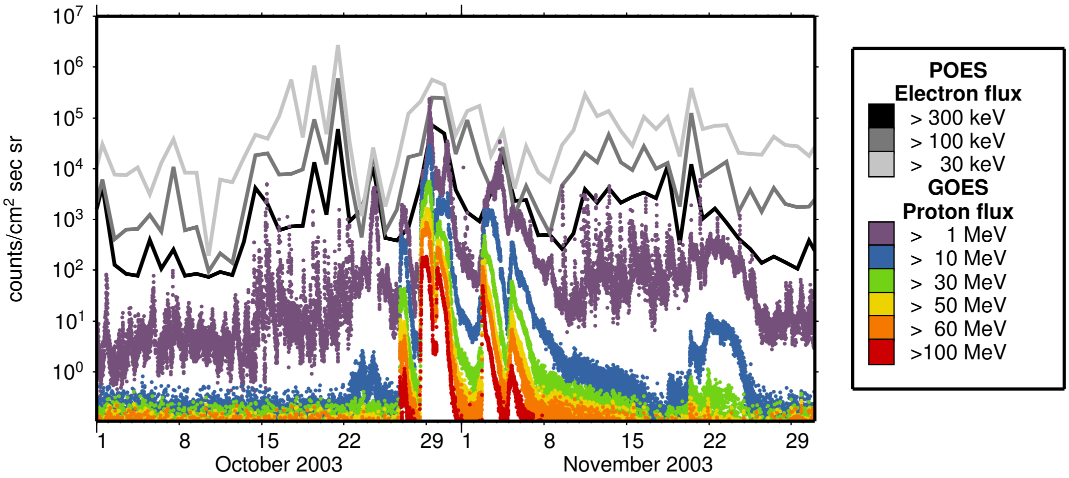

Figure 3.12 *Proton and electron flux for different energies during the October/November Solar Proton Event (SPE) 2003 measured by the GOES and POES satellite respectively.*

that period three X-class flares were observed on 26+28 October and 4 November 2003.

Proton and electron fluxes for the Halloween SPE are shown in Figure 3.12.

Geomagnetic storms can be indicated by three different indices (K_p, A_p, and Dst index). The K_p *index* represents the global magnetic activity. The K_p index for the SPE 2003 in shown in Figure 3.13(a). The major events are very pronounced, as on 29-31 October 2003 and 20 November 2003. Very pronounced geomagnetic inactive days are before the major event during 9-12 October 2003, 23 October 2003, after the first major event on 5 November 2003, 2-4 December 2003, and 18-19 December 2003. These days and periods of very low geomagnetic activities are followed by a strong increase of geomagnetic activity. During these periods high fluxes of geomagnetic particles can be accelerated and precipitate into the Earth's atmosphere. In Section 14.3 the different influences of solar and geomagnetic particles are investigated.

The intensity of the geomagnetic storms can be obtained from the *Dst index*. Values for the Dst index for October-December 2003 are shown in Figure 3.13(b). Very steep and high decrease can be seen for 29 and 30 October 2003, and again on 20 November 2003. As shown by the K_p index, these are periods of high geomagnetic activity and high ionisation rates due to geomagnetic protons and electrons is expected.

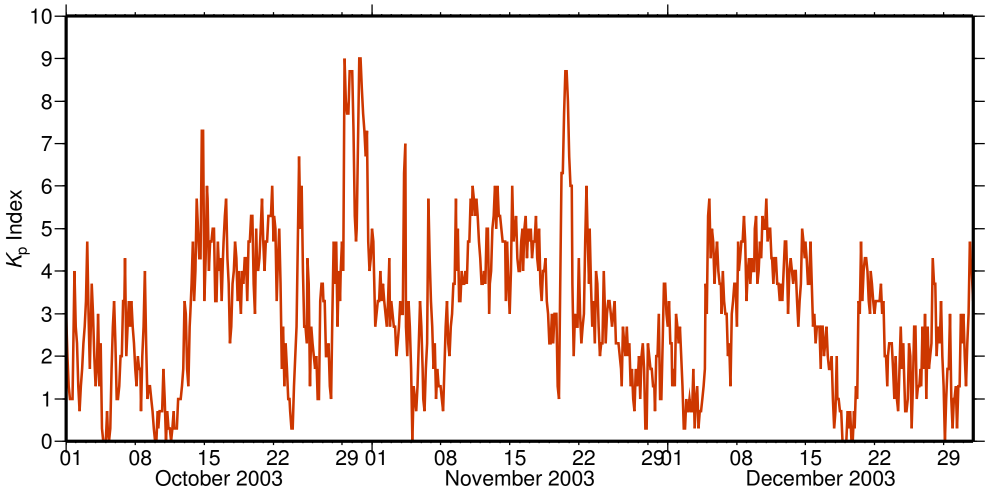

(a) K_p index during the SPE 2003, representing the global geomagnetic activity.

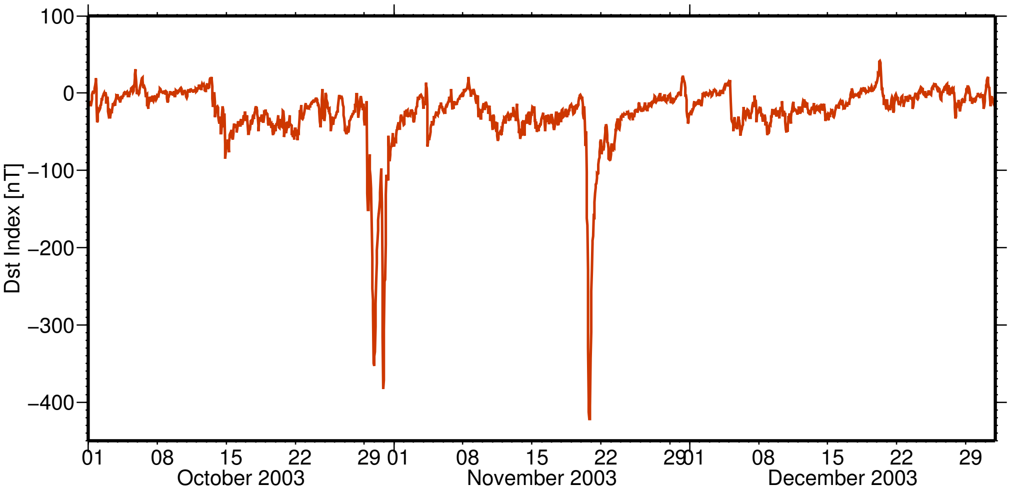

(b) Dst index during the SPE 2003, representing the global geomagnetic storm intensity.

Figure 3.13 *Geomagnetic activity (K_p and Dst index) during the October/November 2003 Solar Proton Event (SPE). The data are obtained from Space Physics Interactive Data Resource (SPIDR),* `http://spidr.ngdc.noaa.gov/spidr/home.do`

4 Some basics about atmospheric modelling

4.1 Different types of atmospheric models

Atmospheric models can be distinguished into different types: General Circulation Models (GCMs), Chemistry and Transport Models (CTMs), and Chemistry and Climate Models (CCMs).

General Circulation Models GCMs calculate the dynamical processes in the atmosphere to simulate the general circulation of the atmosphere in its 'mean' state. They calculate wind fields and distribution of temperature, pressure, density, for the general circulation of the atmosphere.

Examples for GCMs: KMCM, LIMA, etc.

Chemistry and Transport Models CTMs consist mainly of a scheme that solves the chemical equations. They have no dynamical core as GCMs have. CTMs, therefore, use meteorological data as input, such as wind fields and temperatures, to calculate the horizontal and vertical transport of trace gases.

Examples for CTMs: B3dCTM, FINROSE, SLIMCAT, etc.

Chemistry and Climate Models CCMs have a dynamical core as well as a scheme to calculate the chemical equations. For example, a coupled CTM to a GCM, as WACCM.

Examples for CCMs: EMAC, HAMMONIA, WACCM, etc.

These models can also be subdivided into *free running* and *non-free running* models. GCMs as well as CCMs are in general free running models. Free running models have their own dynamical core and are not forced by meteorological data as CTMs. CTMs do not have a dynamical core, but use appropriate external meteorological data sets to calculate the transport of trace gases. Such meteorological data set include wind fields, pressure, and temperature, and can be obtained by CCMs or GCMs and from meteorological reanalysis.

There are both, advantages and disadvantages to all model types. An advantage of the use of meteorological analysis is that results can be directly compared to observations by satellites or ground based instruments because the data have a 'real' underlying date. Two examples of free running models are KMCM and WACCM. A second possibility is to nudge or assimilate a free running dynamical model with analysed meteorological data. Such a model is the LIMA model (Berger, 2008). It is nudged by European Centre for Medium-Range Weather Forecasts (ECMWF) data in the troposphere and stratosphere, and represents therefore a 'real' date, since the ECMWF data are based on observation. See also Section 8.2.2 for more details.

4.2 Solving advection-diffusion equations

Following Jacobson (2005), the advection-diffusion equations are derived by dividing the four dimensional (t, x, y, z) continuity equation

$$\frac{\partial N}{\partial t} + \nabla \cdot (\mathbf{v}N) = (\nabla \cdot \mathbf{K}_h \nabla)N + \sum_{n=1}^{N_{e,t}} R_n \tag{4.1}$$

into three two-dimensional partial differential equations ($[t,x], [t,y], [t,z]$) and a one-dimensional differential equation (t). The operator-split equations of the continuity equation in horizontal (x,y) and vertical (z) direction can be written as

$$\begin{aligned}
\frac{\partial N}{\partial t} + \frac{\partial (uN)}{\partial x} - \frac{\partial}{\partial x}(K_{h,xx}\frac{\partial N}{\partial x}) &= 0 &(4.2)\\
\frac{\partial N}{\partial t} + \frac{\partial (vN)}{\partial y} - \frac{\partial}{\partial y}(K_{h,yy}\frac{\partial N}{\partial y}) &= 0 &(4.3)\\
\frac{\partial N}{\partial t} + \frac{\partial (wN)}{\partial z} - \frac{\partial}{\partial z}(K_{h,zz}\frac{\partial N}{\partial z}) &= 0 &(4.4)
\end{aligned}$$

Each of these equations will be solved individually and in certain order during one time step. The partial differential equation can be solved by different approximation which won't be discussed here. The applied advection scheme in the Bremen 3-dimensional Chemistry and Transport Model (B3dCTM) is the scheme of Prather (1986). The transport of the B3dCTM and the advection scheme are discussed in Section 6.3.

4.3 Solving chemical Ordinary Differential Equations

The change in the abundance of chemical species through chemical reactions is computed by numerically solving a set of Ordinary Differential Equations (ODEs). It can be distinguished between *explicit*, *implicit*, and *semi-implicit* schemes to solve such differential equations. An *explicit* scheme calculates the final terms at time t from values at previous time steps, e.g. $t-h$, $t-2h$, etc.. An *implicit* scheme calculates the final terms from other terms at time t that are calculated simultaneously. *Semi-implicit* schemes evaluate the final terms from both, known values at previous time steps ($t-h$, $t-2h$, etc.) and from other unknown terms at time t. Such a set of chemical reactions is in general a *stiff* system. This is when the life-times of the involved species differ significantly from one another. Efficient methods of solving stiff systems are semi-implicit schemes. The applied scheme to solve the chemical reactions in the model used in this study is the Semi-Implicit Symmetric (SIS) method by Ramaroson *et al.* (1992). This method is described in Section 6.5.

Analytically, the solution of a chemical ODE for a concentration N_i of a species i at time t is given by

$$N_{i,t} = N_{i,t-h}\, e^{-kh} \tag{4.5}$$

with the time step h and the reaction coefficient k of the reaction. The first order approximation of an explicit Taylor series expansion (see equation (.1) in the Appendix) is called the *forward Euler* solution:

$$N_{i,t} = N_{i,t-h} + h\frac{dN_{i,t-h}}{dt} \tag{4.6}$$

This can be written in terms of production P and loss L terms as

$$N_{i,t} = N_{i,t-h} + h(P_{c,i,t-h} - L_{c,i,t-h}) \tag{4.7}$$

For short lived species, the forward Euler method needs very short time steps to prevent negative values.

4.4 The family approach of solving chemical Ordinary Differential Equations

One numerical method of solving chemical ODEs is the family approach. It is mainly used to save computational time. The main theory behind this approach is that within a family (group) of gases, the members of that family transfer very fast among each other, but are lost slowly from the family itself (Jacobson, 2005).

Part II

Model description and further development

5 Introduction

The aim of this PhD work is to simulate the impact of Energetic Particle Precipitation (EPP) events on the chemical composition in the middle and upper atmosphere. For this purpose, the Bremen 3-dimensional Chemistry and Transport Model (B3dCTM) was chosen in order to employ it for the simulation of such events and to further develop the model to simulate these events in the upper atmosphere (upper mesosphere and lower thermosphere). This aim led to the following main modelling tasks:

- to further develop the model in order to simulate the impact in the upper mesosphere and lower thermosphere, see Section 7.1,
- to further develop the B3dCTM in order to simulate the particle precipitation into the atmosphere by implementing appropriate ionisation rates due to the different particle populations, see also Section 8.1,
- to improve the model in the upper atmosphere by implementing a modified family approach of the chemical scheme,
- to employ the improved model to carry out different multi-year and case model simulations.

The B3dCTM and its basic model components are described in Section 6. Each of the above modelling tasks are discussed in more detail in Section 7. The input data that are necessary to run the model simulations, such as meteorological data, ionisation rates, and source gases, are described in Section 8. The different model calculations carried out are described in Section 9.

6 The Bremen 3-dimensional Chemistry and Transport Model

In the following, a brief description of the basic components will be given. The main framework is described in Section 6.1 and the resolution is described in Section 6.2. The advection scheme to calculate the transport in horizontal and vertical direction is summarised in Section 6.3. The radiation scheme to calculate the radiative heating rates is described in Section 6.4, since in the BASE model version of the B3dCTM the vertical transport is calculated on the basis of diabatic heating rates. The chemistry and the chemical solver are described in Section 6.5 and Section 6.5.1, respectively. The parametrisation of the ion-chemistry induced by precipitating particles will be discussed separately from the model chemistry in Section 6.6. The input data to run the model simulations are described in Section 8.

6.1 Model structure

The B3dCTM is structured in a modular way. It can be run as (i) a three dimensional transport model only, (ii) including a linearised ozone chemistry LINOZ (McLinden *et al.*, 2000) and a polar chemistry, or (iii) with a full chemistry scheme. All model simulations in this study have been carried out with the latter full model set up. Several additional program units can be added and enabled respectively, by key variable settings. For example, the impact of precipitating particles can be switched on and off for different case model scenarios and studies. The program sequence of the model is divided into 'cycles' that represent a time period. In the employed model set up each cycle represents the time period of 6 hours. This period was chosen, since the implemented meteorological data are available with a time resolution of 6 hours. That means that the meteorological data are updated every cycle. Each cycle is further subdivided into the overall time step. Within each overall time step the model uses the *operator splitting* technique (see Figure 6.1 for illustration). Each time step, the transport is calculated for a certain time of day and then, for the same time, the chemistry is computed. After such a sequence (transport and chemistry) the time is updated with respect to the chosen overall time step. The main framework of the B3dCTM is schematically displayed in Figure 6.2. The chemical sequence can have a smaller time step than the overall time step, as used in the non-family chemistry scheme (see Section 7.2).

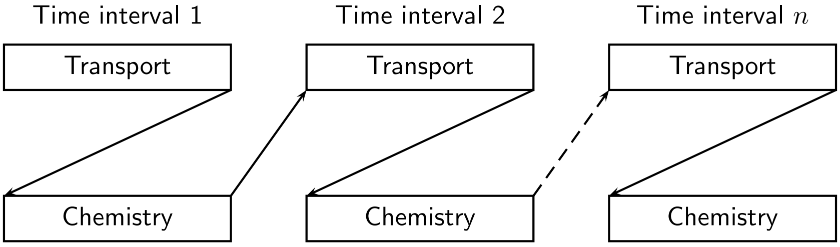

Figure 6.1 *Schematic illustration of the operator splitting technique of the B3dCTM model structure. For each overall time step transport and chemistry are calculated separately and consecutively. This sequence is then executed, for example, n times a day. Illustration adapted from Jacobson (2005).*

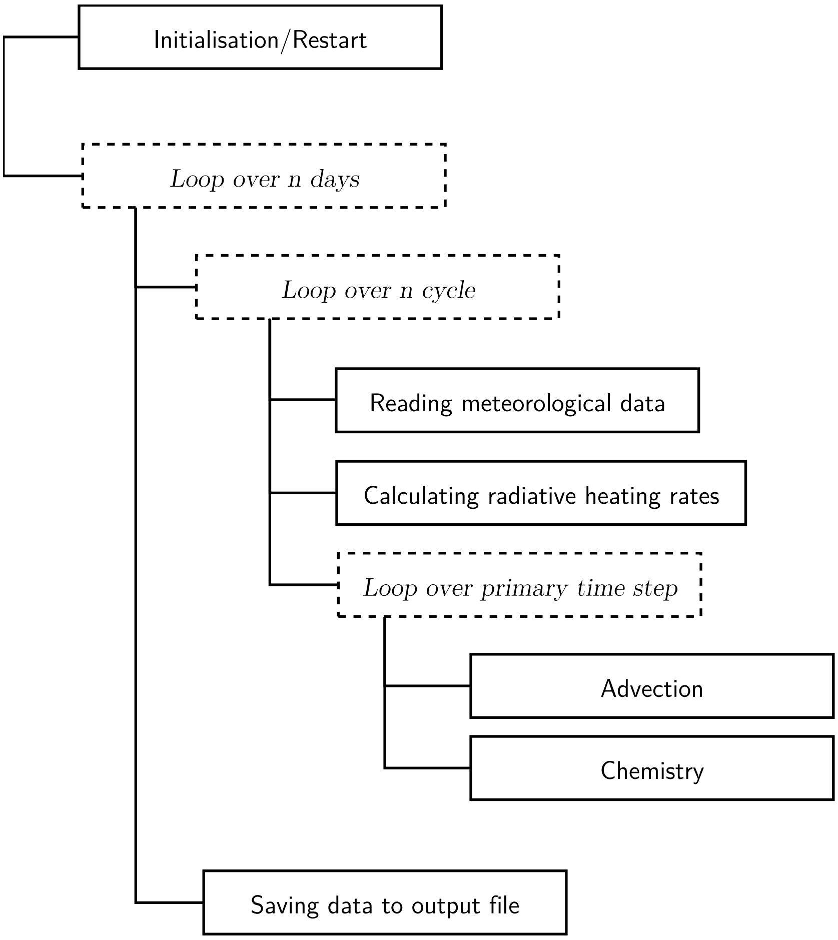

Figure 6.2 *Main framework of the Bremen 3-dimensional Chemistry and Transport Model (B3dCTM).*

6.2 Model resolution

The horizontal resolution of the model is illustrated in Figure 6.3. In longitudinal direction it has 96 grid boxes spanning over 3.75° with the first box centred at the center meridian. In latitudinal direction, the model has 72 grid boxes centred on a Gaussian grid with an approximately distance of 2.5°. This is a grid box area of approximately 417×278 km at the equator (under the assumption that the Earth is a perfect sphere).

The vertical resolution and coverage is depending on the meteorological data set and the chosen model version. The vertical resolutions of the different model versions are described in more detail in Section 7.1.

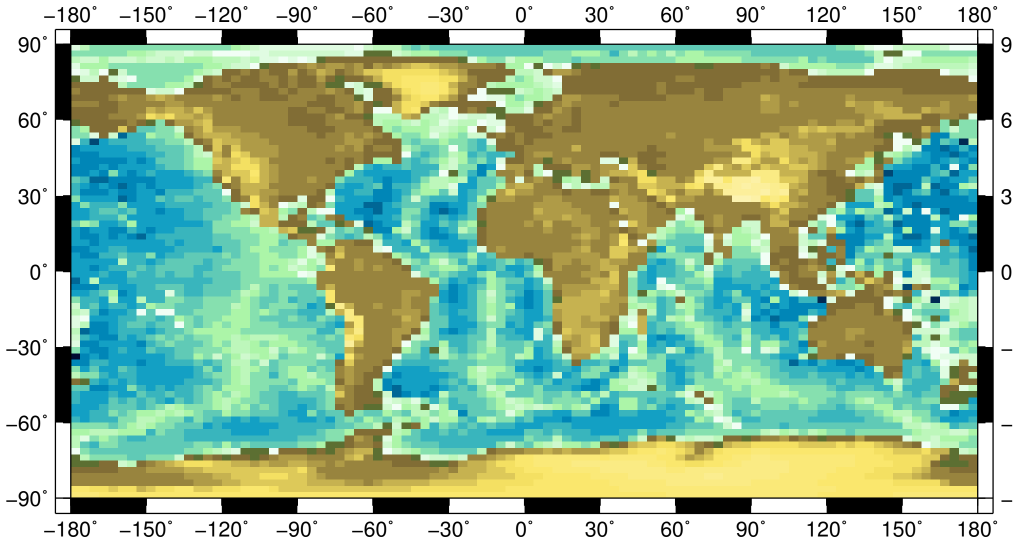

Figure 6.3 *Illustration of the approximately horizontal resolution of the Bremen 3-dimensional Chemistry and Transport Model (B3dCTM). To illustrate the resolution, data for land topography, ocean bathymetry, and ice surface (ETOPO1 Ice Surface) were gridded into the B3dCTM horizontal grid of approx. 3.75°×2.5°. ETOPO1 data are taken from the ETOPO1 Global Relief Model (Amante & Eakins, 2009).*

6.3 Transport

The transport of the B3dCTM depends on the particular model version. The preceding version of the model runs on potential temperature as vertical coordinate. From this model, a model version has been further developed that runs on pressure levels, as described in more detail in Section 7. In both model versions, the horizontal flux between model boxes is calculated with the horizontal wind fields obtained from the meteorological data (e.g. ECMWF or LIMA). The advection is then calculated according to this flux. For the vertical advection, each model version uses a different approach. The isentropic model version calculates the flux across the isentropes through diabatic heating rates. These heating rates are calculated with the Middle Atmosphere Radiation Scheme (MIDRAD) by Shine (1987) (Section 6.4). The version on pressure levels uses the vertical wind provided by the meteorological data to calculate the vertical flux. To account for the advection, both model versions employ the numerical advection scheme by Prather (1986) to calculate the advection in horizontal and vertical direction based on the fluxes derived from the wind fields and/or diabatic heating rates. The Prather (1986) scheme derives the solution to the advection-diffusion equations in which mixing ratios of the tracers are expanded in space by higher-order polynomials (Jacobson, 2005). It conserves the second-order moments of the spatial distribution of the tracers during advection (Prather, 1986).

6.4 The calculation of heating rates by the Middle Atmosphere Radiation Scheme (MIDRAD)

The heating rates are calculated with the MIDRAD scheme. It includes:

- the emission of infrared radiation by CO_2 in the 15 μm band

- the absorption of infrared radiation by O_3 in the 9.6 μm band
- the vibrational-rotational and rotational bands of water vapour
- the absorption of solar UV radiation by O_3 and O_2.

The infrared radiation scheme is based on Shine (1987) and the solar radiation sheme is based on Shine (1989).

During model simulation, a variable input to the MIDRAD scheme is the amount of O_3. The variable amount of O_3 is calculated by the chemistry code of the B3dCTM and passed to the MIDRAD radiation scheme. It is not taken as a prescribed O_3 profile but rather dynamicly from the chemical code during the model calculation. The version of the MIDRAD scheme used here does not apply Curtis matrices. Thus, it does not account for non-LTE conditions (Section 2.4.3). The output of the MIDRAD scheme are heating rates in [K/day]. These heating rates describe heating and cooling, where positive values refer to heating and negative values to a cooling. In the stratospheric version of the B3dCTM, these heating rates are used to calculate the vertical flux of air across isentropic surfaces, and therefore, the vertical transport of trace gases. In the model version that runs on pressure levels, the vertical transport is directly calculated through vertical wind fields as provide by the LIMA model, and the heating rates are investigated in terms of changing ozone values due to EPP events, see Section 16.

6.5 Chemistry

The chemical scheme of the B3dCTM includes 58 tracers and about 180 gas-phase and heterogeneous reactions. The trace gases are listed in Table 6.1. The reactions are listed in Section 2 in the Appendix.

The rate of reactions are taken from the set of recommendations by the Jet Propulsion Laboratory from 2006 (Sander *et al.*, 2006).

Table 6.1 *Trace gases for the chemical scheme of the Bremen 3-dimensional Chemistry and Transport Model (B3dCTM) including the full family approach. (Advected species are set in bold print.)*

Short lived species	$\mathbf{O_x}$ (O_3, $O(^3P)$, $O(^1D)$), $\mathbf{NO_x}$ (N, NO, NO_2), $\mathbf{ClO_x}$ (Cl, ClO, $2\,CL_2O_2$), $\mathbf{BrO_x}$ (Br, BrO), $\mathbf{NO_3}$, $\mathbf{N_2O_5}$, $\mathbf{HNO_3}$, $\mathbf{HNO_4}$, $\mathbf{ClONO_2}$, **HCl**, **HOCl**, $\mathbf{H_2O_2}$, OClO, $BrNO_3$, BrCl, HBr, HOBr,
Long lived species	$\mathbf{H_2O}$, **CO**, $\mathbf{H_2SO_4}$, $\mathbf{CHF_2Cl}$ **(F22)**, $\mathbf{CH_3CCl_3}$ **(MTCFM)**, $\mathbf{CH_4O_2}$ **(MHP)**, **COFCl**, $\mathbf{COF_2}$, **HF**, $\mathbf{CH_3Cl}$,
(source gases)	$\mathbf{N_2O}$, $\mathbf{CH_4}$, $\mathbf{CO_2}$, $\mathbf{CFCl_3}$ **(F11)**, $\mathbf{CF_2Cl_2}$ **(F12)**, $\mathbf{CCl_4}$, $\mathbf{C_2F_3Cl_3}$ **(F113)**, $\mathbf{CH_3Br}$, $\mathbf{CBrF_3}$ **(H1301)**, $\mathbf{CBrClF_2}$ **(H1211)**
Steady state species	H, OH, HO_2, CH_3, CH_3O_2, CH_2O, CH_3O, CH_3OOH, HCO
Fixed species (vmr)	H_2 ($5.0 \cdot 10^{-7}$), O_2 (0.209), N_2 (0.791)

6.5.1 The chemical solver method

For solving the chemical equations, different methods are used in the calculation of the B3dCTM. For short-lived species including the families the equations are solved using the semi-implicit method of Ramaroson *et al.* (1992). It is described in the following (see also Chipperfield (1996)):

The continuity equation of a chemical species i with a concentration n_i can be written as

$$\frac{dn_i}{dt} = P_i - L_i n_i = Q_i, \tag{6.1}$$

with a production term P_i and a loss term L_i. In vectorial form, this is written as

$$\frac{d\vec{n}}{dt} = \vec{Q}(t, \vec{n}(t)) \tag{6.2}$$

Following Ramaroson *et al.* (1992), Equation 6.2 can be developed into the form

$$\vec{n}_{t+\Delta t} - \vec{n}_t = \frac{\Delta t}{2}[\vec{Q}(t, \vec{n}(t)) + \vec{Q}(t + \Delta t, \vec{n}(t + \Delta t))] \tag{6.3}$$

The term $\vec{Q}(t + \Delta t, \vec{n}(t + \Delta t))$ can be expanded into a Taylor series so that Equation 6.3 can be rearranged to form

$$\vec{n}_{t+\Delta t} = \vec{n}_t + \frac{\Delta t}{2}\mathbf{J}_t \vec{n}_{t+\Delta t} \tag{6.4}$$

with the Jacobian matrix $\mathbf{J}_t$:

$$\mathbf{J}_t = \begin{pmatrix} \frac{\partial Q_1}{\partial n_1} & \frac{\partial Q_1}{\partial n_2} & \cdots & \frac{\partial Q_1}{\partial n_N} \\ \frac{\partial Q_2}{\partial n_1} & \frac{\partial Q_2}{\partial n_2} & \cdots & \frac{\partial Q_2}{\partial n_2} \\ \cdots & \cdots & \cdots & \cdots \\ \frac{\partial Q_N}{\partial n_1} & \frac{\partial Q_N}{\partial n_2} & \cdots & \frac{\partial Q_N}{\partial n_N} \end{pmatrix} \tag{6.5}$$

To determine the concentrations at a time $t + \Delta t$ the matrix

$$\mathbf{M} = \mathbf{I} - \frac{\Delta t}{2}\mathbf{J}_t \tag{6.6}$$

has to be inverted.

Long-lived species are solved with the Forward Euler method as described in Section 4.3.

6.5.2 Chemical families

The B3dCTM chemistry uses a family approach in two different modifications. The stratospheric model version that goes to about 60 km altitude applies a family approach including the families O_x, NO_x, HO_x, BrO_x, ClO_x, CHO_x. The individual constituents of each family are given in Table 6.2. The family approach is integrated in the model mainly to reduce computation time. Since the chemical time-scales for the constituents are much shorter than the transport time steps, the transport of the individual compounds within a family is not necessary. Also the members of each family are assumed to be in photochemical equilibrium, and therefore, are not integrated in the chemical solver individually, but only the family itself is transported and integrated within the chemistry code. This approach reduces the size

Table 6.2 *The chemical families in the Bremen 3-dimensional Chemistry and Transport Model (B3dCTM).*

Family	Constituents
O_x	O, O(^{1}D), O_3
NO_x	N, NO, NO_2
HO_x	H, OH, HO_2
BrO_x	Br, BrO
ClO_x	Cl, ClO, $2\,Cl_2O_2$
CHO_x	CH_3, CH_3O_2, CH_3OOH, CH_2O, CH_3O, HCO

of the matrix **M** in the chemical solver described above. The partitioning during night-time when photochemical equilibrium can not be applied is as described in Chipperfield (1996). The HO_x and CHO_x species are solved by putting them into steady state.

This family approach is valid in regions where the transport life-time is much longer than the chemical life-time of the individual family members, but the chemical life-time of the family is longer than the transport life-time. This is true for the stratosphere but gets more and more unrealistic with increasing altitude. To extend the model into the upper atmosphere, a model version has been developed that uses a reduced family approach in the upper stratosphere and Mesosphere and Lower Thermosphere (MLT) region (Section 7.2).

6.6 The parametrisation of the ion-chemistry due to precipitating particles

The chemical scheme of the B3dCTM is a neutral scheme with no ion chemistry explicitly included. Since the precipitating particles induce ion chemistry reactions that produce odd nitrogen and odd hydrogen compounds, this production needs to be parametrised in the neutral model chemistry. The production and loss of odd nitrogen species during ionisation events regarding ionisation and dissociation reactions has been calculated by Rusch *et al.* (1981). They concluded a production between 1.3 and 1.6 odd nitrogen species per ion pair in the middle atmosphere. They also stated that the production of odd nitrogen is increasing in the upper atmosphere. Porter *et al.* (1976), Frederick (1976), Jackman *et al.* (1979), predicted a NO production between 1.2-1.3. Hence, following Jackman *et al.* (1980), the production of odd nitrogen is set to P_{NO_x}=1.25 (NO_x per ion pair production) which is based on the best estimate of 1.27 by Porter *et al.* (1976), and is similar to Rusch *et al.* (1981). As already shown in Section 3.5.5, N can be produced in either the ground state (N(^{4}S)) or in the excited state (N(^{2}D)). Following Porter *et al.* (1976), the partitioning between both states are divided to 45% in the ground state and 55% in the excited state. The reaction of ground state nitrogen with NO can lead to a reduction of NO compounds, whereas the reaction of excited state N(^{2}D) with O_2 (R 3.16) will form NO nearly instantaneously.

Following Porter *et al.* (1976), the production of O directly by ion chemistry is parametrised to P_O=1.15 O per ion pair.

The production of HO_x per ionisation is calculated in the model simulation as a function of the ionisation rate and altitude. In the stratosphere this production rate is nearly a constant profile of P_{HO_x}=2 HO_x constituents produced per ion pair. In the mesosphere, above approx. 60 km, the production is then decreasing with altitude and above 90 km there is

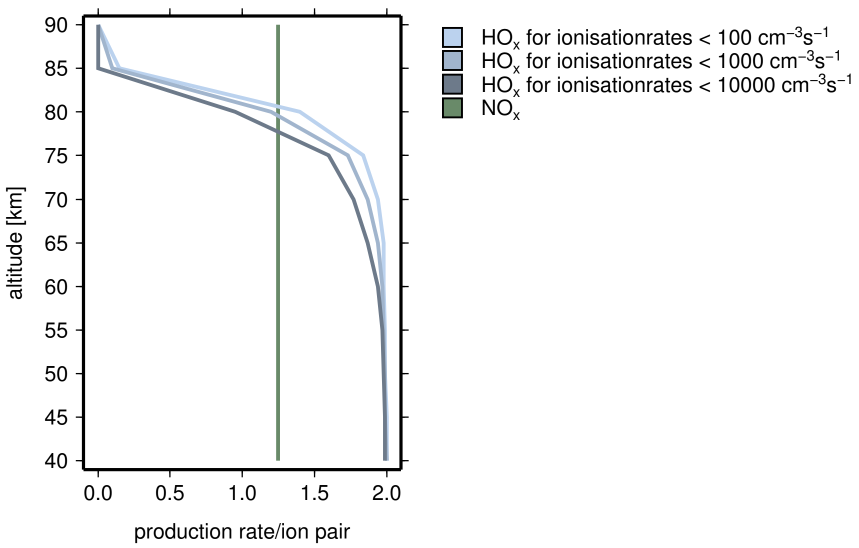

Figure 6.4 *HO_x and NO_x production rates due to EPP events. The NO_x production rate is a constant profile throughout the vertical extent for the model. HO_x production rates depend on ionisation rates and decrease with increasing ionisation rates and altitude. Values are taken from Jackman* et al. *(2005a) and are based on Solomon* et al. *(1981).*

no production of HO_x through ionisation. The HO_x production is also nearly independent of the rate of ionisation in the stratosphere. Above 75 km it is strongly dependent on ionisation rates and is in general lower for higher ionisation rates and increases with decreasing ionisation rates. The HO_x and NO_x production rates are illustrated in Figure 6.4 as a function of altitude and for three different ionisation rates (100 $cm^{-3}s^{-1}$, 1000 $cm^{-3}s^{-1}$, and 10000 $cm^{-3}s^{-1}$). These value are taken from Jackman *et al.* (2005a) and are based on ion chemistry calculations by Solomon *et al.* (1981).

To account for negative ion chemistry reactions that directly affect chlorine compounds, parametrised production rates derived from the University of Bremen Ion Chemistry (UBIC) model (Winkler *et al.*, 2009) (see Section 8.3 for a short description of the model and the computation of the production rates) have been used, in addition to the production rates

Table 6.3 *Parameters of the chlorine production rates lookup table obtained from the University of Bremen Ion Chemistry (UBIC) model.*

Parameter	**Values**
ionisation rate [1/s/ccm]	500, 2500, 10000, 25000
cos (solar zenith angle) [rad]	-0.5, -0.1, -0.03, 0.03, 0.1, 0.25, 0.5
16 pressure altitudes [Pa]	between 2276-0.872 (approx. 24-76 km)
HCl [ppb]	0.4, 1.0, 2.5, 3.5
Cl+ClO [ppb]	0.01, 0.3, 0.8, 1.5
$ClONO_2$ [ppt]	0, 40, 100, 400, 900
NO_x [ppb]	0.2, 5, 10, 50, 100
H_2O [ppm]	0.0002, 0.01, 0.5, 5.0

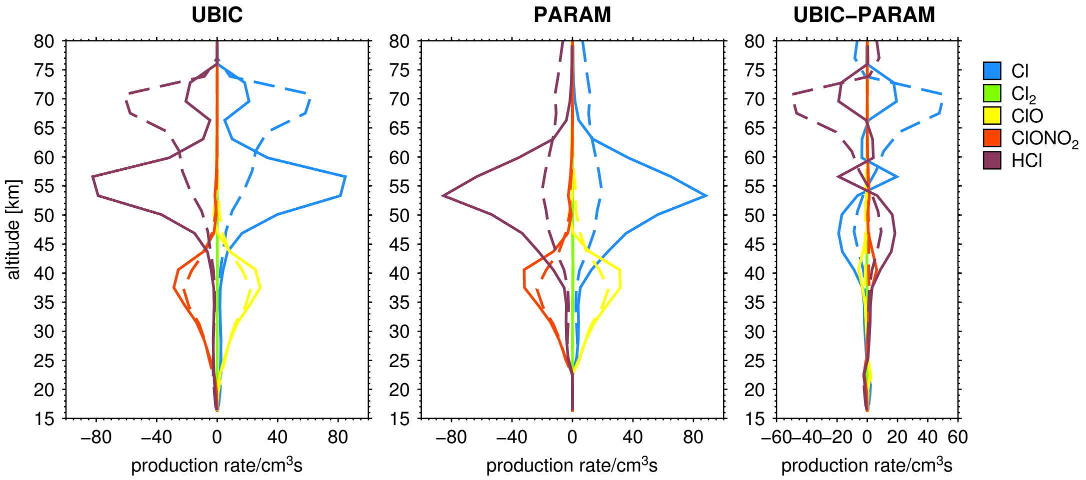

Figure 6.5 *Production rates calculated with the University of Bremen Ion Chemistry (UBIC) model (left panel) and parametrised chlorine production rates (right panel) for Cl, Cl_2, ClO, $ClONO_2$, and HCl on 30 October 2003 00:15 UTC for 75°N. Dashed lines are night-time values for zero meridian, solid lines represent day-time values at 180°E.*

for HO_x and NO_x described above. In the following, the term 'production rates' is used here for positive and negative values. A lookup table containing production rates for HCl, ClO, Cl, and Cl_2, derived from UBIC has then been used to perform model simulations for the October/November 2003 SPE with the B3dCTM. During the computation, production rates for HCl, ClO, Cl, and Cl_2 were extracted from this table by linear interpolation depending on the parameters described in Table 6.3.

In Fig. 6.5 production rates as calculated from UBIC directly (left panel) and as the used

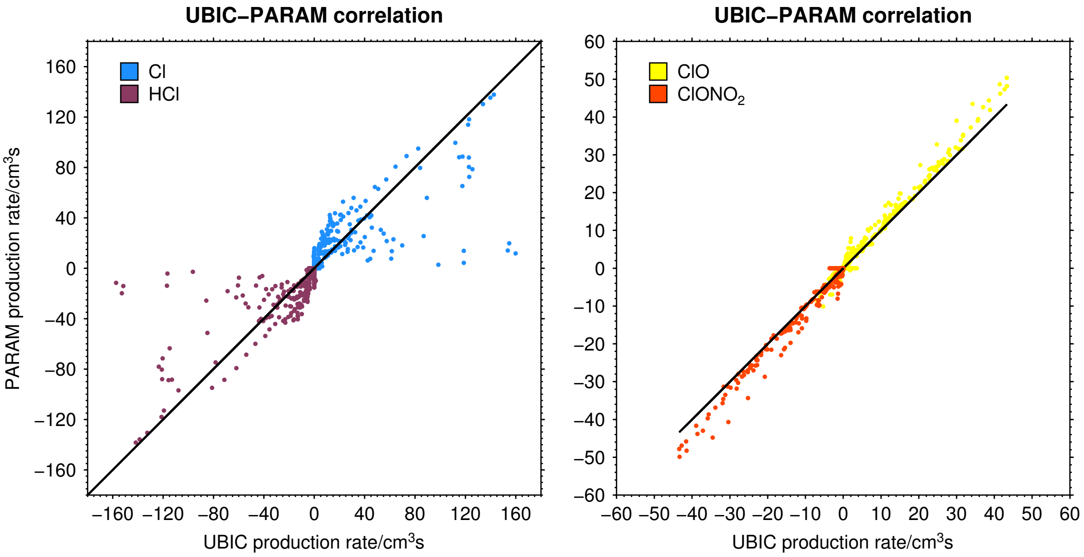

Figure 6.6 *Correlation between chlorine production rates calculated with the University of Bremen Ion Chemistry (UBIC) and parametrised chlorine production rates for Cl and HCl (left panel) and ClO and $ClONO_2$ (right panel).*

parametrisation derived from UBIC (middle panel) for day-time (solid line) and night-time (dashed line) conditions on 30 October 2003 are indicated. The right panel of Figure 6.5 shows the differences between UBIC production rates and the parametrisation. In general, both production rates show similar altitude dependencies, but slightly different absolute values. As described in Sect. 3.5.5, $ClONO_2$ reacts with CO_3^- (R 3.36), that is more abundant in lower altitudes. Hence, the production rate is negative, peaking at around 40 km. HCl reacts with different ions (R 3.35) and has also a negative production rate, peaking between 50-60 km. The production rates for Cl, Cl_2 and ClO are positive, since these compounds are released through recombination reactions. ClO production also peaks at the same altitude as $ClONO_2$, since ClO is produced at the expense of $ClONO_2$ (R 3.36). Cl is formed through recombination reactions with Cl^- that is produced from reactions with HCl (R 3.35), and therefore, shows the opposite behaviour as HCl. The dependency of the production rates on the solar zenith angle is reproduced by the different shapes of the curves. Hence, production rates during night-time conditions are in general smaller than during day-time. But in this comparison of day- and night-time rates it has to be taken into account that the curves corresponds to the same UTC time but to different locations. So the differences also represent different local ionisation rates and concentrations of the other parameters (Table 6.3). Below 50-55 km, the production rates for HCl and Cl are larger in the parametrisation by about 12-25%. Therefore, the conversion of HCl to Cl will be overestimated by the parametrisation. Above 55 km the opposite is true. The parametrisations for HCl and Cl production show lower values as directly obtained from UBIC by 25-60%. The production of Cl in the mesosphere is overestimated by the parametrisation. For ClO and $ClONO_2$, the parametrisation gives larger production rates of about 6% in the stratosphere. Fig. 6.6 shows a correlation between the production rates for 30 October 2003 for Cl, HCl, ClO, and $ClONO_2$ as derived directly from the UBIC model (x-axes) and from the applied parametrisations. ClO and $ClONO_2$ (right figure) show a good correlation, whereas Cl and HCl (left figure) show higher production rates directly by the UBIC model that corresponds to lower production rates in the parametrisation in the mesosphere above 55 km.

7 Further model developments

The Bremen 3-dimensional Chemistry and Transport Model (B3dCTM) is a combination of the three-dimensional CTM developed by B.-M. Sinnhuber (Sinnhuber *et al.*, 2003a) and the chemistry code of the two-dimensional model of the stratosphere and mesosphere. The CTM is based on the SLIMCAT model (Chipperfield, 1999). The chemical scheme is described in, e.g. Sinnhuber *et al.* (2003b) and Winkler *et al.* (2008). The combination of these individual model schemes has been developed within the framework of my diploma thesis (Wieters, 2008) at Institut für Umweltphysik (IUP), University of Bremen. The combined model version and computed results have been used by different research groups within the IUP, and the model is in further development by different colleagues and former members of the institute. A very important improvement of the model has been achieved within the framework of the doctoral thesis of Jan Aschmann (Aschmann, 2011). He, i.a., parallelized the source code to run the model in a suitable time frame. This important adaption of the computer code enabled the realisation of model simulations for a time span of several model years with the full chemistry code included.

The 'basic' version of the B3dCTM, as the underlying CTM, is driven by meteorological data from the UK Met Office (UKMO) (Swinbank & O'Neill, 1994). This data set is provided up to an altitude of about 55 km (0.3 hPa). The model is, therefore, mainly confined to the stratosphere (between 10-55 km). One of the main tasks in the framework of this thesis was to extend the model to the Mesosphere and Lower Thermosphere (MLT), since a major impact of precipitating particles is in the MLT region and originates there. Besides the direct impact in the stratosphere and MLT region, a further impact is, therefore, the downward transport of disturbed species into the stratosphere from above. To include both effects in the model, it needs to include higher altitudes up to the lower thermosphere. One limiting factor of the development of an extended version was the availability of meteorological data that cover this vertical altitude range. A first attempt was to implement data from the European Centre for Medium-Range Weather Forecasts (ECMWF). Two data sets have been used (ECMWF ERA Interim (Dee *et al.*, 2011) and ECMWF Operational), and results are presented here for the ECMWF ERA Interim data set that provides data to 0.1 hPa (approx. 60 km). To extend the vertical coverage of the model to the mesosphere and lower thermosphere, data provided by Dr. Uwe Berger (Leibniz-Institut für Atmosphärenphysik (IAP), Kühlungsborn) derived from the Leibniz-Institute Middle Atmosphere (LIMA) model (Berger, 2008) has been implemented into the B3dCTM as a third source of meteorological data.

A second problem in the extension of the model was the vertical coordinate. The basic stratospheric version of the B3dCTM applies potential temperature (see Section 2.2.3) as vertical coordinate. In the stratosphere, the potential temperature is a continuous variable as it increases with increasing altitude, since temperature is increasing in the stratosphere. In the mesosphere, the temperature gradient is opposite and temperature is decreasing with altitude. Therefore, the potential temperature is not necessarily continuously increasing with altitude. Besides, diabatic processes that describe the vertical flux in the basic stratospheric model version are not only due to radiative processes, as in the stratosphere, but include dynamical heating by wave dissipation, diabatic expansion, and chemical heating. Thus, radiative heating rates are not sufficient to calculate the vertical motion in the upper atmosphere.

The following program units of the model have been adapted to extend the model to the upper atmosphere:

- Implementation of meteorological data that reach up to the lower thermosphere, as derived from the LIMA (Section 7.1).
- The vertical coordinate potential temperature has been exchanged by pressure coordinates.
- The calculation of the vertical flux is now performed by the use of vertical wind data from the implemented meteorological data instead of the calculation through diabatic heating rates due to radiative processes.
- The implementation of a non-family approach in the mesosphere and lower thermosphere. In the further developed version of the B3dCTM that runs on pressure levels, the families O_x and NO_x have been adapted in such a way that each of their members is transported and integrated in the chemistry code explicitly (Section 7.2).

7.1 The extension of the Bremen 3-dimensional Chemistry and Transport Model (B3dCTM) into the mesosphere and lower thermosphere

To investigate the impact of energetic particle events on the middle and upper atmosphere, stratosphere, mesosphere, and lower thermosphere, the B3dCTM has been extended to the mesosphere and lower thermosphere. For this purpose, the ECMWF ERA Interim (Dee *et al.*, 2011) data set was not suitable any more, since these data only reach to the upper stratosphere and lower mesosphere (∼60 km). ECMWF Operational data, however, reach up to 80 km, but these data are only available for February 2006 onwards. Since the purpose was to have a continuous model simulation over the period of available AIMOS ionisation rates (from 2002 to 2010) the operational data were not suitable for this study either. Therefore, it was decided to take data from the Leibniz-Institute Middle Atmosphere (LIMA) GCM by Berger (2008) from the IAP Kühlungsborn. This model and data set is described in more detail in Section 8.2.2. The provided data set covers the time span from 1990 to April 2010 with a vertical coverage from 921.21 hPa up to $4.21 \cdot 10^{-6}$ hPa, and hence, up to the lower thermosphere.

As a first attempt the model was driven with the LIMA meteorological data to a pressure level of 0.00016 hPa (∼100 km) with the same family approach in the chemical scheme as in the basic stratospheric model version. Model simulations that refer to this second model version are indicated in the following by LIMA PR MESO. Model calculations showed for O_3 very much overestimated values above 70 km. The adaptation of the family approach in a third model version of the B3dCTM employing the LIMA data (LIMA PR THERMO) reaches up to about 130-140 km and is described in Section 7.2.

For a case study (Section 16), a forth model version (KMCM PR) was developed that is driven by meteorological data from the Kühlungsborn Mechanistic general Circulation Model (KMCM) by Becker (2009) (IAP). See Section 8 for a description of the B3dCTM model input data.

The vertical resolution and coverage of the four different model versions are shown in Figure 7.1. Center levels are indicated in black lines, inter levels are indicated in grey. The

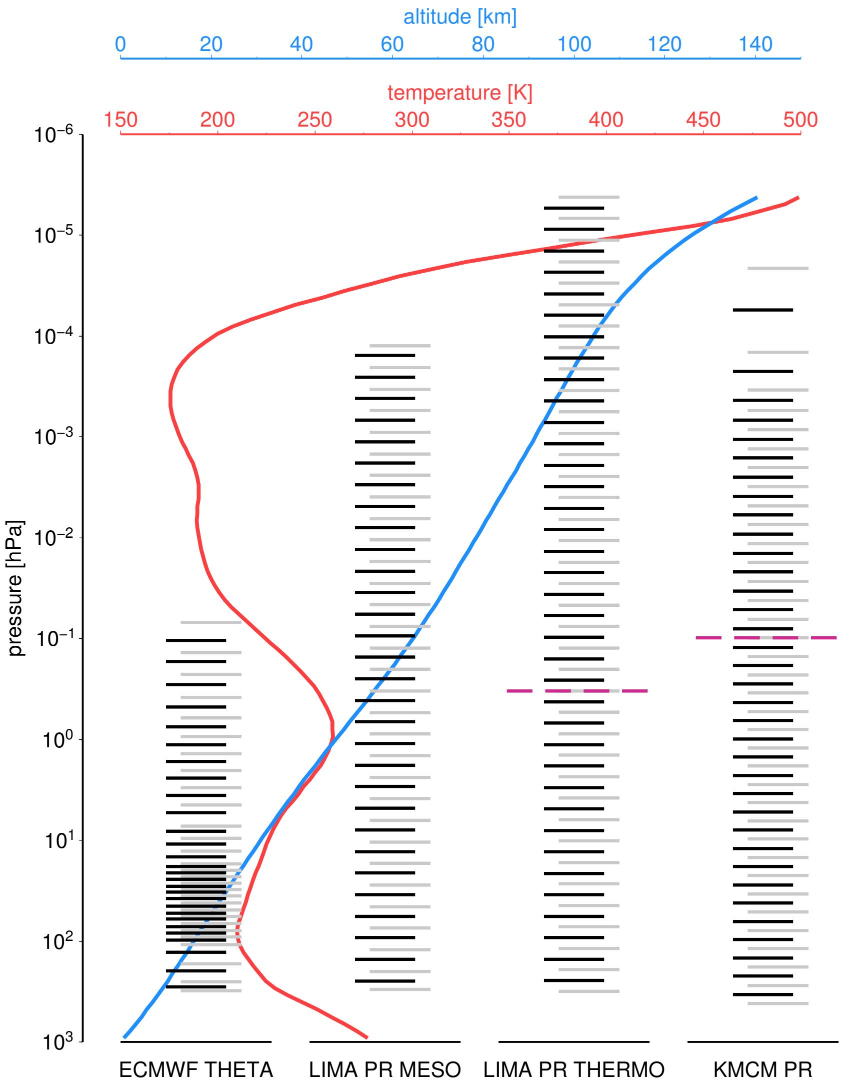

Figure 7.1 *Vertical resolution of the different developed versions of the Bremen 3-dimensional Chemistry and Transport Model (B3dCTM). Model levels at box center (black); model levels between boxes (grey); globally averaged profiles at equinox (2010) for temperature (red) and altitude (blue) from LIMA. Values for* ECMWF THETA *represent the global mean pressure at grid level (potential temperature) for equinox (2010). The purple line indicates the split level of the different implemented family approaches.*

globally averaged temperature profile derived from LIMA at equinox 2010 is plotted as a function of pressure in red. The corresponding globally averaged altitude profile is plotted in blue. The purple dashed line indicates the split level of the different family approaches, discussed in Section 7.2.

7.2 A non-family version for O_x and NO_x

To improve the model in the mesosphere and lower thermosphere, the family approach has been modified by resolving the families O_x (O, $O(^3P)$, $O(^1D)$) and NO_x(N, NO, NO_2) in

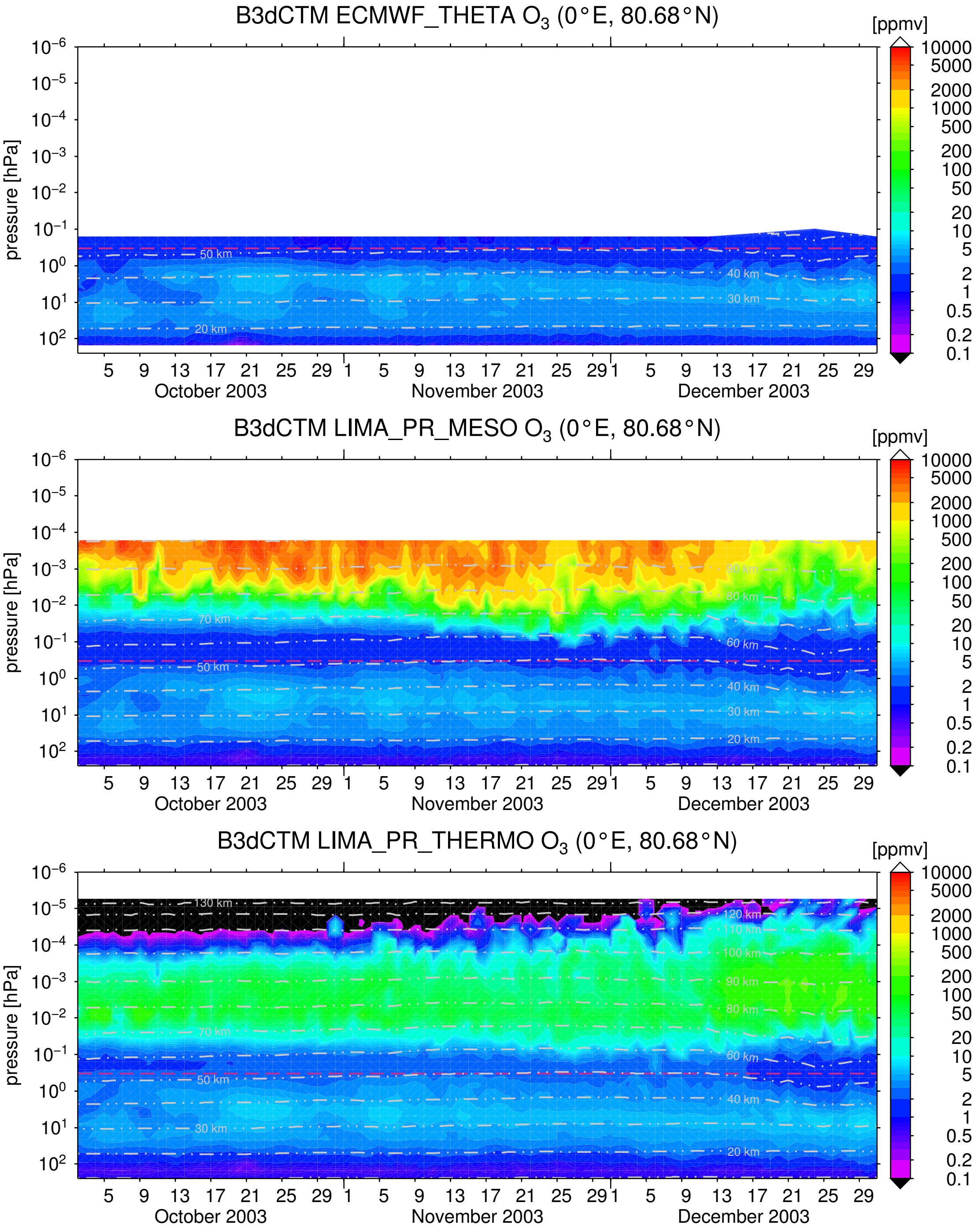

Figure 7.2 *Absolute values of ozone abundance for the different developed model versions. The purple dashed line indicate the pressure level from which the model version* LIMA PR THERMO *(lower most panel) is applied with the reduced family approach (see text for further information).*

the upper atmosphere (upper stratosphere and MLT region). The individual compounds of these families (except for $O(^1D)$ and N) are now transported and integrated in the chemical scheme explicitly. This reduced family approach gives more realistic values especially for ozone with respect to the order of magnitude. For the three different model versions that are driven by meteorological data from ECMWF and LIMA, a time evolution of area weighted averages of 70°-90°N for ozone is shown in Figure 7.2. Results for the ECMWF driven stratospheric model version are presented in the upper panel, and the two LIMA versions are shown in the middle and lower panel, respectively. The lower panel shows results with the reduced family approach model version. Above 0.33 hPa the total family approach is changed to the reduced approach. This is indicated by the dashed purple line. In the MLT region, the full family approach results in significantly higher vmr for ozone that are highly overestimated. In the reduced family approach, ozone increases in the MLT region and peaks at around 80-90 km which corresponds to the second ozone maximum in the upper atmosphere as described in Section 2.3. Below 0.33 hPa all model versions use the full family approach.

For the modified family approach, the chemical time step had to be shortened to 60 seconds, this increased the computing time of the individual simulations by a factor of approximately 2.5.

A further version of the B3dCTM is currently under development that resolves also HO_x in the family approach. First results show that the abundance of ozone becomes smaller in the upper atmosphere due to higher values in HO_x constituents during polar night. This suggests, that ozone values in the LIMA PR THERMO are overestimated because of the equilibrium approach of the HO_x family in the family approach of the chemical scheme. First results also show that the resolved HO_x family results in no significant impact on other species than ozone.

8 Input data for model simulations

8.1 AIMOS ionisation rates

To account for the ionisation during particle precipitation, ionisation rates provided by the Atmospheric Ionization Module Osnabrück (AIMOS) have been implemented in the B3dCTM model calculations. AIMOS is described in more detail in Wissing & Kallenrode (2009) and will be summarised briefly in the following.

AIMOS simulates ion pair production rates due to precipitating particles as observed by different instruments onboard different satellites: EPS onboard GOES 10 and GOES 11 and SEM-2 onboard POES NOAA 15 and 16. From these observations, the model calculates a three dimensional distribution of ionisation rates due to different particle inventories: solar and geomagnetic particles; protons and electrons. The polar cap and the auroral oval expand equatorward with increasing geomagnetic activity. AIMOS accounts for the dependence of the polar cap size on the geomagnetic activity by using POES observations. It calculates the horizontal distribution from particle observations of the two polar orbiting POES satellites. The interaction of the precipitating particles with the atmosphere is simulated using a Monte Carlo simulation based on GEANT4 (Agostinelli *et al.*, 2003). The energy loss due to ionisation as well as the production of Bremsstrahlung by high energy electrons are considered as well as hadronic reactions for very high energies which reduce the ionisation rates. For the calculation of the interaction with the atmosphere a background model atmosphere from the HAMMONIA model is used in the calculations. AIMOS has a horizontal resolution of 3.6°×3.6°and 67 height levels, from the ground to $1.7 \cdot 10^{-5}$ Pa (0 - 250/600 km). The energy range for which AIMOS calculates the ionisation rates is indicated in Table 8.1.

The ionisation rates are provided by AIMOS on the horizontal grid of the B3dCTM. They are interpolated on the vertical B3dCTM grid during model calculations.

The horizontal and vertical distribution of the ionisation rates as provided by AIMOS are shown in Figures 8.1 and 8.2, respectively. Figure 8.1 shows maps for ionisation rates of the two particle populations, protons (left panel) and electrons (right panel), at 0.0013 hPa and for the 29/10/2003 (4-6 UTC). A time evolution of ionisation rates at 0°E, 80°N is presented in Figure 8.2 for protons (upper panel) and electrons (lower panel).

Table 8.1 *Particle energy range spectrum of the Atmospheric Ionization Module Osnabrück (AIMOS).*

Particles	Energy range
protons	150 eV - 500 MeV
electrons	150 eV - 5 MeV
α-particles	4 MeV - 500 MeV

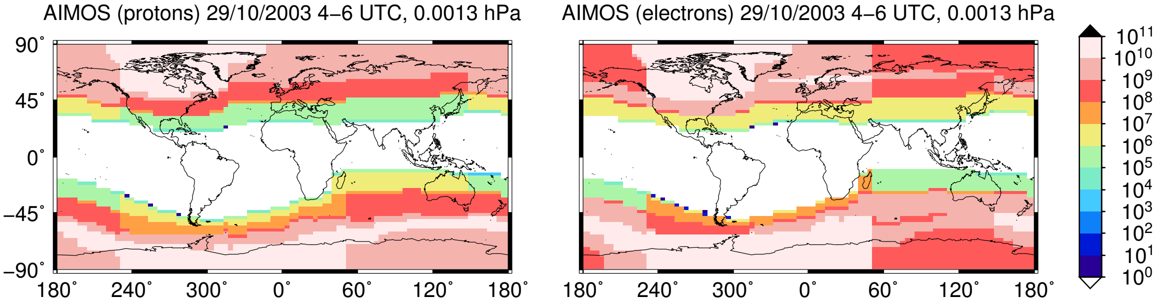

Figure 8.1 *Global distribution of ionisation rates from the Atmospheric Ionization Module Osnabrück (AIMOS) due to protons (left panel) and electrons (right panel) for 29 October 2003.*

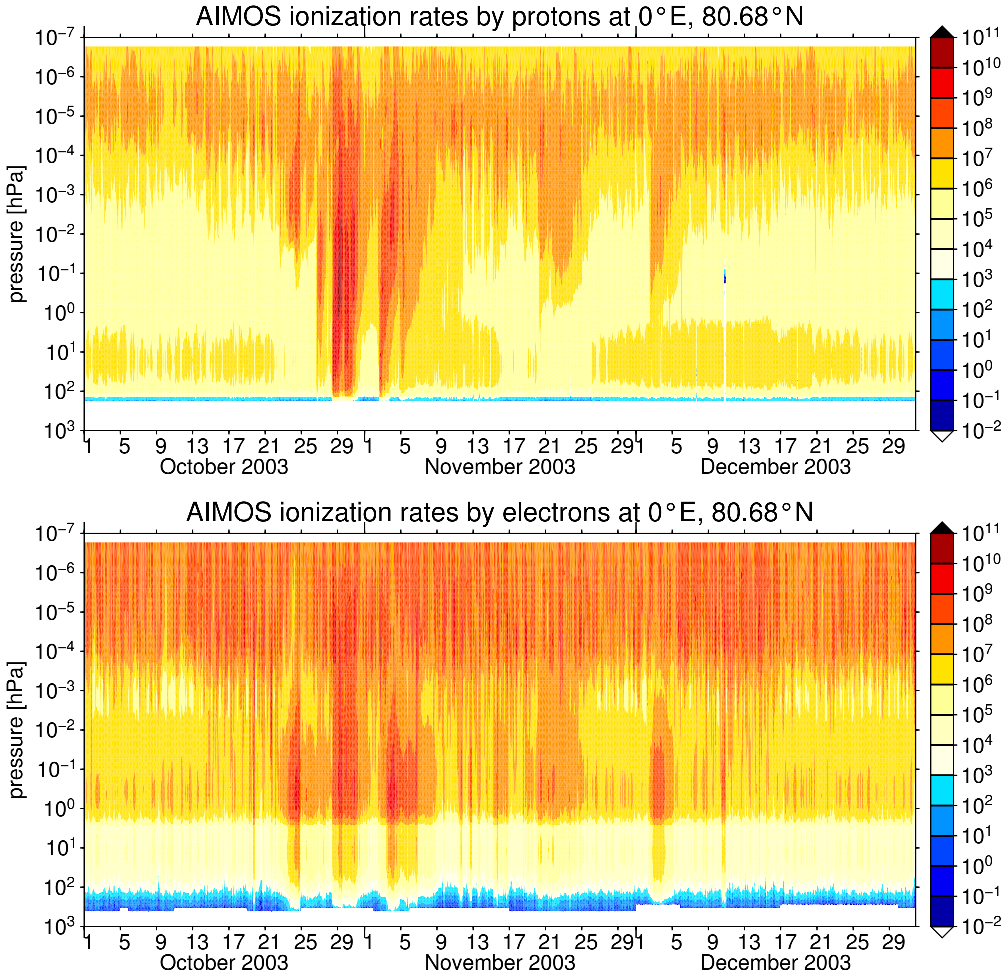

Figure 8.2 *Time evolution of ionisation rates from the Atmospheric Ionization Module Osnabrück (AIMOS) due to proton (upper panel) and electron (lower panel) precipitation at central meridian and 80° North for the period October-December 2003.*

8.2 Meteorological data sets

8.2.1 The European Centre for Medium-Range Weather Forecasts (ECMWF) data

In this study, results a model simulations forced with the ECMWF ERA Interim data set are presented. The ERA Interim data set is a reanalysis of meteorological data produced by the European Centre for Medium-Range Weather Forecasts (ECMWF) and is described in Dee *et al.* (2011). It is based on a forecast model and the assimilation of observational data. The ECMWF ERA Interim data set covers a vertical range up to 0.1 hPa, about 60 km.

8.2.2 The Leibniz-Institute Middle Atmosphere (LIMA) model

The Leibniz-Institute Middle Atmosphere (LIMA) model is described in detail in Berger (2008). LIMA is a GCM of the middle atmosphere. It runs on 118 pressure levels between 921.21 hPa and $4.21037 \cdot 10^{-6}$ hPa (approx. 0–140 km). It is a non-linear, global, Eulerian grid model. It has a triangular grid with a mesh size of approximately 110 km. This fine mesh size enables LIMA to avoid the parametrisation of gravity waves (GWs). In the troposphere and lower mesosphere LIMA assimilates meteorological data from the ECMWF ERA-40 reanalysis (Uppala *et al.*, 2005). The LIMA meteorological data set used in this study was provide by Dr. Uwe Berger from the IAP, Kühlungsborn. The data were provided on a geographical horizontal grid of 1°×1° for the period January 1990 to April 2010.

Zonal mean temperatures from LIMA are displayed in Figure 2.4(a).

8.2.3 Kühlungsborn Mechanistic general Circulation Model (KMCM)

The Kühlungsborn Mechanistic general Circulation Model (KMCM) is described in detail by Becker (2009). It is a global high-resolution GCM. The model resolves the large-scale flow and GWs and includes a parametrisation for turbulence. Vertical and horizontal diffusion is scaled by the Richardson criterion[i] for instability of GWs. This yields to a self-consistent damping of resolved GWs in the MLT region. The model includes a parametrisation for differential heating by temperature relaxation. It is based on a spectral dynamical core with a triangular truncation at total wave number 120. It has 190 hybrid levels from the surface to about 125 km altitude. This corresponds to a minimum horizontal wavelength of 350 km. The KMCM has been used in different studies, see e.g. Becker (2009), Becker & von Savigny (2010), Grygalashvyly *et al.* (2011). The KMCM data set was provided by Prof. Erich Becker from the IAP Kühlungsborn. It includes an annual cycle of wind and temperature fields.

Zonal mean temperatures from KMCM are displayed in Figure 2.4(b).

8.3 The University of Bremen Ion Chemistry (UBIC) model

UBIC is an ion chemistry box model that simulates the time evolution of 138 charged and uncharged species due to more than 600 reactions. A list of all UBIC species can be found in Winkler *et al.* (2009). The model accounts for photo ionisation of NO by Lyman-α radiation, photo dissociation and photo detachment of electrons, as well as particle impact ionisation due to precipitating particles. For further information on the model see Winkler

---

[i] Criterion for instability with respect to buoyancy and shear.

et al. (2009). UBIC has been used as an equilibrium model to assess the impact of ionisation caused by energetic protons and electrons on chlorine species (see Section 6.6 for a description of the obtained production rates). In a first step, systematic UBIC model runs have been performed to identify the key parameters on which the impacts on chlorine species depend. These parameters are: Ionisation rate, solar zenith angle, pressure altitude, HCl, Cl+ClO, $ClONO_2$, NO_x, and H_2O. The neutral chlorine species affected by the ion chemical reactions were found to be HCl, Cl, ClO, $ClONO_2$, and Cl_2. Direct changes of HOCl turned out to be negligible. After the relevant input parameters were known, UBIC simulations have been carried out for all combinations of the values listed in Table 6.3. As a result, the production rate of HCl, Cl, ClO, $ClONO_2$, and Cl_2 as a function of the input parameters were determined. The resulting lookup table allows to account for the ion chemical effects on the middle atmosphere's chlorine chemistry in a global model of the neutral atmosphere without running the time consuming ion chemistry model.

8.4 Source gases

Source gases are included in the model as lower boundary input. The values for the source gases N_2O, CH_4, CO_2, CH_3Cl, $CFCl_3$ (F11), CF_2Cl_2 (F12), $C_2F_2Cl_3$ (F113), CCl_4, CH_3Br, $CBrF_3$ (H1301), and $CBrClF_2$ (H1211) are taken from the WMO report 2010 scenario A1 (Daniel & Velders, 2011). Data for the WMO report 2010 scenario A1 are displayed in Figure 3 in the Appendix.

9 Model simulations and data analysis

9.1 Carried out model simulations

Within the framework of this thesis, a number of model simulations have been carried out. The simulation that are used for the presented results of this thesis are summarised in Table 9.1.

9.2 Publications and working group contributions

Results of model simulations carried out with the ECMWF THETA stratospheric model version have been performed for a study that has been published in cooperation and as co-author in Wissing *et al.* (2010). Model simulations performed in the framework of this thesis have been carried out to investigate the different impacts of ionisation rates due to protons and electrons in the stratosphere and lower mesosphere. Results have been contributed to this study and represented as contour plots that have been provided by me and published in the mentioned publication.

Results of a model simulation carried out with the ECMWF THETA stratospheric model version have been contributed to the international model measurement inter-comparison campaign that was performed as part of the High Energy Particle Precipitation in the Atmosphere (HEPPA) initiative starting in 2010. This inter-comparison involved nine models that have performed model simulations for the Halloween SPE 2003. Results of all the models have been compared to observations by the Michelson Interferometer for Passive Atmospheric Sounding (MIPAS) instrument on-board the Environmental Satellite (ENVISAT). Results from this inter-comparison have been published with co-authorship in Funke *et al.* (2011).

Results of the further developed model version that includes the MLT regions (high-top model version), have contributed to the priority program *Climate and Weather of the Sun Earth System (CAWSES)* by the Deutsche Forschungsgemeinschaft (DFG) and published in Lübken *et al.* (2010) as well as in the review paper by Sinnhuber *et al.* (2012).

A second inter-comparison campaign within the framework of HEPPA was initiated in 2011 about the effect of electron precipitation after the Sudden Stratospheric Warming (SSW) event during the polar winter 2008/2009. Results from the high-top model version including the upper atmosphere that has been evolved out of this PhD project have contributed to this inter-comparison, which presently includes 11 different models and observation from different instruments such as ACE, GOMOS, MIPAS, MLS, Odin, SABER, and SCIAMACHY. The contribution to this HEPPA MMI working group initiative is still in progress, but first results have already shown the importance of high-top models for understanding the processes under investigation. Up to now, only two model that reach to the MLT region participate in this initiative, the Whole Atmosphere Community Climate Model (WACCM) and the B3dCTM.

Table 9.1 *Carried out model simulations.*

Designation	**Meteorol. data**	**Vertical coverage**	**Particle forcing**	**Time period**	**Ion chemistry parametrisation**
ECMWF_THETA_BASE	ECMWF[a]	330-3402 K (10-60 km)	none	1990-2009	none
ECMWF_THETA_SPE			protons		
ECMWF_THETA_EEP			electrons	2002-2009	$\mathrm{NO_x}$, $\mathrm{HO_x}$, $\mathrm{O_x}$
ECMWF_THETA_EPP			protons, electrons		
ECMWF_THETA_PARAM			protons	Oct-Dec 2003	$\mathrm{NO_x}$, $\mathrm{HO_x}$, $\mathrm{O_x}$, $\mathrm{ClO_y}$
LIMA_PR_BASE_MESO	LIMA[b]	300-0.000125 hPa (10-100 km)	none	1990-2010	none
LIMA_PR_SPE_MESO			protons	2002-2010	$\mathrm{NO_x}$, $\mathrm{HO_x}$, O
LIMA_PR_EPP_MESO			protons, electrons		
LIMA_PR_BASE_THERMO		314.8-0.00000421 hPa (10-140 km)	none	2002-2010	none
LIMA_PR_SPE_THERMO			protons		
LIMA_PR_EEP_THERMO			electrons	Oct-Dec 2003	$\mathrm{NO_x}$, $\mathrm{HO_x}$, $\mathrm{O_x}$
LIMA_PR_EPP_THERMO			protons, electrons	2002-2010	
LIMA_PR_THERMO_PARAM			protons	Oct-Nov 2003	$\mathrm{NO_x}$, $\mathrm{HO_x}$, $\mathrm{O_x}$, $\mathrm{ClO_y}$
LIMA_PR_EPP70_THERMO			protons, electrons (>70 km)	Oct-Dec 2003	$\mathrm{NO_x}$, $\mathrm{HO_x}$, $\mathrm{O_x}$
KMCM_PR_BASE	KMCM[c]	416-0.000021 hPa 10-110 km	none	2002-2004	none
KMCM_PR_EPP			protons, electrons (>70 km)		$\mathrm{NO_x}$, $\mathrm{HO_x}$, $\mathrm{O_x}$

---

[a] Dee *et al.* (2011)
[b] Berger (2008)
[c] Becker (2009)

9.3 Data analysis

9.3.1 Area weighted means

In order to obtain the net impact of precipitating particles on the abundance of a certain species in the polar regions as a function of time/date, the difference between the related model scenarios have been plotted as *area weighted* means averaged over a certain area above the polar cap as a chronological sequence. The area weighted average takes into account that the area of the model boxes are becoming smaller towards the poles. An average that is not area weighted overestimates the mean of the same area, since it assumes that each model box has the same area size. High latitude model boxes are than overvalued in the average. Therefore, the average over a polar cap is weighted by the cosine of the considered latitude. The area weighted mean of a value $\bar{X}_{aw}$ over a latitude region $(\varphi_1 \ldots \varphi_N)$ is obtained by

$$\bar{X}_{aw} = \frac{\sum\limits_{i=1}^{n} \cos(\varphi_i) \bar{X}_{\varphi_i}}{\sum\limits_{i=1}^{n} \cos(\varphi_i)}, \tag{9.1}$$

where φ is the latitude and $\bar{X}_{\varphi_i}$ is the zonal mean value of X at latitude φ_i.

9.3.2 Difference to the reference run

To investigate the net impact of the precipitating particles, the difference is taken with respect to a carried out reference simulation as indicated in the corresponding sections. This reference simulation, as described above, includes no consideration of particle precipitation of any particle type and, therefore, do not implement any ionisation rates.

The absolute difference is calculated as follows:

$$\Delta[\text{vmr}] = \text{CASE} - \text{BASE} \tag{9.2}$$

The relative difference is calculated in percent with respect to the reference simulation such that

$$\Delta[\%] = \frac{\text{CASE} - \text{BASE}}{\text{BASE}} \cdot 100\% \tag{9.3}$$

9.3.3 Comparison to observational data

The simulated data are compared to observations obtained by the Michelson Interferometer for Passive Atmospheric Sounding (MIPAS) instrument on-board the Environmental Satellite (ENVISAT) satellite. With the model simulations it is possible to look at a global distribution and abundance of trace gases at any output time. In the regular model output this is, for instance, at 0 UTC. Since the ENVISAT satellite flies in an sun synchronous orbit it passes, e.g. the equator, always at the same local time. So the observations are only available for a certain longitude and latitude and local time, and not for a full global coverage at any time. To compare the model data to the observations, only model values can be compared to which a measurement is also available. Two ways of generating such a model output has been applied during the simulations. A first will write out values at certain latitude and longitudes and global time, where there is a possible MIPAS overpass.

In the comparison, the values have to be checked if values of the observation are available. A second approach is to take all location of retrieved MIPAS observations of a species with a large set of retrieved data (in this case O_3). During the model simulation each value is written to the output file with a corresponding measurement for a geolocation (latitude and longitude) that falls in the considered model box, and if the time of measurement falls into the same time window as the UTC model time. In the comparison, only the retrieved MIPAS values are considered that fits to one of this locations and observation time.

For each comparison, the model results have been convolved with the corresponding averaging kernel of the instrument, to account for the vertical resolution and the sensitivity of the instrument.

9.3.4 Statistical significance

The significance of the impact of the particle precipitation and the applied additional parametrised production rates as described in Section 15 is calculated by

$$\sigma = \frac{\Delta(\mathsf{PARAM} - \mathsf{SPE})}{\sqrt{SEM(\mathsf{PARAM})^2 + SEM(\mathsf{SPE})^2}}, \tag{9.4}$$

where SEM is the standard error of the mean.

To investigate, whether the response to the ionisation rates is significant with regard to the long-term model simulations presented in Appendix 2, the f-test (from IDL) has been applied to the differences of the considered area weighted averages. The f-test calculates, whether the variance of a given sample is significantly different from the variance of another sample. The samples in this study are the different area weighted averages over the polar cap computed in the different model simulations. The first sample of the CASE run and a second sample from the BASE reference simulation. If both, CASE and BASE, values within the polar cap are the same for any location, so no or just a negligible impact of precipitating particles, the variances are not significantly different. Since it is known from the ionisation rates, where the impact within the polar cap occurs, it is not needed to neglect cases where another sample (distribution of the values over the same polar cap) would be significantly different from another (as for the Student t-test). But if we suggest, that everything would stay the same except at known areas in the polar cap, it is only the variance that should change and not the whole distribution of the sample, that may contribute to the same average and give misleading and less significance.

The assumption is that if the variances of the two samples differ and this difference is significant, than the impact of the particle precipitation is also significant. In the plots presented in the Appendix 2, all values that are insignificant are masked out in grey colour.

10 Model climatology

The climatology for different trace gases (CH_4, H_2O, HO_x, NO_x, and O_3) for the three model versions ECMWF THETA, LIMA PR MESO, and LIMA PR THERMO is displayed in Figure 10.1. The values shown are monthly and zonal means interpolated onto the pressure levels of the LIMA PR THERMO version. Except for H_2O, the model versions agree among each other in the stratosphere. In the MLT region, the versions starts to differ. The difference in the model versions LIMA PR MESO and LIMA PR THERMO is, as described in Section 7, the vertical extend and the employed family approach in the upper mesosphere and lower thermosphere. This is visible in NO_x and O_3. The LIMA PR MESO results in much lower NO_x values and much larger O_3 values compared to the LIMA PR THERMO which resolved the families O_x and NO_x in the upper atmosphere above 0.33 hPa. H_2O shows in all model versions too large values and a totally different vertical distribution among the model versions. Unfortunately, it is not quite clear where this difference origins. The large values in the LIMA PR THERMO are probably due to an error in the computational code, this it currently under investigation.

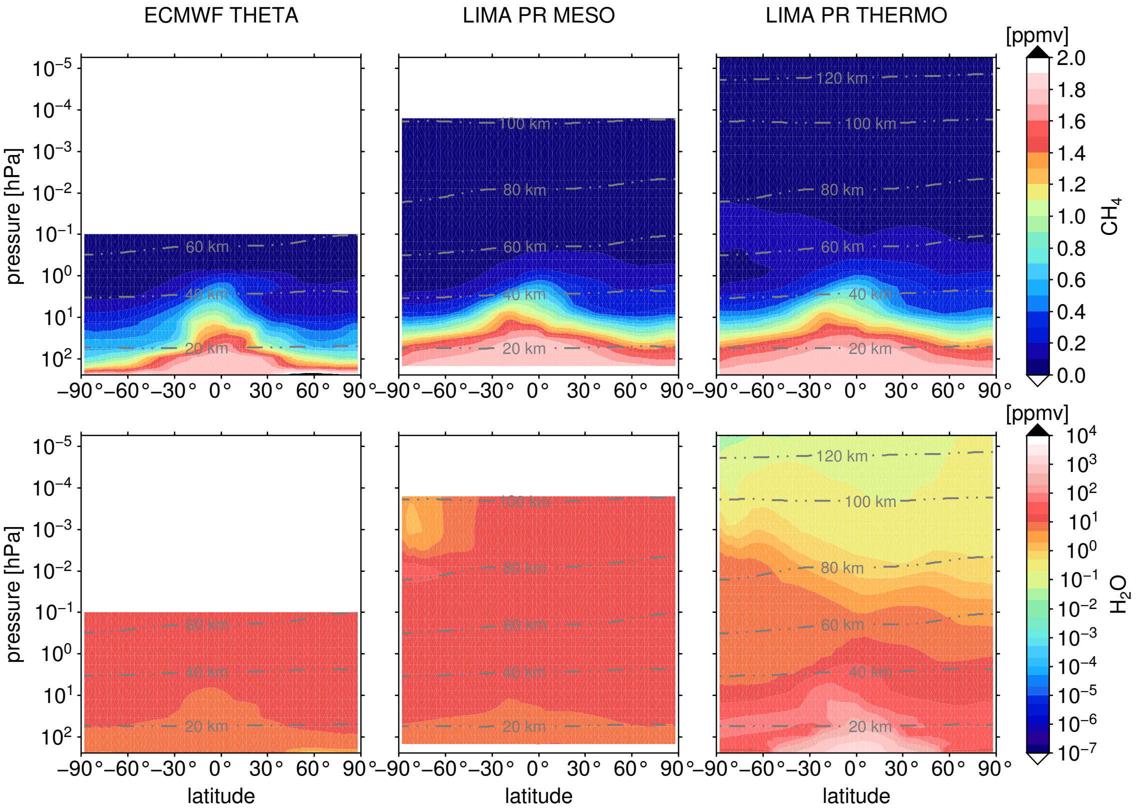

Figure 10.1 *Model climatology for CH_4 (upper panel) and H_2O (lower panel). Values are displayed as zonally averaged monthly means for January 2004. The data are taken from the reference simulation without disturbance of precipitating particles.*

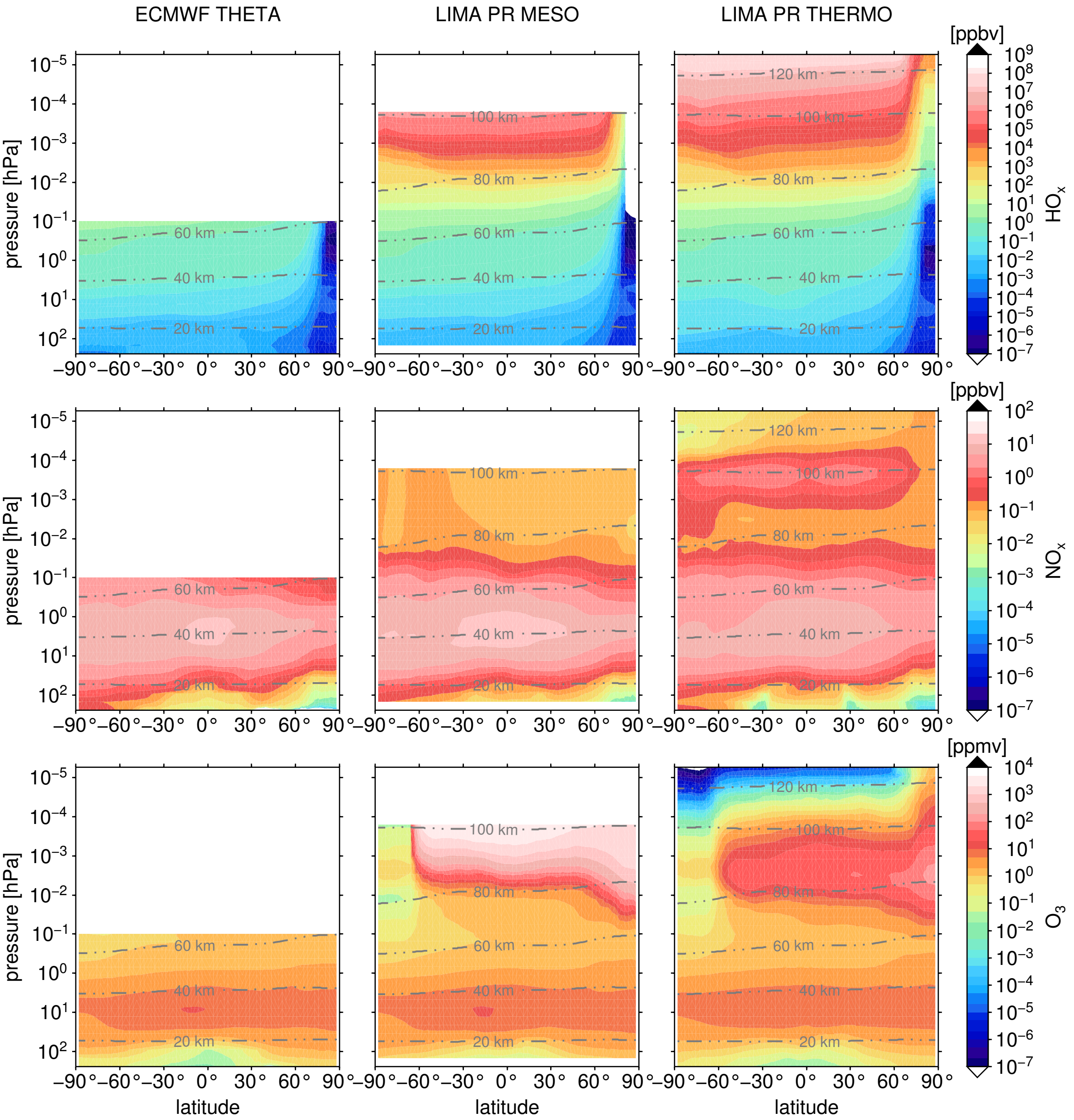

Figure 10.1 (continued) *The same as previous figure but for HO_x (upper panel), NO_x (middle panel), O_3 (lower panel).*

Part III

Results & Discussion

11 Preamble and introductory summary

As described in Section 3.5, Energetic Particle Precipitation (EPP) events have an impact on the chemical composition of the stratosphere, mesosphere, and lower thermosphere. A direct impact is the increase in HO_x and NO_x abundance which can impact very significantly the stratosphere and mesosphere during large Solar Proton Events (SPEs), like the Halloween Storm October/November 2003. In the stratosphere this direct impact is due to proton precipitation that has sufficient energy to cause a disturbance directly in these altitudes. The impact of the electron precipitation causes a direct impact more in the upper atmosphere (mesosphere and thermosphere). But when these enhanced particle fluxes occur during polar winter, as the SPE 2003, increased NO_x values due to protons and electrons are affected by the downward transport within the polar vortex. This can transport the effect of NO_x increase down to the stratosphere, since the life-time of NO_x during northern polar winter and night-time conditions is long due to the absence of photolysis. This leads to an ozone depletion even in the lower stratosphere that can last for several weeks after such an event of enhanced particle precipitation. This adds a dynamical and seasonal aspect to the effect of EPP events. Dynamical effects can make the influence of electron precipitation that has their major impact mainly in the mesosphere and thermosphere even during solar and geomagnetic rather inactive periods of major importance for stratospheric ozone chemistry. In addition to the direct impact of precipitating protons transported NO_x from higher altitudes can contribute significantly to the ozone depletion during SPEs that are accompanied by large electron precipitations, as during the SPE 2003. Also, after Sudden Stratospheric Warming (SSW), significant amounts of NO produced by electron precipitation in the upper atmosphere can be transported into the stratosphere and contribute to an ozone depletion there without the presence of large SPEs.

The effects of the EPP events themselves can affect other atmospheric tracers. Chlorine species are affected by ion chemistry involving negative ions. The depletion of O_3 changes the amount of heating in the atmosphere by disturbed absorption of UV radiation and disturbed absorption and emission of long wave radiation. Also the increase in HO_x constituents change the heating rates due to exothermic reactions involving HO_x as well as O_3.

From this, the following questions arise to study the impact of EPP events on the upper atmosphere:

- How do the further developed model versions of the B3dCTM, as described in Section 7, reproduce the impact of precipitating particles on the chemical composition of the stratosphere, mesosphere, and lower thermosphere?
- How different are the effects on NO_x abundance during different strong SPEs and during different dynamical conditions and during solar and geomagnetic inactive periods?
- Where and how strong are the different impacts of each of the particle populations, protons and electrons?
- What impact do SPEs have on chlorine compounds by parametrising the effect of negative ion chemistry?
- Which impact has the O_3 loss and HO_x increase during strong EPP events on the radiative and chemical heating in the middle and upper atmosphere?

This part is therefore subdivided in the following sections:

Section 12 The impact of energetic particle precipitation events on the chemical composition in the middle and upper atmosphere.

Section 13 Model simulation of energetic particle precipitation events for 2002-2009.

Section 14 The different impacts of ionisation rates due to protons and electrons.

Section 15 The impact of energetic particle precipitation on chlorine compounds.

Section 16 The impact of energetic particle precipitation events on radiative and chemical heating rates.

In Section 12, results from the upper atmosphere version of the B3dCTM will be presented and discussed for the increase in $\mathrm{HO_x}$ and $\mathrm{NO_x}$ and the subsequent decrease in $\mathrm{O_3}$. The modelled impact on these species is presented exemplarily on the major SPE in October/November 2003, since this event was one of the strongest events during the past solar cycle. To investigate how well the model represents the impact of EPP events on the chemical composition, the model results will be compared to observations done by the MIPAS instrument.

In Section 13, model results will be presented for a multi-year model simulation for the period 2002-2009, for the declining phase of the past solar cycle 23. Results of the impact on $\mathrm{NO_x}$ for different strong proton events, during rather inactive periods, and during different meteorological conditions over the northern polar cap are presented.

In Section 14, the impact of different particle populations will be discussed. For this purpose, model results from two different model versions will be presented and compared. Since the different direct and indirect impacts can be placed in different altitude regions.

In Section 15, results of the impact on chlorine compounds induced by negative ion chemistry and parametrised from the University of Bremen Ion Chemistry (UBIC) are discussed.

The decreasing abundance in $\mathrm{O_3}$ leads to a change in radiative heating, which can lead to a change in atmospheric circulation. Again, for the SPE 2003, heating rates, calculated with the MIDRAD radiation scheme by Shine (1987), will be presented and discussed in Section 16. Several $\mathrm{HO_x}$ components, such as OH, are involved in exothermic reactions. Since these compounds are strongly increased during EPP events, chemical heating rates are also affected. Results for different exothermic reactions are presented here.

12 The impact of energetic particle precipitation events on the chemical composition in the middle and upper atmosphere

12.1 Introduction

Within the chemical code of the B3dCTM, the impact of precipitating particles during EPP events is prescribed by (i) the ionisation rates Q (Section 8.1) and (ii) the parametrised production rates P_{HO_x} and P_{NO_x} (Section 6.6). In the following, results of model simulations including the impact of particle precipitation described by these rates are presented. The ionisation rates that are considered are due to proton and electron precipitation. The different effects of each of the particle specific induced ionisation are discussed in Section 14. The production rates P_{HO_x} and P_{NO_x} prescribe the formation of HO_x (H, OH, HO_2) and NO_x (N, NO, NO_2) due to ion reactions involving positive ions (Section 3.5.5). The simulated impact on these constituents will be discussed in the following exemplarily for the SPE 2003, as this event was one of the largest events that took place in the simulated period (2002-2010) during northern polar winter (Section 3.7.1).

The impact on HO_x and NO_x is presented in Section 12.2 and 12.3, respectively. The subsequent response in O_3 is discussed in Section 12.4. The effect on total ozone abundance is presented in Section 12.5.

12.2 HO_x

The direct impact during EPP events is the production of HO_x prescribed by $P_{HO_x} \lesssim 2\,Q$. Ionisation rates (Q) for the discussed SPE 2003 are displayed in Figure 8.2. The simulated impact on HO_x for the period October-November 2003 is presented in Figure 12.1 as differences of area weighted averages (Section 9.3.1) over the northern polar cap between 70°-90° N. The differences are calculated with respect to an undisturbed reference model run (see Section 9.1 for further information on the carried out model scenarios). The upper panel shows the absolute difference of vmr and the lower panel shows the relative change of vmr in percent with respect to the reference model run. A pronounced increase in HO_x is calculated from the upper stratosphere to the lower thermosphere. The HO_x differences are increasing with altitude. This impact on HO_x throughout the upper atmosphere is present until the middle of November 2003. After that, it turns into a decrease in HO_x in the lower thermosphere above 70/90 km. This decrease already appears temporarily during October between 70-80 km. The impact on HO_x shows several peaks and a generally more varying chronological sequence in the upper stratosphere and mesosphere with peak enhancements reaching even below during some pronounced time periods. Since the production rate of HO_x depends on the rate of ionisation, the highest increase is expected during periods of high ionisation rates. Therefore, high ionisation rates lead to very pronounced production of HO_x compounds during the particle events on 24 and 28-31 October, 2-4 November and around 22 November, and again 3-5 December 2003. For the impact on O_3 abundance, the increase in HO_x above 45 km is of essential importance. During the strongest event between 28-30 October, an increase in HO_x is in the order of more than 0.1 ppbv above 40 km. It increases with altitude reaching values larger than 100 ppbv above 75 km. This enhancement lasts until 31 October decreasing again to differences of below 0.1 ppbv until the next

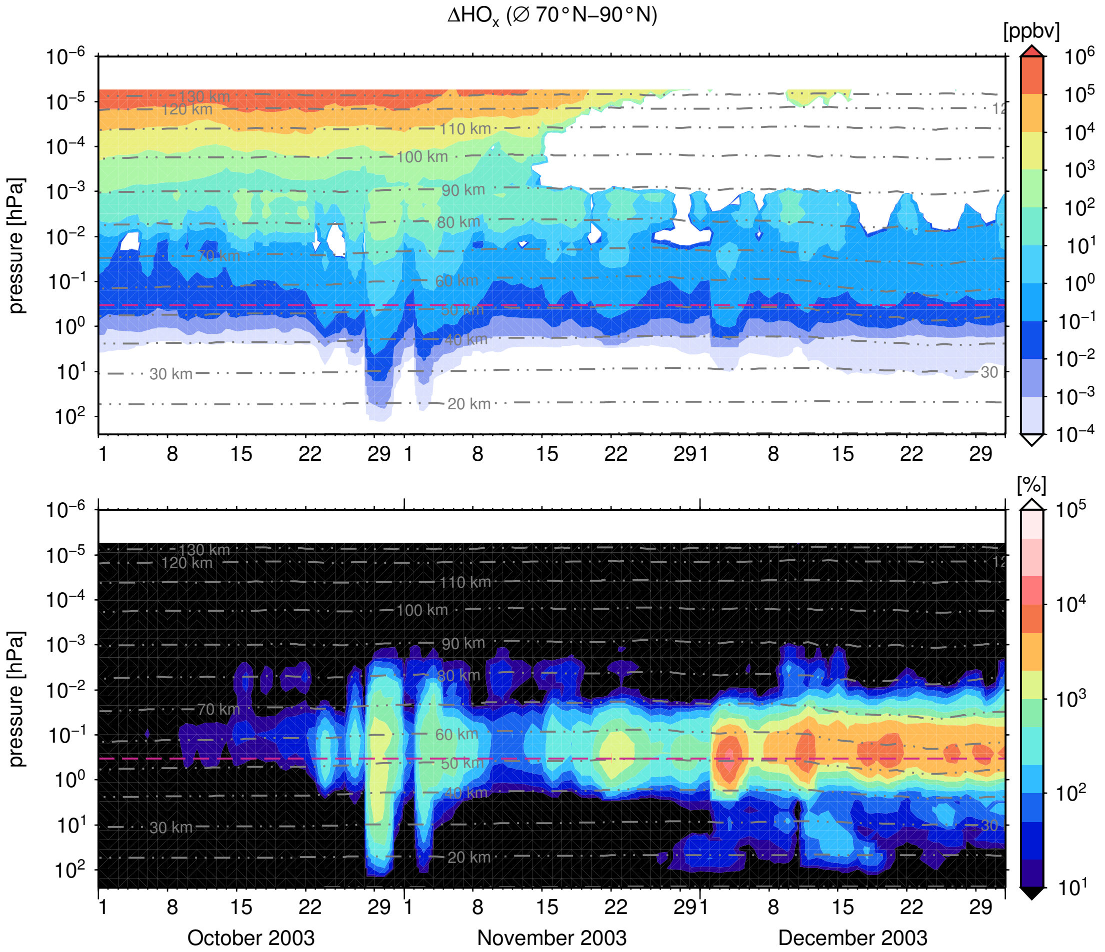

Figure 12.1 *Simulated time evolution of the impact on* HO_x *(H, OH,* HO_2*) during the Solar Proton Event (SPE) 2003. The upper panel shows absolute differences to the reference run without particle influence (EPP-BASE) that are calculated from area weighted averages over the 70°-90° northern polar cap. Values are presented as vmr in ppbv. Note that only increased values (positive differences) are indicated as coloured contours. Differences less than* 10^{-4} *ppbv are colour coded in white as well as decreased values (negative differences). The lower panel shows the relative change with respect to the reference run ((EPP-BASE/BASE)×100%) with values larger than 10%. In both panels, grey dashed dotted contour lines indicate the area weighted mean altitude. The purple dashed line indicates the split level between family (below) and non family chemistry code (above).*

event starting on the 2 November. During this second major enhancement, HO_x increased by more than 0.1 ppbv above 40 km and also reaches values that are enhanced by 10 to 100 ppbv between 70-80 km. These enhancements last for a few days in the stratosphere and mesosphere. In the thermosphere, this increase in HO_x does not show sporadic peaks during storm periods, but stays enhanced until middle of November and increases very rapidly with altitude reaching values of more than a few thousand ppbv above 100 km. Compared to the absolute difference, the relative increase in HO_x with respect to the reference run is more pronounced with enhancements above 10% in the stratosphere and mesosphere. It also shows a peak in relative enhancement around 50 km with maximum increases during

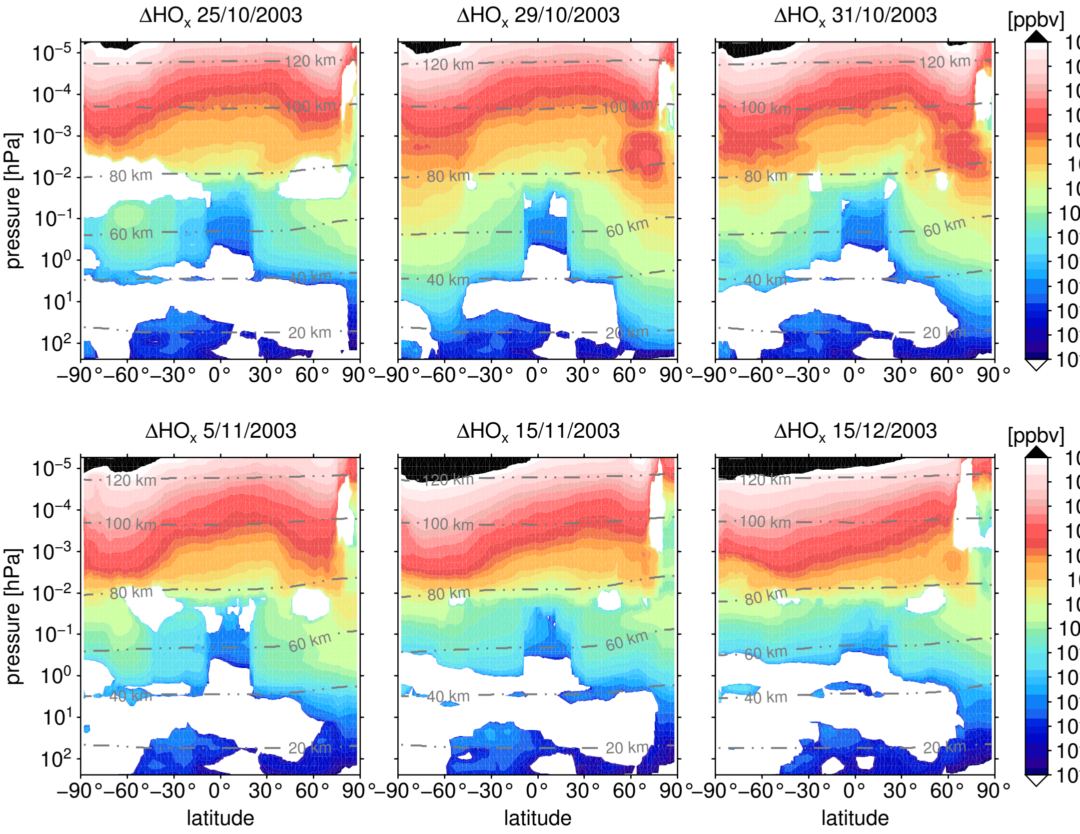

Figure 12.2 *HO_x zonal mean differences to the reference model run for different days at 0 UTC during October-December 2003. The upper panel shows changes in HO_x absolute values before (25/10/2003) and during the event (29+31/10/2003). The lower panel shows changes for three different days (5/11/2003, 15/11/2003, and 15/12/2003). Note that values below 10^{-7} ppbv and negative values are colour coded in white. Grey dashed dotted contour lines indicate zonal mean altitudes.*

December of up to a few 10000%. During the events in October and November the relative HO_x increases reach values of more than 2000%. The relative increase of more than 10% starts already in the middle of October reaching enhancements between 200-1000% on 23 and 27 October and during the strongest event between 28-31 October showing increases by 2000% between 30-70 km, and again by more than 1000% during 2-7 November. The same amounts of increases are again reached starting in the middle of November reaching maximum increases on 22 November.

The zonally averaged increase as a function of latitude are presented for HO_x, H, OH, and HO_2 in the Figures 12.2, 12.3, 12.4, and 12.5, respectively. Each figure shows zonal averages for three days before (25/10/2003) and during the event (29+31/10/2003), and on 5/11/2003, 15/11/2003, and 15/12/2003. In all HO_x constituents, the main increase in their abundance is during the event. The main increase in HO_x above 80 km is due to the increase in H. Above that altitude, the increase is increasing with altitude in all latitudes. In high northern latitudes, N values are decreasing, which contributes to the decrease in HO_x values in the same altitudes. Below 80 km, the increases in OH and HO_2 contribute most to the HO_x enhancement and show similar patterns also in both hemispheres. Both, H and OH,

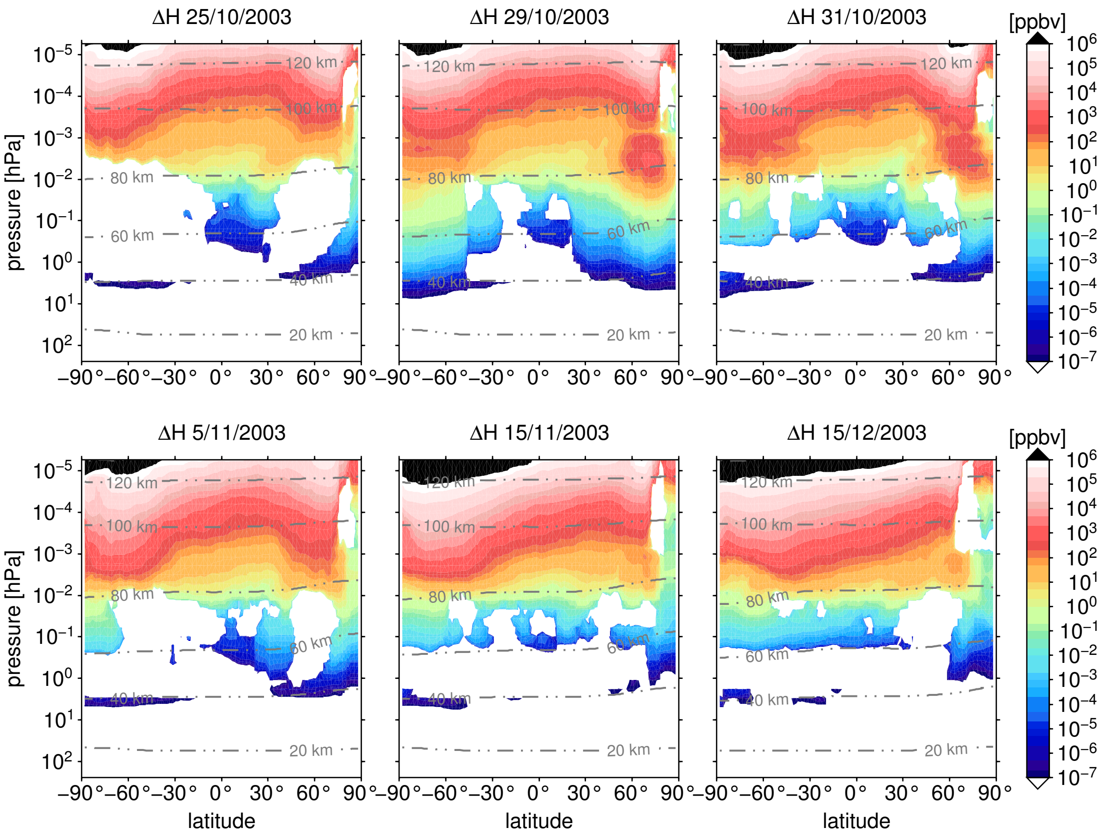

Figure 12.3 *H zonal mean differences to the reference model run for different days at 0 UTC during October-December 2003. The upper panel shows changes in H absolute values before (25/10/2003) and during the event (29+31/10/2003). The lower panel shows changes for three different days (5/11/2002, 15/11/2003, and 15/12/2003). Note that values below 10^{-7} ppbv and negative values are colour coded in white. Grey dashed dotted contour lines indicate zonal mean altitudes.*

have a maximum increase in high latitudes from 60° on polewards. Both species have larger increases in the Northern Hemisphere which peak at around 70 km and reaching down far into the stratosphere during the event on 31/10/2003. This is true for both hemispheres.

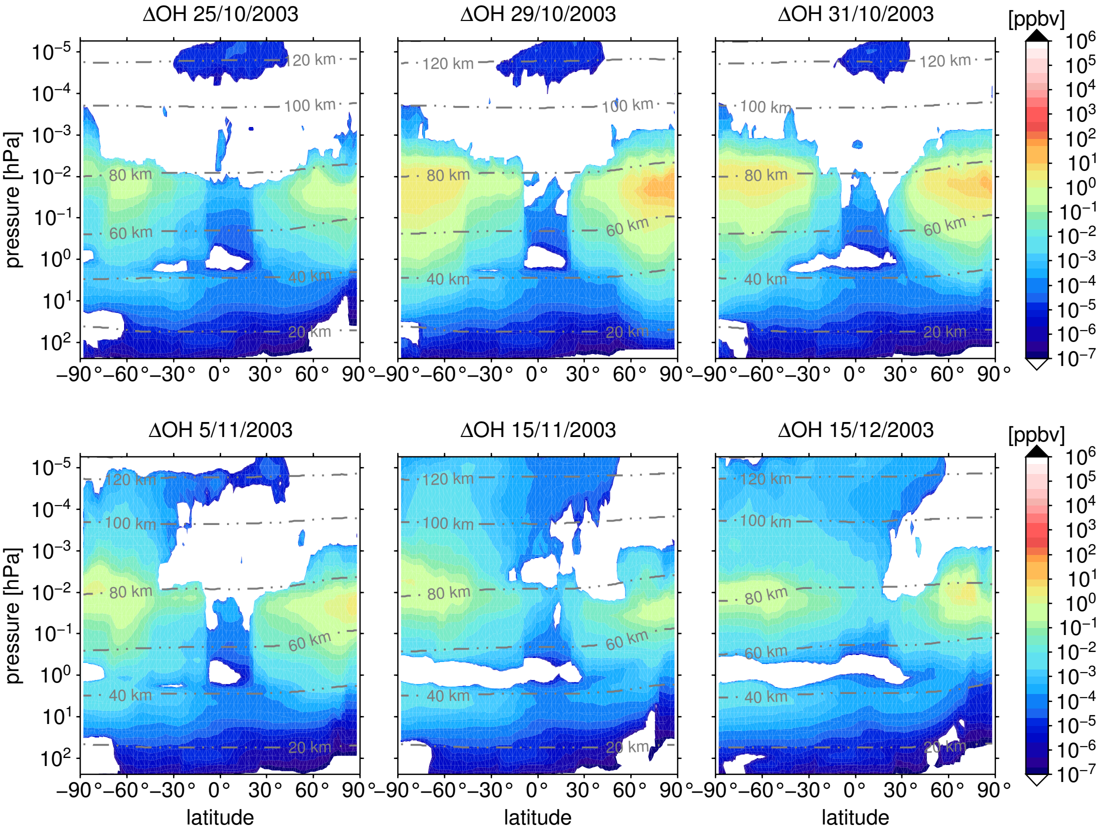

Figure 12.4 *OH zonal mean differences to the reference model run for different days at 0 UTC during October-December 2003. The upper panel shows changes in OH absolute values before (25/10/2003) and during the first event (29+31/10/2003). The lower panel shows changes for three different days (5/11/2003, 15/11/2003, and 15/12.2003). Note that values below 10^{-7} ppbv and negative values are colour coded in white. Grey dashed dotted contour lines indicate zonal mean altitudes.*

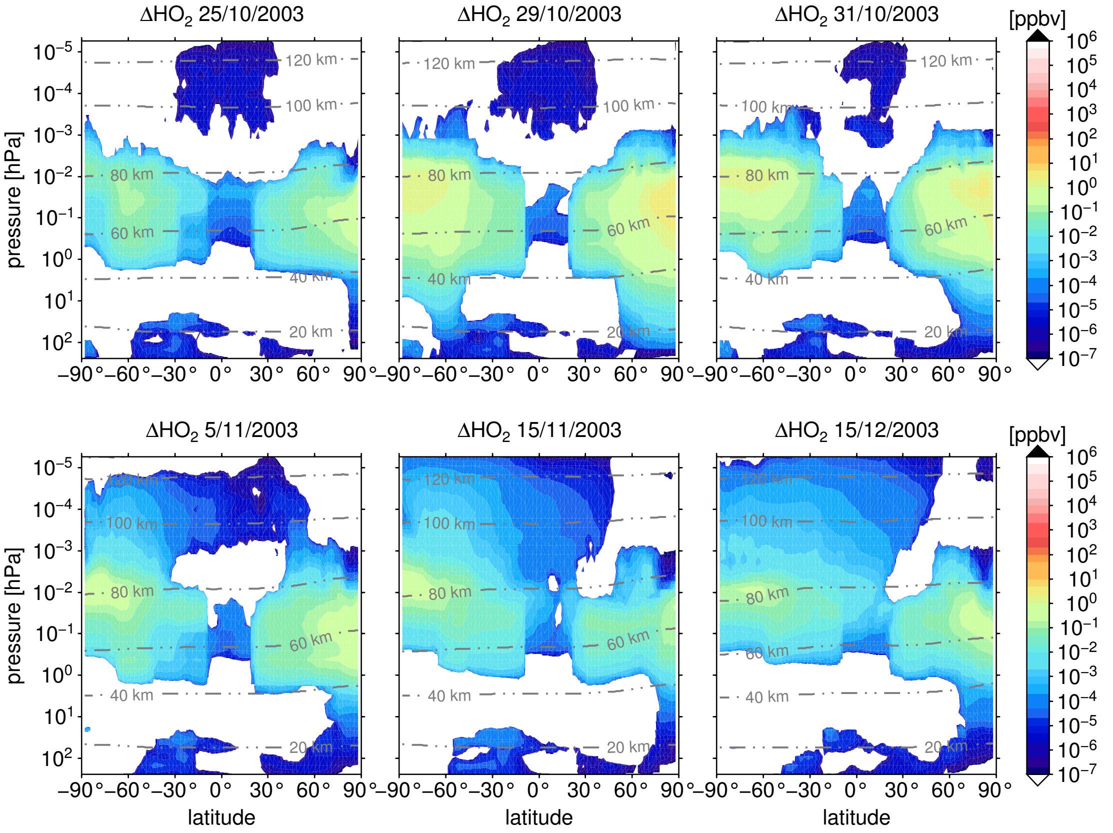

Figure 12.5 *HO_2 zonal mean differences to the reference model run for different days at 0 UTC during October-December 2003. The upper panel shows changes in HO_2 absolute values before (25/10/2003) and during the event (29+31/10/2003). The lower panel shows changes for three different days (5/11.2003, 15/11/2003, and 15/12/2003). Note that values below 10^{-7} ppbv and negative values are colour coded in white. Grey dashed dotted contour lines indicate zonal mean altitudes.*

12.3 NO_x

The second effect of EPP events is the formation of NO_x compounds. In Figure 12.6, the impact of the precipitating particles on NO_x is presented. Values are shown as differences to a reference run as area weighted values averaged over the northern polar cap between 70°-90°N. NO_x values are enhanced, as well as HO_x, for the whole period and this enhancement is increasing with altitude reaching differences of up $5 \cdot 10^5$ ppbv (500 ppmv). Compared to HO_x, increases during the respective events are not so pronounced, but a general increase starting around the end of October that lasts until the beginning/middle of December. During this period, NO_x values are enhanced by many orders of magnitude relative to the abundance in the reference run in all altitudes. For the abundance of O_3, the increase

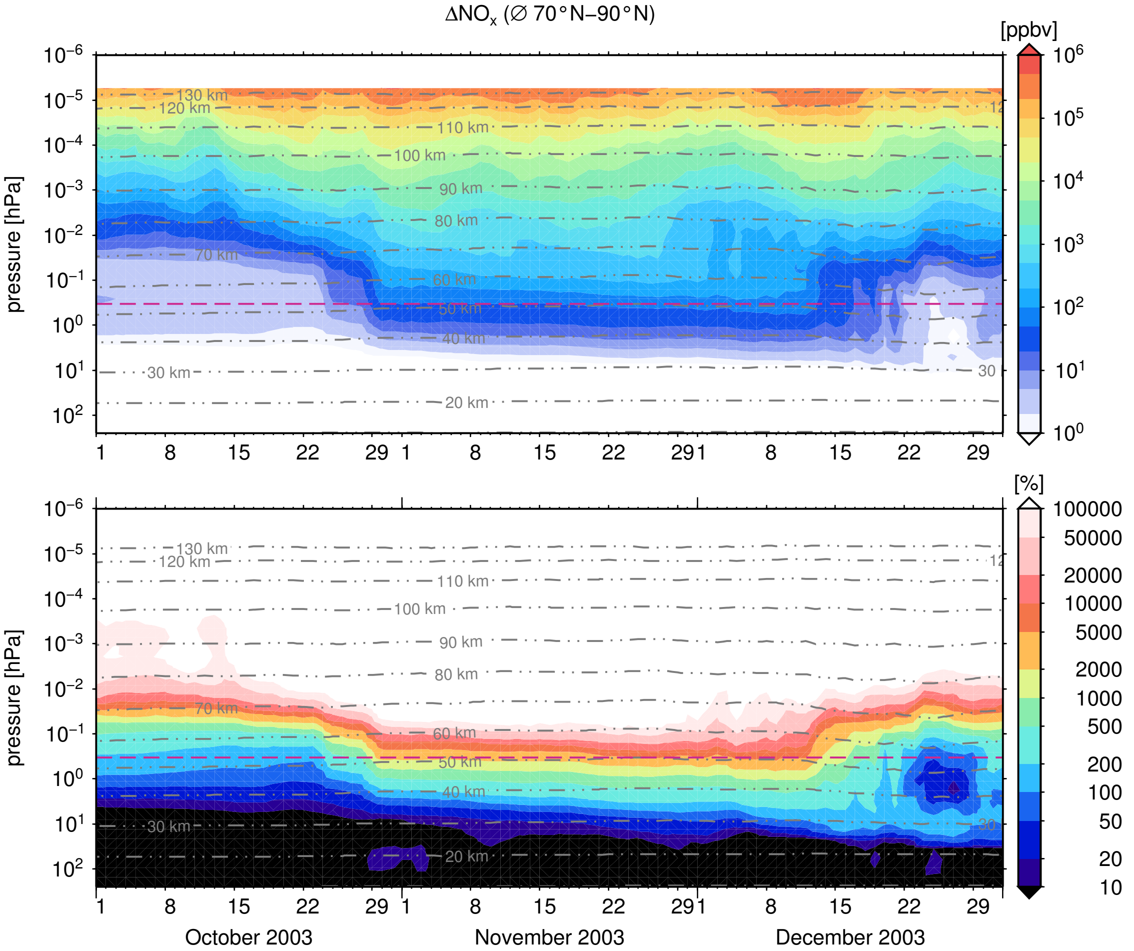

Figure 12.6 *Simulated impact on NO_x (N, NO, NO_2) during the Solar Proton Event (SPE) 2003. The upper panel shows absolute differences to a reference run without particle influence from area weighted values averaged over the 70°-90° northern polar cap. Values are presented as vmrs. The lower panel shows the relative change with respect to the reference run ((EPP-BASE/BASE)×100%). White colours indicate values that are larger than 100000%. In both panels, grey dashed dotted contour lines indicate the area weighted mean altitude. The purple dashed line indicates the split level between family (below) and non family chemistry code (above).*

in NO_x below 45 km is of most importance. Starting during the events in late October throughout the whole period shown until the middle of December, NO_x show enhancements in the altitude range between 40-60 km of more than 100% increasing with altitude and reaches enhancements of up to 20000% in the upper stratosphere. During this phase of enhancement, the gained NO_x is transported to lower altitudes until the end of December and beyond increasing by more than 100% down to altitudes below 30 km. The NO_x increase by 100% correlates with the 10% O_3 depletion contour slightly below 40 km. This is true until the middle of December, when a break up in the NO_x increase occurs and O_3 values are less decreased. This end of NO_x increase is due a SSW and a break up of the polar vortex that occurred by the end of December (Manney *et al.*, 2005).

Zonally averaged values for NO_x and its constituents, N, NO, and NO_2, are presented in the Figures 12.7, 12.8, 12.9, and 12.10, respectively. Each figure shows the difference in the abundance of each species with respect to the reference run before (25/10/2003) and during (29+31 October) the first event, and on 5/11/2003, 15/11/2003, and 15/12/2003, respectively. In NO_x and its compounds, the different hemispheres show a different behaviour in the increase due to the precipitating particles. This is different as compared to the impact on HO_x. In general, the increase in NO_x is larger in the Northern Hemisphere, due to polar winter conditions and a, therefore, longer life-time in the abundance of NO_x constituents. During the events in October and in the beginning of November, after the second event around 3 November, NO_x is increasing in both hemispheres. In the Southern Hemisphere, increased values are in general more pronounced in the mesosphere and thermosphere, whereas in the Northern Hemisphere NO_x is enhanced down to the stratopause at 55 km already during the event and down to the stratosphere by the beginning of November. In the Southern Hemisphere, a peak in NO_x increase appears during the whole period shown at an altitude of 60 km with a maximum around the beginning of November, and stays there until the end of December. In comparison, in the Northern Hemisphere, the abundance in NO_x is increasing until the beginning of December, reaching down below 40 km. In the middle and at the end of December, the enhanced values decrease again to values prior to the event. The different NO_x constituents show different patterns during this period. N and NO contribute to the increased abundance of NO_x primarily above 60 km. N is mainly enhanced in both polar regions by the same amount. In the Southern Hemisphere it shows a small increase in high latitudes during the event but it stays only a few days and reaches values prior to the event by the beginning of November. In the Northern Hemisphere, values show only a small increase during the first event and are decreasing again in very high northern latitudes in the lower thermosphere and mesosphere by the middle of November. NO shows the same behaviour as NO_x above 60/80 km. Below 60/80 km, the change in NO_2 becomes more important. It shows a peak enhancement in the Northern Hemisphere at around 70 km altitude in latitudes polewards of 70°N. This peak increase is getting larger until the beginning of November reaching again values prior to the event by the end of December. The peak height is lowered to 50/60 km altitude by the beginning of November. In the Southern Hemisphere, a small increase in NO_2 abundance appears only after the first and second event, and at the end of November, but lasts only for a short period. In the northern mesosphere and thermosphere, NO_2 differences increase during the whole period, and peaks at around 120 km.

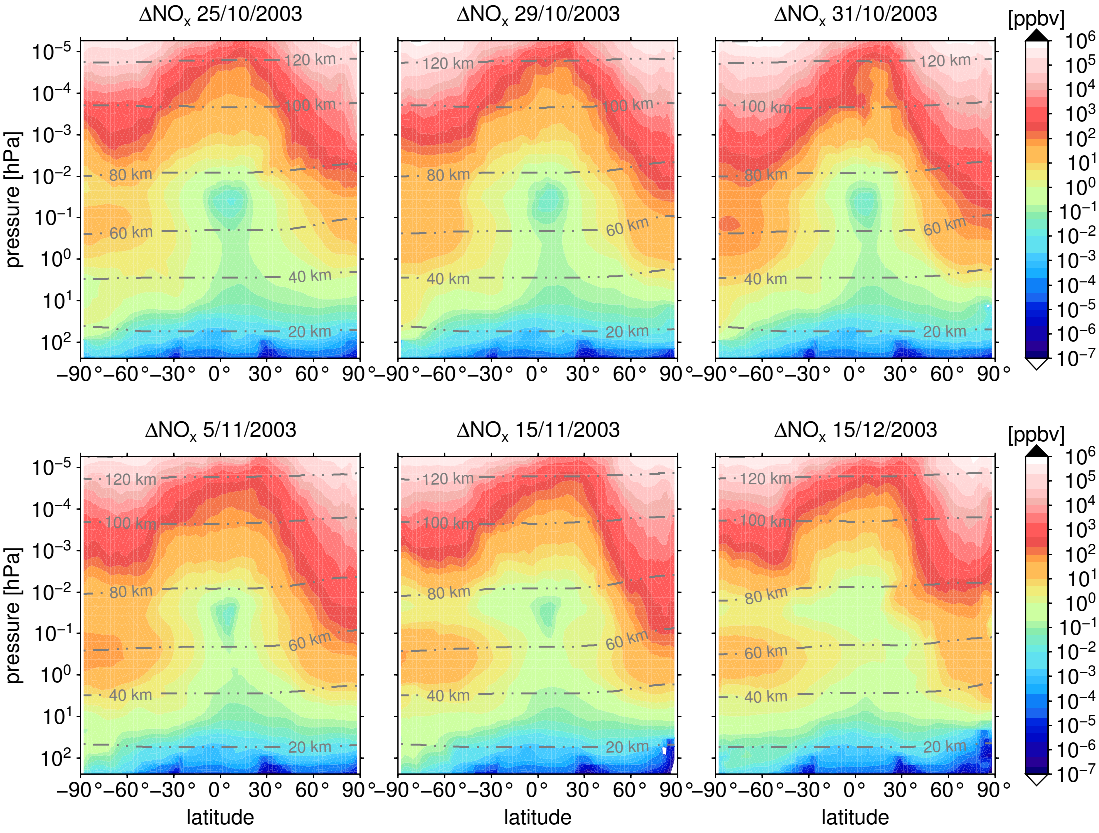

Figure 12.7 *NO_x zonal mean differences to the reference model run for different days at 0 UTC during October-December 2003. The upper panel shows changes in NO_x absolute values before (25/10/2003) and during the event (29+31/10/2003). The lower panel shows changes for three different days (5/11/2003, 15/11/2003, and 15/12/2003). Note that values below 10^{-7} ppbv and negative values are colour coded in white. Grey dashed dotted contour lines indicate zonal mean altitudes.*

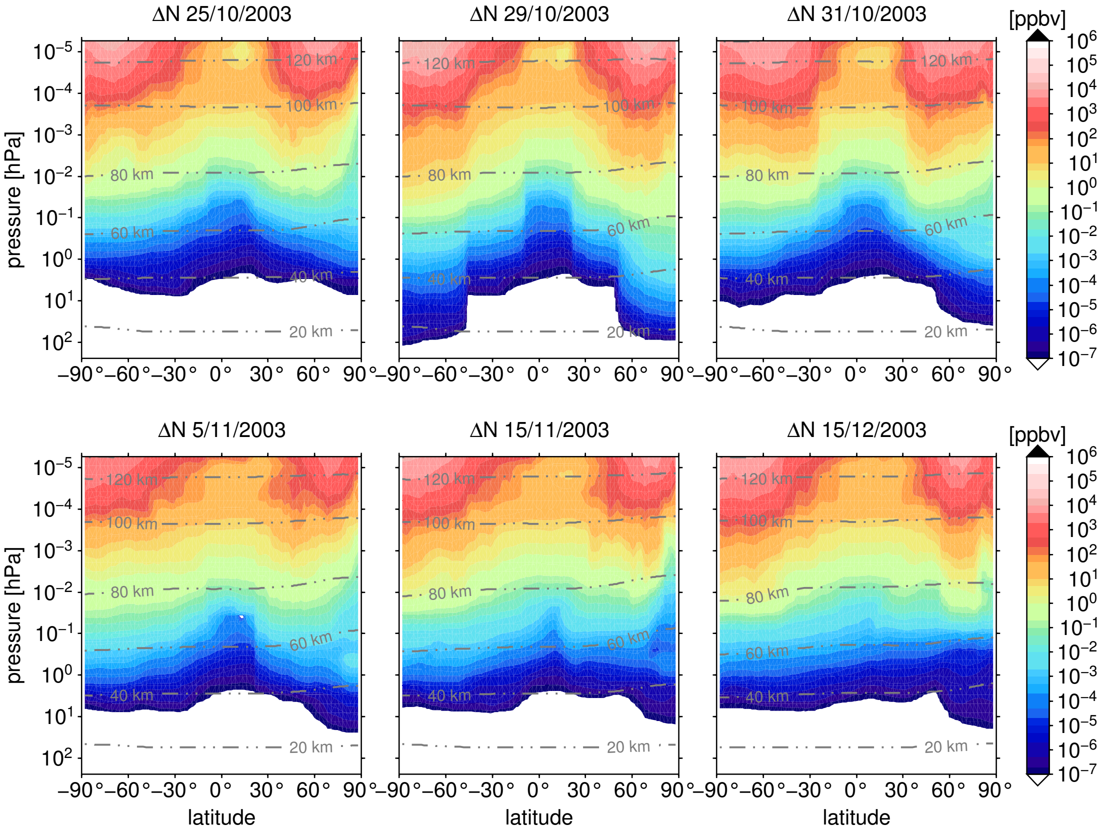

Figure 12.8 *N zonal mean differences to the reference model run for different days at 0 UTC during October-December 2003. The upper panel shows changes in N absolute values before (25/10/2003) and during the event (29+31/10/2003). The lower panel shows changes for three different days (5/11.2003, 15/11/2003, and 15/12/2003). Note that values below* 10^{-7} *ppbv and negative values are colour coded in white. Grey dashed dotted contour lines indicate zonal mean altitudes.*

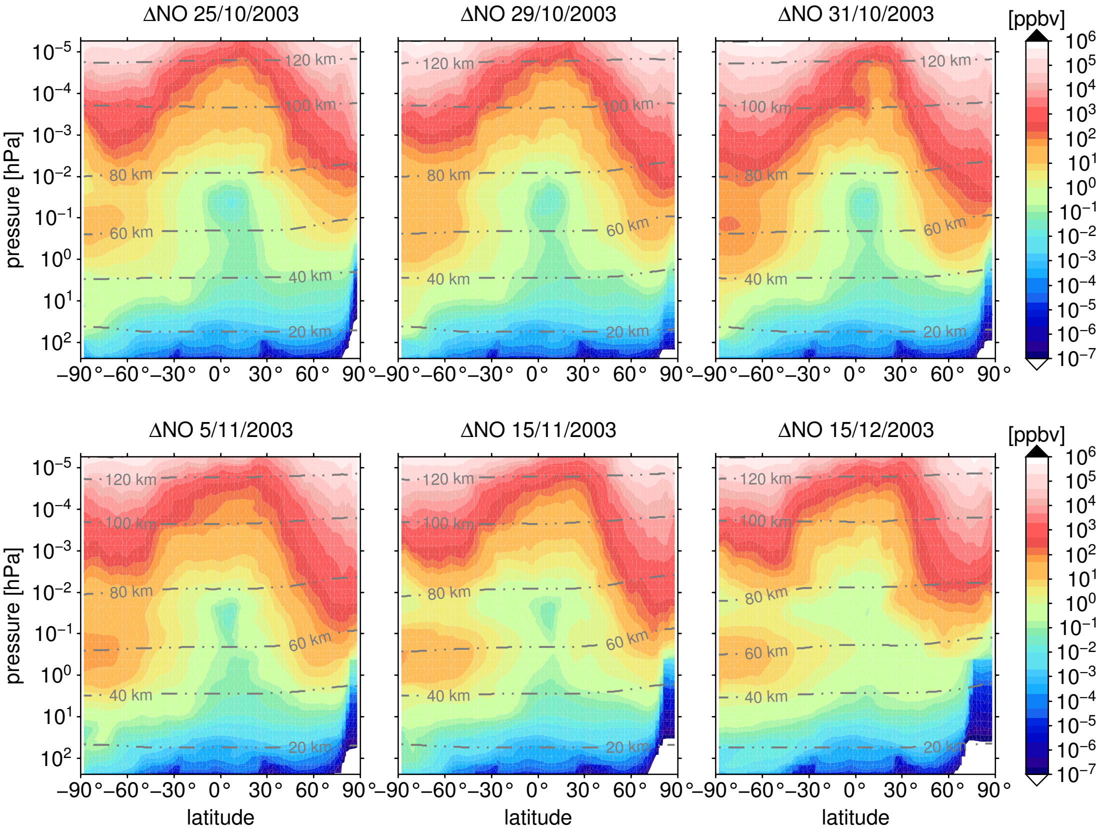

Figure 12.9 *NO zonal mean differences to the reference model run for different days at 0 UTC during October-December 2003. The upper panel shows changes in NO absolute values before (25/10/2003) and during the event (29+31/10/2003). The lower panel shows changes for three different days (5/11.2003, 15/11/2003, and 15/12/2003). Note that values below* 10^{-7} *ppbv and negative values are colour coded in white. Grey dashed dotted contour lines indicate zonal mean altitudes.*

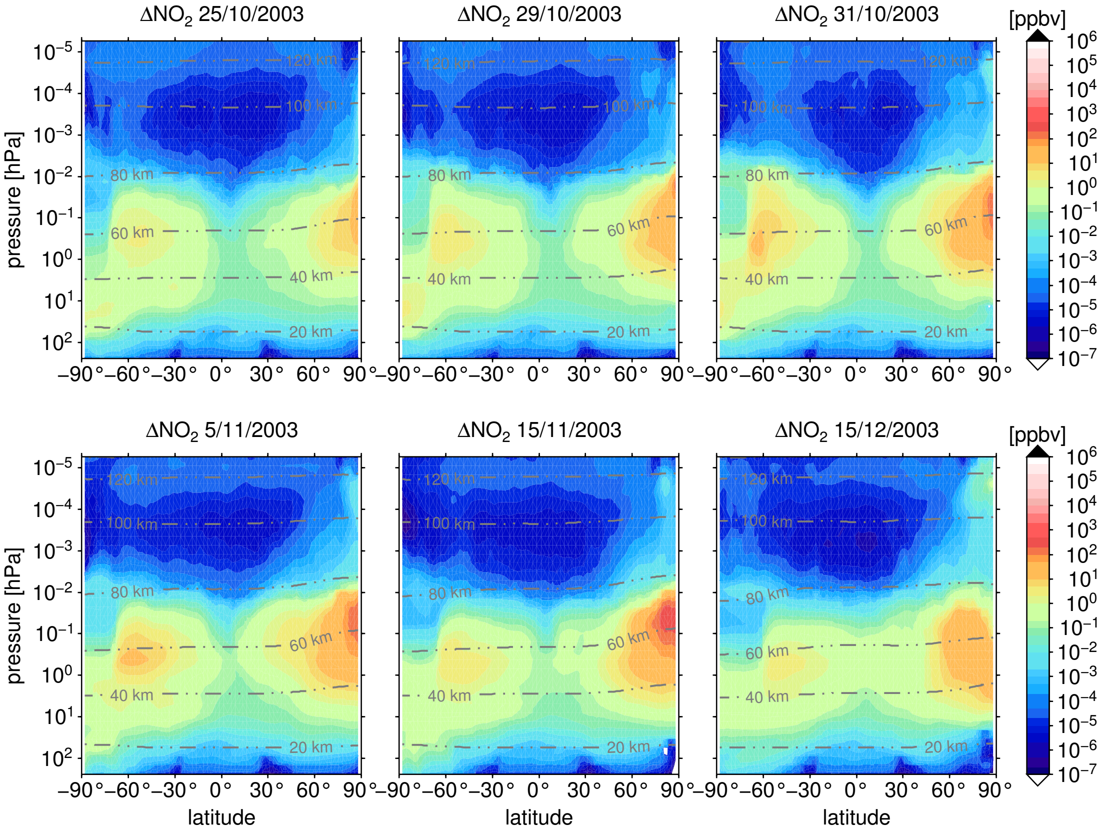

Figure 12.10 *NO_2 zonal mean differences to the reference model run for different days at 0 UTC during October-December 2003. The upper panel shows changes in NO_2 absolute values before (25/10/2003) and during the event (29+31/10/2003). The lower panel shows changes for three different days (5/11.2003, 15/11/2003, and 15/12/2003). Note that values below 10^{-7} ppbv and negative values are colour coded in white. Grey dashed dotted contour lines indicate zonal mean altitudes.*

12.4 O_3

As already described above, HO_x and NO_x species destroy O_3 in catalytic cycles. The percentage change for O_3 with respect to the reference simulation is shown in Figure 12.11. The direct impact of HO_x is perspicuously in the O_3 response in altitudes between 45-80 km. During the first major event on 29 to 31 October, this leads to an O_3 depletion of more than 90% immediately during the event. Since the life-time of the HO_x species is rather short (hours), the impact on O_3 also lasts only for a short period. After that, O_3 values are recovering again. This is true for all events during the SPE 2003 between 45-80 km. Below 45 km the O_3 depletion is primarily driven by NO_x species. As NO_x is transported downwards within the polar vortex during polar winter, it destroys O_3 down to altitudes below 40 km with an O_3 depletion of about 10-20% until the middle of December 2003. The relative zonally averaged change of O_3 is presented in Figure 12.12. A decrease in O_3 is present in both hemispheres during the first two events. But in general, the effect is larger in the Northern Hemisphere. Also, in both hemispheres, the impact on O_3 is most pronounced in high polar latitudes polewards of 60°. In the Southern Hemisphere there are depletions of up to 70/80% and above 90% during the first event on 29/31 October. It is decreasing below 30% by the beginning of November and gone by December. In the Northern Hemisphere the O_3 depletion lasts until the middle of December with decreases in the order of more than 20% in very high latitudes. This decrease in ozone depletion is again due to the onset of a SSW and the break up of the polar vortex by the end of December 2003. The highest depletion in O_3 is on the 31 October after the first event in an altitude between 60-80 km, when OH and HO_x in general shows the main increases. During November and until middle of December, the peak height of O_3 depletion is going down to lower altitudes until is reaches 40 km with decreased values up to 20%.

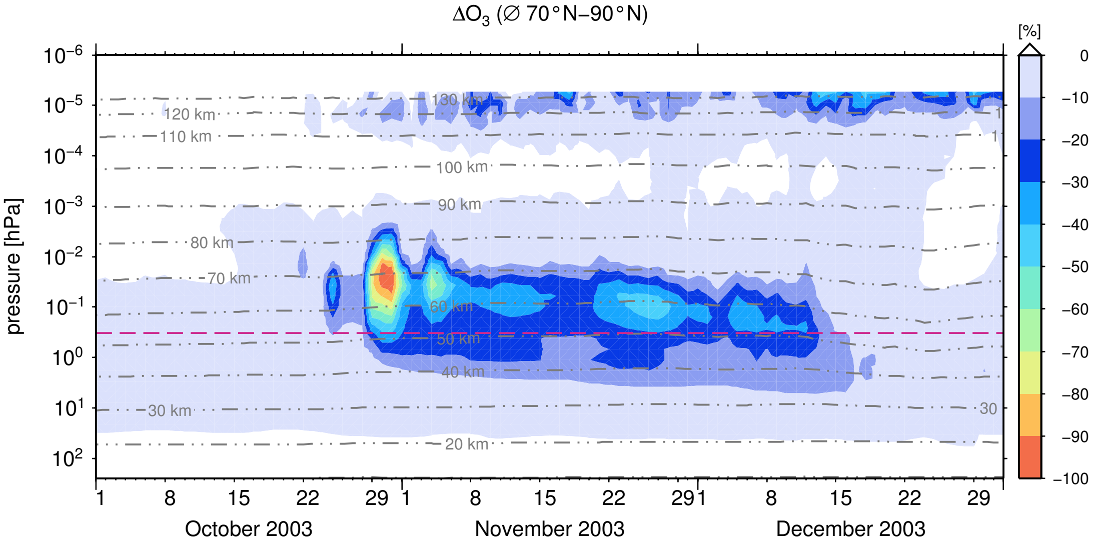

Figure 12.11 *Simulated impact on O_3 during the Solar Proton Event (SPE) 2003. The values are differences to a reference run without particle influence from values averaged over the 70°-90° northern polar cap. Values are presented in percent with respect to the reference run ((EPP-BASE/BASE)×100%).*

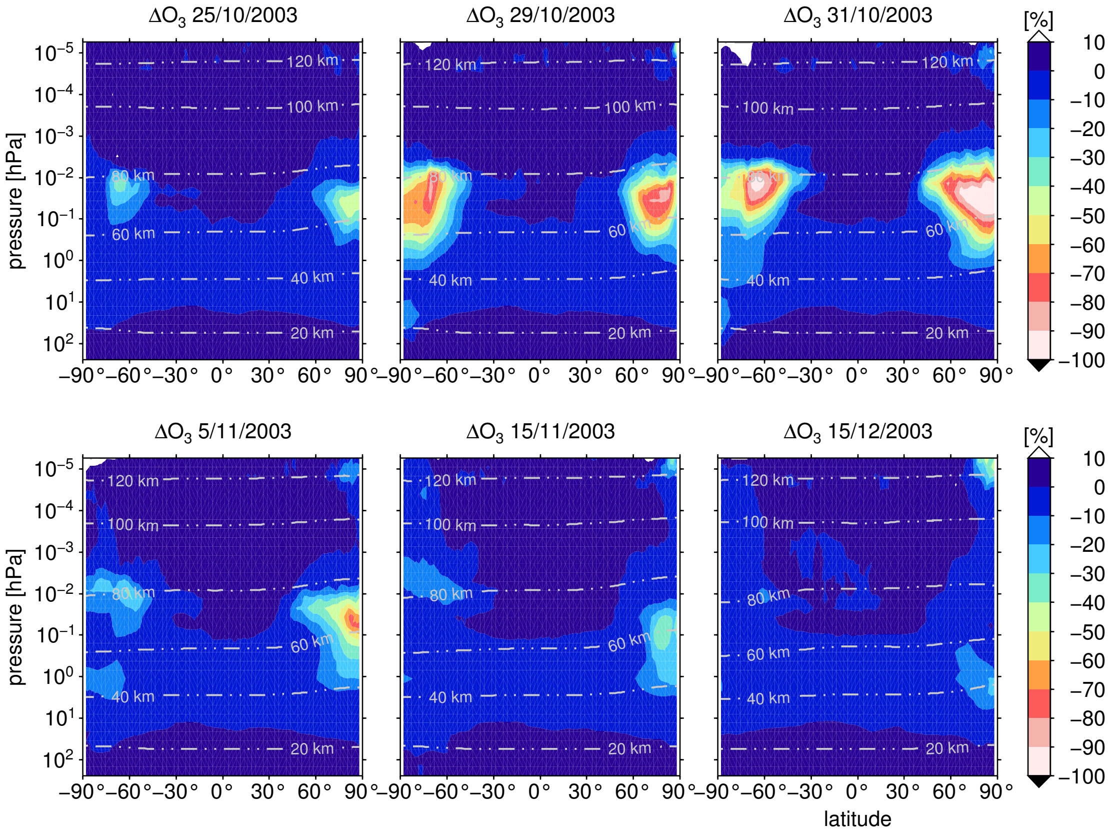

Figure 12.12 *O_3 zonal mean differences to the reference model run for different days at 0 UTC during October-December 2003. The upper panel shows relative changes in O_3 values before (25/10/2003) and during the event (29+31/10/2003). The lower panel shows changes for three different days (5/11/2003, 15/11/2003, and 15/12/2003). Grey dashed dotted contour lines indicate zonal mean altitudes.*

These results agree to observations of previous studies. López-Puertas *et al.* (2005) investigated the impact of the SPE 2003 on NO_x and O_3 for both hemispheres by looking at observations carried out with the MIPAS instrument which were the first observations during the SPE 2003 in both hemispheres. They found individual profiles of NO_x increasing to values of up to 180 ppbv in the upper stratosphere. For NO_x they also found a lower response in the Southern Hemisphere during day-time conditions. For ozone they found the largest depletion in the Northern Hemisphere also during the first event on 29 October and in a generally lower mean depletion in the Southern Hemisphere which is also represented by the model simulation. The area weighted means of the model results agree to the observed means of López-Puertas *et al.* (2005). Note that results are only qualitatively comparable, since the difference in López-Puertas *et al.* (2005) are compared to a chosen reference day on 25 October 2003. The model results are compared to a undisturbed scenario. A comparison also to MIPAS data is presented in Section 12.6. López-Puertas *et al.* (2006) observed again with MIPAS a peak enhancement in NO_2 at 60-70 km from the middle of November until middle of December which is also simulated in the model calculation. They stated that this is due to enhanced NO_x production above and a following downward transport into the lower mesosphere and stratosphere that leads to this enhanced NO_2 values up to a few weeks after the event.

Results of the multi-year simulation for the impact on HO_x, NO_x, and O_3 is presented in Section 2 in the Appendix.

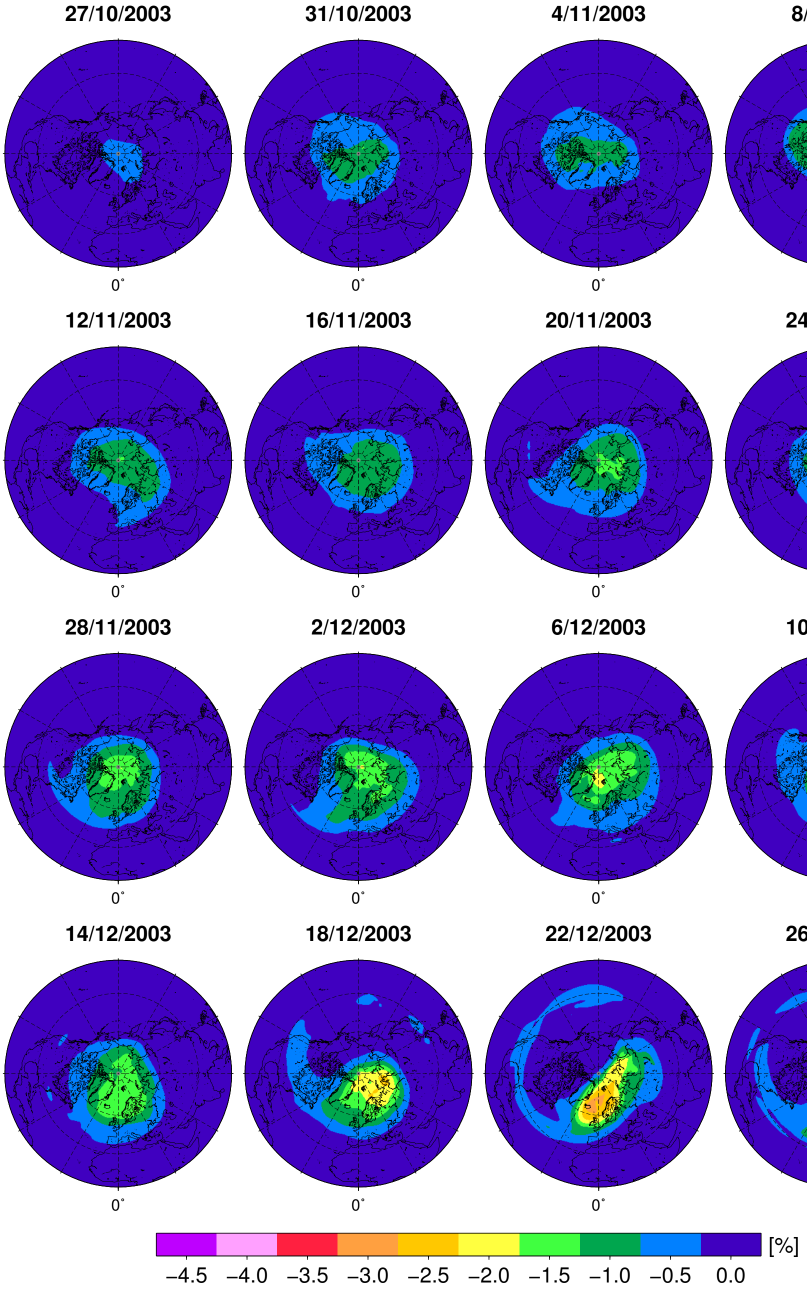

Figure 12.13 *Simulated impact on total ozone over the Northern Hemisphere for every forth day from 27 October to 26 December 2003. Values are percentage differences to a case model scenario without particle precipitation impact.*

12.5 Total ozone

The impact of the particle precipitation on O_3 leads to a reduction as much as it can be seen in the total ozone column abundance (Section 2.2.2). The total ozone amount over the Northern Hemisphere is presented in Figure 12.13 for the period of 27 October to 26 December 2003 for every forth day. The decrease in the total ozone abundance is continuously increasing for the presented period. By the end of December total ozone values are reduced by more than 3%. This decrease is mainly driven by enhancements in NO_x, see Figure 12.6, which is enhanced during the same period and causes an ozone depletion to the lower stratosphere by the end of December as it is transported into the stratosphere during December.

12.6 Comparison to observations with MIPAS

The simulated values for NO_2 and O_3 are compared to observations obtained by the MIPAS instrument (Fischer *et al.*, 2008) on-board the ENVISAT satellite. Absolute values are compared for different days during the SPE 2003 (25/10/2003, 31/10/2003) and after the event (4/11/2003, 16/11/2003, 2/12/2003, 18/12/2003) and presented in Figures 12.14 and 12.15, respectively. Each map shows the northern polar cap between 60°-90°N. Simulated values are displayed by the underlying bigger circles, MIPAS observations are displayed as the smaller circles on top. The model results correspond to the time and location of the observations and are convolved with the averaging kernels of the instrument (Section 9.3.3).

For NO_2, both, model results as well as observations show lower values at 40 km altitude than in 60 km. In general, the area over the northern pole that is enhanced due to the precipitating particles is well represented in the model results at 60 km altitude and also at 40 km altitude. This increase reaches 40 km altitude by the middle/beginning of November/December, where areas of enhanced values in 60 km are becoming smaller again, or/and move to a restricted area northwards of 75°N.

O_3 shows larger values at 40 km than at 60 km as expected. The values in both altitudes agree well with the observations, but are higher during middle of December. This is gone again a few days later. The area of lowest O_3 values agree well with the observations and are primarily northwards of 60°N.

In general, the model reproduces the response in NO_2 and O_3 during the SPE 2003 and a few weeks after the event until the end of December very well. A more detailed comparison with respect to the different particles are presented in Section 14.3.4.

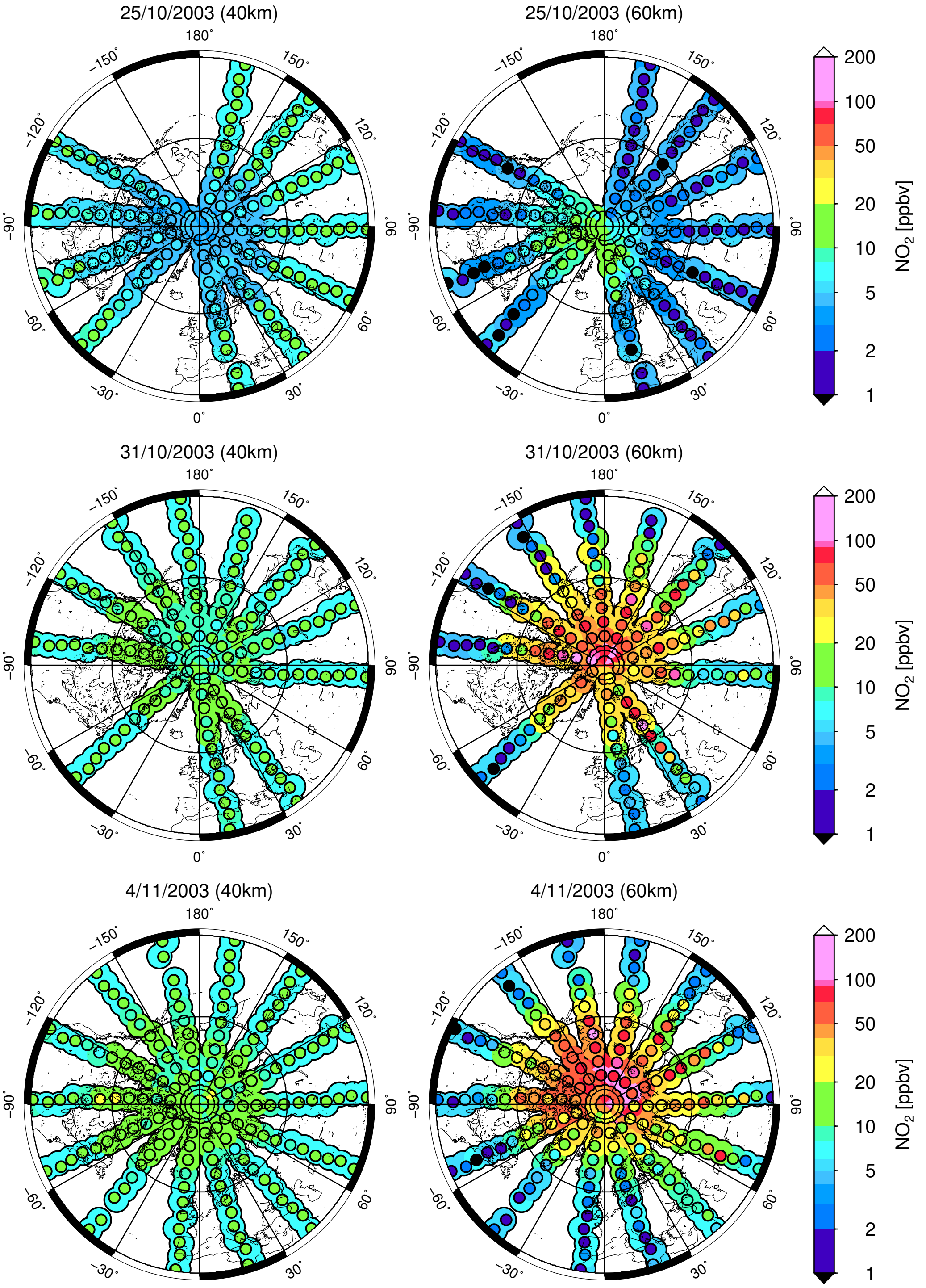

25/10/2003 (40km)

25/10/2003 (60km)

31/10/2003 (40km)

31/10/2003 (60km)

4/11/2003 (40km)

4/11/2003 (60km)

Figure 12.14 *Simulated NO_2 values compared to observations during the Solar Proton Event (SPE) 2003 on three different days (25/10/2003, 31/10/2003, 5/11/2003) at 40 km (left panel) and 60 km (right panel). Simulated values are displayed as the underlying colour coded circles. Observations obtained from the Michelson Interferometer for Passive Atmospheric Sounding (MIPAS) instrument in ascending mode are displayed in colour coded smaller circles. Values are presented over the northern polar cap between 60°-90° N.*

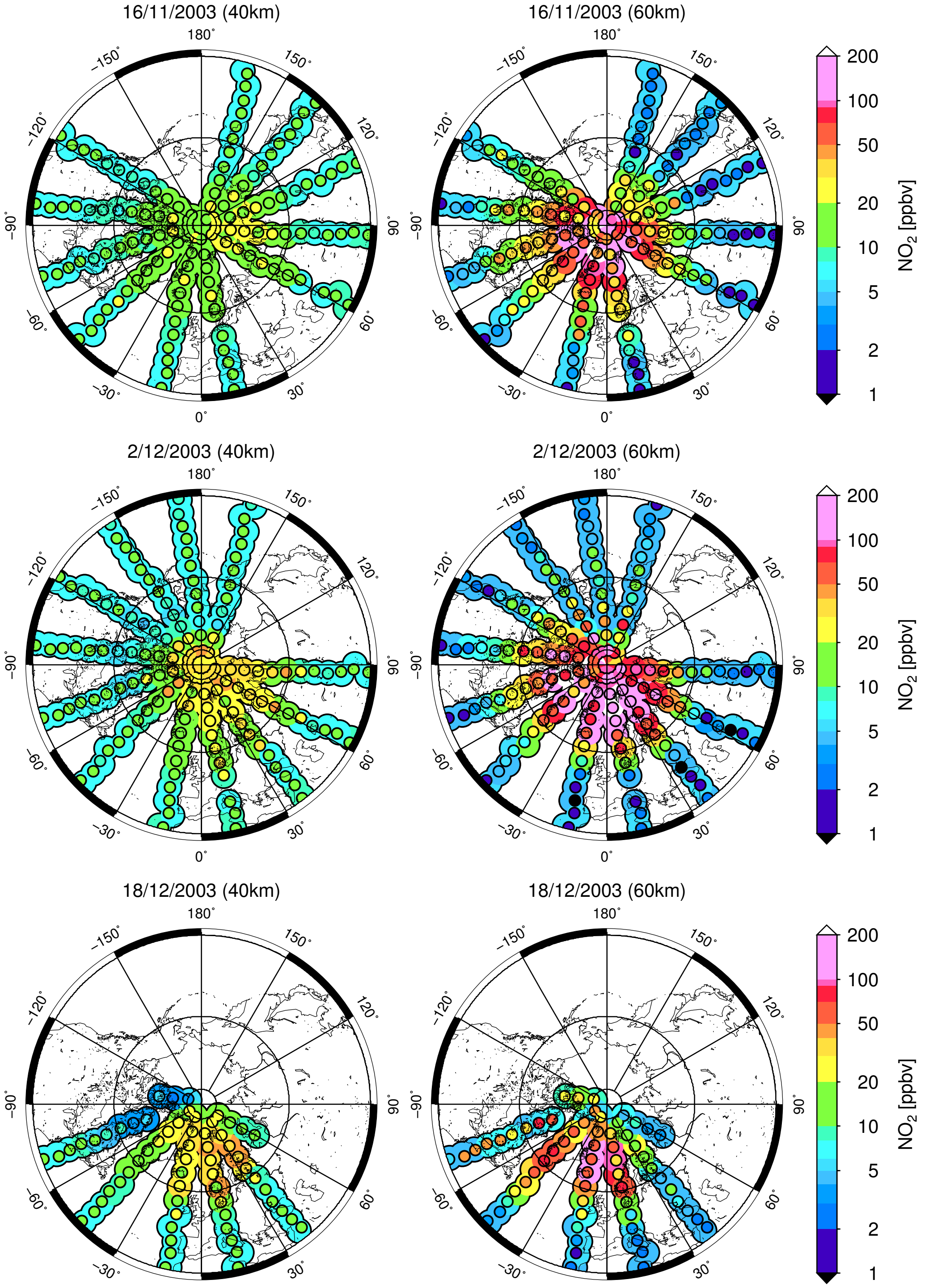

Figure 12.14 (continued) *Simulated NO_2 values compared to observations after the Solar Proton Event (SPE) 2003 on three different days (16/11/2003, 2/12/2003, 18/12/2003) at 40 km (left panel) and 60 km (right panel). Simulated values are displayed as the underlying colour coded circles. Observations obtained from the Michelson Interferometer for Passive Atmospheric Sounding (MIPAS) instrument in ascending mode are displayed in colour coded smaller circles. Values are presented over the northern polar cap between 60°-90° N.*

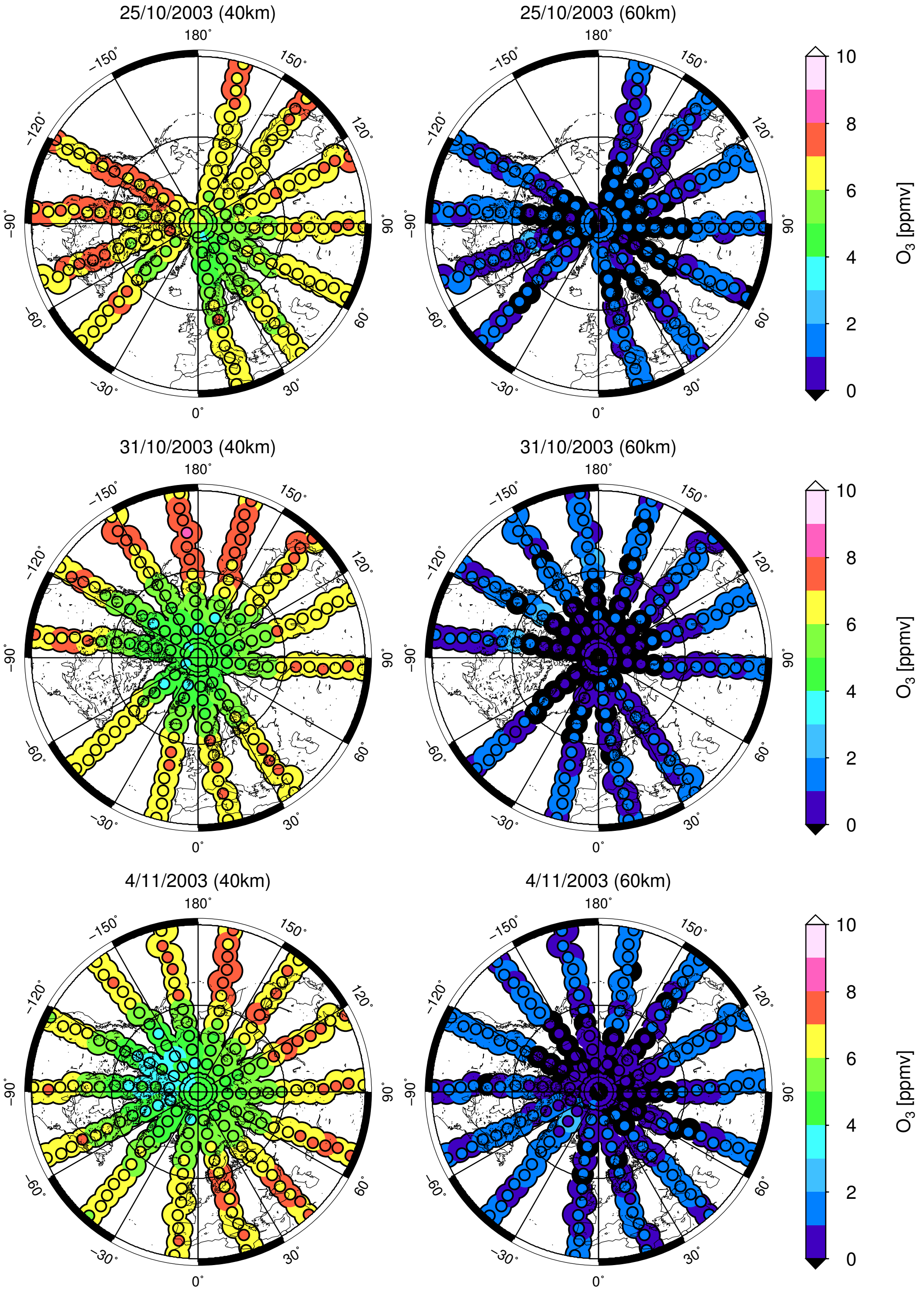

Figure 12.15 *Simulated O_3 values compared to observations during the Solar Proton Event (SPE) 2003 at three different days (25/10/2003, 31/10/2003, 5/11/2003) at 40 km (left panel) and 60 km (right panel). Simulated values are displayed as the underlying colour coded circles. Observations obtained from the Michelson Interferometer for Passive Atmospheric Sounding (MIPAS) instrument in ascending mode are displayed in colour coded smaller circles. Values are presented over the northern polar cap between 60°-90° N.*

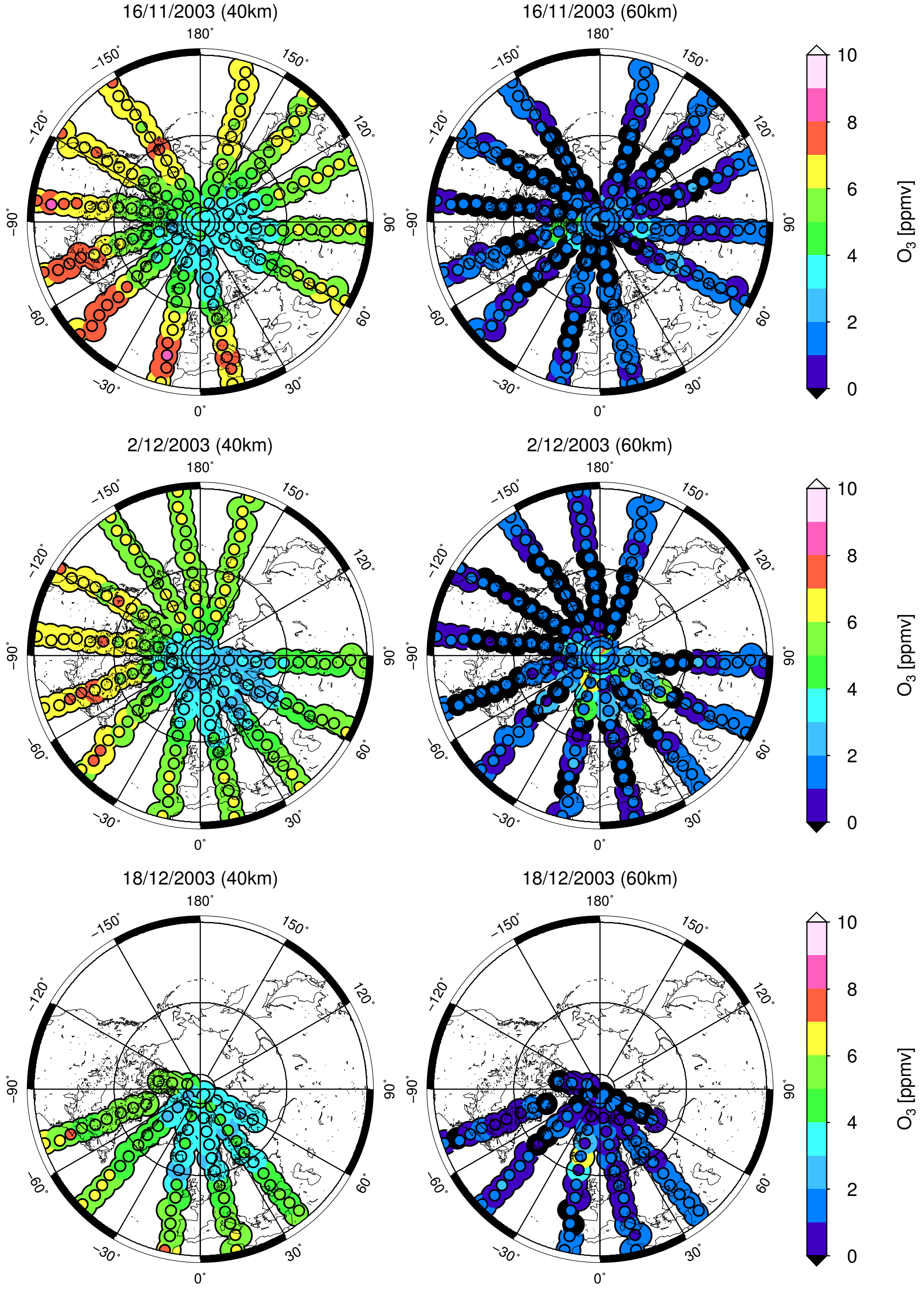

Figure 12.15 (continued) *Simulated O_3 values compared to observations after the Solar Proton Event (SPE) 2003 at three different days (16/11/2003, 2/12/2003, 18/12/2003) at 40 km (left panel) and 60 km (right panel). Simulated values are displayed as the underlying colour coded circles. Observations obtained from the Michelson Interferometer for Passive Atmospheric Sounding (MIPAS) instrument in ascending mode are displayed in colour coded smaller circles. Values are presented over the northern polar cap between 60°-90° N.*

13 Model simulation of energetic particle precipitation events for 2002-2009

13.1 Introduction

This chapter is focused on the impact on NO_x in the middle and upper atmosphere during different events in the period 2002-2009. For this period, a multi-year simulation has been performed, since for this period AIMOS ionisation rates are available. This chapter will focus on the following question:

- How different are the effects on NO_x abundance during strong and medium SPEs and during low solar activity, and how different are the effects during different northern polar seasons?

13.2 The comparison of different strong SPEs

The results in the previous chapter were presented to show the main impact on HO_x, NO_x, and O_3 during a large solar proton event and how the impact maintains for some weeks after the event. In this chapter, the impact on NO_x for different strong events and events during different time periods are presented. It is also presented for quiet conditions, to distinguish the background impact on particle fluxes. Therefore, the impact on NO_x is compared to the amount of proton fluxes, in the abundance of different strong SPEs. To distinguish the different amounts of NO_x that are produced during precipitating particles events.

In the following, results from a multi-year simulation are presented, to compare different strengths of SPEs with particle flux units of protons >10 MeV of larger than 1000 pfu (Figure 3.10). In Figures 13.1 to 13.6 proton fluxes measured by the GOES satellite are compared to their impact on NO_x abundance. GOES proton fluxes are shown in the upper panel of each figure and the impact on NO_x compared to a reference run is shown in each lower panel. The GOES proton fluxes are plotted for the energies 1, 10, 30, 50, 60, and >100 MeV. The SPEs can be placed in respect to the pfu in the following order (from high to low pfu values): 1.) October/November 2003 (29500, 1570), 2.) January 2005 (5040), 3.) May 2005 (3140), 4.) April 2002 (2520), 5.) July 2004 (2086), 6.) December 2006 (1980), and 7.) September 2005 (1880). In this comparison no results for the SPE April 2002 are presented, since it happened too short after the initialisation of the simulation.

The SPE October/November 2003 has been discussed in detail in Section 12. The next SPE with pfu >1000 took place during July 2004 and was the fifth strongest event during the period 2002-2009. Besides the lower proton fluxes during this event it is a major difference that this event occurred during northern polar summer. In 2005, three SPEs happened with pfu >1000. One SPE occurred during end of polar winter 2005 and was the second largest event during 2002-2009. The next SPE was again during northern polar summer and was the third strongest event. The last SPE happened before the onset of northern polar winter and was the weakest event with pfu larger than 1000.

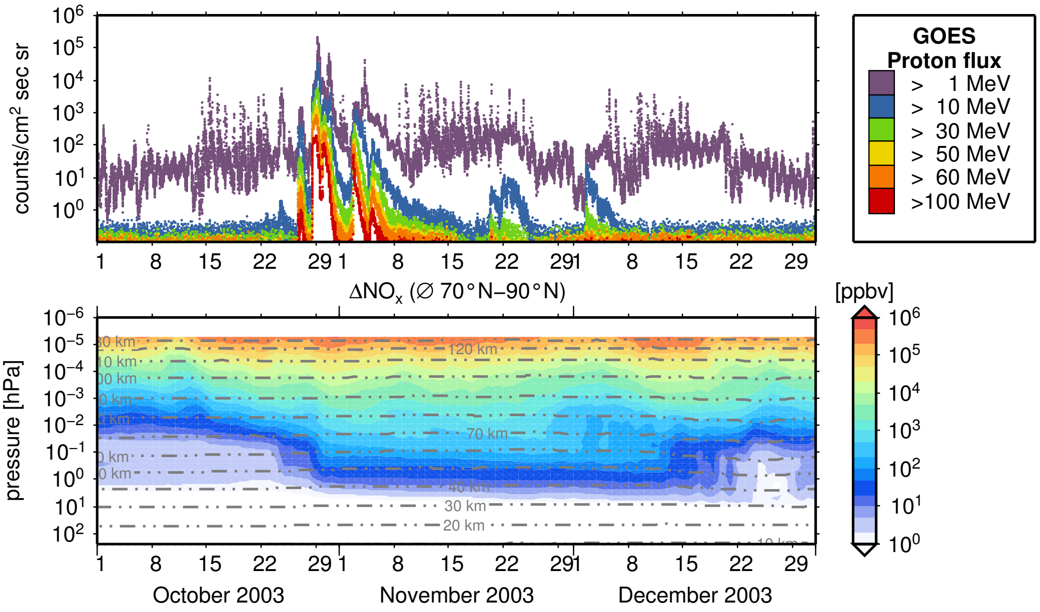

Figure 13.1 *Solar Proton Event (SPE) October/November 2003. The proton fluxes for energies 1, 10, 30, 50, 60, and >100 MeV are shown in the upper panel. The lower panel shows the impact on NO_x abundance compared to a reference simulation. The SPE October/November was the strongest event during the simulated period 2002-2009. See also Section 3.7.2.*

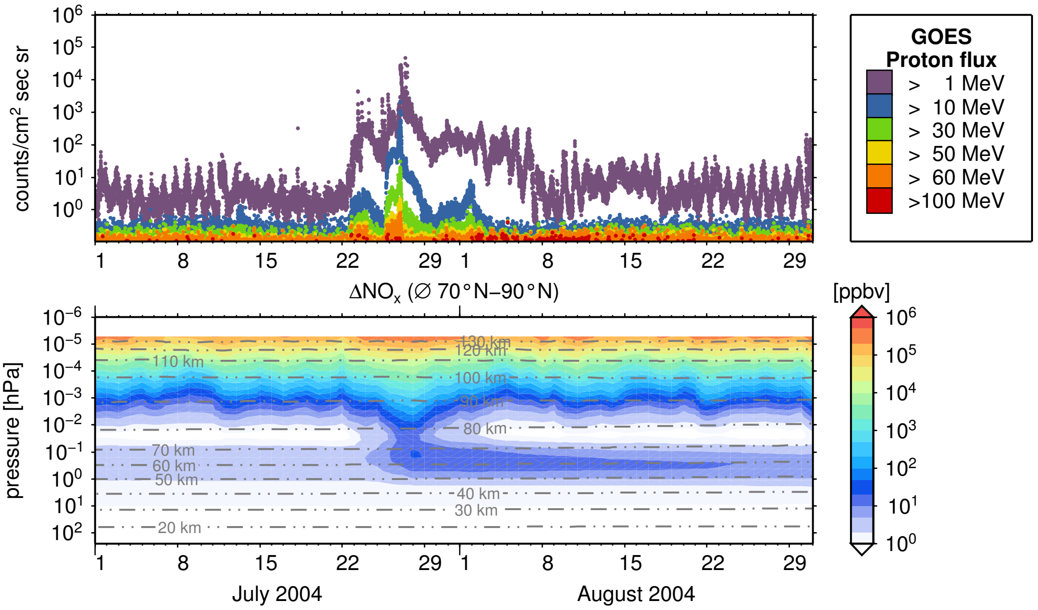

Figure 13.2 *Solar Proton Event (SPE) July 2004. The proton fluxes for energies 1, 10, 30, 50, 60, and >100 MeV are shown in the upper panel. The lower panel shows the impact on NO_x abundance compared to a reference simulation. This event was the fifth largest event during 2002-2009.*

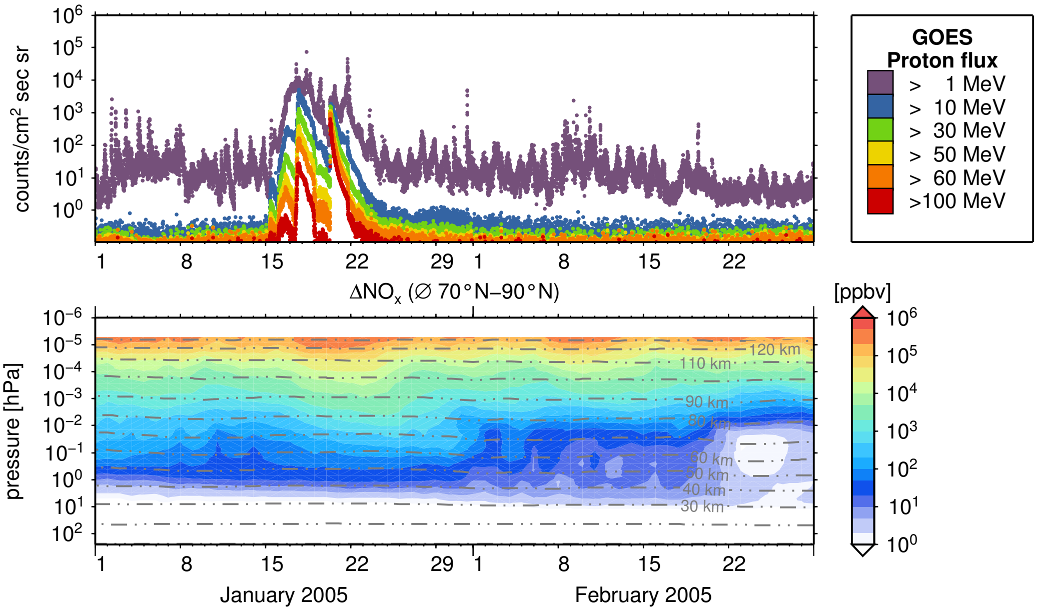

Figure 13.3 *Solar Proton Event (SPE) January 2005. The proton fluxes for energies 1, 10, 30, 50, 60, and >100 MeV are shown in the upper panel. The lower panel shows the impact on* NO_x *abundance compared to a reference simulation. This event was the second largest event during 2002-2009.*

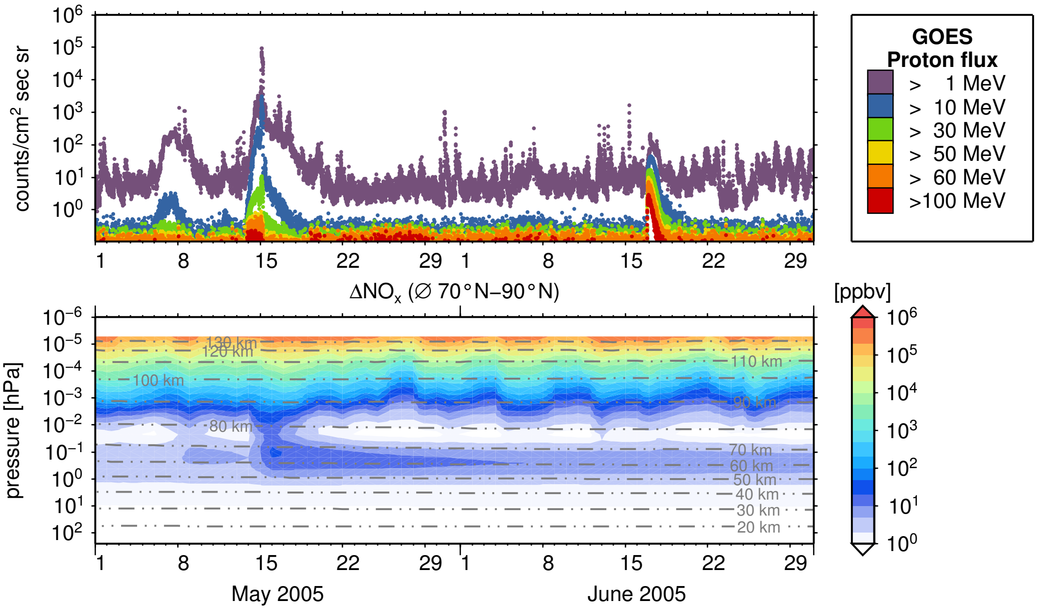

Figure 13.4 *Solar Proton Event (SPE) May 2005. The proton fluxes for energies 1, 10, 30, 50, 60, and >100 MeV are shown in the upper panel. The lower panel shows the impact on* NO_x *abundance compared to a reference simulation. This event was the third largest event during 2002-2009.*

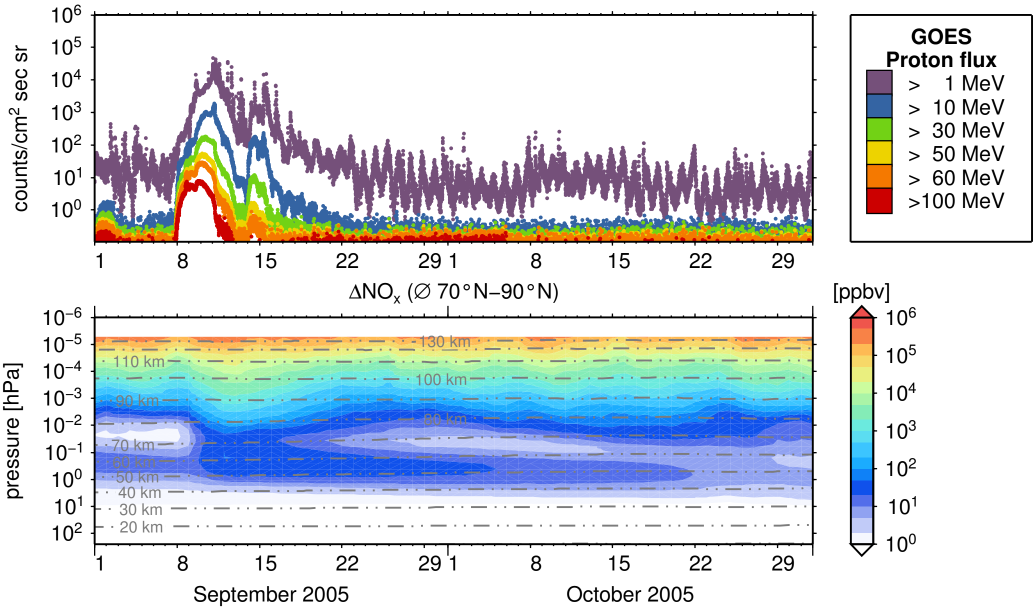

Figure 13.5 *Solar Proton Event (SPE) September 2005. The proton fluxes for energies 1, 10, 30, 50, 60, and >100 MeV are shown in the upper panel. The lower panel shows the impact on* NO_x *abundance compared to a reference simulation. This event was the seventh largest event during 2002-2009.*

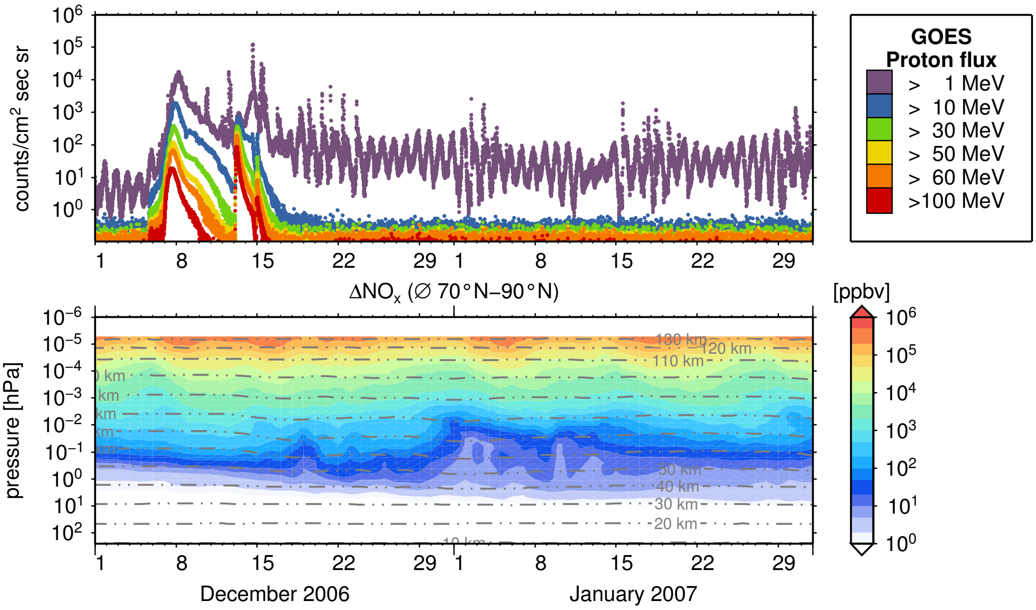

Figure 13.6 *Solar Proton Event (SPE) December 2006. The proton fluxes for energies 1, 10, 30, 50, 60, and >100 MeV are shown in the upper panel. The lower panel shows the impact on* NO_x *abundance compared to a reference simulation. This event was the sixth largest event during 2002-2009.*

13.3 Influence of a weaker solar proton event and during quiet conditions 2007-2010

In comparison to the previous section, a relative weak event occurred during the beginning of November 2004.

The declining phase of the solar cycle 23 was a very solar inactive period (Figure 3.10 and 3.4.) Two periods, the first half of northern polar winter (October-December 2007) and northern polar summer (June-August 2008) are compared in Figures 13.8 and 13.9, respectively.

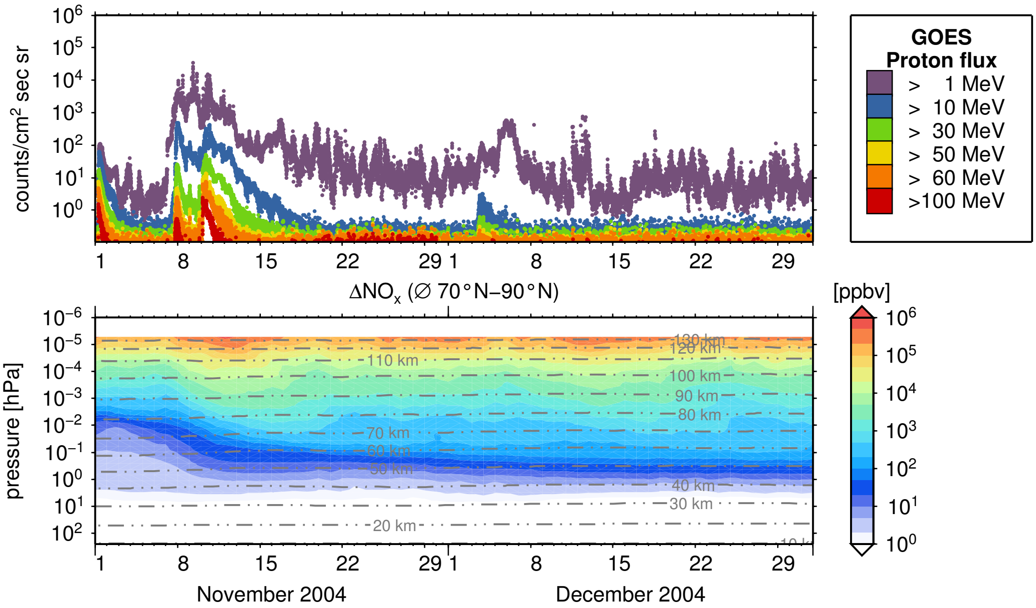

Figure 13.7 *Solar Proton Event (SPE) November 2004. The proton fluxes for energies 1, 10, 30, 50, 60, and >100 MeV are shown in the upper panel. The lower panel shows the impact on NO_x abundance compared to a reference simulation.*

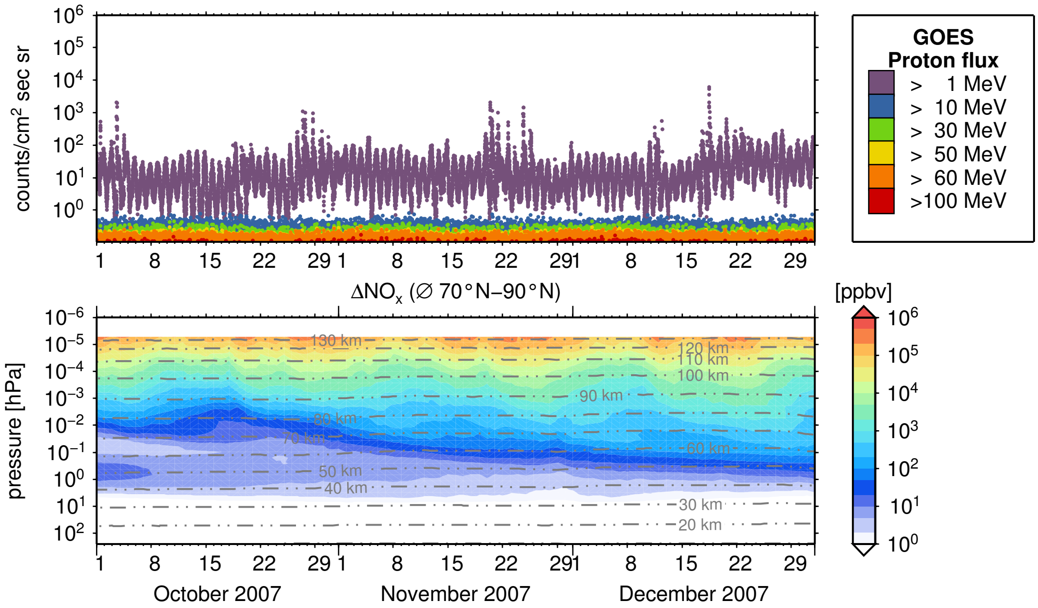

Figure 13.8 *Proton flux and change in NO_x for the period October-December 2007. The proton fluxes for energies 1, 10, 30, 50, 60, and >100 MeV are shown in the upper panel. The lower panel shows the impact on NO_x abundance compared to a reference simulation.*

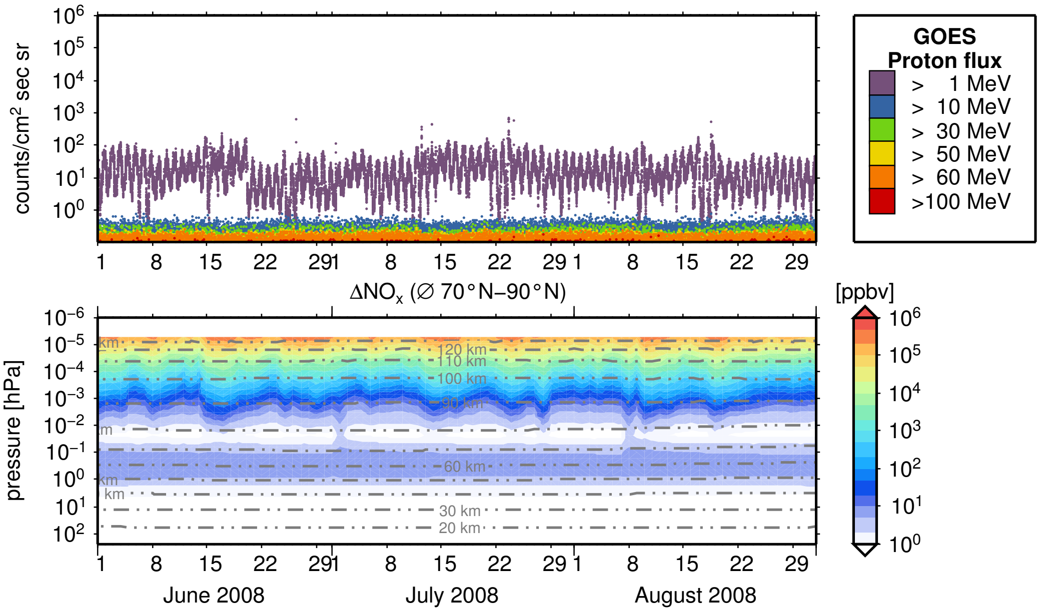

Figure 13.9 *Proton flux and change in NO_x for the period June-August 2008. The proton fluxes for energies 1, 10, 30, 50, 60, and >100 MeV are shown in the upper panel. The lower panel shows the impact on NO_x abundance compared to a reference simulation.*

14 The different impacts of ionisation rates due to protons and electrons

14.1 Introduction

In this Chapter, the impacts of different particle populations during the SPE 2003 will be discussed. For this purpose, different model studies for the SPE 2003 have been performed considering the different particle precipitations provided by the AIMOS model (due to protons and electrons). During the SPE 2003, both particle precipitations occurred during the time period October-December 2003. To distinguish the different magnitude of each precipitation, case model simulations for each type of precipitation alone have been performed. Therefore, four simulations of the SPE 2003 have been carried out, (i) with ionisation rates from precipitating protons, (ii) with ionisation rates from precipitating electrons, (iii) with ionisation rates from both precipitating particles (protons and electrons), and (iv) a simulation with no ionisation rates included. The latter simulation serves as a reference run, to distinguish the background level of the atmosphere's composition. To get the net impact of the individually particle population, the result of the BASE simulation is subtracted from each of the CASE simulations.

This chapter is divided into three sections to address the following topics:

- The direct impact of precipitating protons during SPE 2003 on the stratosphere, mesosphere, and lower thermosphere.
- A possible direct impact of precipitating electrons on the stratosphere and lower mesosphere.
- The impact of the top height level of the used model version with respect to both particle populations.
- The indirect effect of precipitating electrons that lead to the transport of NO_x from the upper atmosphere to the stratosphere.

14.2 The direct impact during solar proton events on the chemical composition in the stratosphere and lower mesosphere

As described above, the different impacts of proton and electron precipitation events will be discussed separately in this chapter. This section focuses therefore on the impact of highly energetic proton precipitation and its effect on the chemical composition of the middle and upper atmosphere. As in Section 12, the effect will by discussed for the large SPE 2003. The additional impact of electron precipitation will by discussed in Section 14.3 and Section 14.4.

In comparison to the last section, it will be focused on model results carried out with the impact of AIMOS ionisation rates due to protons only and will be compared to the previous section, when ionisation rates due to both particle populations were considered. The direct impact of the precipitating particles is again on hydrogen and nitrogen, via positive ion-chemistry, which is therefore parametrised as described in Section 6.6. The impact on ozone and other tracers is then due to the change in these hydrogen and nitrogen compounds.

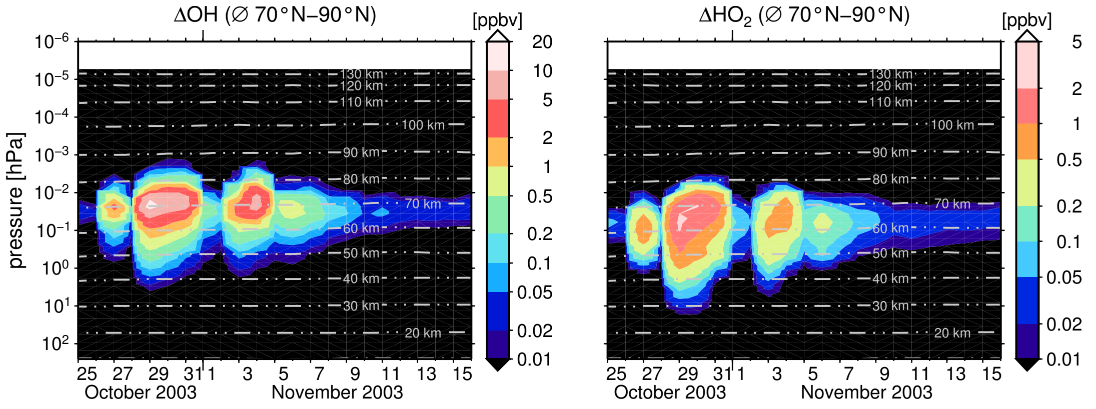

(a) Northern Hemisphere

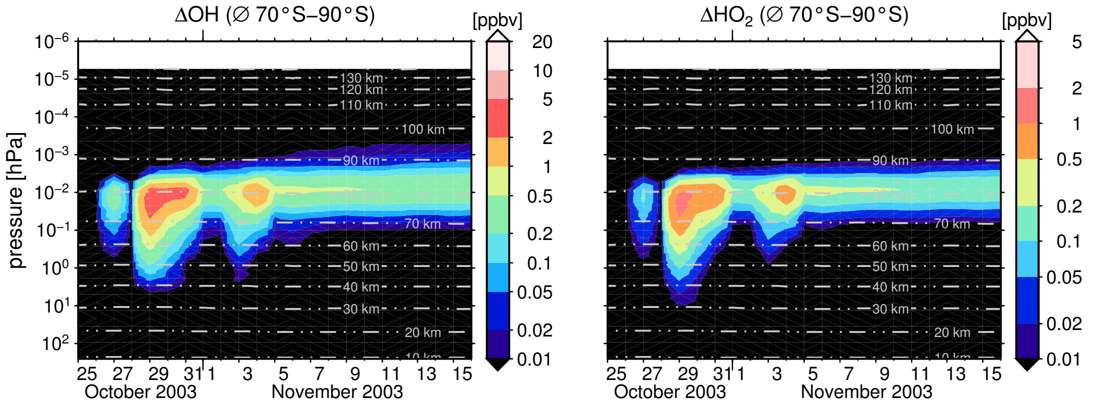

(b) Southern Hemisphere

Figure 14.1 *The impact of ionisation by precipitating protons on OH (left panels) and HO_2 (right panels) during October/November 2003. Values are shown as differences to a reference run from area weighted averages over the 70°-90° Northern (a) and Southern (b) polar cap.*

No other direct chemical influence on, for example, chlorine compounds due to negative ion chemistry, as discussed in more detail in Section 15, is considered here. The effect of precipitating protons will be discussed qualitatively and compared to the impact of both particle populations (Section 12).

14.2.1 The impact on hydrogen compounds

One of the direct effects of the ionisation by energetic particles is the production of odd hydrogen. As described in Section 3.5.5, atomic hydrogen and OH are produced through recombination reactions of water cluster ions with secondary electrons or ions. Figure 14.1 shows the change in OH and HO_2 compared to a model simulation without any ionisation impact by precipitating protons for both hemispheres as differences of area weighted averages between 70°-90°N and S, respectively. The values represent the volume mixing ratio at 0 UTC. In the Northern Hemisphere this means night-time conditions and in the Southern Hemisphere day-time conditions, respectively, throughout the whole time period shown. In both hemispheres, and therefore, during day as well as night-time conditions, a major enhancement in OH due to the main SPE starting on 28 October 2003 and can be seen in the model simulations (Figure 14.1, left panels). Since the chemical life-time of OH and H is very short (seconds to minutes) (Brasseur & Solomon, 2005), the effect of the ionisation is also quite short, and lasts only as long as the ionisation rates (see Figure 8.2) are enhanced. Even more pronounced to the ionisation rate increase is the change in HO_2. Very clear enhancements on the major events on 28 October 2003 and 3 November 2003 are seen in the HO_2 change. In the absence of sunlight, HO_2 is the dominant HO_x compound. Therefore, the HO_2 increase is not so pronounced in the Southern Hemisphere as in the Northern Hemisphere, since during day-time, HO_2 will be quickly photolysed. The effect on OH and HO_2 as a function of altitude is in both hemispheres quite similar. OH enhancements are clearly visible down to altitudes around 40 km, and HO_2 values start to increase already above 30 km altitude in the Northern Hemisphere, and still above 45 km in the Southern Hemisphere.

14.2.2 The impact on nitrogen compounds

The main difference in the impact on nitrogen compounds in the Northern Hemisphere is the absence of sunlight. In the Southern Hemisphere, during the presence of sunlight, NO_2 forms NO through the reaction with atomic oxygen or photolysis. In the absence of photolysis, NO_2 is therefore very long-lived in the Northern Hemisphere, during the time period shown in Figure 14.2. This makes the event in October/November 2003 quite interesting, since the impact of atmospheric dynamics yields a very pronounced effect during the period of enhanced nitrogen compounds. Since these enhanced nitrogen compounds have such long life-times during polar night, they will be transported into the lower stratosphere, as enhanced values of around 20-50 ppbv are transported within the polar vortex from altitudes above 50 km produced during the event, which stays enhanced and will be transported to lower altitudes to below 45 km in a time period of a few days/weeks. These chemically and dynamically enhanced nitrogen compounds lead to large ozone depletion down to the lower stratosphere, as described in the next section.

The impact of proton forcing on nitrogen compounds such as NO_2 and NO (Figure 14.2) is very different in the two hemispheres. In the Northern Hemisphere, in the absence of sunlight (Figure 14.2, upper panel), NO_2 is enhanced right from the onset of the main SPE event in 28 October, and is continuously enhanced through out the whole time period shown, and is increased for several weeks after the event, as will be described later. NO is produced during high proton forcing through reactions with atomic nitrogen and O_2, as described in Section 3.5.5. This is shown in the model simulations for NO in the Northern Hemisphere (Figure 14.2, right upper panel) as increased values during the major events on 28 October 2003 and 3 November 2003. In the Southern, sunlit hemisphere, NO_2 and NO show an opposite behaviour as in the Northern Hemisphere. NO_2 is less enhanced in the Southern Hemisphere, and more pronounced in the middle stratosphere, of altitudes between 35 and 50 km, whereas in the Northern Hemisphere, NO_2 is enhanced throughout the whole stratosphere, reaching down to 30 km. NO is more enhanced throughout the middle and upper stratosphere and mainly above 45 km in the Southern Hemisphere.

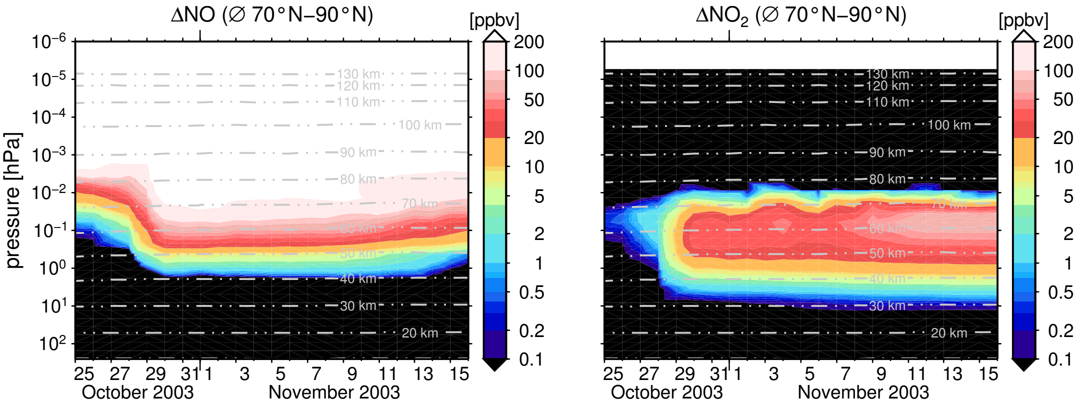

(a) Northern Hemisphere

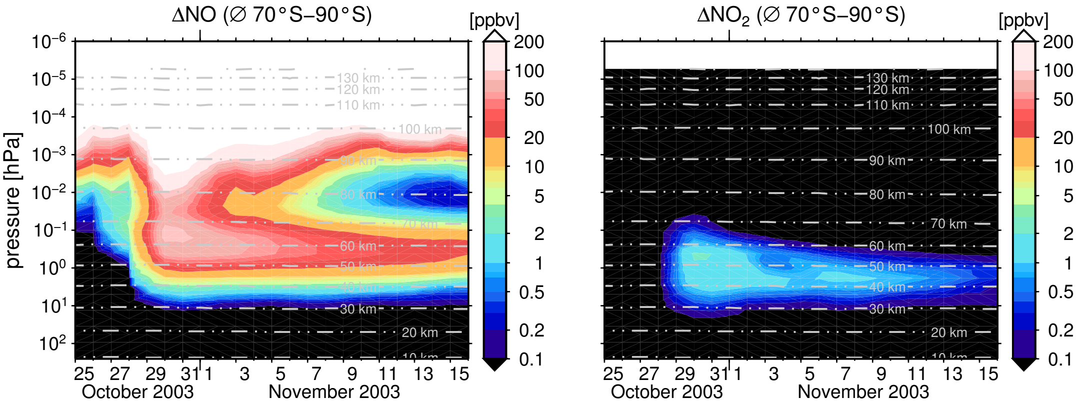

(b) Southern Hemisphere

Figure 14.2 *The impact of ionisation by precipitating protons on NO (left panels) and* NO_2 *(right panels) during October/November 2003. Values are shown as differences to a reference run from area weighted averages over the 70°-90° Northern (a) and Southern (b) polar cap.*

14.2.3 The impact on ozone

The direct increase in HO_x and NO_x due to the ionisation by protons leads to a following ozone depletion in the stratosphere. Figure 14.3 shows the change in O_3 in percentages (right panels) and absolute values (left panels) for the Northern Hemisphere (upper panels) and Southern Hemisphere (lower panels). In Northern and Southern Hemispheres, the impact on ozone is very different, in absolute values and in the peak height. In the Northern Hemisphere, the ozone depletion is largest in absolute and relative differences between 70-80 km and 50-80 km, respectively, during the event on 28/31 October and on 3/4 November 2003. In the Southern Hemisphere the absolute difference is smaller and more pronounced to altitudes below 40-50 km, but the relative difference peaks in the stratosphere between 70-80 km. A main difference in the compared hemispheres that is visible in relative difference is that the ozone depletion lasts much longer in the Northern Hemisphere. As discussed in previous sections, in the absence of sunlight during polar winter, enhanced NO_x has a longer life-time in the Northern Hemisphere, and can contribute to an ozone depletion of more than 10-20% until December 2003.

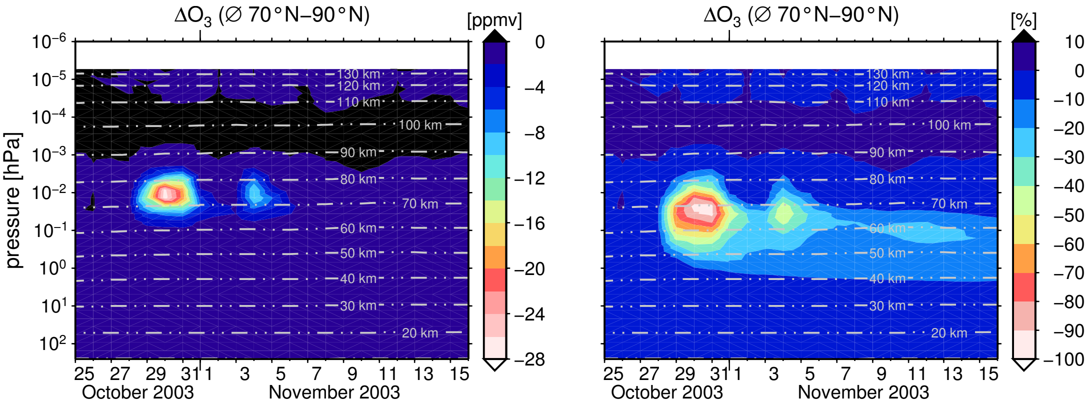

(a) Northern Hemisphere

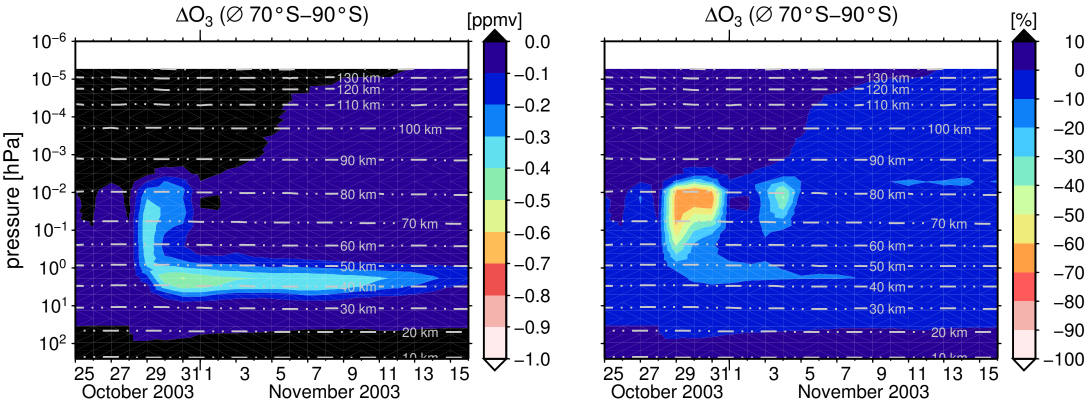

(b) Southern Hemisphere

Figure 14.3 *The impact of ionisation by precipitating protons on ozone during October/November 2003. Values are shown as differences to a reference run from area weighted averages over the 70°-90° Northern (a) and Southern (b) polar cap. The ozone change is plotted as absolute differences (left panels) and in percentage (right panels). The correspondent area weighted altitude is indicated by grey contours.*

14.2.4 The different impact due to proton precipitation compared to both particle populations

To compare the impact of precipitating protons during SPEs compared to the combined effect of precipitating protons and electrons during EPP events, time evolutions for HO_x, NO_x, and O_3 are presented in Figures 14.4, 14.5, and 14.6, respectively. The direct impact of protons precipitation will be discussed in comparison to the results presented in Section 12 (Figures 12.1, 12.6, and 12.11). The main differences will be discussed qualitatively.

For HO_x, the main difference compared to the combined impact of proton and electron precipitation is largest during periods with no enhanced proton flux. During the main events on 28/31 October and 3/4 November the difference is rather small. In the absence of high proton flux, the impact of electron precipitation quite significant. Results for the proton simulation shows much lower impact, starting shortly after the second event on 3/4 November and is continuously lower for the whole period shown. A lower impact is also

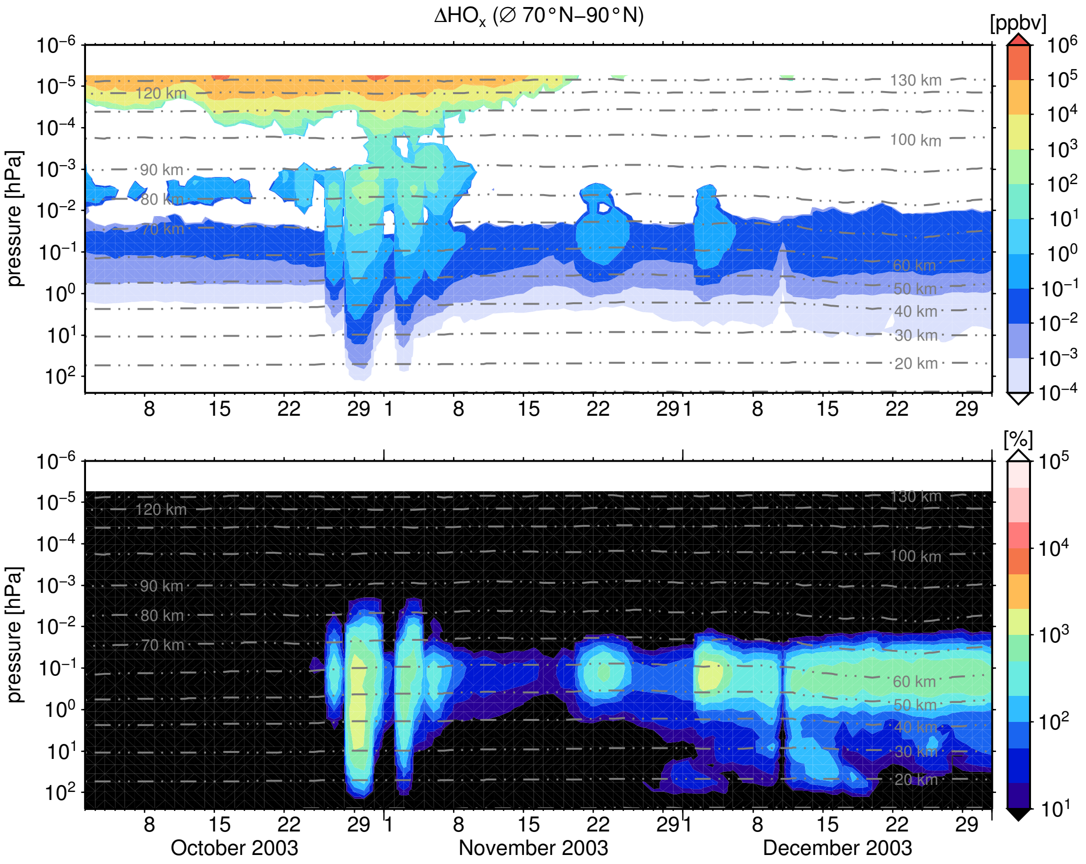

Figure 14.4 *Simulated time evolution of the impact on HO$_x$ (H, OH, HO$_2$) during the Solar Proton Event (SPE) 2003. The upper panel shows absolute differences to the reference run without particle influence (SPE-BASE) that are calculated from area weighted averages over the 70°-90° northern polar cap. Values are presented as vmr in ppbv. Note that only increased values (positive differences) are indicated as coloured contours. Differences less than 10^{-4} ppbv are colour coded in white as well as decreased values (negative differences). The lower panel shows the relative change with respect to the reference run ((SPE-BASE/BASE)×100%) with values larger than 10%. In both panels, grey dashed dotted contour lines indicate the area weighted mean altitude. The purple dashed line indicates the split level between family (below) and non family chemistry code (above).*

visible that increases with latitude. Above 90 km, the impact of electrons becomes larger in the absolute differences also during periods with large proton flux. The relative influence is in the upper atmosphere in both simulations rather small and peaks in the same altitude region between 20-80 km during the events, and 50-70 km during November and December. The relative impact due to protons only is pronounced before the first event, before 28 October and from middle of November. This relative difference in increasing with time and leads to changes in HO$_x$ that are lower in the SPE by up to 30% during the whole December 2003 between 50-60 km.

The impact on NO$_x$ with respect to only proton precipitation is in general lower. This is especially true with increasing altitude. Large absolute differences between the SPE and EPP impact is the missing production before the first event, before 28 October 2003, and

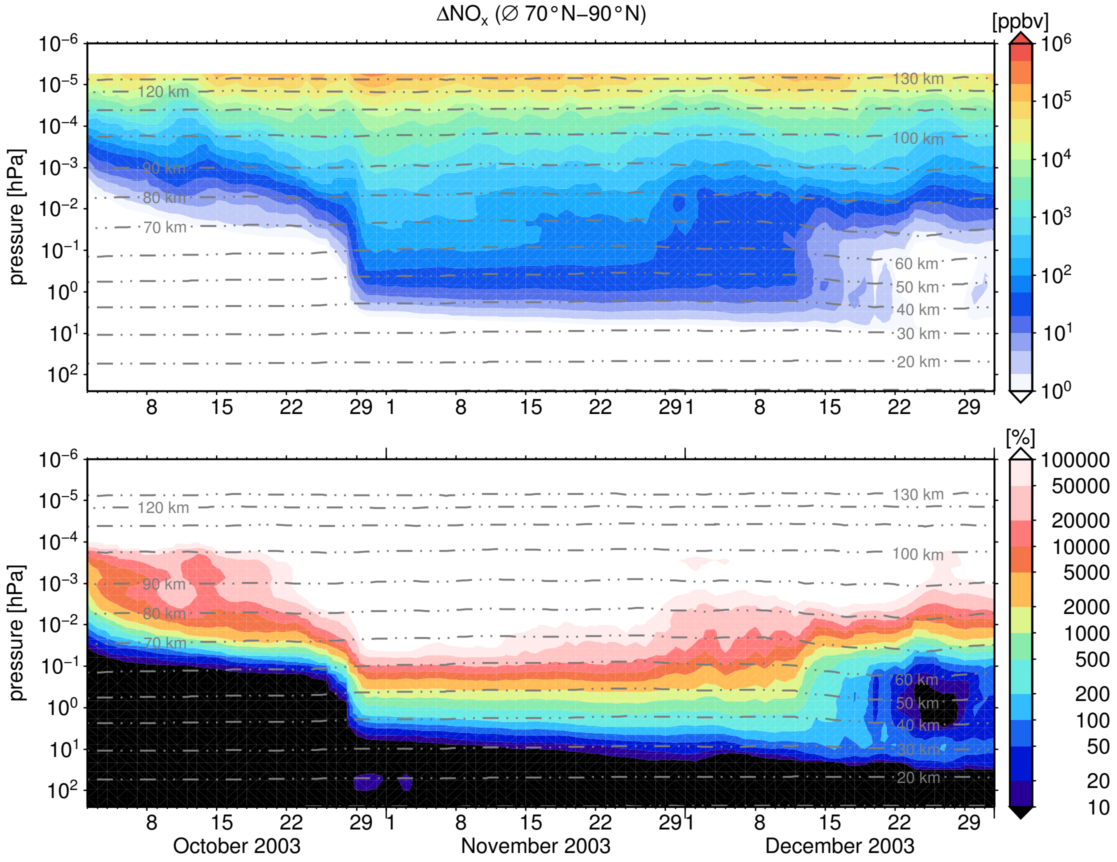

Figure 14.5 *Simulated impact on* NO_x *(N, NO,* NO_2*) during the Solar Proton Event (SPE) 2003. The upper panel shows absolute differences to a reference run without particle influence (SPE-BASE) that are calculated from area weighted values averaged over the 70°-90° northern polar cap. Values are presented as vmrs. The lower panel shows the relative change with respect to the reference run ((SPE-BASE/BASE)×100%). White colours indicate values that are larger than 100000%. In both panels, grey dashed dotted contour lines indicate the area weighted mean altitude. The purple dashed line indicates the split level between family (below) and non family chemistry code (above).*

a large missing amount of NO_x that is transported to altitudes around 50 km by the end of November. In the SPE simulations, the same values reach to an altitude 10 km and only until the middle of November. The EPP simulation also reaches differences 10 days earlier down to an altitude of 40 km before the onset of the SSW by the end of December. The additional impact due to electron precipitation below 70 km is largest during times with less proton precipitation, until the onset of the proton flux 28/31 October and from the middle of November on, probably due to too production above 70 km and too low values that are transported downwards resulting in missing enhancements in NO_x in the stratosphere by the beginning of December. A possible direct impact of precipitating electrons on the production of NO_x, NO_2, and O_3 is discussed in Section 14.3.

The different results in the simulation of the impact of precipitating protons and electrons on HO_x and NO_x leads to a significantly different simulation of the impact on O_3. Again, during the large proton flux on 28/31 October and 3/4 November 2003, the difference is a

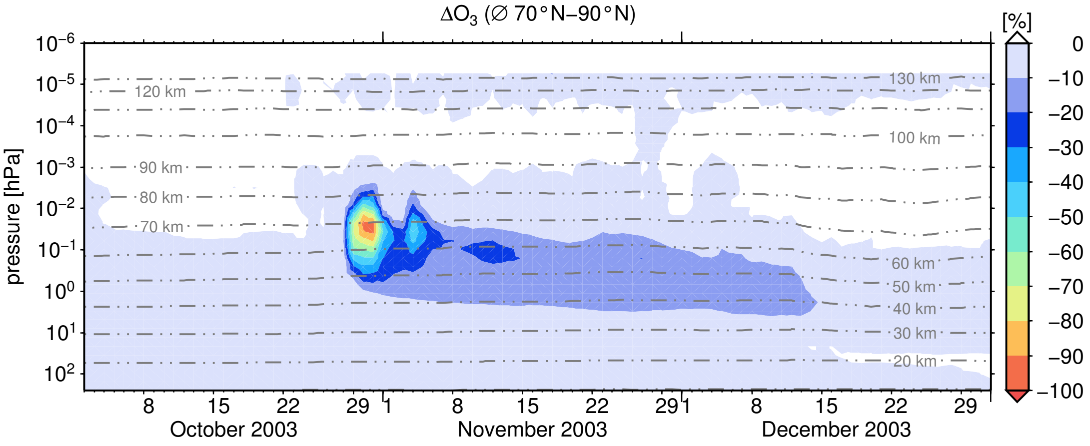

Figure 14.6 *Simulated impact on O_3 during the Solar Proton Event (SPE) 2003. The values are differences to a reference run without particle influence from values averaged over the 70°-90° northern polar cap. Values are presented in percent with respect to the reference run ((SPE-BASE/BASE)×100%).*

less ozone depletion in the SPE simulation of 5-10%. A larger difference in both simulations is before the first event with high ozone depletion on 24 October and a very pronounced lower ozone depletion during November until middle of December. The EPP simulation results in a larger ozone depletion by up to 30% between 45-65 km that is most probable due to both larger production in HO_x and NO_x due to the additional impact of the electrons during November and until the middle of December. After the break-up of the polar vortex, the impact on ozone is significantly lower in both simulations than before, since enhanced NO_x values vanished also. This indicates the dominant depletion impact of NO_x on ozone during the period before the onset of the SSW. The SPE run also results in less ozone depletion above 120 km, which is probably not significant.

14.3 The direct impact of precipitating protons and electrons on the middle atmosphere and lower mesosphere as simulated with two different model versions

14.3.1 Introduction

A model study by Wissing *et al.* (2010) showed that ionisation rates due to protons and electrons from the AIMOS model lead to an impact on the chemical composition in the stratosphere and lower mesosphere directly. These results can not by verified by observations, see e.g. Funke *et al.* (2011). For the above mentioned study by Wissing *et al.* (2010), four different model simulations with the stratospheric version of the B3dCTM were performed: including (i) ionisation rates due to both (proton and electron precipitations), (ii) only protons, (iii), only electrons, and (iv) a control run with no ionisation rates included in the model. Model simulations were performed for the SPE 2003. Additionally, this study has been re-performed with both model versions, the stratospheric version and the version covering the atmosphere up to the lower thermosphere. Since one main difference of the model versions is the model top height (lower mesosphere and lower thermosphere), the precipitation of electrons should contribute to the total amount of NO_x abundance in the mesosphere as well as in the stratosphere. This is because the main level of ionisation through electrons is in the thermosphere and mesosphere. This part of the atmosphere is not entirely included in the ECMWF THETA version, so a major amount of NO_x is missing in the formation during EPP events in this region. This is also true during the event as well as after the event that occurred during polar winter, since the produced NO_x is transported from the upper atmosphere to lower altitudes. This is also described as indirect effect and discussed in more detail in Section 14.4. In the current Section, the direct effects of both particles (protons and electrons) are investigated with two different model versions covering different altitude regions. Since this direct effect of the electrons in the stratosphere is not verified by observations, a possible explanation is given in Section 14.3.5.

14.3.2 Model results

Model results for NO_x for each simulation are presented in Figure 14.7. The impacts of the different ionisation rates due to protons, electrons, and protons and electrons are shown in the upper, middle, and lower panel, respectively. The different impact of the different particle populations show significantly different results for the SPE 2003. Figure 14.7 shows results for NO_x for the ECMWF THETA simulation (left panels) and the LIMA PR THERMO model version (right panels). For this model comparison, the ECMWF THETA model results have been interpolated on the pressure levels of the LIMA PR THERMO version. Values are differences of area weighted averages between 70°-90°N compared to a corresponding reference simulation. White contours show absolute values in CO of the presented case simulation. Decreasing values with time show downward processes during that time period. Both model versions show clear differences in the effect of the different particles to the formation of NO_x. In the ECMWF THETA run, the SPE scenario shows the larger impact on NO_x than EEP events. But the main effect is in both scenarios around 50 km and above. This main impact is largest during the period of the main events, end of October and beginning of November. This is different in the LIMA PR THERMO version. It shows similar effects of the various particles but during different time periods. For SPEs only, the largest increase in NO_x is during end of October and beginning of November, so during and right after the events themselves. The impact of the precipitating electrons is dominating in the second half of November with a strong increase in NO_x until end of November which is transported downwards by 5 km since the onset of the first event. This transport of NO_x is also in the ECMWF THETA run, but it has a maximum value at around 45 km by the end of November. This tongue is not in the LIMA PR THERMO version at all. This indicates, that in the ECMWF THETA version too large values will be produced during the event, which then leads to too high values that are transported into low altitudes and leads there to too high values in the stratosphere. This is also true for the EEP events. Enhancements above 50 km are transported faster into lower altitudes than in the LIMA PR THERMO version. In the ECMWF THETA version, the effect of the proton precipitation is very strongly influenced by transport. This is also in the LIMA PR THERMO version below 50 km. Above that, the NO_x enhancement during the event in decreasing with time and reaches an enhancement that is halved by the end of November. The transported NO_x from the mesosphere and lower thermosphere is in the LIMA PR THERMO simulation due to electron precipitation that causes NO_X enhancements reaching the stratosphere during the downward transport in November starting right after the event in the end of October.

The same comparison as discussed above, but for O_3, is presented in Figure 14.8. O_3 depletions show similar features as the NO_x enhancement during November. It shows similar high decreases during the event, but the ECMWF THETA run shows higher decreases down to lower altitudes. As the NO_x increases are transported to lower altitudes with a peak at slightly above 40 km, the O_3 depletion travels down into the stratosphere and increases for the protons even again by the end of November. This peak in O_3 depletion that proceeds down in the stratosphere is not in the LIMA PR THERMO version. It shows an increasing O_3 depletion with altitude and time, but only a strong maximum decrease during the event, that is most probably due to HO_x increase, but does not lead to a peak O_3 depletion that slowly reaches lower altitudes with time. The peak decrease in O_3 is in the LIMA PR THERMO model in the mesosphere and not in the stratosphere. The effect of the different particles is in both model versions more pronounced due to protons.

The effects in the ECMWF THETA model are, in general, stronger in the stratosphere than in the LIMA PR THERMO model version. The same is true for the effect of the precipitating electrons alone. The signal of the particle precipitation effect in the upper stratosphere is proceeding too fast or too far down to the lower stratosphere. This is in particular true for constituents that are affected to transport, like NO_x.

14.3.3 The disagreement of model results of the different model versions

Model results from the different model versions give very different results in the impact of both particle populations. This is very pronounced in the result for NO_x (Figure 14.7) which show a higher production in the lower mesosphere that leads to a significantly larger abundance of NO_x that is transported into the lower and middle stratosphere. This then leads to a larger O_3 depletion in the stratosphere during the following weeks to months. In the comparison to the MIPAS observations, the results from the LIMA PR THERMO version agree better in values in the stratosphere and mesosphere, where the ECMWF THETA version show larger values by one order of magnitude. This is also true for other species like HCl (not shown here), that shows a large production in the upper model height boxes. Compared to that, HOCl shows not so large disagreements in both model versions. A possible explanation for this disagreement could be:

- The lower top height of the ECMWF THETA model version and no transport over the uppermost box (no flux out and into the uppermost box). If there is a vertical upward transport present, this may lead to a overflow of the uppermost model boxes. These overestimated values in the uppermost box can then lead to an overestimated downward transport in the following winter polar vortex.

- The family approach in the ECMWF THETA version in the mesosphere and upper stratosphere may result in a wrong partitioning in NO_x and O_x.

- The usage of adiabatic heating rates to calculate the vertical transport across the vertical level of potential temperature is not appropriate to apply in the mesosphere and leads to a wrong and maybe too fast vertical downward transport.

- Different dynamical processes that are included in the driving force of the meteorological data in the different underlying model (ECMWF and LIMA).

14.3.4 Model measurement comparison of the direct impact of precipitating electrons

Model results for NO_2 and O_3 of the LIMA PR THERMO model version considering the different particle populations have been compared to measurements from the satellite instrument MIPAS. Figure 14.9 and Figure 14.10 show daily mean values for NO_2 averaged over the 70°-90°northern polar cap. Figure 14.11 shows the corresponding impact on O_3. For NO_2 the model results including electron precipitation are in better agreement with the measurements. The absolute values of NO_2 and its vertical extent agree better than the result for only protons. In general the agreement is good between the EPP simulations and the MIPAS observations. This is true for the stratosphere, but in the mesosphere the model simulations show higher values between 45 and 60 km and 70 km before 15 November 2003. In contrast to the higher values of NO_2 in the lower mesosphere, values above 60 km are underestimated in the model during the second half of November and during December 2003. This may be due to two different causes in the simulations. The ionisation rates are probably too high below 70 km (see Section 14.3.5 for the possible reasons), or the production of odd nitrogen is underestimated by the model parametrisation in the chemical scheme. A third possible reason could be underestimated vertical transport during polar winter by the meteorological data. For O_3 the comparison shows a slightly different result. In general the model overestimated the O_3 abundance in absolute values in the stratosphere by approx. 1 ppmv. More significant in the mesosphere, that must be due to a problem in the chemical code in the mesosphere and lower thermosphere that needs to be further investigated. O_3 values around 60 km are slightly lower compared to the observations especially during the days of high ionisation impact at the end of October 2003, until middle of November, and again during middle of December. But values for the second half of November agree better with the observations and the O_3 decrease is smaller in this period and altitude in the model simulation that only considers proton precipitations.

14.3.5 What are the reasons for this modelled direct impact of electron precipitation in the lower mesosphere?

Funke *et al.* (2011) stated, that there is no clear evidence of a direct impact of precipitating electrons in the stratosphere. All enhanced values in NO_x can be correlated to a transport effect from the lower mesosphere into the stratosphere. They correlated enhanced NO_x values to enhanced CO values, and there were no enhancements of NO_x in the stratosphere in periods of high electron flux as after a geomagnetic storm on 22 November 2003.

A possible reason for an overestimation of the impact of precipitating electrons in the model simulation is too large ionisation rates due to electrons. Funke *et al.* (2011) give the following reasons for too large ionisation rates:

- Uncertainties in the modelling of electron precipitation in the energy range 300 keV to 5 MeV. The energy range of the used POES channel for this energy range is not clear, and for sure lower than 5 MeV. To model the electron precipitation, the energy spectrum to 5 MeV has been extrapolated (Wissing & Kallenrode, 2009).
- Uncertainties in the GOES proton flux observations.

Other reasons for too high ionisation rates:

- It is now known that the POES electron channels are contaminated by protons, especially during SPEs.

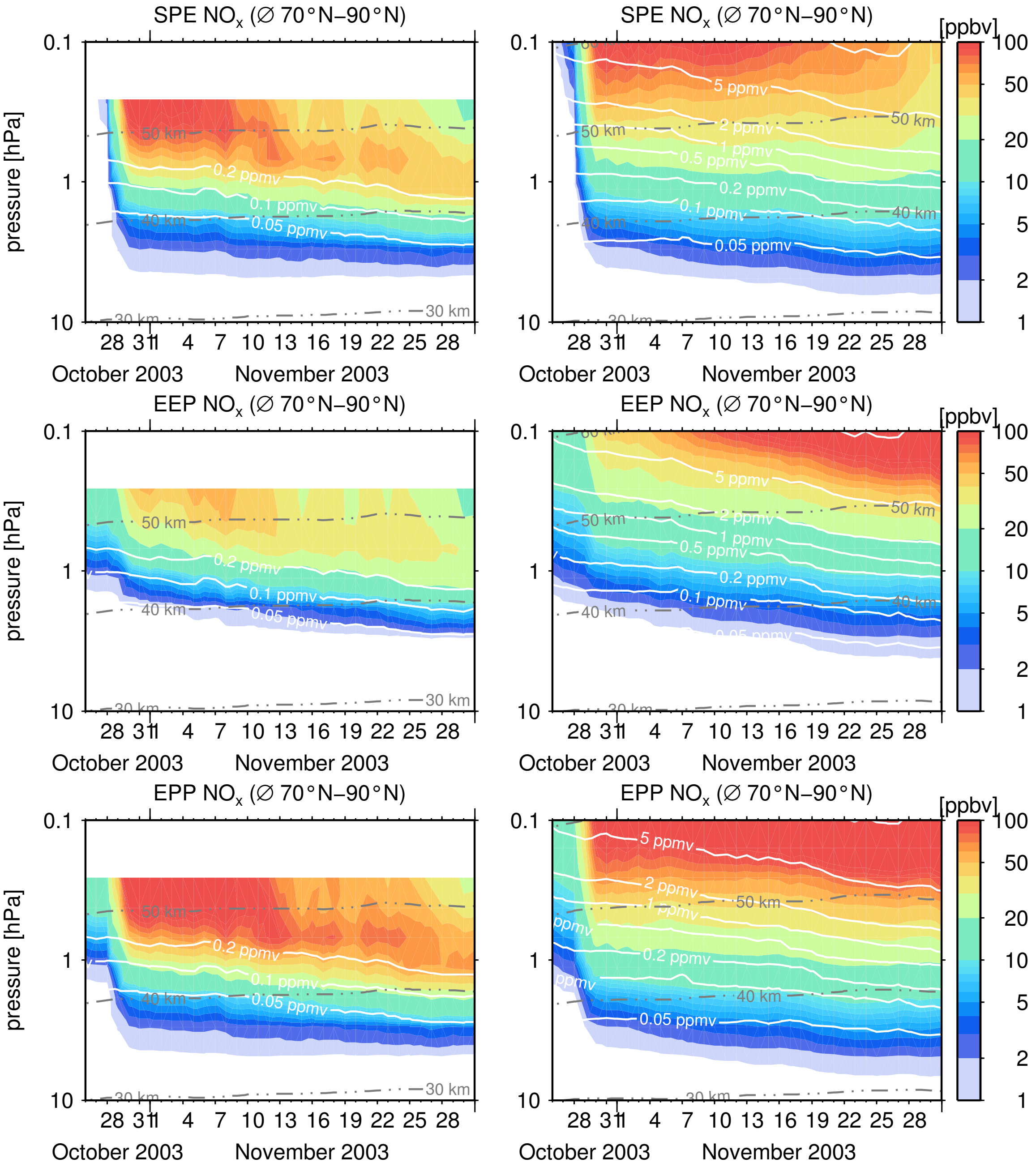

Figure 14.7 *The different impacts of ionisation due to different particle populations for the* ECMWF THETA *version (left panel) and the* LIMA PR THERMO *model version (right panel). The effect of the different ionisation rates due to protons (upper panel), electrons (middle panel), and protons and electrons (lower panel) are calculated as differences of area weighted averages over 70°-90°N compared to a reference simulation. The white contours represent absolute values in CO abundance which is an indicator of transport related processes. Grey contours show area weighted averaged altitudes. The* ECMWF THETA *model results have been interpolated on the pressure levels of the* LIMA PR THERMO *version. The model versions highly deviate from each other. Results from the* ECMWF THETA *run show larger values in lower altitudes by one order of magnitude and a stronger increase with altitude as the* LIMA PR THERMO *run.*

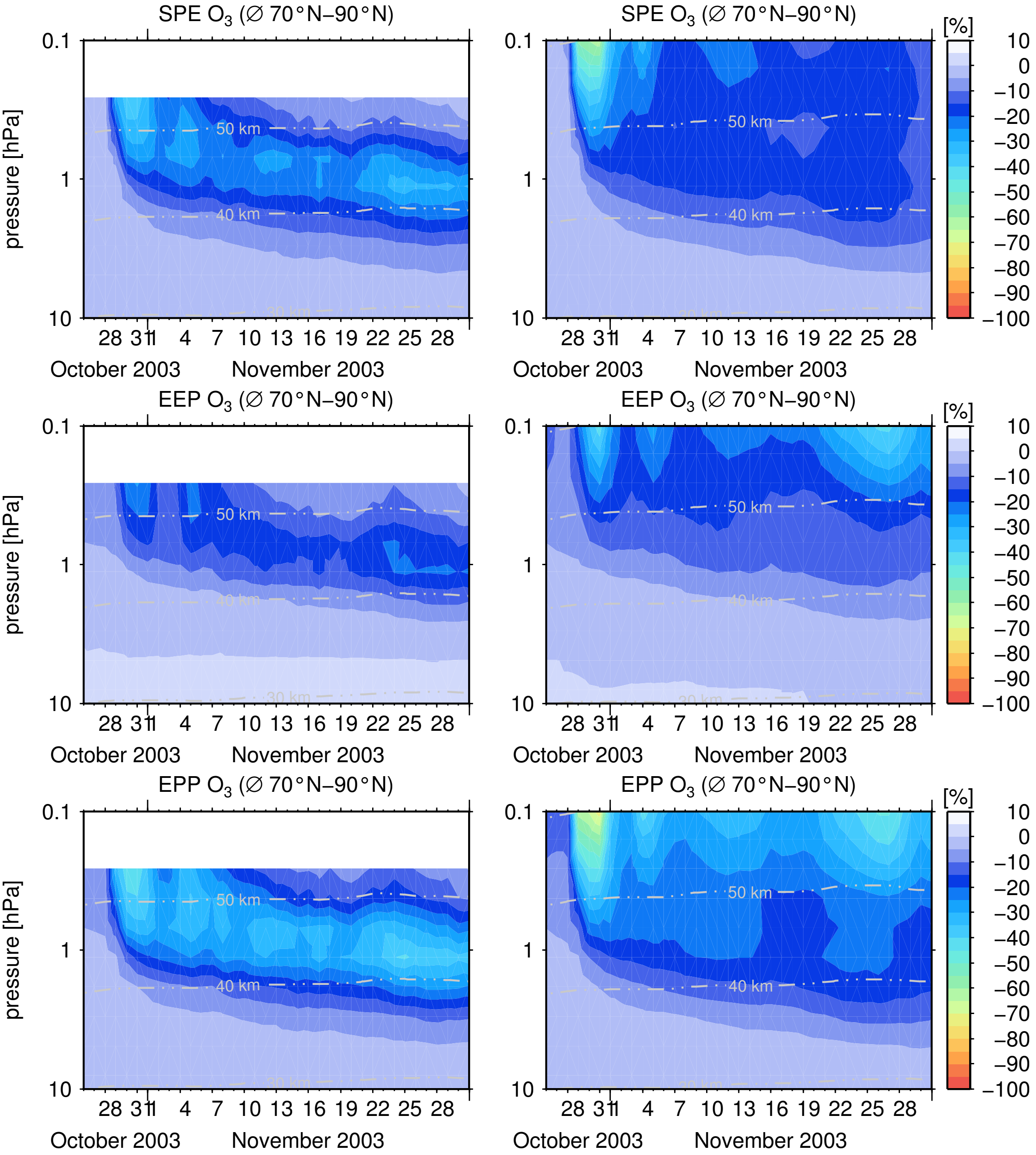

Figure 14.8 *The different impacts of ionisation due to different particle populations for the* ECMWF THETA *version (left panel) and the hybrid model version (right panel). The effect of the different ionisation rates due to protons (upper panel), electrons (middle panel), and protons and electrons (lower panel) are calculated as differences of area weighted averages over 70°-90°N compared to a reference simulation. Grey contours show area weighted averaged altitudes. The* ECMWF THETA *model results have been interpolated on the pressure levels of the* LIMA THERMO *version. The model versions highly deviate from each other. Results from the* ECMWF THETA *run show larger* O_3 *depletions in lower altitudes.*

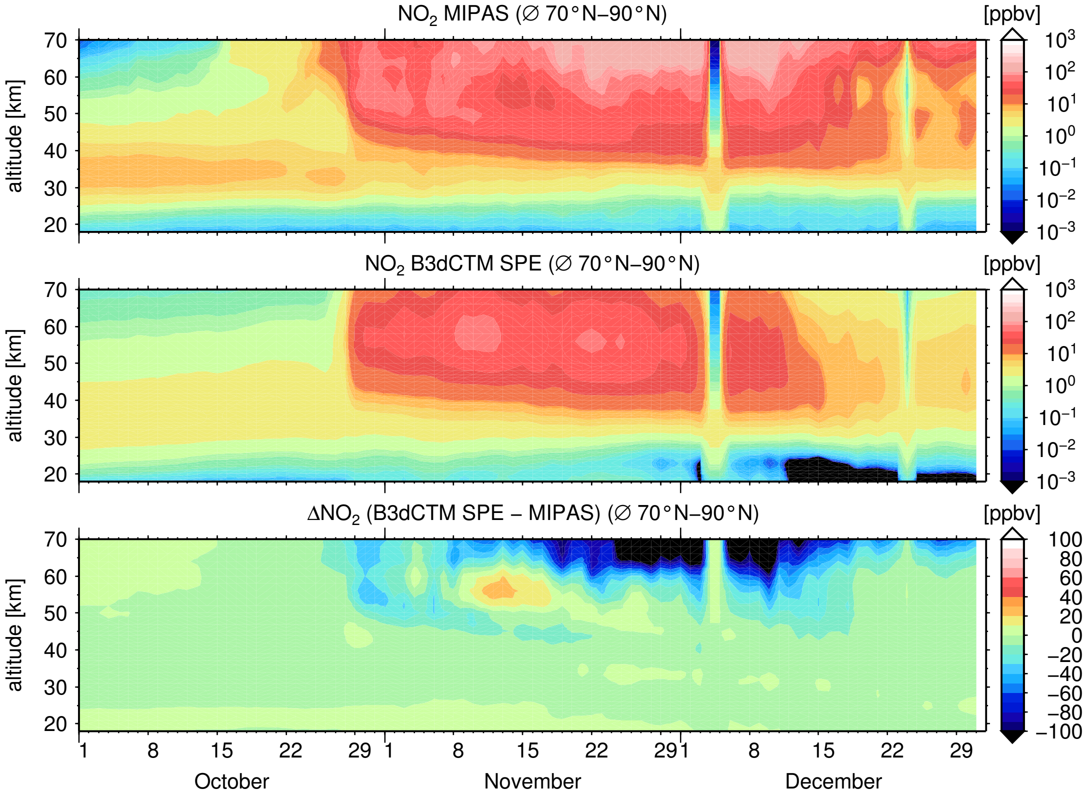

Figure 14.9 *The abundance of NO_2 as observed by the Michelson Interferometer for Passive Atmospheric Sounding (MIPAS) (upper panel) and simulated in the disturbed model scenario including ionisation due to protons (middle panel). The lower panel shows the difference between simulation and observation. Values are shown as averages over the 70°-90°Northern polar cap.*

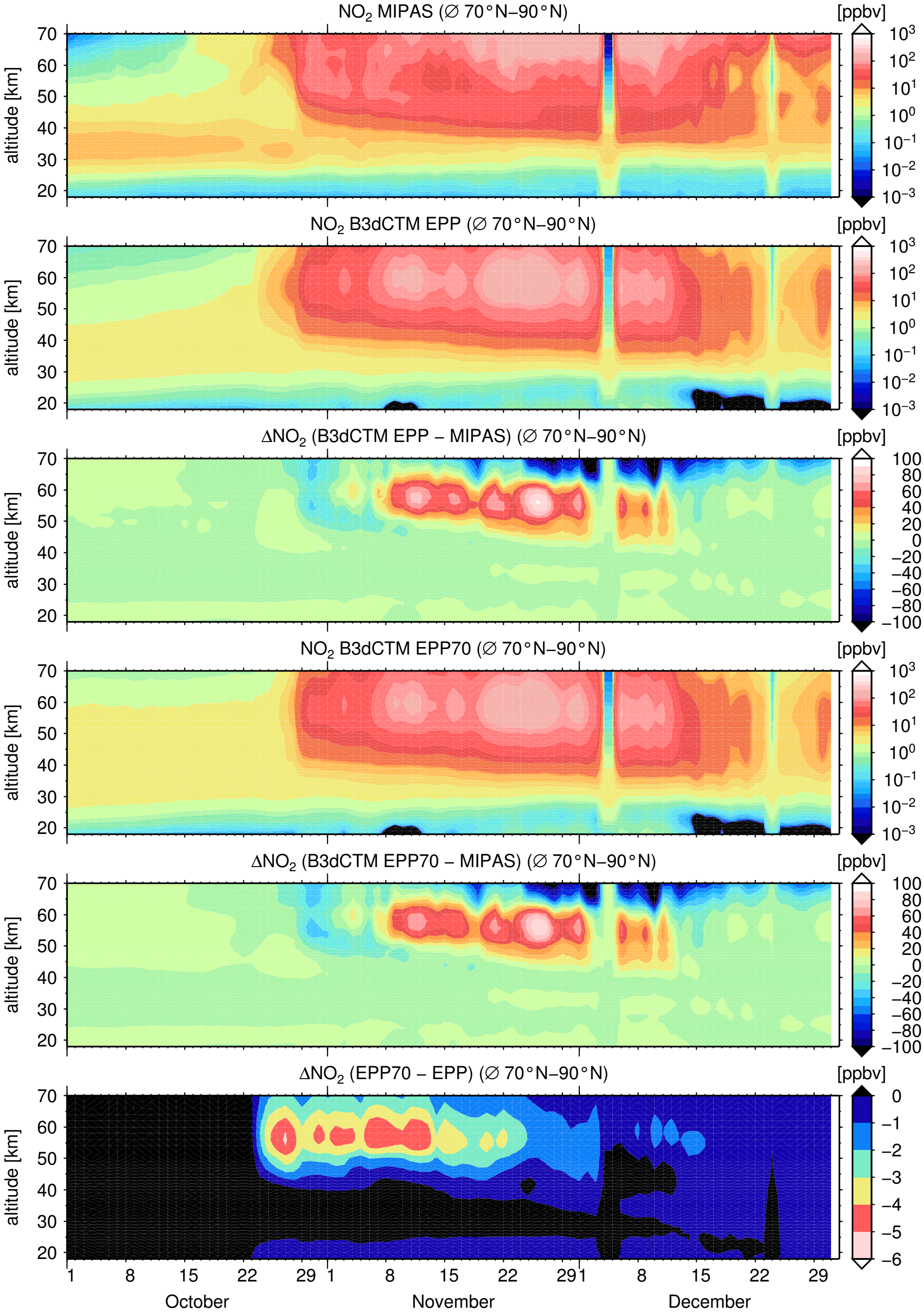

Figure 14.10 *The abundance of NO$_2$ as observed by the Michelson Interferometer for Passive Atmospheric Sounding (MIPAS) (upper panel) and simulated in the disturbed model scenario including ionisation due to protons and electrons (EPP) (second panel from above). The third panel from above shows the difference between simulation and observation. The forth panel shows results for a EPP simulation with no ionisation due to electrons below ∼70 km (EPP70). The fifth panel shows the difference to the observation. The lower most panel shows the difference between the EPP and EPP70 model simulation.*

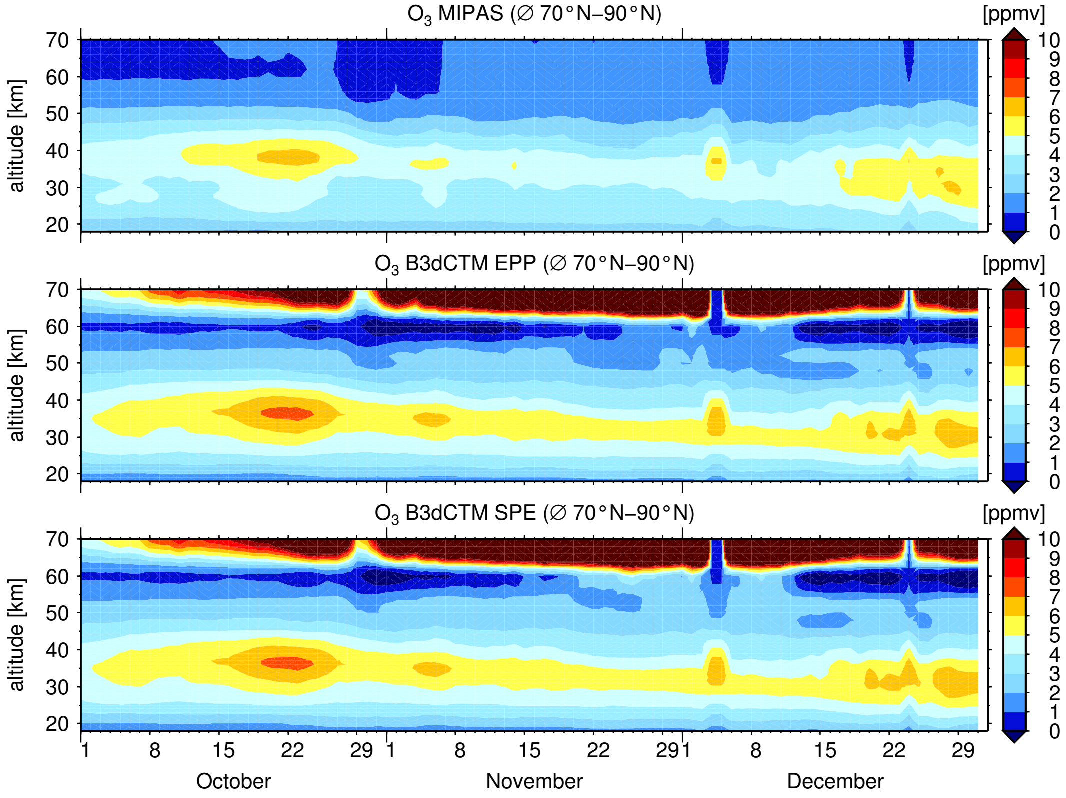

Figure 14.11 *The abundance of O_3 as observed by the Michelson Interferometer for Passive Atmospheric Sounding (MIPAS) (upper panel) and simulated in the disturbed model scenario including ionisation due to protons and electrons (EPP) (middle panel) and the disturbed model scenario including ionisation due to protons (SPE) (lower panel).*

14.4 The indirect impact of precipitating electrons

To illustrate the indirect amount of NO_x that is transported from the MLT region into the stratosphere, results from the ECMWF THETA simulation have been subtracted from the LIMA PR THERMO simulation. Figure 14.12 shows this transported NO_x for the SPE 2003 and Figure 14.13 for the period during the event and for the following year 2004. Both model simulations include AIMOS ionisation rates from protons and electrons. The difference is, therefore, the missing transported amount in NO_x from above the upper edge in the ECMWF THETA model version. Note that these results are not area weighted averages and that the results for the ECMWF THETA are too high by about one order of magnitude. But already during the SPE 2003, a very high fraction of the amount of NO_x in the stratosphere is transported from the MLT regions into the stratosphere and not produced directly there. This is again very pronounced during 2004 after the SSW starting in February 2004. A significant amount in NO_x is transported down to altitudes of about 40 km and these enhanced values stay until the beginning of March. Therefore, precipitating electrons have a very high impact on the middle atmosphere through dynamical processes even weeks after a large SPE or during no enhanced proton fluxes at all. This indirect effect is very important to account for, especially during dynamically disturbed periods after SSW, when large amounts of NO_x will be transported down to the middle atmosphere and can contribute to ozone depletion there.

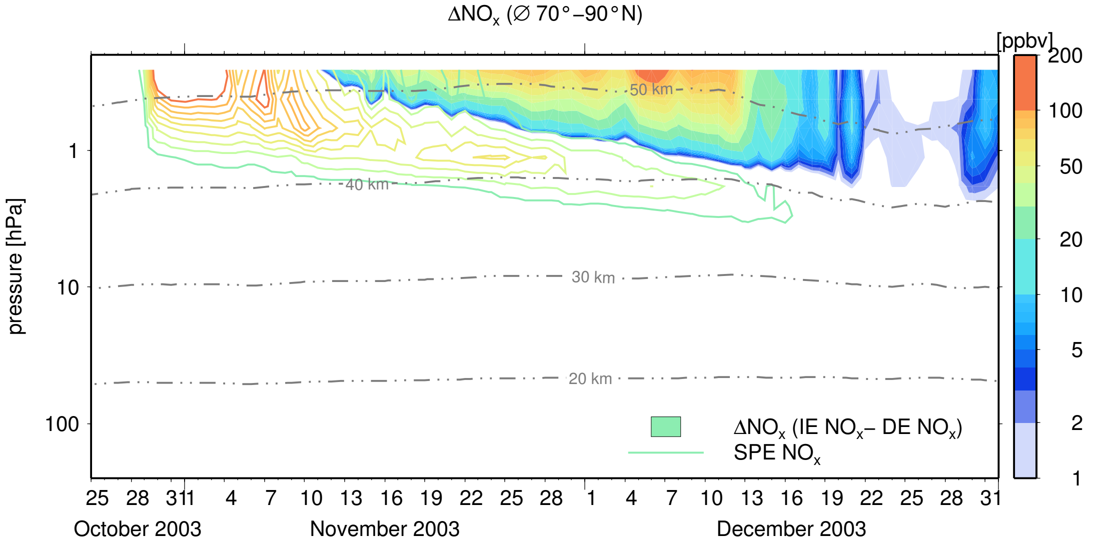

Figure 14.12 *The indirect effect on NO_x due to precipitating electrons during and after the Solar Proton Event (SPE) 2003. The coloured contours represent the ECMWF THETA simulation with ionisation due to protons only. The filled contours indicate the net amount of NO_x (EPP-SPE) that is transported from the Mesosphere and Lower Thermosphere (MLT) region into the stratosphere. Note that the absolute amount on the ECMWF THETA simulation is too high by approx. an order of magnitude (see Section 14.3). Values are presented as averages over 70°-90°N. Grey contours indicate averaged altitudes.*

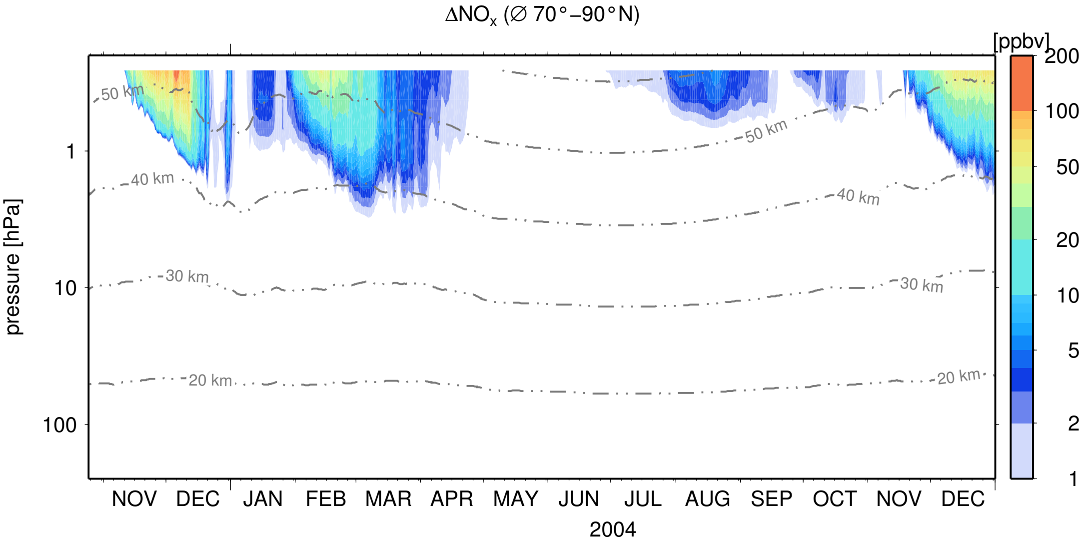

Figure 14.13 *The indirect effect on NO$_x$ due to precipitating electrons during the Solar Proton Event (SPE) 2003 and 2004. The filled contours indicate the net amount of NO$_x$ (EPP-SPE) that is transported from the Mesosphere and Lower Thermosphere (MLT) region into the stratosphere. Values are presented as averages over 70°-90°N. Grey contours indicate averaged altitudes.*

15 The impact on chlorine compounds

15.1 Introduction

In this study, parametrisations for production rates of HCl, ClO, Cl, Cl_2, and $ClONO_2$ from the University of Bremen Ion Chemistry (UBIC) model (see Section 6.6 for a description of the parametrisation and Section 8.3 for a description of the model) are implemented into the B3dCTM. Model simulations for the November/October 2003 Solar Proton Event (SPE) were carried out, and model results as well as comparisons to observations from the Michelson Interferometer for Passive Atmospheric Sounding (MIPAS) instrument (Fischer *et al.*, 2008) will be presented. This section is structured as follows: The different model simulations that have been carried out with the B3dCTM are described in Section 15.2. Model results for the October/November 2003 SPE are presented in Section 15.3, and a comparison to MIPAS observations is presented in Section 15.4.

15.2 Model simulations

Three model simulations have been carried out for this study. The first simulation is a comparative run, with no consideration of energetic particle influence, as an undisturbed reference simulation. It will be referred to as BASE in the following. The second simulation includes the parametrisation of the ionisation impact due to precipitating protons on NO_x and HO_x and is designated in the text with SPE. The third model simulation is basically the same as the second simulation, but with an additional parametrised impact on chlorine compounds such as HCl, ClO, Cl, Cl_2, and $ClONO_2$ derived from the UBIC model. It is referred to in the following as PARAM. The two latter model simulations are initialised from the BASE run on 1 October 2003 and carried out for October and November 2003. Therefore, all model runs only differ in the consideration of precipitating protons. All other components, like advection, meteorological data, etc., are identical. The designation of the different simulations as they are used within the following text is also described in Table 15.1.

15.3 Model simulation results

In this section, model results for different chlorine compounds are presented in Figures 15.1 and 15.2 as differences of area weighted averages over the northern polar cap between 70°-90°N. The differences are calculated to either the BASE run (Fig. 15.1) or to the SPE run (Figures 15.2 and 15.3).

Table 15.1 *Designation of the three model simulations used within the text.*

Model run designation	Parametrised ionisation effect on
BASE	none
SPE	HO_x, NO_x
PARAM	HO_x, NO_x, ClO_y

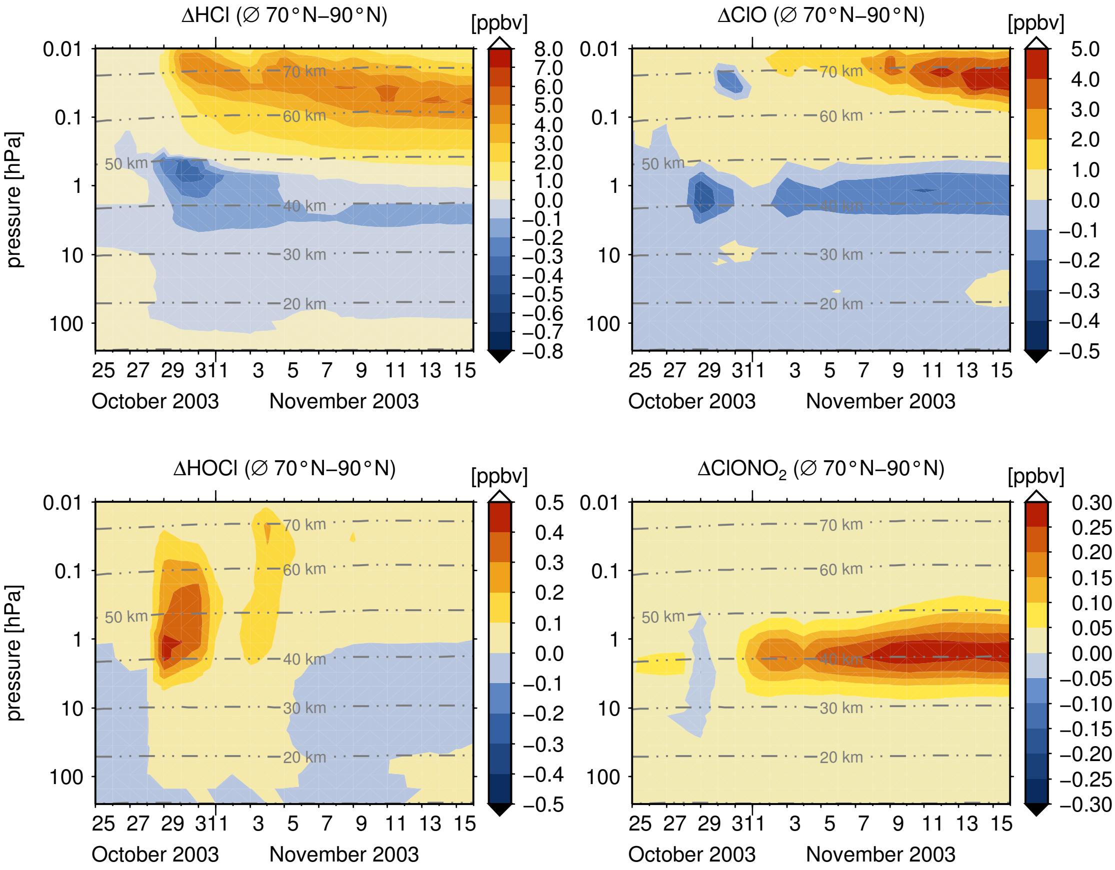

Figure 15.1 *Change in HCl and ClO (upper panel), HOCl and $ClONO_2$ (lower panel) of 70°-90° North area weighted averages for the period 25 October to 15 November 2003. The differences are calculated between the PARAM and BASE model simulations.*

15.3.1 The impact on chlorine compounds

The response of several chlorine compounds to the SPE is presented in Figure 15.1. The impact of the SPE on the chlorine compounds is calculated as the difference from the PARAM simulation to the BASE reference model scenario. As described in Section 3.5.5, there are changes in chlorine compounds to be expected due to neutral reactions with enhanced HO_x values. The increase in OH, for instance, will result in enhanced Cl values through reaction (R 3.31). Cl then reacts with O_3 via reaction (R 3.32), forming ClO, which will then react with enhanced HO_2 values through reaction (R 3.33) producing HOCl. HOCl is therefore an indicator of enhanced production of ClO. Since both HCl and ClO react with enhanced HO_x compounds, the impact on HCl and ClO is highest during the events, since HO_x species have a very short life-time and the increase in HO_x lasts only a few days, as shown before. HCl (Figure 15.1, upper panel, left figure) is decreasing with maximum values of up to 0.4 ppbv between 40-50 km, and by 0.1-0.2 ppbv down to altitudes between 35-40 km. In the mesosphere between 60-70 km, HCl is increasing with maximum values of 5-6 ppbv during and after the event and for the whole period shown. The increase in ClO by maximum values of 0.2 ppbv is restricted to altitudes above 50 km during the first event until 1 November 2003 and again by 0.1 ppbv on the second event on 3 November 2003. ClO

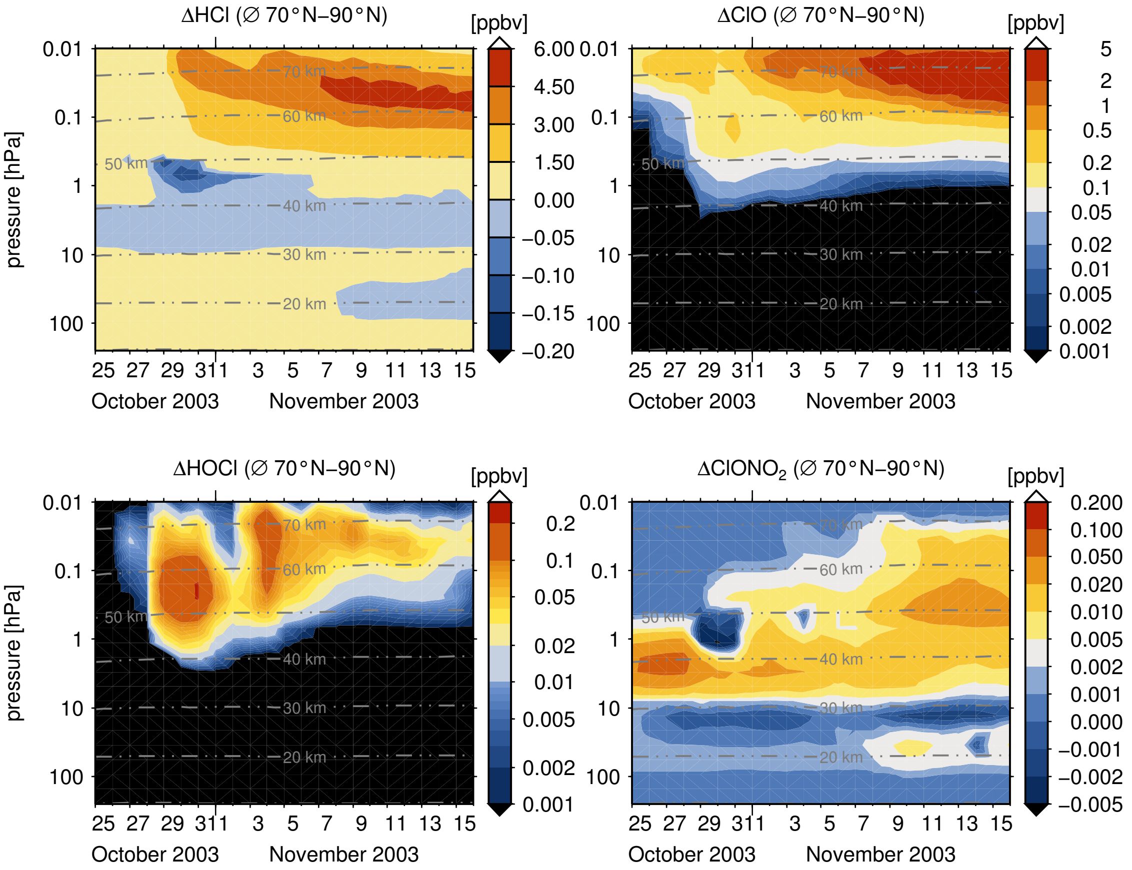

Figure 15.2 *Change in HCl and ClO (upper panel), HOCl and ClONO$_2$ (lower panel) of 70°-90° North area weighted averaged values for the period 25 October to 15 November 2003. The differences are calculated between the PARAM and SPE model simulations.*

is decreasing in altitudes between 35-50 km with maximum values of up to 0.3 ppbv during the first and second event, on which HOCl also shows the main enhancements. ClO reacts with enhanced NO$_2$ values to form ClONO$_2$. ClO is therefore decreased during the whole November with a maximum around 40-45 km and correlates to a ClONO$_2$ enhancement in the same altitudes. ClO increases, like HCl, in the mesosphere reaching increased values of 4-5 ppbv around 70 km by the middle of November 2003. ClONO$_2$ increases, starting just after the first event, and this increase reaches values of 0.1 ppbv by the middle of November with a maximum enhancement at 40 km. During the event on 28/31 October ClONO$_2$ shows a decrease of up to 0.005 ppbv and of about 0.001 ppbv in altitudes between 25-30 km. HOCl is increased by 0.4-0.5 ppbv in altitudes between 40-55 km during the first event and again by 0.1-0.2 ppbv on the second event on 3 November 2003.

15.3.2 The impact of parametrised production rates due to negative ion chemistry on chlorine compounds and ozone

The response in chlorine compounds to the parametrised chlorine production rates is presented in Figure 15.2. Values are presented as differences between the PARAM simulation and the SPE simulation without parametrised production rates for chlorine compounds. Since

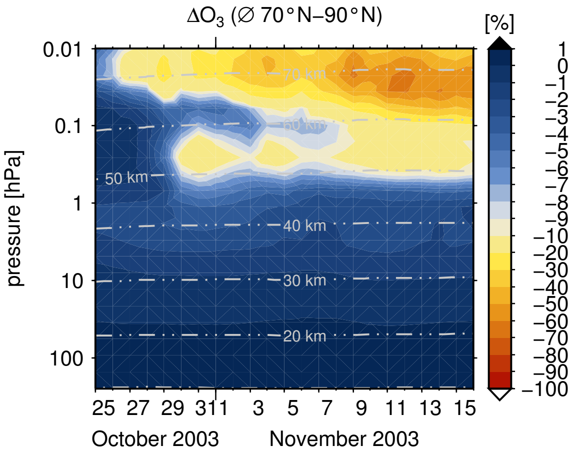

Figure 15.3 *Response in O_3 due to the parametrised production of chlorine compounds by negative ions. The difference is calculated for the PARAM simulation compared to the SPE simulation. The differences are calculated from area weighted averages between 70°-90° North.*

the parametrised production rates are dependent on ionisation rates, the highest impact is expected to be during the major events, at the end of October and beginning of November 2003. This is represented by the model simulations in all considered chlorine compounds which are directly affected by the parametrisation, HCl, ClO, and $ClONO_2$. HCl responses with an additional decrease by up to 0.15 ppbv between 40-50 km compared to the SPE simulation. Above 50 km, HCl increased by values of up to 6 ppbv until after middle of November. ClO increases by more than 0.1 ppbv above 45 km on 29 October 2003. This enhancement increases with altitude and reaches values of up to 5 ppbv until past middle of November. As a result of the enhanced ClO and HO_2 values, HOCl also increases, highest during both events and in altitudes between 40-70 km by values of up to 0.2 ppbv compared to the SPE run. HOCl stays enhanced until the middle of November. $ClONO_2$ shows an increase before, during, and after the events above 30 km and a peak increase at 50 km in the middle of November. The decrease is maximum by 0.06 ppbv at altitudes below 30 km. The maximum decrease is in accordance with the parametrised production rate for $ClONO_2$, as shown in Figure 6.5, peaking in the same altitude. Since the increase is not obviously dependent on ionisation rate, it is likely to be a response to the opposed mechanisms of production and destruction of $ClONO_2$. Above the peak in the $ClONO_2$ decrease at slightly below 30 km, enhanced ClO values due to negative ion chemistry (R 3.34) will react with enhanced NO_2 values (R 3.36), leading to the net enhancement of $ClONO_2$.

A result of the additional activation of reactive chlorine compounds is an enhanced ozone depletion, as shown in Figure 15.3. The additional depletion shows a two-layered structure. Above 60 km, an additional depletion by more than 10% starts already on 26 October 2003. In this altitude, the ozone depletion increases to 70% by the middle of November, probably due to the increase in ClO. Between 50-55 km, the decrease in ozone is between 10-20% and very pronounced during the events on 28-31 October and 3 November 2003. This decrease also stays until mid of November.

Compared to the SPE simulation, the parametrisation leads to an increase in ClO_x and a decrease in HCl compared to the neutral chlorine release. This is partitioned mainly to ClO and HOCl, with more ClO above 50 km and more HOCl between 40-70 km. For the comparison to the MIPAS observation, it is to be expected that the parametrisation affects HOCl mostly. Above 50 km, ClO should improve, however, there, the measurements are not very sensitive. Hence, a significant improvement on ClO is not expected in the comparison. This is also the case for $ClONO_2$, since it is affected only very little by the parametrisation, probably below the MIPAS detection limit.

15.4 Comparison of the model results to satellite observations

To verify the modelled results they are compared to observations by the MIPAS on-board the ENVISAT satellite. For this comparison MIPAS/IMK V3O data for the time period of 25 October to 15 November 2003 have been used. The model output corresponds to the local time of the observation. The modelled data are compared to the observations by looking at zonally averaged values of 5° latitude bins. To calculate the zonal mean, the model output is first interpolated to the altitude levels as provided in the MIPAS data set and then convolved with the averaging kernels of the instrument. The convolved data are interpolated onto a 5° latitude grid starting at 87.5°N. The zonal mean is averaged for each 5° latitude bin over all longitudes with a corresponding measurement. The MIPAS data are binned into the same latitude grid and averaged over all observed longitudes within each bin. The comparison of the zonal mean values is carried out by (i) comparing the absolute values of two different days, before and after the first major SPE, and (ii) by comparing differences of the zonal averages to the reference day 25 October 2003 as a day prior to the event on which the proton flux was around background level to verify the actual reproduction of the response to the SPE.

15.4.1 How are absolute values reproduced by the model?

First, the agreement between model and observations in terms of absolute values for NO_2, O_3, ClO, HOCl, and $ClONO_2$ are discussed. Zonally averaged volume mixing ratios before and after the major event on 28/29 October 2003 are compared. Therefore, zonal means for 25 October 2003 as the reference day and 30 October 2003 have been compared to corresponding MIPAS averages (see Figure 15.4).

The agreement of the simulated results to the observations differs for each species. The model results show a generally good agreement on both days for NO_2, O_3, and HOCl (Figure 15.4, first and second panel from above, and second panel from below). The model results for NO_2 are lower on both days than the observed values. The observations show larger values below 40 km altitude. Modelled O_3 values are a little bit higher on both days at altitudes of 35 km. For HOCl the model is slightly higher between 80°-85°N, and lower southwards of 75°N on 30 October.

MIPAS ClO values are rather difficult to compare to the reference day, since the data sets belong to different calibration periods which produces an artifact which affects mainly hard-to-retrieve species like ClO (Funke *et al.*, 2011). However, the absolute zonal mean values are presented here and they differ very much from the model simulation. The modelled values are in general much lower than the observations, even more pronounced on the 30 October at around 40 km altitude. Besides this, the modelled ClO values do not show a minimum around 80°N and a following increase towards the North Pole. Despite the underestimation in the model results, both, model and observations, show a decrease in ClO compared to

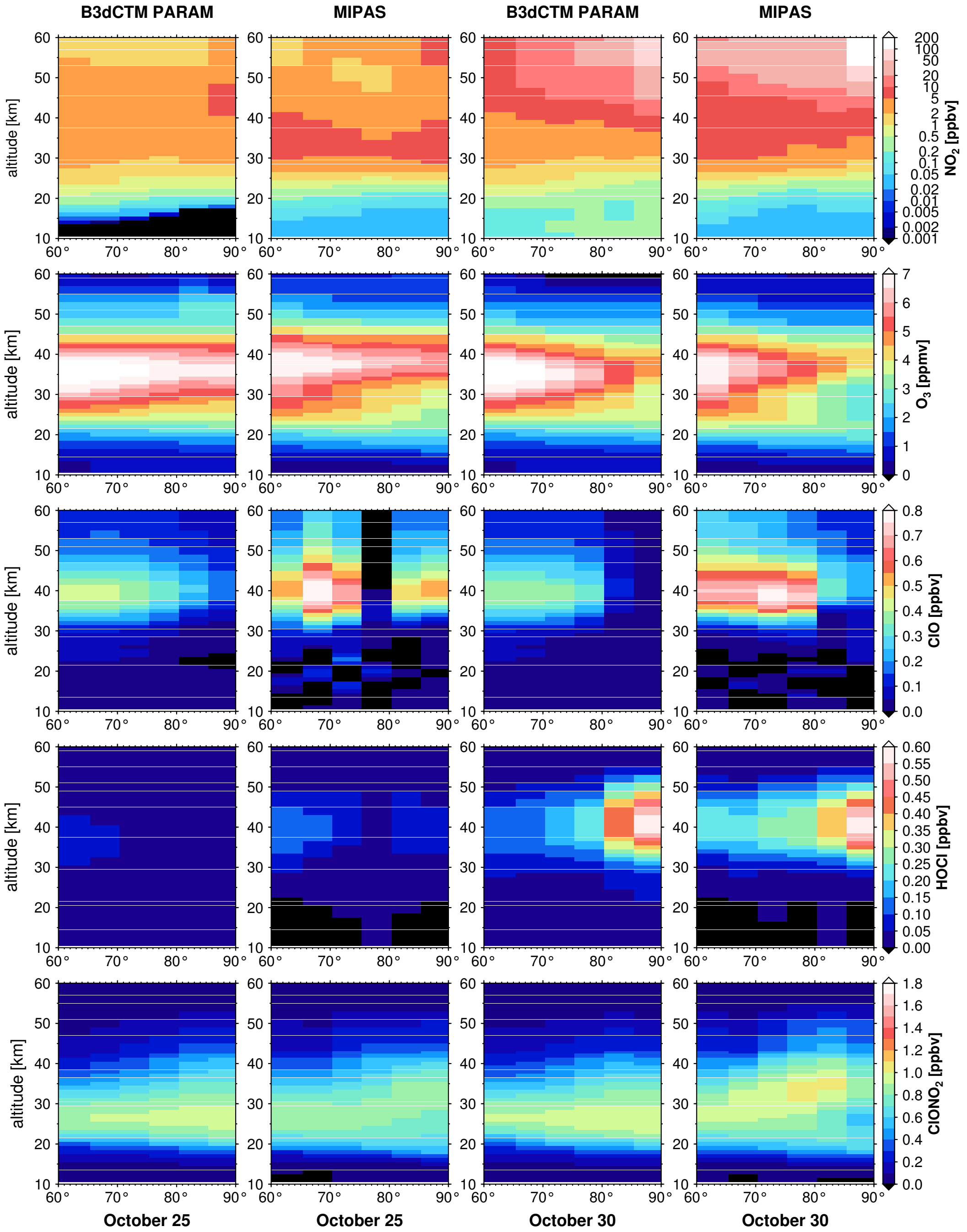

Figure 15.4 *Zonal mean absolute values for NO_2, O_3, ClO, HOCl, and $ClONO_2$ (from above) for the* PARAM *model simulation (leftmost and third panel) compared to zonal mean absolute values from MIPAS observations (second and rightmost panel). The respective two left panels show values for the reference day 25 October 2003 and the respective two right panels show values for the 30 October 2003 after the first major Solar Proton Event (SPE). All modelled values are convolved with MIPAS averaging kernels. See Section 15.4 for a detailed description, of how the model values are prepared for the comparison.*

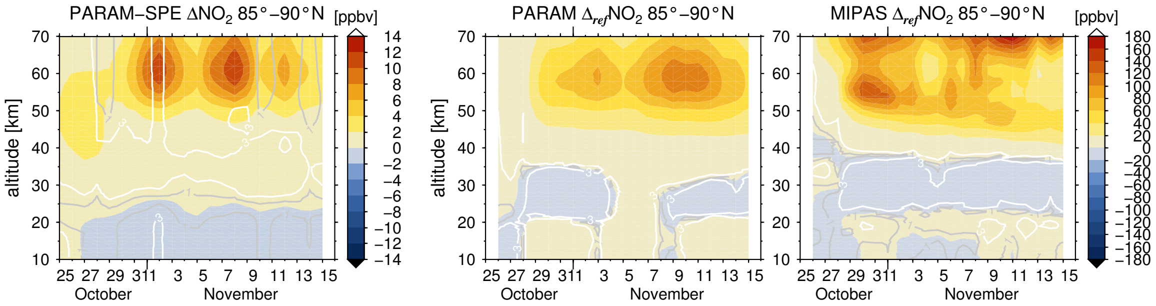

Figure 15.5 *Comparison of simulated values for NO_2 as differences from the PARAM model simulation to the SPE simulation (left panel) for the latitude bin 85-90°N. Zonally averaged simulated differences to a reference day (25 October 2003, here indicated as Δ_{ref}) for the same latitude bin with complying differences from MIPAS observations are presented in the middle and left panel, respectively. Values are shown for the period 26 October to 15 November 2003. Modelled values are convolved with MIPAS averaging kernels. The grey and white contours represent the significance level of 1σ and 3σ, respectively.*

the reference day at 40 km altitude an high latitudes. Also slightly different compared to the observations are modelled values for $ClONO_2$. The model shows generally higher values in altitudes between 20-30 km on the reference day. The values agree better in terms of absolute values on the 30 October, but differ in altitude.

Since the absolute values differ very much compared to the MIPAS observations for some compounds, the net impact of the proton precipitation will be discussed and it will be focused in the following comparisons on the differences to the reference day 25 October 2003. For completeness ClO data will be shown but the differences are probably not very robust due to different calibrations of the MIPAS data during the presented period.

15.4.2 How does the simulated net impact of the Solar Proton Event relates to the observations?

In the following section data are compared to a reference day prior to the SPE. The following comparison is based on differences of zonal means to the reference day 25 October 2003 for the period 26 October to 15 November 2003 for latitude bin 85°-90°N.

15.4.2.1 Δ_{ref} NO_2

The direct impact due to precipitating protons is a strongly increased production of NO_2. As described above, this enhancement is related to positive ion chemistry and dissociation of N_2. To validate this direct impact of the precipitating protons the modelled response in NO_2 is compared to observed MIPAS data for the period 26 October to 15 November 2003. The change in NO_2 abundance is calculated for the latitude bin 85°-90°N (Figure 15.5). As already indicated in the model results for NO_x (see Section 14.3.2), both, model and observations show a very distinct increase of NO_2 during each period of enhanced proton flux on 28/29 October and 3-5 November 2003. The difference to the reference day for each latitude are presented in the respective two right panels of Figure 15.5. The response to the SPE is of the same magnitude in the model result and the observation but the maximum values are lower in the model simulation by about 40 ppbv and peak above 55 km slightly between the peaks in the observation at 55 km and above 65 km. The downward transport during the presented period is captured in the model simulation but with a slightly weaker gradient as in the observations. Besides the lower differences in the model simulation, the time evolution of the impact on NO_2 is simulated in the model in good agreement to the observation. Both, model and observations, show maximum increases for the same days, however, in slightly different altitudes at 6 and 8 November 2003. The modelled increase in NO_2 due to proton precipitation is significant with values $> 3\sigma$ (in terms of standard deviation of the zonal mean) as indicated by the white contours in the respective middle panels of Figure 15.5. The impact of the additional parametrised chlorine production rates on NO_2 is calculated as the difference to the model simulation without this parametrisation (PARAM-SPE) and presented in the respective left panels of Figure 15.5. This difference is very small and not significant.

15.4.2.2 Δ_{ref} $ClONO_2$, Δ_{ref} ClO, and Δ_{ref} HOCl

The change in the abundance of chlorine compounds due to positive and negative ion chemistry is presented in Figure 15.6. Changes of zonal mean values for $ClONO_2$, ClO, and HOCl (upper, middle, and lower panel respectively) for the time period 25 October to 15 November 2003 are compared to observed changes by the MIPAS instrument.

The response of $ClONO_2$ to the parametrisation is small but significant ($> 3\sigma$) during the first event 29-31 October 2003 in altitudes below 30 km and leads to a decrease in $ClONO_2$ abundance. In terms of absolute values, $ClONO_2$ is slightly overestimated by the model on the reference day, and the difference to the reference day is much smaller in the model than in the MIPAS observations. It is therefore not clear from the model simulation results if the decrease in $ClONO_2$ due to the parametrisation leads to more realistic values. The same is true for ClO.

For ClO, the influence of the parametrised production of ClO during the event leads to an additional but very small increase in ClO abundance (Figure 15.6, middle panel, left figure). Compared to the MIPAS observations, ClO values are underestimated in terms of absolute values (see Figure 15.4). Although the PARAM simulation results in higher ClO values compared to the SPE run, the difference to the reference day in ClO is underestimated by the model. The model indicates a general decrease in ClO over the presented period that is not confirmed by the observations which show a highly altering response in ClO during the same time period. Since the MIPAS observations belong to two different calibrations within the presented period, the difference to the chosen reference day is not very robust. The low absolute values of ClO may also caused by too low Cl production by the parametrisation as indicated by the correlation in Figure 6.6. These too low Cl values may lead to too low values of ClO through reaction (R 3.32).

For HOCl, which is not directly affected by the additional parametrisation, the model simulation including the parametrisation agrees better to the observations than the results for the SPE run (Figure 15.6, lower panel, middle and rightmost figure), and the simulation of the PARAM run is in good agreement with the observation. The impact of the parametrised production rate due to negative ion chemistry on HOCl (Figure 15.6, lower panel, left figure) is significant ($> 3\sigma$) for the time period during the first major event 29-31 October 2003 in altitudes between 30-55 km with an increase of up to 0.2 ppbv on 30 October 2003.

The additional parametrisation of negative ion chemistry induced production rates results

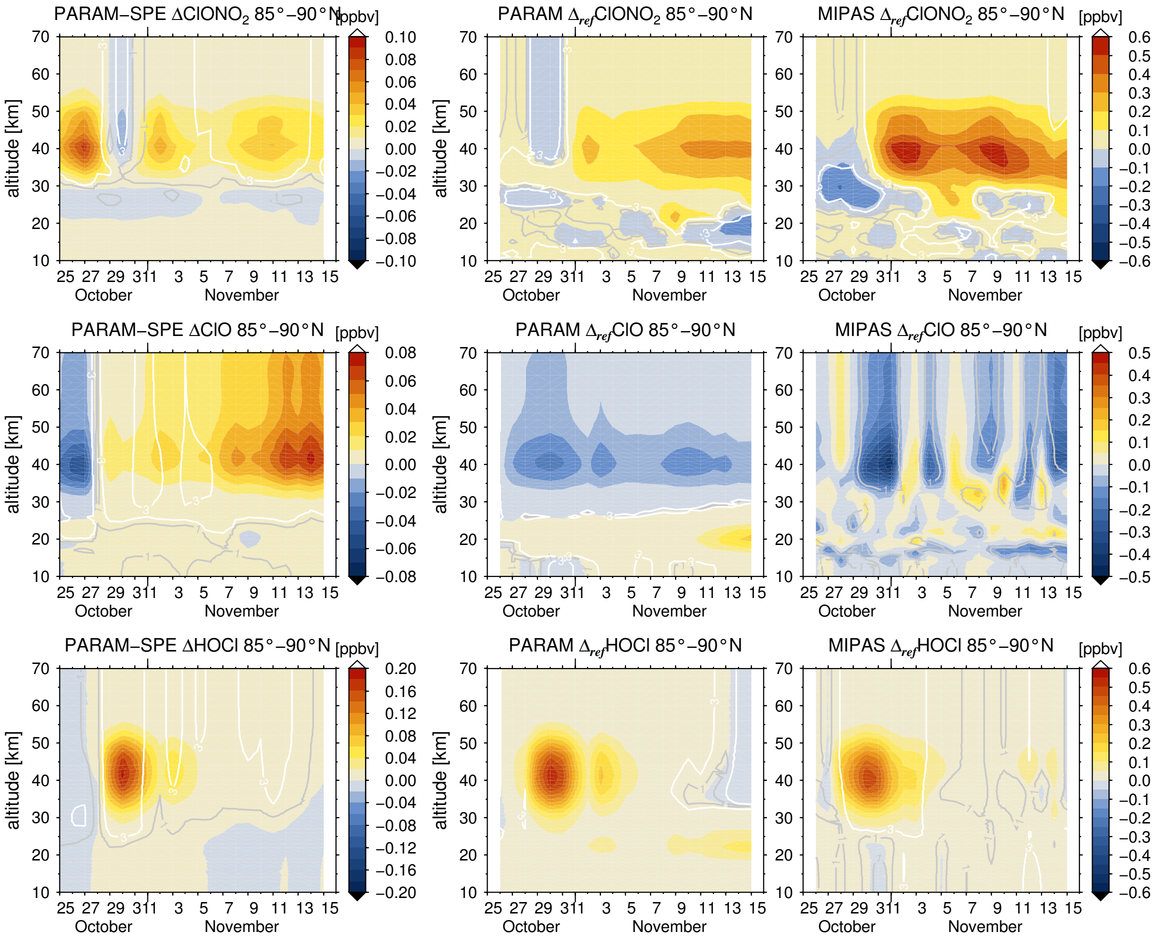

Figure 15.6 *Comparison of simulated values for $ClONO_2$ (upper panel), ClO, and HOCl (lower panel) as differences from the PARAM model simulation to the SPE simulation (left panels) for two different latitude bins (70-75°N (upper left panel) and 85-90°N (lower left panel)). Zonally averaged simulated differences to a reference day (25 October 2003, here indicated as to Δ_{ref}) for the same two latitude bins with complying differences from MIPAS observations are presented in the middle and left panels, respectively. Values are shown for the period 26 October to 15 November 2003. Modelled values are convolved with MIPAS averaging kernels. The grey and white contours represent the significance level of 1σ and 3σ, respectively.*

in a better agreement to MIPAS observations only for HOCl, but not clearly for $ClONO_2$ and ClO. Since HOCl is produced through reaction with ClO (R 3.33), the enhanced HOCl values may be the indication of increased ClO production due to the parametrisation. The underestimated difference to the reference day in ClO during the event, is probably not only due to an underestimation of the ion chemistry impact, but rather because of too low ClO abundance in terms of absolute values already before the event (see also Funke *et al.* (2011)). The higher abundance in $ClONO_2$ that is formed from the reaction of ClO with NO_2, may be the reason why there is too little absolute ClO before and during the event, resulting in too low changes in ClO during the SPE.

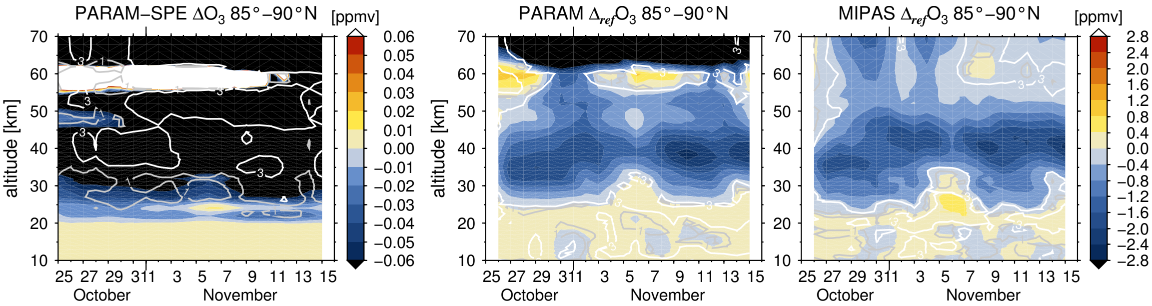

Figure 15.7 *Impact of the parametrisation on ozone. The Grey and white contours indicate the significance level of 1σ and 3σ, respectively. Ozone difference to reference day 25 October 2003 for 85°-90°N (two right panels). Modelled values are convolved with MIPAS averaging kernels.*

15.4.3 How does the additional parametrised production of chlorine species affects ozone?

Since chlorine compounds destroy ozone in catalytic cycles it is expected to get a change in ozone abundance by changes in chlorine abundances. The additional impact on ozone is presented in the left panel of Figure 15.7. A significant ozone depletion of up to 2 ppmv can be seen right after the first and second solar proton event in altitudes between 30-50 km. The impact of the solar proton event as differences to the reference day are presented in the two right panels of Figure 15.7. The values agree well with the observations in terms of amount and temporal evolution. The values of the model simulation are in good agreement to the MIPAS observations below 60 km. Above 60 km, the model shows a very high overestimation in the response in ozone. This is probably due to too high absolute values in the upper mesosphere at around 80 km, as already discussed in Section 7.2.

16 The impact of energetic particle precipitation events on radiative and chemical heating rates

16.1 Introduction

Measurements as well as model studies show that EPP events do influence atmospheric temperatures and dynamics as an indirect effect of such events. Krivolutsky *et al.* (2006) performed three-dimensional model simulations to investigate the impact of the July 2000 SPE on O_3, wind, and temperature. They show that the calculated response in O_3 in the Northern Hemisphere results in a cooling and reduced zonal winds in the region of reduced O_3 abundance. This effect is believed to be connected to the interaction between GW and the zonal mean circulation. Jackman *et al.* (2007) performed GCM simulations to study the influence on atmospheric dynamics for the SPE 2003. They found a cooling in the lower mesosphere, temperature changes of up to ±2.6 K, wind perturbation by 20-25% and that this effects last for a few weeks after the event. Seppälä *et al.* (2009) investigated ECMWF ERA 40 and operational surface air temperatures with respect to different geomagnetic activity levels (A_p index). They found a significant change in temperature compared for years with high and low A_p index by up to ±4.5 K and that geomagnetic activity has an influence on sea surface temperature. Nesse Tyssøy *et al.* (2010) found a temperature increase due to particle precipitation above 100 km. They also found a cooling effect in the mesosphere for the SPE 2003. Becker & von Savigny (2010) performed case model studies with the KMCM to investigate the heating of the polar summer mesopause during and after a SPE. They showed that this heating is a dynamical response to the temporary diabatic cooling in the lower mesosphere above the summer pole that results from the temporary O_3 depletion. They stated that the cooling results in a shift of the gravity wave drag to lower altitudes and a resulting shift of the residual circulation that results in a dynamical heating at the polar summer mesopause. Baumgaertner *et al.* (2011) did GCM model simulations about the effect on polar surface temperature due to geomagnetic activity. They found a temperature increase in the polar winter mesosphere due to a decrease in O_3 radiative cooling and a cooling below the stratopause.

The above stated temperature and dynamical changes due to EPP events that have been observed and simulated by different authors are caused by the effect on atmospheric heating rates. During an EPP event, atmospheric heating rates are affected mainly through the following processes: (i) by Joule heating in the upper mesosphere and lower thermosphere, (ii) radiative heating in the upper stratosphere and lower mesosphere due to the destruction of O_3, (iii) chemical heating because of odd hydrogen production and catalytic O_3 loss in the mesosphere, and (iv) a consequential dynamically induced adiabatic heating. The change in Joule heating and chemical heating is rather short-lived. Jackman *et al.* (2007) stated that the effect by Joule heating is not significant during even strong SPEs. The effect on the chemical heating rates involves reactions including hydrogen compounds that are only affected by the precipitating particles during the main events. The effect is therefore diminished very shortly after the event. The effect on heating rates induced by a change in UV absorption and infrared emission by O_3 can be rather long-lived and even propagate to lower altitude regions during the polar winter, since heating rates are disturbed as long as O_3 values remain affected by the enhanced HO_x and especially NO_x abundance.

16.2 Model simulations

For this study, the B3dCTM was driven with an annual cycle of meteorological data obtained from the KMCM (Section 8.2.3). This data set includes three-dimensional wind and temperature fields. As in the simulations with the LIMA data, the vertical flux is calculated from vertical wind data from the KMCM. Since this data set only represents an 'average' state of the atmosphere and not an actual time period, annual data were reused for every simulated year. The simulation has been initiated by a two dimensional model calculation with the B2dCTM (Sinnhuber *et al.*, 2003b) and were carried out for three years (2002-2004). A reference simulation has been performed with this model set up. A disturbed model calculation has been performed using the AIMOS ionisation rates due to protons for the same time period (2002-2004). Since these data can be related to an actual date, this simulation is referenced to the ionisation condition of this particular period. Since the meteorological data do not represent the 'real' atmosphere, results can not be compared to observations, or at least only quantitatively. For the period of the October/November SPE 2003 case model studies have been carried out to calculate the heating radiative rates due to solar and thermal infrared radiation and the change in chemical heating was calculated following Mlynczak & Solomon (1991), see also Section 2.4.2.

16.3 Model results

Figures 16.1 and 16.2 show the impact of the AIMOS ionisation rates in an average state atmosphere for the period 2002-2004. The impact is calculated as the difference to a reference run from area weighted averages over the 70°-90° Northern polar cap. Values for NO_x are shown in ppbv and for O_3 in percent. The white contours in Figure 16.1 represent area weighted absolute CO values to indicate the vertical transport, since atmospheric CO

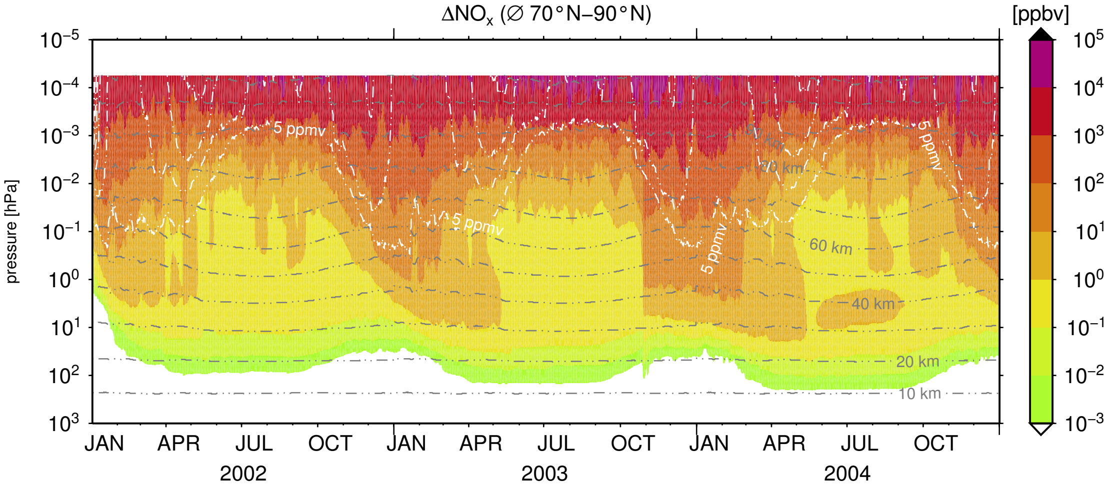

Figure 16.1 *Response in NO_x compared to a reference simulation due to ionisation rates from the Atmospheric Ionization Module Osnabrück (AIMOS). Differences are calculated from area weighted averages over 70°-90° Northern polar cap. Grey contours indicate area weighted averaged altitudes. White contours represents area weighted averaged absolute CO values to indicate the vertical transport.*

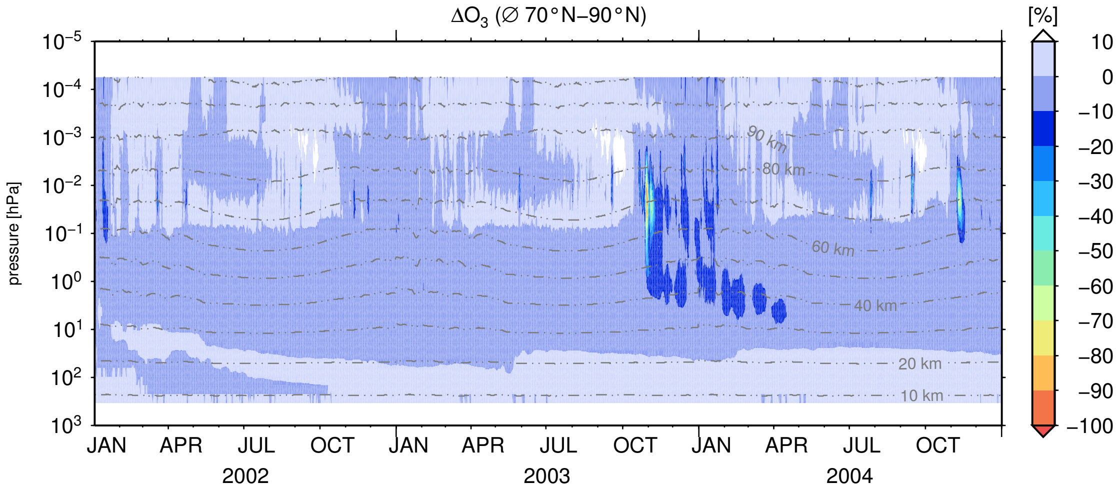

Figure 16.2 *Response in O_3 compared to a reference simulation due to ionisation rates from the Atmospheric Ionization Module Osnabrück (AIMOS). Differences are calculated from area weighted averages over 70°-90° Northern polar cap. Grey contours indicate area weighted averaged altitudes.*

is chemically rather inactive and mainly influenced by transport processes. Enhanced NO_x values that reach the stratosphere during northern polar winter are clearly related to enhanced CO values reaching into lower altitudes and, therefore, to vertical transport processes during this period, as in all winter periods starting around October. A very pronounced increase in NO_x in October 2003 due to enhanced ionisation rates and the subsequent NO_x downward transport in the following winter is also captured as expected in the model simulation and can be qualitatively compared to the simulations with the meteorological data obtained from LIMA. A main difference compared to the model simulations based on the 'real' meteorological data input is, for instance, the missing stratospheric warming event and breakup of the polar vortex in December 2003. This would influence the downward transport of NO_x into the lower stratosphere that in reality ended by middle of December (e.g. Figure 12.6).

Figure 16.2 shows the percentage change in O_3 due to the ionisation rates. It is qualitatively comparable to the simulations with LIMA data. But for the same reasons as for NO_x, the missing stop of downward transport in December, the O_3 depletion is in this model simulations longer lasting as in the 'real' modelled case. This study has the purpose to qualitatively quantify the response in heating rates in a 'realistic' disturbance scenario. When compared to the model simulation with the LIMA data, these case simulation results give reasonably response to the disturbance of the ionisation rates.

16.3.1 Radiative heating rates

As described in Section 2.4, the main heating in the stratosphere is driven by absorption of solar radiation by O_3. As O_3 is decreasing significantly during particle precipitation events, the heating rate in the stratosphere is also expected to decrease. Figure 16.3 shows the change in radiative heating rates with respect to the reference simulation after the event on 31 October as zonal averages for the radiative heating rates due to thermal infrared (left

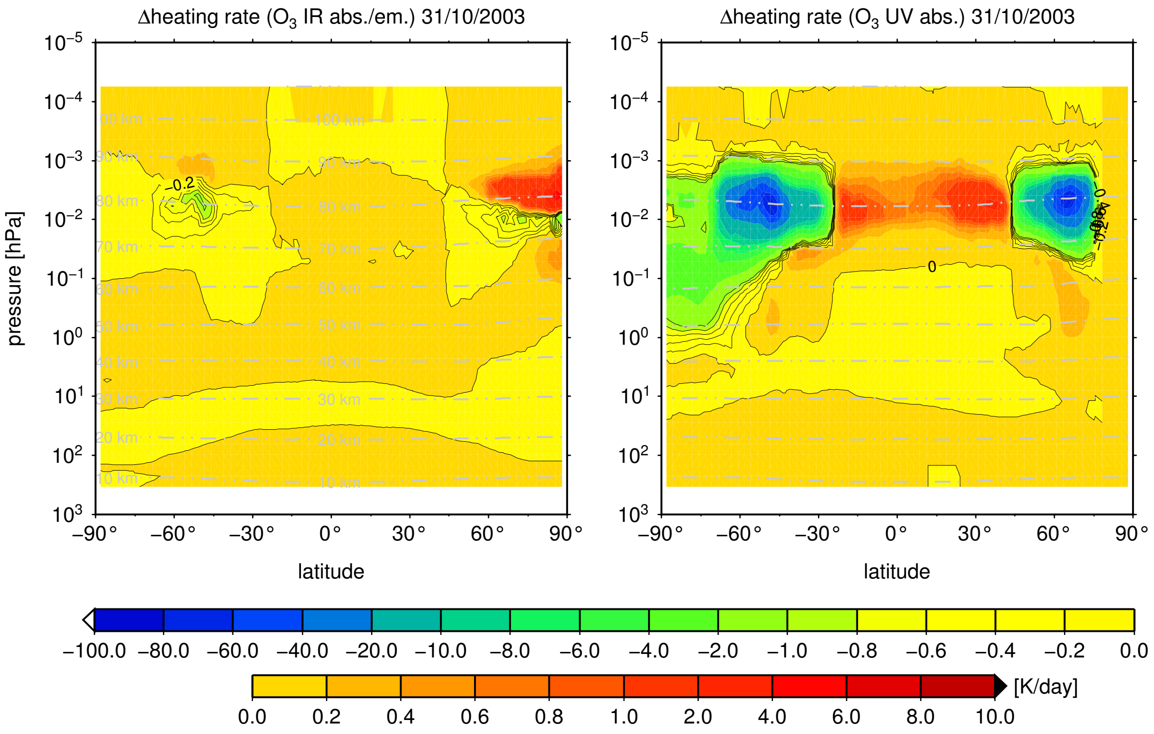

Figure 16.3 *Zonal mean change in radiative heating rates due to change in absorption of UV (upper panel) and IR (lower panel) radiation by O_3 after the Solar Proton Event (SPE) 2003 event on 31 October 2003 0 UTC.*

panel) and solar UV (right panel) radiation. The presented differences in both radiative heating rates is solely due to the change in O_3, since O_3 is the only variable compound in the calculation for the heating rates that is calculated on-line. A climatology, for instance for CO_2 is used for other involved trace gases. The presented values are differences calculated as SPE-BASE.

In high northern latitudes, in the absence of sunlight, the change in O_3 has no influence on the radiative heating rates due to solar UV radiation. This change is only pronounced in the sun lit latitude regions equatorward of approx. 70°N. Heating rates change very strongly in altitudes around 80 km with increasing heating rates in the tropics between 30°S and 45°N, and decreasing heating rates in northern mid latitudes and mid and high southern latitudes. These changes correspond to the relative decrease in O_3 at the same altitude and latitudes (see Figure 12.12). Since O_3 is decreased, it absorbs less solar UV radiation but also emits less thermal radiation which leads to a change in the heating rates that is negative.

The change in heating rates due to thermal infrared radiation is shown in the left panel of Figure 16.3. Lower O_3 values absorb less thermal radiation, so when O_3 is decreased due to the ionisation, the change in heating rates is negative. This is visible just above 70 km with negative heating rate changes in high northern latitudes. Above and below are areas of positive heating rate changes which might be due to less thermal radiation below and above is absorbed and can penetrate to higher or lower altitudes.

Figure 16.4 shows the change in infrared radiation by O_3 as differences of area weighted averages for the October/November SPE 2003 period. The main change in heating rates is

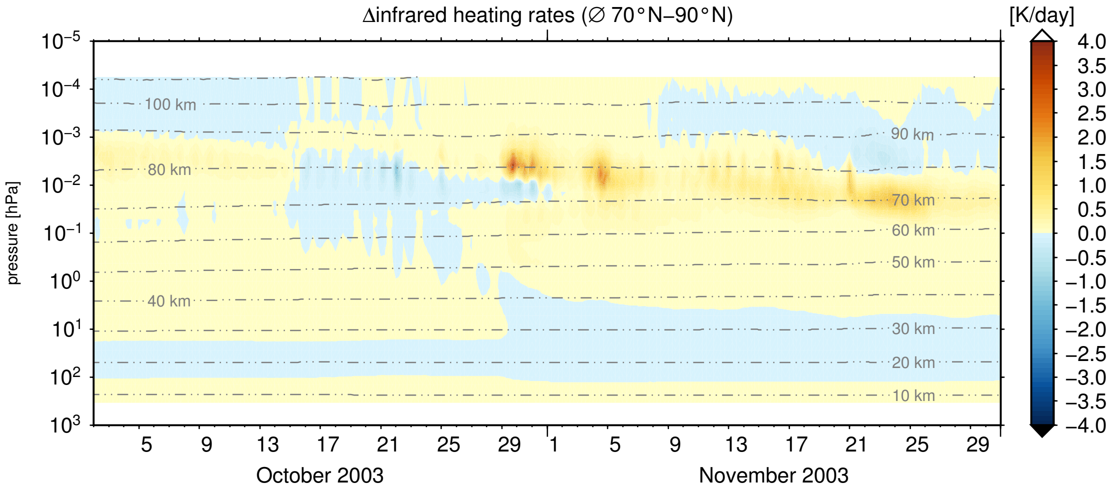

Figure 16.4 *Area weighted averaged differences in radiative heating rates due to infrared absorption and emission by O_3 during ionisation condition equivalent to the Solar Proton Event (SPE) 2003.*

in the altitude region between 60-90 km. In general a positive difference to the undisturbed reference run is calculated in the first half of October (before the onset of precipitating protons) and again from the beginning of November. In the period of enhanced ionisation rates, at the end of October, the difference in heating rates due to infrared radiation is negative. During the events and already starting in the middle of October, the change in absorption and emission of infrared radiation by O_3 leads to more cooling in the MLT region.

16.3.2 Chemical heating rates

The chemical heating rates due to exothermic reactions involving odd hydrogen and oxygen are calculated as described in Section 2.4.2 based on Mlynczak & Solomon (1991).

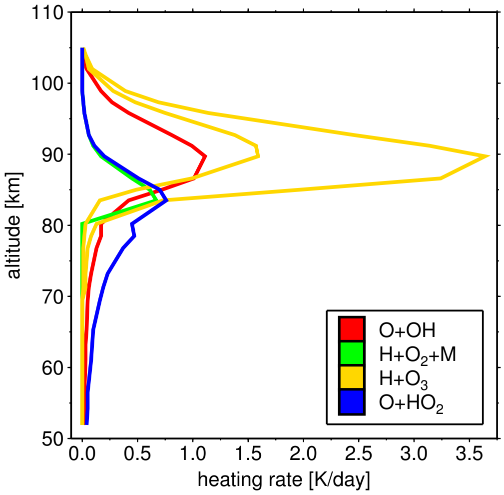

Figure 16.5 *Chemical heating rates for different exothermic reactions involving hydrogen compounds. Data taken from Mlynczak & Solomon (1991)*

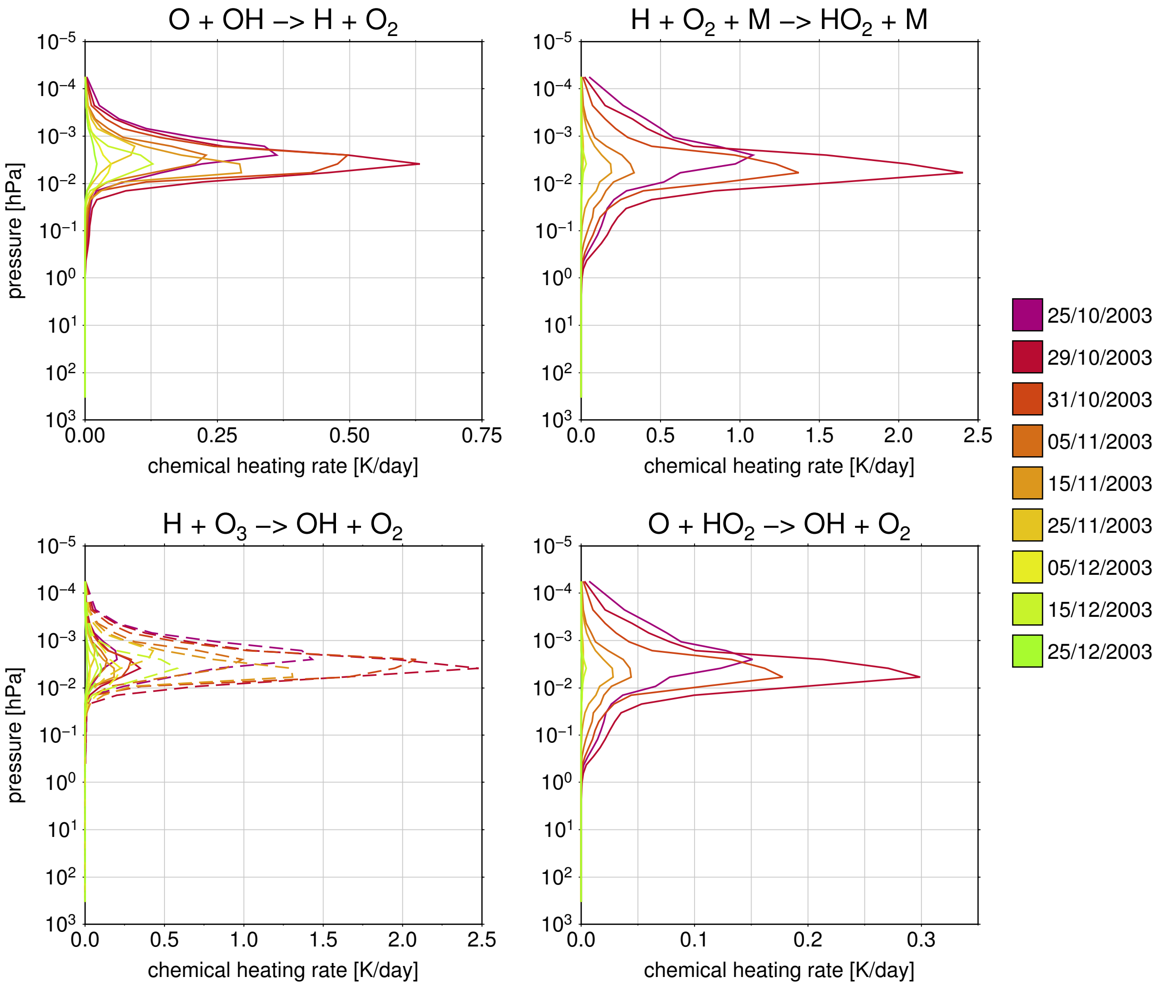

Figure 16.6 *Chemical heating rates the four different exothermic reactions* $O + OH \longrightarrow H + O_2$ *(upper left panel),* $H + O_2 + M \longrightarrow HO_2 + M$ *(upper right panel),* $H + O_3 \longrightarrow OH + O_2$ *(lower left panel), and* $O + HO_2 \longrightarrow OH + O_2$ *(lower right panel) for different days during ionisation condition equivalent to the Solar Proton Event (SPE) 2003.*

Figure 16.5 shows daily averaged global chemical heating rates for different exothermic reactions involving odd hydrogen compounds. The highest contribution is due to the reaction $H + O_3 \longrightarrow OH + H_2$. The amount of heat of this reaction is very dependent on how many OH molecules will be in the excited states.

In Figure 16.6 simulated chemical heating rates are displayed for different reactions ($O + OH \longrightarrow H + O_2$, $H + O_2 + M \longrightarrow HO_2 + M$, $H + O_3 \longrightarrow OH + O_2$, and $O + HO_2 \longrightarrow OH + O_2$). Each panel shows vertical profiles for different days during ionisation conditions equivalent to the SPE 2003. These absolute values are comparable to values by Mlynczak & Solomon (1991). The values are in the same order of magnitude and show the same peak height at around 80 km. The values are not directly comparable, since they are averaged differently.

For every reaction, the heating rate increases after the first event on 28/29 October 2003. After this increase, it decreases to values even below the 25 October indicating, that values on the 25 October are already enhanced due to the particle precipitation. The disturbance in the chemical heating rate is therefore rather short, which is due to the short effect in the involving odd hydrogen compounds, as described in Section 12.2.

17 Summary, Conclusions & Outlook

The impact of precipitating particles on the chemical composition of the atmosphere has been investigated on the basis of model simulations. Especially the impact on HO_x, NO_x, and ozone has been studied regarding the following questions:

- The response of the chemical composition in the middle and upper atmosphere to Energetic Particle Precipitation (EPP) events, as given by a chemistry and transport model of the middle and upper atmosphere, the Bremen 3-dimensional Chemistry and Transport Model (B3dCTM).
- The different impacts of EPP events with different strengths and during different time periods in the Northern Hemisphere.
- The individual impacts of the different particle populations (proton and electron precipitation) and the impact of the top height of the employed model version.
- The impact of negative ion chemistry on the activation of reactive chlorine compounds.
- The impact on heating rates and possibly on dynamics.

To investigate the above stated questions, model simulations for the time period 2002-2009 have been carried out driven by atmospheric ionisation rates as induced by EPP events. To consider all aspects of EPP events, the B3dCTM which covered in its basic version only the stratosphere, has been extended to the mesosphere and lower thermosphere, through

- the implementation of three-dimensional ionisation rates from the Atmospheric Ionization Module Osnabrück (AIMOS) that were available for the period 2002-2010,
- the implementation of meteorological data derived from the Leibniz-Institute Middle Atmosphere (LIMA) model for the period 2002-2010 and
- the exchange of the vertical coordinate and the change in the calculation of the vertical flux to extent the vertical grid of the B3dCTM to the lower thermosphere,
- the improvement of the chemistry of the B3dCTM in the upper stratosphere and Mesosphere and Lower Thermosphere (MLT) by resolving O_x and NO_x families in the family approach of the chemical code.

These further model developments of the B3dCTM improved the model resulting in a modelling tool that is suitable to simulate the chemical composition and the impact of EEP events on the stratosphere and MLT region. Comparisons to previous studies by, e.g. López-Puertas *et al.* (2005, 2006), Jackman *et al.* (2005b), Rohen *et al.* (2005), as well as to observations from the Michelson Interferometer for Passive Atmospheric Sounding (MIPAS) instrument during the very strong SPE 2003 show that the model does capture the chemical impact of the EPP events reasonable well. This is also due to the implementation of appropriate ionisation rates and meteorological data.

The direct impact of the precipitating protons has been investigated and compared to model results that include both particle populations. The following different model results can be summarised. The direct impact on HO_x due to proton precipitation in the stratosphere and lower mesosphere is in general similar to the impact simulated including the electron precipitation during the strong proton flux on 28-31 October and 3 November, but with slightly lower increases in HO_x above 80 km. The major difference in the impact that arises from the electrons on HO_x when the proton flux is lower before, between, and after the events. This is even more pronounced when looking at the relative impact on HO_x, that shows the main additional impact of the electrons in the stratosphere and mesosphere between 40-70 km. For NO_x, significantly more is formed at altitudes above 50 km, if both the proton and electron precipitations are considered. After the events, less NO_x is transported into lower altitudes when only proton precipitation is considered. A very significant difference in the impact is resulting in the ozone depletion between 50-70 km. Up to 30% less ozone depletion is simulated when only protons are considered.

The comparison of the results for the different model versions of the B3dCTM indicates the importance of the upper model top height in the study of EPP events to address the following questions:

- the direct impact on HO_x and NO_x abundance in the stratosphere and lower mesosphere,
- the direct impact of NO_x in the upper mesosphere and lower thermosphere,
- an overestimated or non existing direct impact of precipitating electrons on the lower mesosphere and stratosphere.

The simulation results from the basic stratospheric version show that this model overestimates the produced amount of NO_x in the upper stratosphere and lower mesosphere and thus overestimates the amount of NO_x that is transported to the middle and lower stratosphere. This leads to a too large ozone depletion in the stratosphere. However, the low top height model does not include the downward transport of NO_x and NO produced in the MLT region. The overestimation in the stratosphere and lower mesosphere was also stated in Funke *et al.* (2011). They stated that the family approach of the stratospheric B3dCTM version is a possible reason for the too high NO_x production during the SPE 2003. They also stated that the family approach alone is not sufficient enough to explain the overestimated impact on NO_x in the stratosphere. Too high ionisation rates due to the electron precipitation could be another reason, as a case simulation with the WACCM CCM that only considers ionisation rates due to protons also indicates (Funke *et al.*, 2011). Following the investigations based on observations by Funke *et al.* (2005, 2011) and López-Puertas *et al.* (2006), electron precipitations are not expected to have a direct effect in the stratosphere: their effect on the stratosphere is always indirect, and hence, related to transport processes from altitudes above. In Wissing *et al.* (2010) a direct impact of electron precipitating was investigated with results from the stratospheric B3dCTM. A recalculation has been performed with the extended model in this investigation. Both model versions show a direct impact of electron precipitation in the stratosphere which, however, is larger in the stratospheric version of the model. A case model simulation with the extended model version that neglect all ionisation due to electrons below approx. 70 km show a very similar result, so the direct impact of the electrons appears to be small in the stratosphere. This may indicate, that these larger values are also because of transport processes of an possibly overestimated production in the mesosphere due to too high ionisation rates for electrons there. First results within the HEPPA 2 initiative that investigates the indirect effect of transported NO into the stratosphere from above after a SSW suggest that the production of NO is overestimated due to an uncertainty in the ionisation rates derived from the AIMOS model. Further studies are under investigation.

Model simulations for the October/November 2003 SPE have been performed to investigate a parametrisation of production rates to account for the impact of negative ion chemistry during a SPE on neutral chlorine compounds. A clear improvement by the parametrisation as compared to observations can be determined for HOCl. The impact on the abundance of ClO is small and the modelled response to the SPE is underestimated still, probably because of too low ClO abundances in terms of absolute values before and during the event. Therefore, the response to the SPE is too low in general, because of too low available ClO. The opposite is probably true for $ClONO_2$, showing too high absolute values and too little response to the SPE itself and also to the parametrisation. ClO and $ClONO_2$ show changes in the expected way during the presented period, but these changes are too small. HOCl values agree to the observations on both days, before and during the event, in absolute values and in the response to the SPE. Thus, for HOCl, the parametrisation derived from the UBIC model leads to values that are more in agreement to observations for high latitudes then without. The discrepancy in the agreement of the absolute values for ClO and $ClONO_2$ in the model has to be investigated further in more detail.

A case model study with the B3dCTM driven by meteorological date from the Kühlungsborn Mechanistic general Circulation Model (KMCM) GCM has been performed to investigate the influence on low ozone values during EPP events on atmospheric radiative and chemical heating rates. Results show a change in radiative heating due to the disturbed absorption of infrared radiation of up to 4 K per day in an altitude of 70-80 km over the norther polar cap. In the stratosphere the simulated changes in the heating rates are comparable to Jackman *et al.* (2007). The cooling in the lower mesosphere by Becker & von Savigny (2010) above the summer pole is also captured in the model result with an additional cooling of a few K per day above 50 km. However, the impact on radiative heating rates due to less absorption of UV radiation due to the depletion of ozone as a results of the EPP event is quite large in the upper mesosphere at around 80 km south of terminator (approx. <70°N). This is probably due to a still overestimated ozone abundance in the model results at 80-90 km. A possible reason is the steady state solution of the HO_x family in the chemical code of the B3dCTM and further model developments are needed to improved ozone chemistry in the MLT. The effect of increased HO_x values results in increasing heating rates due to exothermic reactions. Calculated chemical heating rates for different exothermic reactions show enhanced values during the SPE event 28/31 October 2003 between 0.2-2 K per day, depending on the reaction.

Appendix

Fundamentals

1 Spectrum of electromagnetic radiation

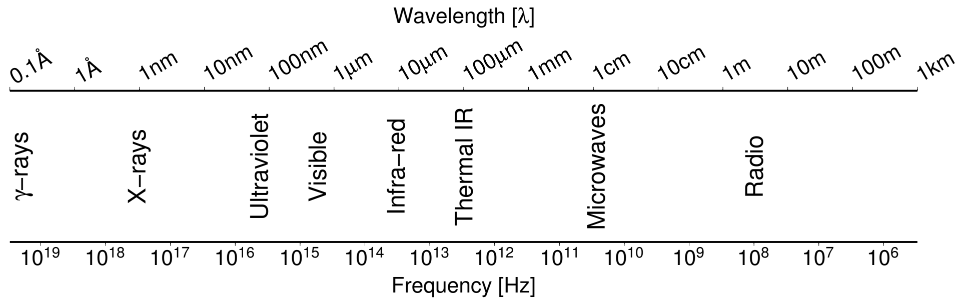

Figure 1 *Spectrum of electromagnetic radiation*

2 Taylor series expansion

$$N_{i,t} = N_{i,t-h} + h\frac{dN_{i,t-h}}{dt} + \frac{h^2}{2}\frac{d^2N_{i,t-h}}{dt^2} + \frac{h^3}{6}\frac{d^3N_{i,t-h}}{dt^3} + \dots \qquad (.1)$$

Chemical and photo chemical reactions of the B3dCTM

1	$O + O + M$	$\longrightarrow$	$O_2 + M$
2	$O + O_2 + M$	$\longrightarrow$	$O_3 + M$
3	$O + O_3$	$\longrightarrow$	$2\,O_2$
4	$O(^1D) + O_3$	$\longrightarrow$	$2\,O_2$
6a	$O(^1D) + N_2$	$\longrightarrow$	$O + N_2$
6b	$O(^1D) + O_2$	$\longrightarrow$	$O + O_2$
7	$O(^1D) + H_2O$	$\longrightarrow$	$2\,OH$
8	$OH + O$	$\longrightarrow$	$H + O_2$
9	$O_2 + H + M$	$\longrightarrow$	$HO_2 + M$
10	$HO_2 + O$	$\longrightarrow$	$OH + O_2$
11	$OH + O_3$	$\longrightarrow$	$HO_2 + O_2$
12	$H + O_3$	$\longrightarrow$	$OH + O_2$
13	$OH + HO_2$	$\longrightarrow$	$H_2O + O_2$
14	$OH + OH$	$\longrightarrow$	$H_2O + O$
14b	$OH + OH + M$	$\longrightarrow$	$H_2O_2 + M$
15a	$H + HO_2$	$\longrightarrow$	$OH + OH$
15b	$H + HO_2$	$\longrightarrow$	$H_2 + O_2$
15c	$H + HO_2$	$\longrightarrow$	$H_2O + O$
16	$NO_2 + O$	$\longrightarrow$	$NO + O_2$
17	$NO + O_3$	$\longrightarrow$	$NO_2 + O_2$
18	$NO_2 + O_3$	$\longrightarrow$	$O_2 + NO_3$
20	$HNO_3 + OH$	$\longrightarrow$	$H_2O + NO_3$
21	$NO_2 + OH + M$	$\longrightarrow$	$HNO_3 + M$
22a	$O(^1D) + N_2O$	$\longrightarrow$	$2\,NO$
22b	$O(^1D) + N_2$	$\longrightarrow$	$N_2 + O_2$
24	$HO_2 + HO_2$	$\longrightarrow$	$H_2O_2 + O_2$
26	$H_2O_2 + OH$	$\longrightarrow$	$H_2O + HO_2$
29	$H_2O_2 + \text{rain}$	$\longrightarrow$	
30	$OH + CH_4$	$\longrightarrow$	$H_2O + CH_3$
31a	$O(^1D) + CH_4$	$\longrightarrow$	$CH_3 + OH$
31b	$O(^1D) + CH_4$	$\longrightarrow$	$CH_2O + H_2$
32	$O(^1D) + H_2$	$\longrightarrow$	$H + OH$
34	$CO + OH$	$\longrightarrow$	$CO_2 + H$
35	$NO + HO_2$	$\longrightarrow$	$NO_2 + OH$
36	$HO_2 + O_3$	$\longrightarrow$	$OH + 2\,O_2$
37	$HO_2 + NO_2 + M$	$\longrightarrow$	$HO_2NO_2 + M$
38	$HNO_3 + \text{rain}$	$\longrightarrow$	
39	$HO_2NO_2 + M$	$\longrightarrow$	$HO_2 + NO_2 + M$
40	$HO_2NO_2 + OH$	$\longrightarrow$	$H_2O + O_2 + NO_2$
41	$HO_2NO_2 + \text{rain}$	$\longrightarrow$	
48	$O(^1D) + CFCl_3$	$\longrightarrow$	$2\,Cl + COFCl$
49	$O(^1D) + CF_2Cl_2$	$\longrightarrow$	$2\,Cl + COF_2$
50	$Cl + O_3$	$\longrightarrow$	$ClO + O_2$

51	$ClO + O$	$\longrightarrow$	$Cl + O_2$
52	$Cl + H_2O_2$	$\longrightarrow$	$HCl + HO_2$
53	$ClONO_2 + OH$	$\longrightarrow$	$HOCl + NO_3$
54	$ClONO_2 + Cl$	$\longrightarrow$	$2\,Cl + NO_3$
55	$ClO + NO$	$\longrightarrow$	$Cl + NO_2$
57	$Cl + CH_4$	$\longrightarrow$	$HCl + CH_3$
58	$Cl + H_2$	$\longrightarrow$	$HCl + H$
59	$Cl + HO_2$	$\longrightarrow$	$HCl + O_2$
59b	$Cl + HO_2$	$\longrightarrow$	$OH + ClO$
60	$OH + HCl$	$\longrightarrow$	$H_2O + Cl$
61	HCl + rain	$\longrightarrow$	
61	HBr + rain	$\longrightarrow$	
61	HF + rain	$\longrightarrow$	
62	$ClO + NO_2 + M$	$\longrightarrow$	$ClONO_2 + M$
63	$ClONO_2 + O$	$\longrightarrow$	$ClO + NO_3$
64b	$Cl + HOCl$	$\longrightarrow$	$HCl + ClO$
65	$HO_2 + ClO$	$\longrightarrow$	$HOCl + O_2$
65b	$HO_2 + ClO$	$\longrightarrow$	$HCl + O_3$
66	$OH + HOCl$	$\longrightarrow$	$H_2O + ClO$
67	$O + HOCl$	$\longrightarrow$	$OH + ClO$
68	$ClO + ClO + M$	$\longrightarrow$	$Cl_2O_2 + M$
68b	$ClO + ClO$	$\longrightarrow$	$2\,Cl + O_2$
68c	$ClO + ClO$	$\longrightarrow$	$Cl + OClO$
69	$Cl_2O_2 + M$	$\longrightarrow$	$ClO + ClO + M$
70	$N + NO$	$\longrightarrow$	$N_2 + O$
71	$N + O_2$	$\longrightarrow$	$NO + O$
72	$N + O_3$	$\longrightarrow$	$NO + O_2$
75a	$OH + ClO$	$\longrightarrow$	$Cl + HO_2$
75b	$OH + ClO$	$\longrightarrow$	$HCl + O_2$
77	$Cl_2O_2 + Cl$	$\longrightarrow$	$3\,Cl + O_2$
80	$O(^1D) + CCl_4$	$\longrightarrow$	$4\,Cl$ + products
81	$O(^1D) + CH_3Cl_3$	$\longrightarrow$	$3\,Cl$ + products
82	$OH + CH_3Cl_3$	$\longrightarrow$	$3\,Cl$ + products
83	$O(^1D) + CH_3Cl$	$\longrightarrow$	Cl + products
84	$OH + CH_3Cl$	$\longrightarrow$	Cl + products
85	$O(^1D) + CF_2ClH$	$\longrightarrow$	$Cl + COF_2$ + products
86	$OH + CF_2ClH$	$\longrightarrow$	$Cl^{+}COF_2$ + products
87	$O(^1D) + C_2F_3Cl_3$	$\longrightarrow$	$2\,Cl + COF_2 + COFCl$ + products
91	$NO_2 + NO_3 + M$	$\longrightarrow$	$N_2O_5 + M$
92	$N_2O_5 + M$	$\longrightarrow$	$NO_3 + NO_2 + M$
94	$NO_3 + NO$	$\longrightarrow$	$NO_2 + NO_2$
95	$NO_3 + O$	$\longrightarrow$	$NO_2 + O_2$
100	$CH_3 + O_2 + M$	$\longrightarrow$	$CH_3O_2 + M$
101	$CH_3O_2 + NO$	$\longrightarrow$	$CH_3O + NO_2$
102	$CH_3O_2 + HO_2$	$\longrightarrow$	$CH_3OOH + O_2$
103	$CH_3O_2 + CH_3O_2$	$\longrightarrow$	$2\,CH_3O + O_2$

104a	$CH_3OOH + OH$	$\longrightarrow$	$CH_3O_2^{+}H_2O$
104b	$CH_3OOH + OH$	$\longrightarrow$	$CH_2O + OH + H_2O$
105	$CH_3O + O_2$	$\longrightarrow$	$CH_2O + HO_2$
106	$CH_2O + OH$	$\longrightarrow$	$CHO + H_2O$
107	$CH_2O + O$	$\longrightarrow$	$CHO + OH$
108	$HCO + O_2$	$\longrightarrow$	$CO + HO_2$
109	$H_2 + OH$	$\longrightarrow$	$H_2O + H$
110	$CH_2O + Cl$	$\longrightarrow$	$CHO + HCl$
112	$CH_2O + \mathrm{rain}$	$\longrightarrow$	
113	$CH_3OOH + \mathrm{rain}$	$\longrightarrow$	
114	$CH_3O_2 + ClO$	$\longrightarrow$	$CH_3O + Cl + O_2$
120	$Br + O_3$	$\longrightarrow$	$BrO + O_2$
121	$BrO + O$	$\longrightarrow$	$Br + O_2$
123	$BrO + NO$	$\longrightarrow$	$Br + NO_2$
124	$BrO + OH$	$\longrightarrow$	$Br + HO_2$
125a	$BrO + ClO$	$\longrightarrow$	$Br + OClO$
125b	$BrO + ClO$	$\longrightarrow$	$Br + Cl + O_2$
125c	$BrO + ClO$	$\longrightarrow$	$BrCl + O_2$
127	$BrO + BrO$	$\longrightarrow$	$Br + Br + O_2$
128	$BrO + NO_2 + M$	$\longrightarrow$	$BrONO_2 + M$
130	$BrO + HO_2$	$\longrightarrow$	$HOBr + O_2$
130b	$BrO + HO_2$	$\longrightarrow$	$HBr + O_3$
131	$O + HOBr$	$\longrightarrow$	$OH + BrO$
134	$Br + CH_2O$	$\longrightarrow$	$HBr + CHO$
135	$Br + HO_2$	$\longrightarrow$	$HBr + O_2$
136	$HBr + OH$	$\longrightarrow$	$Br + H_2O$
137	$HBr + O(^1D)$	$\longrightarrow$	$Br + OH$
138	$CBrClF_2 + O(^1D)$	$\longrightarrow$	$Br + Cl + 2\,F + \mathrm{products}$
139	$HBr + O$	$\longrightarrow$	$Br + OH$
140	$O(^1D) + CBrF_3$	$\longrightarrow$	$Br + 3\,F + \mathrm{products}$
142	$OH + CH_3Br$	$\longrightarrow$	$Br + \mathrm{products}$
143	$O(^1D) + CH_3Br$	$\longrightarrow$	$Br + \mathrm{products}$
145	$BrONO_2 + O$	$\longrightarrow$	$BrO + NO_3$
146	$BrONO_2 + Br$	$\longrightarrow$	$2\,Br + NO_3$
150	$N_2O_5(g) + H_2O(f)$	$\longrightarrow$	$2\,HNO_3(f)$
151	$ClONO_2(g) + H_2O(f)$	$\longrightarrow$	$HOCl(g) + HNO_3(f)$
152	$ClONO_2(g) + HCl(f)$	$\longrightarrow$	$2\,Cl(g) + HNO_3(f)$
153	$N_2O_5(g) + HCl(f)$	$\longrightarrow$	$Cl(g) + NO_2(g) + HNO_3(f)$
154	$HOCl(g) + HCl(f)$	$\longrightarrow$	$2\,Cl(g) + H_2O(f)$
155	$HOBr(g) + HBr(f)$	$\longrightarrow$	$2\,Br(g) + H_2O(f)$
156	$HOBr(g) + HCl(f)$	$\longrightarrow$	$BrCl(g) + H_2O(f)$
157	$HOCl(g) + HBr(f)$	$\longrightarrow$	$BrCl(g) + H_2O(f)$
158	$BrONO_2(g) + HBr(f)$	$\longrightarrow$	$2\,Br(g) + HNO_3(f)$
159	$BrONO_2(g) + HCl(f)$	$\longrightarrow$	$BrCl(g) + HNO_3(f)$
160	$ClONO_2(g) + HBr(f)$	$\longrightarrow$	$BrCl(g) + HNO_3(f)$
161	$BrONO_2(g) + H_2O(f)$	$\longrightarrow$	$HOBr(g) + HNO_3(f)$

162	$N_2O_5(g) + HBr(f)$	$\longrightarrow$	$Br(g) + NO_2 + HNO_3(f)$
180	$O(^1D) + COF_2$	$\longrightarrow$	$2\,HF$ + products
181	$O(^1D) + COFCl$	$\longrightarrow$	$Cl + HF$ + products
J_2	$O_2 + h\nu$	$\longrightarrow$	$O + O$
J_{3a}	$O_3 + h\nu$	$\longrightarrow$	$O(^1D) + O_2$
J_3	$O_3 + h\nu$	$\longrightarrow$	$O(^3P) + O_2$
J_{NO}	$NO + h\nu$	$\longrightarrow$	$N + O$
J_{NO2}	$NO_2 + h\nu$	$\longrightarrow$	$NO + O$
J_{NO31}	$NO_3 + h\nu$	$\longrightarrow$	$NO + O_2$
J_{NO32}	$NO_3 + h\nu$	$\longrightarrow$	$NO_2 + O$
J_{N2O5}	$N_2O_5 + h\nu$	$\longrightarrow$	$NO_2 + NO_3$
J_{JONO}	$N_2O_5 + h\nu$	$\longrightarrow$	$O + NO_2 + NO_3$
J_{HO2}	$HO_2 + h\nu$	$\longrightarrow$	$OH + O$
J_{HNO3}	$HNO_3 + h\nu$	$\longrightarrow$	$OH + NO_2$
J_{PNA}	$HO_2NO_2 + h\nu$	$\longrightarrow$	$HO_2 + NO_2$
J_{CNIT}	$ClONO_2 + h\nu$	$\longrightarrow$	$Cl + NO_3$
J_{CNT2}	$ClONO_2 + h\nu$	$\longrightarrow$	$ClO + NO_2$
J_{HOCl}	$HOCl + h\nu$	$\longrightarrow$	$OH + Cl$
J_{HCl}	$HCl + h\nu$	$\longrightarrow$	$H + Cl$
J_{CLO}	$ClO + h\nu$	$\longrightarrow$	$O + Cl$
J_{Cl2O2}	$Cl_2O_2 + h\nu$	$\longrightarrow$	$Cl + Cl + O_2$
J_{CLOOCL}	$CL_2O_2 + h\nu$	$\longrightarrow$	$ClO + ClO$
J_{OClO}	$OClO + h\nu$	$\longrightarrow$	$O + ClO$
J_{BrO}	$BrO + h\nu$	$\longrightarrow$	$Br + O$
J_{BNIT}	$BrONO_2 + h\nu$	$\longrightarrow$	$Br + NO_3$
J_{BrCl}	$BrCl + h\nu$	$\longrightarrow$	$Br + Cl$
J_{HBr}	$HBr + h\nu$	$\longrightarrow$	$Br + H$
J_{HOBr}	$HOBr + h\nu$	$\longrightarrow$	$Br + OH$
J_{H2O2}	$H_2O_2 + h\nu$	$\longrightarrow$	$2\,OH$
J_{N2O}	$N_2O + h\nu$	$\longrightarrow$	$N_2 + O$
J_{H2O}	$H_2O + h\nu$	$\longrightarrow$	$H + OH$
J_{CH4}	$CH_4 + h\nu$	$\longrightarrow$	$CH_3 + H$
J_{C2OA}	$CH_2O + h\nu$	$\longrightarrow$	$CHO + H$
J_{C2OB}	$CH_2O + h\nu$	$\longrightarrow$	$CO + H_2$
J_{MHP}	$CH_3OOH + h\nu$	$\longrightarrow$	$CH_3O + OH$
J_{CH3Cl}	$CH_3Cl + h\nu$	$\longrightarrow$	$CH_3 + Cl$
J_{MCFM}	$CH_3CCl_3 + h\nu$	$\longrightarrow$	$3\,Cl$ + products
J_{COFCL}	$COFCl + h\nu$	$\longrightarrow$	$Cl + HF$ + products
J_{F11}	$CFCl_3 + h\nu$	$\longrightarrow$	$3\,Cl$ + products
J_{F12}	$CF_2Cl_2 + h\nu$	$\longrightarrow$	$2\,Cl$ + products
J_{F22}	$CHF_2Cl + h\nu$	$\longrightarrow$	Cl + products
J_{F113}	$C_2F_3Cl_3 + h\nu$	$\longrightarrow$	$3\,Cl$ + products
J_{CCl4}	$CCl_4 + h\nu$	$\longrightarrow$	$4\,Cl$ + products
J_{CH3Br}	$CH_3Br + h\nu$	$\longrightarrow$	$CH_3 + Br$
J_{F12B1}	$CBrClF_2 + h\nu$	$\longrightarrow$	$Br + Cl$ + products
J_{F13B1}	$CF_3Br + h\nu$	$\longrightarrow$	Br + products

J_{COF2}	$\mathrm{COF_2} + h\nu$	$\longrightarrow$	$2\,\mathrm{HF}$ + products

Long-term impact of model constituents

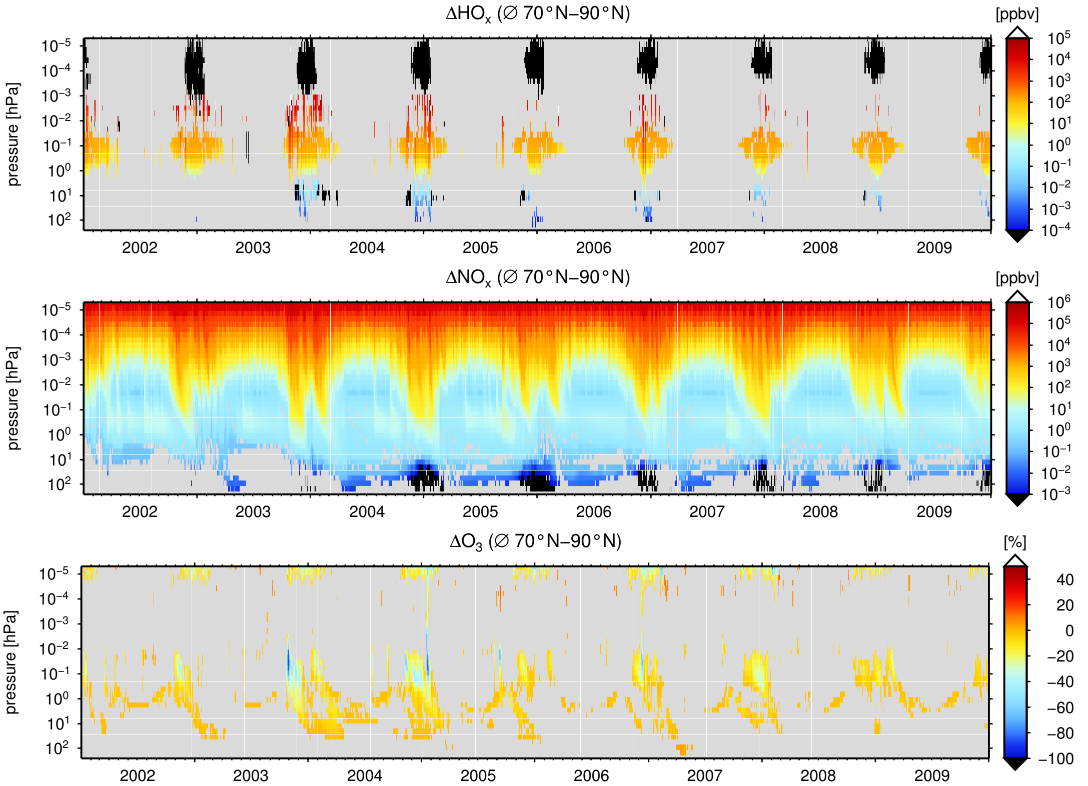

Figure 2 *Multi-year simulation of the impact on HO_x, NO_x, and O_3.*

WMO 2010 Scenario A1

The lower boundary conditions for input of green house gases and halo carbons from the troposphere into the stratosphere are taken from the WMO 2010 A1 scenario (Daniel & Velders, 2011).

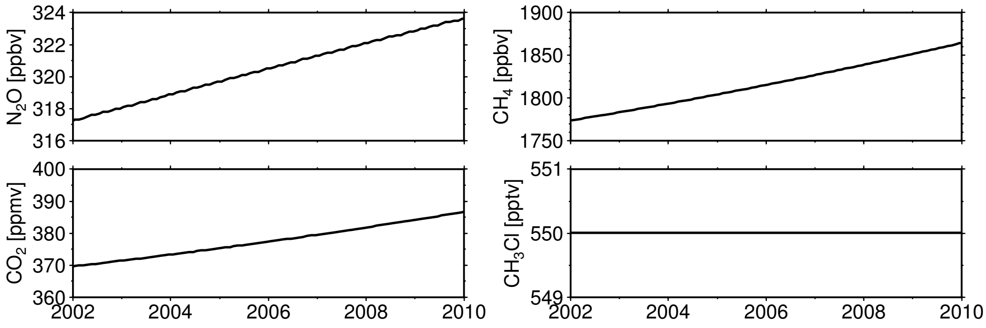

(a) Greenhouse gases

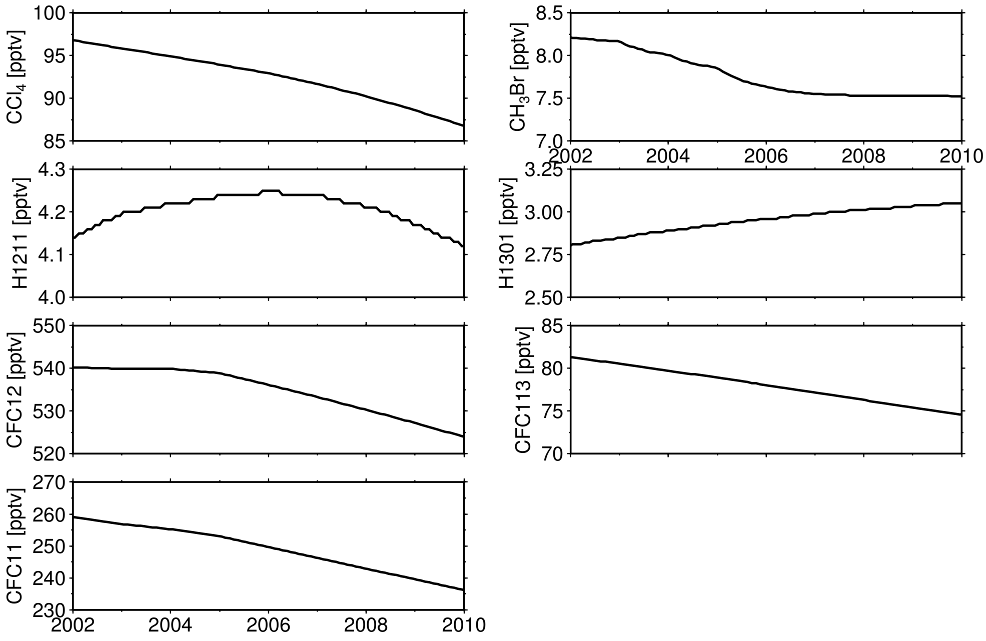

(b) Halo carbons

Figure 3 *Greenhouse gases (upper figure) and halo carbons (lower figure) lower model boundary input from WMO 2010 scenario A1 (Daniel & Velders, 2011) for the simulated period 2002-2010.*

Publications and presentations which evolved out of the framework of this thesis

Peer-reviewed paper

Funke, B., Baumgaertner, A., Calisto, M., Egorova, T., Jackman, C. H., Kieser, J., Krivolutsky, A., López-Puertas, M., Marsh, D. R., Reddmann, T., Rozanov, E., Salmi, S.-M., Sinnhuber, M., Stiller, G. P., Verronen, P. T., Versick, S., von Clarmann, T., Vyushkova, T. Y., Wieters, N., & Wissing, J. M. 2011. Composition changes after the "Halloween" solar proton event: the High Energy Particle Precipitation in the Atmosphere (HEPPA) model versus MIPAS data intercomparison study. *Atmos. Chem. Phys.*, **11**(17), 9089–9139.

Sinnhuber, M., Nieder, H., & Wieters, N. 2012. Energetic Particle Precipitation and the Chemistry of the Mesosphere/Lower Thermosphere. In: Crucial Processes Acting in the Mesosphere/Lower Thermosphere, E. Becker & M. Rycroft (ed.) *Surveys in Geophysics, Springer Netherlands*, **33**, 1281-1334.

Wissing, J. M., Kallenrode, M.-B., Wieters, N., Winkler, H., & Sinnhuber, M. 2010. Atmospheric Ionization Module Osnabrück (AIMOS): 2. Total particle inventory in the October-November 2003 event and ozone. *J. Geophys. Res. (Space Phys.)*, **115**(A2).

Book contributions

Sinnhuber, M., Wieters, N., & Winkler, H. 2012. The Impact of Energetic Particle Precipitation on the Chemical Composition of the Middle Atmosphere: Measurements and Model Predictions. *In:* Lübken, F.-J. (ed), *Climate And Weather of the Sun-Earth System (CAWSES): Highlights from a Priority Program.* Springer.

Wieters, N., Winkler, H., Sinnhuber, M., Wissing, J. M., & Notholt, J. 2012. Three Dimensional Model Simulations of the Impact of Solar Proton Events on Nitrogen Compounds and Ozone in the Middle Atmosphere. *In:* Lohmann, G. et al. (ed), *Earth System Science: Bridging the Gaps Between Disciplines: Perspectives from a Multi-Disciplinary Helmholtz Research School.* Springer.

Conference contributions

Wieters, N. 2008. *B3dCTM model results in comparison with MIPAS measurements.* Oral presentation. MIPAS Data-User Meeting and HEPPA MIPAS-Model Intercomparison, Karlsruhe, Germany, 2008.

Wieters, N., Sinnhuber, M., Winkler, H., Sinnhuber, B.-M., & Notholt, J. 2009. *Investigating the impact of solar proton events on the middle atmosphere on the basis of three dimensional model studies.* Oral presentation. DPG Frühjahrstagung, Hamburg, Germany, 2009.

Wieters, N., Sinnhuber, M., Winkler, H., Wissing, J. M., Stiller, G. P., Funke, B., & Notholt, J. 2010a. *Model simulations of the impact of energetic particle precipitation onto the upper and middle atmosphere.* Oral presentation. COSPAR, Bremen, Germany, 2010.

Wieters, N., Sinnhuber, M., Winkler, H., Sinnhuber, B.-M., Notholt, J., Wissing, J. M., & Stiller, G. P. 2010b. *Modeled impact of atmospheric ionisation by solar protons and magnetospheric electrons on upper stratospheric constituents compared with MIPAS measurements.* Oral presentation. 2nd International High Energy Particle Precipitation in the Atmosphere (HEPPA) Workshop, Boulder, Colorado, USA, 2010.

Wieters, N., Becker, E., Berger, U., Notholt, J., v. Savigny, C., Sinnhuber, M., Winkler, H., & Wissing, J. M. 2011. *Model simulations of the influence of EPPs on odd-hydrogen and ozone and the resultant effect on heating rates.* Oral presentation. 3rd HEPPA Workshop, Granada, Spain, 2011.

Poster presentations

Wieters, N., Winkler, H., Sinnhuber, M., Notholt, J., Stiller, G. P., von Clarmann, T., Funke, B., & Berger, U. 2010. *Three dimensional model simulations of the impact of ion-chemistry induced by solar particle precipitation on chlorine species.* SCOSTEP, 12.-16. July 2010, Berlin, Germany.

Wieters, N., Winkler, H., Sinnhuber, M., Notholt, J., Wissing, J. M., Berger, U., Stiller, G. P., von Clarmann, T., & Funke, B. 2011. *Three dimensional model simulations of the impact of solar particle precipitation on the upper polar atmosphere.* EGU General Assembly 2011, Vienna, Austria.

Wieters, N., Becker, E., Notholt, J., von Savigny, C., Sinnhuber, M. & Wissing, J. M. 2012. *Model simulations of the impact of energetic particle precipitation on the chemical composition and heating rates in the middle and upper atmosphere.* 4th International HEPPA Workshop in conjunction with SPARC/SOLARIS, 9.-12. October 2012, Boulder, Colorado, USA.

Bibliography

Agostinelli, S., Allison, J., Amako, K., Apostolakis, J., Araujo, H., Arce, P., Asai, M., Axen, D., Banerjee, S., Barrand, G., Behner, F., Bellagamba, L., Boudreau, J., Broglia, L., Brunengo, A., Burkhardt, H., Chauvie, S., Chuma, J., Chytracek, R., Cooperman, G., Cosmo, G., Degtyarenko, P., Dell'Acqua, A., Depaola, G., Dietrich, D., Enami, R., Feliciello, A., Ferguson, C., Fesefeldt, H., Folger, G., Foppiano, F., Forti, A., Garelli, S., Giani, S., Giannitrapani, R., Gibin, D., Gómez Cadenas, J. J., González, I., Abril, G. G., Greeniaus, G., Greiner, W., Grichine, V., Grossheim, A., Guatelli, S., Gumplinger, P., Hamatsu, R., Hashimoto, K., Hasui, H., Heikkinen, A., Howard, A., Ivanchenko, V., Johnson, A., Jones, F. W., Kallenbach, J., Kanaya, N., Kawabata, M., Kawabata, Y., Kawaguti, M., Kelner, S., Kent, P., Kimura, A., Kodama, T., Kokoulin, R., Kossov, M., Kurashige, H., Lamanna, E., Lampén, T., Lara, V., Lefebure, V., Lei, F., Liendl, M., Lockman, W., Longo, F., Magni, S., Maire, M., Medernach, E., Minamimoto, K., de Freitas, P. M., Morita, Y., Murakami, K., Nagamatu, M., Nartallo, R., Nieminen, P., Nishimura, T., Ohtsubo, K., Okamura, M., O'Neale, S., Oohata, Y., Paech, K., Perl, J., Pfeiffer, A., Pia, M. G., Ranjard, F., Rybin, A., Sadilov, S., Di Salvo, E., Santin, G., Sasaki, T., Savvas, N., Sawada, Y., Scherer, S., Seil, S., Sirotenko, V., Smith, D., Starkov, N., Stoecker, H., Sulkimo, J., Takahata, M., Tanaka, S., Tcherniaev, E., Tehrani, E. S., Tropeano, M., Truscott, P., Uno, H., Urban, L., Urban, P., Verderi, M., Walkden, A., Wander, W., Weber, H., Wellisch, J. P., Wenaus, T., Williams, D. C., Wright, D., Yamada, T., Yoshida, H., & Zschiesche, D. 2003. GEANT4-a simulation toolkit. *Nuclear Instruments & Methods in Physics Research Section A-Accelerators, Spectrometers, Detectors and Associated Equipment*, **506**(3), 250–303.

Akasofu, S.-I. 1964. The development of the auroral substorm. *Planetary and Space Science*, **12**(4), 273–282.

Alfvén, H. 1977. Electric Currents In Cosmic Plasmas. *Rev. Geophys.*, **15**(3), 271–284.

Amante, C., & Eakins, B. W. 2009. *ETOPO1 1 Arc-Minute Global Relief Model: Procedures, Data Sources and Analysis.* Tech. rept. National Geophysical Data Center, Marine Geology and Geophysics Division, Boulder, Colorado.

Aschmann, J. 2011. *Impact of Very Short-Lived Substances on Stratospheric Bromine Loading.* Ph.D. thesis, University of Bremen, Bremen.

Bates, D. R., & Nicolet, M. 1950. The photochemistry of atmospheric water vapor. *J. Geophys. Res.*, **55**(3), 301–327.

Baumgaertner, A. J. G., Seppääe, A., Jöckel, P., & Clilverd, M. A. 2011. Geomagnetic activity related NO_x enhancements and polar surface air temperature variability in a chemistry climate model: modulation of the NAM index. *Atmos. Chem. Phys.*, **11**(9), 4521–4531.

Becker, E. 2009. Sensitivity of the Upper Mesosphere to the Lorenz Energy Cycle of the Troposphere. *J. Atmos. Sci.*, **66**(3), 647–666.

Becker, E., & von Savigny, C. 2010. Dynamical heating of the polar summer mesopause induced by solar proton events. *J. Geophys. Res. (Atmos.)*, **115**(D1).

Berger, U. 2008. Modeling of middle atmosphere dynamics with LIMA. *J. Atmos. Solar Terr. Phys.*, **70**(8-9), 1170–1200.

Bönisch, H., Engel, A., Birner, Th., Hoor, P., Tarasick, D. W., & Ray, E. A. 2011. On the structural changes in the Brewer-Dobson circulation after 2000. *Atmos. Chem. Phys.*, **11**(8), 3937–3948.

Brasseur, G. P., & Solomon, S. 2005. *Aeronomy of the Middle Atmosphere: Chemistry and Physics of the Stratosphere and Mesosphere.* 3., rev. and enl. ed. edn. Atmospheric and Oceanographic Sciences Library, vol. 32. Dordrecht: Springer. XII, 644 S. : Ill.

Chapman, S. 1930. *A Theory of Upper-atmospheric Ozone.* Memoirs of the Royal Meteorological Society. Edward Stanford.

Chipperfield, M. 1996. *The TOMCAT Offline Chemical Transport Model Part I. Stratospheric Chemistry Code.* Tech. rept. Centre for Atmospheric Science, University of Cambridge.

Chipperfield, M. P. 1999. Multiannual simulations with a three-dimensional chemical transport model. *J. Geophys. Res. (Atmos.)*, **104**(D1), 1781–1805.

Cliver, E. W. 2008. History of research on solar energetic particle (SEP) events: the evolving paradigm. *Proceedings of the International Astronomical Union*, **4**(9), 401–412.

Crutzen, P. J. 1971. Ozone Production Rates in an Oxygen-Hydrogen-Nitrogen Oxide Atmosphere. *J. Geophys. Res.*, **76**(30), 7311–7327.

Crutzen, P. J., Isaksen, I. S. A., & Reid, G. C. 1975. Solar Proton Events: Stratospheric Sources of Nitric-Oxide. *Science*, **189**(4201), 457–459.

Daniel, J. S., & Velders, G. J. M. 2011. Scientific Summary Chapter 5: A Focus on Information and Options for Policymakers. *In: Scientific Assessment of Ozone Depletion: 2010, Global Ozone Research and Monitoring Project - Report No. 52.* World Meteorological Organization, Geneva, Switzerland.

Dee, D. P., Uppala, S. M., Simmons, A. J., Berrisford, P., Poli, P., Kobayashi, S., Andrae, U., Balmaseda, M. A., Balsamo, G., Bauer, P., Bechtold, P., Beljaars, A. C. M., van de Berg, L., Bidlot, J., Bormann, N., Delsol, C., Dragani, R., Fuentes, M., Geer, A. J., Haimberger, L., Healy, S. B., Hersbach, H., Hólm, E. V., Isaksen, L., Kållberg, P., Köhler, M., Matricardi, M., McNally, A. P., Monge-Sanz, B. M., Morcrette, J.-J., Park, B.-K., Peubey, C., de Rosnay, P., Tavolato, C., Thépaut, J.-N., & Vitart, F. 2011. The ERA-Interim reanalysis: configuration and performance of the data assimilation system. *Q. J. R. Meteorol. Soc.*, **137**(656, Part a), 553–597.

Evans, W. F. J., & Llewellyn, E. J. 1972. Measurements of Mesospheric Ozone from Observations of 1.27μ Band. *Radio Sci.*, **7**(1), 45–50.

Feldstein, Y. I., & Starkov, G. V. 1967. Dynamics of auroral belt and polar geomagnetic disturbances. *Planet. Space Sci.*, **15**(2), 209–229.

Feofilov, A. G., & Kutepov, A. A. 2012. Infrared Radiation in the Mesosphere and Lower Thermosphere: Energetic Effects and Remote Sensing. *Surv. Geophys.*, **33**(6, SI), 1231–1280.

Fischer, H., Birk, M., Blom, C., Carli, B., Carlotti, M., von Clarmann, T., Delbouille, L., Dudhia, A., Ehhalt, D., Endemann, M., Flaud, J. M., Gessner, R., Kleinert, A., Koopman, R., Langen, J., López-Puertas, M., Mosner, P., Nett, H., Oelhaf, H., Perron, G., Remedios, J., Ridolfi, M., Stiller, G., & Zander, R. 2008. MIPAS: an instrument for atmospheric and climate research. *Atmos. Chem. Phys.*, **8**(8), 2151–2188.

Frederick, J. E. 1976. Solar Corpuscular Emission and Neutral Chemistry in the Earth's Middle Atmosphere. *J. Geophys. Res. (Space Phys.)*, **81**(19), 3179–3186.

Funke, B., López-Puertas, M., Gil-López, S., von Clarmann, T., Stiller, G. P., Fischer, H., & Kellmann, S. 2005. Downward transport of upper atmospheric NO_x into the polar stratosphere and lower mesosphere during the Antarctic 2003 and Arctic 2002/2003 winters. *J. Geophys. Res. (Atmos.)*, **110**(D24).

Funke, B., Baumgaertner, A., Calisto, M., Egorova, T., Jackman, C. H., Kieser, J., Krivolutsky, A., López-Puertas, M., Marsh, D. R., Reddmann, T., Rozanov, E., Salmi, S.-M., Sinnhuber, M., Stiller, G. P., Verronen, P. T., Versick, S., von Clarmann, T., Vyushkova, T. Y., Wieters, N., & Wissing, J. M. 2011. Composition changes after the "Halloween" solar proton event: the High Energy Particle Precipitation in the Atmosphere (HEPPA) model versus MIPAS data intercomparison study. *Atmos. Chem. Phys.*, **11**(17), 9089–9139.

Gopalswamy, N., Yashiro, S., Michalek, G., Kaiser, M. L., Howard, R. A., Reames, D. V., Leske, R., & von Rosenvinge, T. 2002. Interacting Coronal Mass Ejections and Solar Energetic Particles. *The Astrophysical Journal Letters*, **572**(1), L103–L107.

Gopalswamy, N., Barbieri, L., Cliver, E. W., Lu, G., Plunkett, S. P., & Skoug, R. M. 2005. Introduction to violent Sun-Earth connection events of October-November 2003. *J. Geophys. Res. (Space Phys.)*, **110**(A9).

Grygalashvyly, M., Becker, E., & Sonnemann, G. R. 2011. Wave mixing effects on minor chemical constituents in the MLT region: Results from a global CTM driven by high-resolution dynamics. *J. Geophys. Res. (Atmos.)*, **116**(D18).

Jackman, C. H., Porter, H. S., & Frederick, J. E. 1979. Upper limits on production rate of NO per ion pair. *Nature*, **280**(5718), 170.

Jackman, C. H., Frederick, J. E., & Stolarski, R. S. 1980. Production of Odd Nitrogen in the Stratosphere and Mesosphere: An Intercomparison of Source Strengths. *J. Geophys. Res. (Oceans)*, **85**(C12), 7495–7505.

Jackman, C. H., DeLand, M. T., Labow, G. J., Fleming, E. L., Weisenstein, D. K., Ko, M. K. W., Sinnhuber, M., & Russell, J. M. 2005a. Neutral atmospheric influences of the solar proton events in October-November 2003. *J. Geophys. Res. (Space Phys.)*, **110**(A9).

Jackman, C. H., DeLand, M. T., Labow, G. J., Fleming, E. L., Weisenstein, D. K., Ko, M. K. W., Sinnhuber, M., Anderson, J., & Russell, J. M. 2005b. The influence of the several very large solar proton events in years 2000-2003 on the neutral middle atmosphere. *Adv. Space Res.*, **35**(3), 445–450. Influence of the Sun's Radiation and Particles on the Earth's Atmosphere and Climate.

Jackman, C. H., Roble, R., & Fleming, E. L. 2007. Mesospheric dynamical changes induced by the solar proton events in October-November 2003. *Geophys. Res. Lett.*, **34**(4).

Jacobson, M. Z. 2005. *Fundamentals of Atmospheric Modeling.* 2nd edn. Cambridge University Press.

Kallenrode, M. B. 2003. Current views on impulsive and gradual solar energetic particle events. *J. Phys. G: Nucl. Part. Phys.*, **29**(5), 965–981.

Kiehl, J. T., & Solomon, S. 1986. On the Radiative Balance of the Stratosphere. *J. Atmos. Sci.*, **43**(14), 1525–1534.

Krivolutsky, A. A., Klyuchnikova, A. V., Zakharov, G. R., Vyushkova, T. Yu., & Kuminov, A. A. 2006. Dynamical response of the middle atmosphere to solar proton event of July 2000: Three-dimensional model simulations. *Adv. Space Res.*, **37**(8), 1602–1613. Particle Acceleration; Space Plasma Physics; Solar Radiation and the Earth's Atmosphere and Climate.

Lary, D. J. 1997. Catalytic destruction of stratospheric ozone. *J. Geophys. Res. (Atmos.)*, **102**(D17), 21515–21526.

López-Puertas, M., & Taylor, F. W. 2001. *Non-LTE Radiative Transfer in the Atmosphere.* Series on Atmospheric, Oceanic and Planetary Physics, vol. 3. Singapore: World Scientific.

López-Puertas, M., Funke, B., Gil-López, S., von Clarmann, T., Stiller, G. P., Höpfner, M., Kellmann, S., Fischer, H., & Jackman, C. H. 2005. Observation of NO_x enhancement and ozone depletion in the Northern and Southern Hemispheres after the October-November 2003 solar proton events. *J. Geophys. Res. (Space Phys.)*, **110**(A9).

López-Puertas, M., Funke, B., Von Clarmann, T., Fischer, H., & Stiller, G. P. 2006. The Stratospheric and Mesospheric NO_y in the 2002-2004 Polar Winters as measured by MIPAS/ENVISAT. *Space Sci. Rev.*, **125**(1-4), 403–416.

Lübken, F.-J., Austin, J., Langematz, U., & Oberheide, J. 2010. Introduction to special section on Climate and Weather of the Sun Earth System. *J. Geophys. Res. (Atmos.)*, **115**(D1).

Manney, G. L., Krüger, K., Sabutis, J. L., Sena, S. A., & Pawson, S. 2005. The remarkable 2003-2004 winter and other recent warm winters in the Arctic stratosphere since the late 1990s. *J. Geophys. Res. (Atmos.)*, **110**(D4).

Marsh, D., Smith, A., Brasseur, G., Kaufmann, M., & Grossmann, K. 2001. The existence of a tertiary ozone maximum in the high-latitude middle mesosphere. *Geophys. Res. Lett.*, **28**(24), 4531–4534.

McLinden, C. A., Olsen, S. C., Hannegan, B., Wild, O., Prather, M. J., & Sundet, J. 2000. Stratospheric ozone in 3-D models: A simple chemistry and the cross-tropopause flux. *J. Geophys. Res. (Atmos.)*, **105**(D11), 14653–14665.

Mewaldt, R. A., Cohen, C. M. S., Labrador, A. W., Leske, R. A., Mason, G. M., Desai, M. I., Looper, M. D., Mazur, J. E., Selesnick, R. S., & Haggerty, D. K. 2005. Proton, helium, and electron spectra during the large solar particle events of October-November 2003. *J. Geophys. Res. (Space Phys.)*, **110**(A9).

Milan, S. E., Hutchinson, J., Boakes, P. D., & Hubert, B. 2009. Influences on the radius of the auroral oval. *Ann. Geophys.*, **27**(7), 2913–2924.

Mlynczak, M. G., & Solomon, S. 1991. Middle atmosphere heating by exothermic chemical-reactions involving odd-hydrogen species. *Geophys. Res. Lett.*, **18**(1), 37–40.

Nesse Tyssøy, H., Stadsnes, J., Sørbø, M., Mertens, C. J., & Evans, D. S. 2010. Changes in upper mesospheric and lower thermospheric temperatures caused by energetic particle precipitation. *J. Geophys. Res. (Space Phys.)*, **115**(A10).

Porter, H. S., Jackman, C. H., & Green, A. E. S. 1976. Efficiencies for production of atomic nitrogen and oxygen by relativistic proton impact in air. *J. Chem. Phys.*, **65**(1), 154–167.

Prather, M. J. 1986. Numerical Advection by Conservation of Second-Order Moments. *J. Geophys. Res.*, **91**(D6), 6671–6681.

Pulkkinen, T. 2007. Space Weather: Terrestrial Perspective. *Living Reviews in Solar Physics*, **4**(1).

Ramaroson, R., Pirre, M., & Cariolle, D. 1992. A Box Model for Online Computations of Diurnal-Variations in a 1D Model: Potential for Application in Multidimensional Cases. *Ann. Geophys.*, **10**(6), 416–428.

Randall, C. E., Harvey, V. L., Manney, G. L., Orsolini, Y., Codrescu, M., Sioris, C., Brohede, S., Haley, C. S., Gordley, L. L., Zawodny, J. M., & Russell, J. M. 2005. Stratospheric effects of energetic particle precipitation in 2003-2004. *Geophys. Res. Lett.*, **32**(5).

Reames, D. V. 1999. Particle acceleration at the Sun and in the heliosphere. *Space Sci. Rev.*, **90**(3-4), 413–491.

Reames, D. V. 2002. Magnetic Topology of Impulsive and Gradual Solar Energetic Particle Events. *The Astrophysical Journal Letters*, **571**(1), L63–L66.

Reames, D. V., Barbier, L. M., & Ng, C. K. 1996. The Spatial Distribution of Particles Accelerated by Coronal Mass Ejection-driven Shocks. *Astrophysical Journal*, **466**(1), 473–486.

Rohen, G., von Savigny, C., Sinnhuber, M., Llewellyn, E. J., Kaiser, J. W., Jackman, C. H., Kallenrode, M. B., Schröter, J., Eichmann, K. U., Bovensmann, H., & Burrows, J. P. 2005. Ozone depletion during the solar proton events of October/November 2003 as seen by SCIAMACHY. *J. Geophys. Res. (Space Phys.)*, **110**(A9).

Rusch, D. W., Gerard, J. C., Solomon, S., Crutzen, P. J., & Reid, G. C. 1981. The effect of particle precipitation events on the neutral and ion chemistry of the middle atmosphere–I. Odd nitrogen. *Planet. Space Sci.*, **29**(7), 767–774.

Russell, C. T. 2000. The solar wind interaction with the Earth's magnetosphere: A tutorial. *IEEE T. Plasma. Sci.*, **28**(6), 1818–1830.

Salby, M. L. 2012. *Physics of the Atmosphere and Climate.* [2. ed.], rev. edn. Cambridge Univ. Press.

Sander, S. P., Friedl, R. R., Ravishankara, A. R., Golden, D. M., Kolb, C. E., Kurylo, M. J., Molina, M. J., Moortgat, G. K., Keller-Rudek, H., Finlayson-Pitts, B. J., Wine, P., Huie, R. E., & Orkin, V. L. 2006. *Chemical Kinetics and Photochemical Data for Use in Atmospheric Studies, Evaluation Number 15, JPL Publication 06-2.* Jet Propulsion Laboratory, Pasadena.

Schrijver, C. J., & Siscoe, G. L. (eds). 2010. *Heliophysics: Space Storms and Radiation: Causes and Effects.* Cambridge Univ. Press.

Schwenn, R. 2006. Space Weather: The Solar Perspective. *Living Reviews in Solar Physics*, **3**(2).

Seppälä, A., Randall, C. E., Clilverd, M. A., Rozanov, E., & Rodger, C. J. 2009. Geomagnetic activity and polar surface air temperature variability. *J. Geophys. Res. (Space Phys.)*, **114**(A10).

Shine, K. 1989. Sources and sinks of zonal momentum in the middle atmosphere diagnosed using the diabatic circulation. *Q. J. R. Meteorol. Soc.*, **115**(486, Part B), 265–292.

Shine, K. P. 1987. The Middle Atmosphere in the Absence of Dynamical Heat Fluxes. *Q. J. R. Meteorol. Soc.*, **113**(476), 603–633.

Sinnhuber, B.-M., Weber, M., Amankwah, A., & Burrows, J. P. 2003a. Total ozone during the unusual Antarctic winter of 2002. *Geophys. Res. Lett.*, **30**(11).

Sinnhuber, M., Burrows, J. P., Chipperfield, M. P., Jackman, C. H., Kallenrode, M. B., Kunzi, K. F., & Quack, M. 2003b. A model study of the impact of magnetic field structure on atmospheric composition during solar proton events. *Geophys. Res. Lett.*, **30**(15).

Sinnhuber, M., Nieder, H., & Wieters, N. 2012. Energetic Particle Precipitation and the Chemistry of the Mesosphere/Lower Thermosphere. *Surv. Geophys.*, **33**(6), 1281–1334.

Smith, A. K. 2012. Interactions Between the Lower, Middle and Upper Atmosphere. *Space Sci. Rev.*, **168**(1-4), 1–21.

Smith, A. K., & Marsh, D. R. 2005. Processes that account for the ozone maximum at the mesopause. *J. Geophys. Res. (Atmos.)*, **110**(D23).

Sofieva, V. F., Kyrölä, E., Verronen, P. T., Seppälä, A., Tamminen, J., Marsh, D. R., Smith, A. K., Bertaux, J.-L., Hauchecorne, A., Dalaudier, F., Fussen, D., Vanhellemont, F., Fanton d'Andon, O., Barrot, G., Guirlet, M., Fehr, T., & Saavedra, L. 2009. Spatio-temporal observations of the tertiary ozone maximum. *Atmos. Chem. Phys.*, **9**(13), 4439–4445.

Solomon, S., Rusch, D. W., Gérard, J. C., Reid, G. C., & Crutzen, P. J. 1981. The effect of particle precipitation events on the neutral and ion chemistry of the middle atmosphere: II. Odd hydrogen. *Planet. Space Sci.*, **29**(8), 885–893.

Swider, W., & Keneshea, T. J. 1973. Decrease of ozone and atomic oxygen in the lower mesosphere during a PCA event. *Planet. Space Sci.*, **21**(11), 1969–1973.

Swinbank, R., & O'Neill, A. 1994. A Stratosphere-Troposphere Data Assimilation System. *Mon. Weather Rev.*, **122**(4), 686–702.

Tsurutani, B. T., Gonzalez, W. D., Tang, F., Akasofu, S. I., & Smith, E. J. 1988. Origin of Interplanetary Southward Magnetic-Fields Responsible for Major Magnetic Storms Near Solar Maximum (1978-1979). *J. Geophys. Res. (Space Phys.)*, **93**(A8), 8519–8531.

Uppala, S. M., Kållberg, P. W., Simmons, A. J., Andrae, U., Bechtold, V. D., Fiorino, M., Gibson, J. K., Haseler, J., Hernandez, A., Kelly, G. A., Li, X., Onogi, K., Saarinen, S., Sokka, N., Allan, R. P., Andersson, E., Arpe, K., Balmaseda, M. A., Beljaars, A. C. M., Van De Berg, L., Bidlot, J., Bormann, N., Caires, S., Chevallier, F., Dethof, A., Dragosavac, M., Fisher, M., Fuentes, M., Hagemann, S., Hólm, E., Hoskins, B. J., Isaksen, L., Janssen, P. A. E. M., Jenne, R., McNally, A. P., Mahfouf, J. F., Morcrette, J. J., Rayner, N. A., Saunders, R. W., Simon, P., Sterl, A., Trenberth, K. E., Untch, A., Vasiljevic, D., Viterbo, P., & Woollen, J. 2005. The ERA-40 re-analysis. *Q. J. R. Meteorol. Soc.*, **131**(612, Part B), 2961–3012.

von Clarmann, T., Glatthor, N., Höpfner, M., Kellmann, S., Ruhnke, R., Stiller, G. P., Fischer, H., Funke, B., Gil-López, S., & López-Puertas, M. 2005. Experimental evidence of perturbed odd hydrogen and chlorine chemistry after the October 2003 solar proton events. *J. Geophys. Res. (Space Phys.)*, **110**(A9).

Weeks, L. H., Corbin, J. R., & Cuikay, R. S. 1972. Ozone Measurements in the Mesosphere During The Solar Proton Event of 2 November 1969. *J. Atmos. Sci.*, **29**(6), 1138–1142.

Wieters, N. 2008. *Entwicklung eines dreidimensionalen Chemie-Transport-Modells (B3dCTM) durch Kopplung eines dreidimensionalen stratosphärischen Transport-Modells mit einem stratosphärischen Chemie-Schema.* Diplomarbeit, Universität Bremen, Institut für Umweltphysik.

Winkler, H., Sinnhuber, M., Notholt, J., Kallenrode, M.-B., Steinhilber, F., Vogt, J., Zieger, B., Glassmeier, K.-H., & Stadelmann, A. 2008. Modeling impacts of geomagnetic field variations on middle atmospheric ozone responses to solar proton events on long timescales. *J. Geophys. Res. (Atmos.)*, **113**(D2).

Winkler, H., Kazeminejad, S., Sinnhuber, M., Kallenrode, M.-B., & Notholt, J. 2009. Conversion of mesospheric HCl into active chlorine during the solar proton event in July 2000 in the northern polar region. *J. Geophys. Res. (Atmos.)*, **114**(D1).

Winkler, H., Kazeminejad, S., Sinnhuber, M., Kallenrode, M.-B., & Notholt, J. 2011. Correction to "Conversion of mesospheric HCl into active chlorine during the solar proton event in July 2000 in the northern polar region". *J. Geophys. Res. (Atmos.)*, **116**(D17).

Wissing, J. M., & Kallenrode, M.-B. 2009. Atmospheric Ionization Module Osnabrück (AIMOS): A 3-D model to determine atmospheric ionization by energetic charged particles from different populations. *J. Geophys. Res. (Space Phys.)*, **114**(A6).

Wissing, J. M., Kallenrode, M.-B., Wieters, N., Winkler, H., & Sinnhuber, M. 2010. Atmospheric Ionization Module Osnabrück (AIMOS): 2. Total particle inventory in the October-November 2003 event and ozone. *J. Geophys. Res. (Space Phys.)*, **115**(A2).

Acronyms

AIMOS	Atmospheric Ionization Module Osnabrück
B3dCTM	Bremen 3-dimensional Chemistry and Transport Model
CAWSES	Climate and Weather of the Sun Earth System
CCM	Chemistry and Climate Model
CIR	Corotating Interaction Region
CME	Coronal Mass Ejection
CTM	Chemistry and Transport Model
DFG	Deutsche Forschungsgemeinschaft
DU	Dobson Unit
ECMWF	European Centre for Medium-Range Weather Forecasts
EEP	Energetic Electron Precipitation
ENVISAT	Environmental Satellite
EPP	Energetic Particle Precipitation
ESSReS	Earth System Sciences Research School
FAP	Flare Accelerated Particle
GCM	General Circulation Model
GW	gravity wave
HEPPA	High Energy Particle Precipitation in the Atmosphere
IAP	Leibniz-Institut für Atmosphärenphysik
ICME	Interplanetary Coronal Mass Ejection
IMF	Interplanetary Magnetic Field
IUP	Institut für Umweltphysik
KMCM	Kühlungsborn Mechanistic general Circulation Model
LIMA	Leibniz-Institute Middle Atmosphere
LTE	Local Thermodynamical Equilibrium
MIDRAD	Middle Atmosphere Radiation Scheme
MIPAS	Michelson Interferometer for Passive Atmospheric Sounding

MLT	Mesosphere and Lower Thermosphere
ODE	Ordinary Differential Equation
PACS	Particle Accelerated at CME Shock
SEP	Solar Energetic Particle
SIS	Semi-Implicit Symmetric
SPE	Solar Proton Event
SSW	Sudden Stratospheric Warming
TEM	Transformed Eulerian Mean
UBIC	University of Bremen Ion Chemistry
UKMO	UK Met Office
vmr	volume mixing ratio
WACCM	Whole Atmosphere Community Climate Model

Acknowledgements

I would like to thank Prof. Dr. Justus Notholt for supervising this PhD work and giving me the opportunity to do this work in his research group. I would also like to cordially thank Dr. Miriam Sinnhuber for her enormous support during the work on this PhD thesis. I am especially grateful to Dr. Holger Winkler for being a great colleague, for sharing the same office, and answering all my silly questions.

I would also like to thank Dr. Jan Aschmann for his support in many computational problems and questions related to the model. I am especially grateful to Dr. Christoph Hoffmann for his collegial support during my work at the IUP. I also would like to thank all other colleges in the research group. I appreciate my work in this very friendly and supportive environment.

I thank Dr. Jan Maik Wissing from the University of Osnabrück for providing the AIMOS ionisation rates, Dr. Uwe Berger and Dirk Rachholz from Leibniz-Institut für Atmosphärenphysik (IAP), Kühlungsborn for providing the LIMA data, and also Prof. Dr. Erich Becker and Annekatrin Kirsch from IAP, Kühlungsborn for providing the KMCM data.

I thank Birgit Teuchert for her support concerning all bureaucratic matters. For their great support in overcoming all small and big IT obstacles I want to thank Peter Grupe, as well as Heiko Schellhorn and Heiko Schröter.

A appreciated for the opportunity to join the graduate school Earth System Sciences Research School (ESSReS) and would like to thank especially Dr. Klaus Grosfeld for his great effort in making this a very insightful and enjoyable time. I also would like to thank Prof. Dr. Christian von Savigny and Dr. Ralph Lehmann for their support as members of my ESSReS PhD committee.

Part of this work was financially supported by the German Research Council (DFG) within the priority programme CAWSES (Climate and Weather of the Sun-Earth System) and in the DFG project 'Implifications of energetic particle precipitation events for the temperature and dynamics of the atmosphere - a model study'.